UNIVERSITY OF SOUTHAMPTON

SATELLITE AND LAGRANGIAN OBSERVATIONS OF MESOSCALE SURFACE PROCESSES IN THE SOUTHWESTERN ATLANTIC OCEAN

by
Ronald Buss de Souza

Thesis submitted in partial fulfilment of the requirements for the degree of Doctor of Philosophy

School of Ocean and Earth Science
Faculty of Science

March 2000

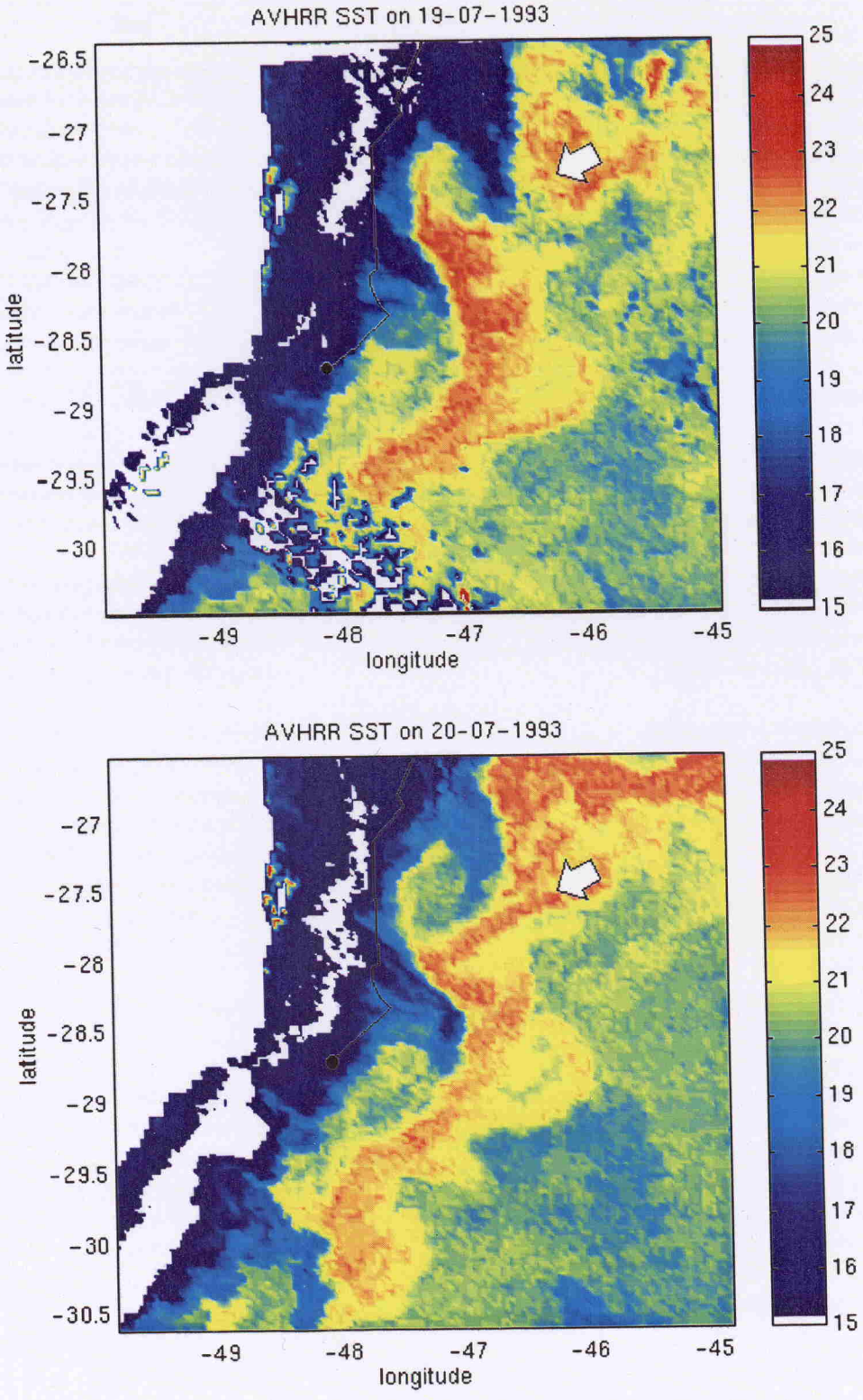

Frontispiece. *One-day sequence of AVHRR images taken in 19 July 1993 and 20 July 1993. The sequence illustrates the development of a mushroom-like structure in the Brazil Current (BC) in the vicinity of Santa Marta Cape at 28°S (indicated by the arrows). The trajectory of a Low Cost Drifter moving northwards in the Brazilian Coastal Current (BCC) is also seen. The sequence illustrates the complex interaction between BC and BCC waters at the shelf break in the southern coast off Brazil.*

Para Tati e Bela este trabalho e todos os outros

2nd

"Who cares about the sailor's birthplace,
To where he belongs, which is his home?...
He loves the rhythm of the verse
Taught to him by the old sea!
Sing! 'cause the night is divine!
The brig slips to the bowline
Like a fast dolphin
Tied to the rear mast
A nostalgic flag waves
To the wakes it leaves behind.

The Spaniard's cantilenas
Broken with languor
Resemble the dark-haired girls
The Andalucians in flower.
From Italy the indolent son
Sings a sleepy Venice
- Land of love and treason -
Or perhaps in the gulf's lap
Remembers the verses of Tasso
Beside the lava of the Volcano!

The Englishman – cold sailorman,
Who, when born, found himself at the sea
(Because England is a ship,
That God anchored in the Channel)
Stiffly proclaims his country's glories,
Proudly remembering stories
Of Nelson and Aboukir.
The Frenchman – predestined
Sings the past laurels
And the laurel trees of future...

The Hellenic sailors,
Created by the Ionian wave,
Beautiful dark-skinned pirates
Of the sea that Ulysses crossed,
Men shaped by Pheidias,
Go singing in clear nights
Verses that Homer moaned...
...Sailors from all over the place!
You know how to find in the waves
The melodies of the sky..."

2º

"Que importa do nauta o berço,
Donde é filho, qual seu lar?...
Ama a cadência do verso
Que lhe ensina o velho mar!
Cantai! que a noite é divina!
Resvala o brigue à bolina
Como um golfinho veloz.
Presa ao mastro da mezena
Saudosa bandeira acena
Às vagas que deixa após.

Do espanhol as cantilenas
Requebradas de langor,
Lembram as moças morenas,
As andaluzas em flor.
Da Itália o filho indolente
Canta Veneza dormente
– Terra de amor e traição –
Ou do golfo no regaço
Relembra os versos do Tasso
Junto às lavas do Vulcão!

O inglês – marinheiro frio,
Que ao nascer no mar se achou
(Porque a Inglaterra é um navio,
Que Deus na Mancha ancorou),
Rijo entoa pátrias glórias,
Lembrando orgulhoso histórias
De Nelson e de Aboukir.
O francês – predestinado –
Canta os louros do passado
E os loureiros do porvir...

Os marinheiros helenos,
Que a vaga iônica criou,
Belos piratas morenos
Do mar que Ulisses cortou,
Homens que Fídias talhara,
Vão cantando em noite clara
Versos que Homero gemeu...
...Nautas de todas as plagas!
Vós sabeis achar nas vagas
As melodias do céu..."

(Castro Alves, The Slave Ship, 1868)
Translation by R. Souza

University of Southampton

ABSTRACT

FACULTY OF SCIENCE

OCEANOGRAPHY

Doctor of Philosophy

Satellite and Langrangian observations of mesoscale surface processes in the Southwestern Atlantic Ocean

by Ronald Buss de Souza

This work presents a study of the mesoscale surface processes occurring in the Southwestern Atlantic Ocean. Two regions in this ocean, the Brazil-Malvinas (Falkland) Confluence (BMC) Zone and the South Brazilian Continental Shelf (SBCS) are studied by means of a 14 year long series of low-resolution Multi-Channel Sea Surface Temperature (MCSST) images of the Advanced Very High Resolution Radiometer (AVHRR) together with high-resolution data from the same sensor and Lagrangian (buoy) data for the period between March 1993 and July 1994. The AVHRR and buoy data were available from the project COROAS (Oceanic Circulation in the Western Region of the South Atlantic), the Brazilian contribution to the World Ocean Circulation Experiment (WOCE).

The variability of the sea surface temperature (SST) fields in the South Atlantic is investigated for the period between January 1982 and December 1995 utilising Principal Component analysis techniques on the MCSST data set. The distribution and oscillation of the SST fields of the South Atlantic are compared to those present in the BMC and SBCS regions, as described by the high-resolution AVHRR and buoy data.

The oceanographic surface frontal systems observed in the AVHRR images and buoy trajectories are also studied for the BMC and SBCS regions during 1993 and 1994. Direct measurements of currents taken by the buoys are utilised to describe the characteristics of the Brazil Current (BC), the South Atlantic Current (SAC) and the Brazilian Coastal Current (BCC). These currents are described by their mean surface velocities, kinetic energies, temperature statistics and oscillations. The BCC is a newly described current, very poorly understood in the past and very important for fisheries and, possibly, for the weather of the southern region of Brazil. The surface component of the BCC is described in this thesis as a coastal, northeasterly current flowing in opposition to the BC main flow and with a seasonal behaviour off the South American coast.

The eddy field present in the BMC and SBCS regions during 1993 and 1994 is investigated in this work as well. Distinct behaviour and driving mechanisms are reported for the eddies present in these two areas of the Southwestern Atlantic. For the first time in the known literature, small scale and shelfbreak eddies are described for the SBCS region. The nature of these small scale eddies is discussed in relation to that of the mesoscale, geostrophically balanced BMC eddies already known to occur in the study area. The importance of the shear instabilities in the oceanographic front between the BC and the BCC for the eddy generation and mixture processes is emphasised here. Comparing AVHRR and buoy data, empirical relationships are obtained for linking eddy sizes to their rotational periods and tangential velocities. The relationships are useful for monitoring the effects of the eddies in the ocean by remote sensing techniques when *in situ* data are lacking.

The question of whether the high-resolution satellite images utilised in this work are truly representing the SST of the ocean is also addressed here. Moreover, with the support of extra satellite data from the Along-Track Scanning Radiometer (ATSR) and *in situ* data from ships of opportunity, we investigate the nature of the temperature differences (deltaT) between 'skin' and 'bulk' SSTs in the study area. 'Match-ups' between satellite and *in situ* SSTs demonstrated the presence of a bias in the satellite estimates of SST. DeltaT images also indicated that, owing to the highly dynamic nature of the BMC and BC/BCC fronts, large errors can arise when matching-up buoy with satellite data in these areas.

Declaration

I hereby declare that the work presented within this thesis is my own and was undertaken wholly whilst registered as a full-time postgraduate at the University of Southampton.

Ronald Buss de Souza
March 2000

Table of Contents

List of Figures iv

List of Tables viii

Acknowledgements ix

Acronyms x

Chapter 1. Introduction 1

1.1. Preface 1

1.2. Objectives 4

1.3. Structure of the thesis 6

Chapter 2. Surface circulation of the Southwestern Atlantic Ocean 7

2.1. Currents and water masses 7

2.2. Brazil Current transport and coastal interactions 12

2.3. Mesoscale processes and features 13

2.4. Measurements of the Brazil-Malvinas Confluence variability 14

2.5. Lagrangian measurements of currents and kinetic energies 19

2.6. Brazil-Malvinas Confluence eddies 21

Chapter 3. Satellite observations of the ocean 25

3.1. Historical perspective 25

3.2. Thermal infrared imagery 28
3.2.1. Satellites and sensors 28
3.2.2. Sea surface temperature estimates 33

Chapter 4. Data and data processing methods 37

4.1. Low Cost Drifters 37
4.1.1. Characteristics of the buoys and associated data 37
4.1.2. Data processing 44
4.1.2.1. Pre-processing and quality control 44
4.1.2.2. Time series 44
4.1.2.3. Mean current and kinetic energies 45
4.1.2.4. FFT analysis 48
4.1.2.5. Eddy observations 50

4.2. AVHRR images 53
4.2.1. High-resolution images 53

4.2.2. MCSST global dataset..... 58
4.2.3. Location of the Subtropical Front and of the BC and BCC extremes..... 59
4.2.4. Eddy observations..... 61
4.2.5. Principal Component analysis..... 62

4.3. ATSR images..... 65

4.4. Bulk temperatures from ships of opportunity..... 66

4.5. Match-ups between *in situ* and satellite sea surface temperatures..... 67

4.6. Temperature difference images..... 70

4.7. Superimposition of buoy tracks onto satellite images..... 72

Chapter 5. Mesoscale surface processes in the Brazil-Malvinas Confluence Zone.... 73

5.1. Introduction..... 73

5.2. Variability of the SST fields in the South Atlantic Ocean..... 74
5.2.1. The climatological SST fields..... 74
5.2.2. The anomaly SST fields..... 84

5.3. SST fields in the BMC region and its vicinity in 1993 and 1994..... 95
5.3.1. MCSST fields..... 95
5.3.2. High-resolution SST fields..... 98
5.3.3. Frontal activity..... 103
5.3.3.1. Spatial distribution..... 103
5.3.3.2. Thermal gradients..... 107

5.4. Lagrangian measurements..... 113
5.4.1. Trajectories..... 113
5.4.2. Buoy time series..... 117
5.4.3. Velocity, kinetic energy and temperature statistics..... 119
5.4.4. BC and SAC energy spectra..... 121

5.5. Summary and final remarks..... 141

Chapter 6. The Brazilian Coastal Current..... 145

6.1. Introduction..... 145

6.2. The BCC in 1993 and 1994..... 147
6.2.1. Trajectories and high-resolution imagery..... 147
6.2.2 Current velocity, kinetic energies and temperatures..... 153
6.2.3. BCC energy spectra..... 155

6.3. The BCC and BC extreme positions..... 159

6.4. Summary and final remarks..... 166

Chapter 7. Eddy observations and characterisation..... 169

7.1. Introduction..... 169

7.2. The eddies in the buoy trajectories..... 171

7.3. The eddies in the high-resolution AVHRR images..... 180

7.4. Summary and final remarks..... 188

Chapter 8. The relationship between *in situ* and satellite sea surface temperatures.. 191

8.1. Introduction..... 191

8.2. Match-ups between *in situ* and satellite sea surface temperatures..... 192

8.3. ATSR and temperature difference images..... 201

8.4. Summary and final remarks..... 219

Chapter 9. Conclusions and future work..... 221

References..... 225

List of Figures

Figure 1.1. The Southwestern Atlantic Ocean: bathymetry and main features..... 2
Figure 2.1. Surface circulation in the South Atlantic..... 8
Figure 2.2. T-S diagram for the Southwestern Atlantic Ocean..... 11
Figure 2.3. High and low atmospheric pressure systems in the South Atlantic ocean at reduced sea level: summer mean..... 16
Figure 2.4. High and low atmospheric pressure systems in the South Atlantic ocean at reduced sea level: winter mean..... 17
Figure 2.5. Surface winds in the South Atlantic ocean: summer mean..... 18
Figure 2.6. Surface winds in the South Atlantic ocean: winter mean..... 19
Figure 2.7. AVHRR image of the Brazil-Malvinas Confluence zone obtained in February 1985..... 22
Figure 3.1. ATSR scan geometry..... 31
Figure 4.1. Photograph of the WOCE standard Low Cost Drifter (LCD) fabricated at INPE..... 38
Figure 4.2. Squematic of the LCD..... 39
Figure 4.3. Overall trajectories of the LCDs used in this work..... 43
Figure 4.4. Frequency histogram of the locations per day for the LCDs..... 43
Figure 4.5. Frequency histogram of the eddies rotational periods..... 52
Figure 4.6. Frequency histogram of the eddies perimeters..... 52
Figure 4.7. Frequency histogram of the AVHRR eddies perimeters..... 62
Figure 4.8. Frequency distribution of the number of match-up points between *in situ* and AVHRR temperatures..... 70
Figure 5.1. Climatological monthly averaged images representing the period between 1982 and 1995..... 76
Figure 5.2. SST fields for the Southwestern Atlantic in January and July..... 79
Figure 5.3. PC1, PC2, PC3 and PC4 derived from the climatological MCSST images..... 80
Figure 5.4. Temporal amplitudes or eigenvectors of the MCSST monthly climatological PC1, PC2, PC3 and PC4..... 83
Figure 5.5. Factor loadings of the MCSST monthly climatological PC1, PC2, PC3 and PC4..... 84
Figure 5.6. PC1, PC2, PC3 and PC4 derived from the seasonally averaged MCSST anomalies..... 86
Figure 5.7. Eigenvalues of the seasonally averaged MCSST anomalies..... 87
Figure 5.8. Idealised circulation scheme in the Southwestern Atlantic Ocean..... 88
Figure 5.9. Temporal amplitudes for the seasonally averaged MCSST anomalies PC1, PC2, PC3 and PC4..... 90
Figure 5.10. MCSST seasonal anomalies in the South Atlantic for the period between January 1982 to December 1995: Spatial mean, standard deviation, minumum and maximum..... 91
Figure 5.11. Energy preserving spectra for temporal amplitudes of the seasonally averaged MCSST anomalies PC1, PC2, PC3 and PC4..... 91
Figure 5.12. Factor loadings for the seasonally averaged MCSST anomalies PC1, PC2, PC3 and PC4..... 93
Figure 5.13. Seasonally averaged MCSST anomalies for the winter 1993, autumn 1994, spring 1982 and spring 1991..... 95
Figure 5.14. MCSST and anomaly images for March 1993, September 1993 and March 1994..... 97
Figure 5.15. Temporal sequence of SST in the BMC region and its vicinity..... 100

Figure 5.16. BC/BCC and western Subtropical fronts as defined by the 20°C isoline positions taken from all the high-resolution AVHRR images available for the period between March 1993 and July 1994 104
Figure 5.17. BC/BCC and western Subtropical fronts as defined by the 20°C isoline positions taken from a set of 15 images representing the consecutive months between March 1993 and June 1994 105
Figure 5.18. AVHRR images of 11 March 1994 and 5 May 1994 superimposed onto buoy tracks in the BMC region 106
Figure 5.19. AVHRR SST image of 10 March 1993 and the SST profile in 2 particular transects across the image 110
Figure 5.20. AVHRR SST image of 27 April 1993 and the SST profile in 2 particular transects across the image 110
Figure 5.21. AVHRR SST image of 3 August 1993 and the SST profile in 2 particular transects across the image 111
Figure 5.22. AVHRR SST image of 8 November 1993 and the SST profile in 1 particular transect across the image 111
Figure 5.23. AVHRR SST image of 27 January 1994 and the SST profile in 1 particular transect across the image 112
Figure 5.24. AVHRR SST image of 5 May 1994 and the SST profile in 2 particular transects across the image 112
Figure 5.25. Trajectories described by the LCDs in the Brazil Current 113
Figure 5.26. Tracks of buoys 32446 and 32458 in the BC and SAC 114
Figure 5.27. Trajectories described by the LCDs in the South Atlantic Current 116
Figure 5.28. Time series of longitude, latitude and temperature for the Brazil Current ... 117
Figure 5.29. Time series of longitude, latitude and temperature for the South Atlantic Current 118
Figure 5.30. Energy preserving spectra of the LCD no. 3179's temperature, instantaneous zonal velocity and instantaneous meridional velocity time series in the Brazil Current 124
Figure 5.31. Energy preserving spectra of the LCD no. 3181's temperature, instantaneous zonal velocity and instantaneous meridional velocity time series in the Brazil Current 125
Figure 5.32. Energy preserving spectra of the LCD no. 3182's temperature, instantaneous zonal velocity and instantaneous meridional velocity time series in the Brazil Current 126
Figure 5.33. Energy preserving spectra of the LCD no. 3185's temperature, instantaneous zonal velocity and instantaneous meridional velocity time series in the Brazil Current 127
Figure 5.34. Energy preserving spectra of the LCD no. 3187's temperature, instantaneous zonal velocity and instantaneous meridional velocity time series in the Brazil Current 128
Figure 5.35. Energy preserving spectra of the LCD no. 3188's temperature, instantaneous zonal velocity and instantaneous meridional velocity time series in the Brazil Current 129
Figure 5.36. Energy preserving spectra of the LCD no. 3189's temperature, instantaneous zonal velocity and instantaneous meridional velocity time series in the Brazil Current 130
Figure 5.37. Energy preserving spectra of the LCD no. 3190's temperature, instantaneous zonal velocity and instantaneous meridional velocity time series in the Brazil Current 131
Figure 5.38. Energy preserving spectra of the LCD no. 3191's temperature, instantaneous zonal velocity and instantaneous meridional velocity time series in the Brazil Current 132

Figure 5.39. Energy preserving spectra of the LCD no. 3192's temperature, instantaneous zonal velocity and instantaneous meridional velocity time series in the Brazil Current..... 133
Figure 5.40. Energy preserving spectra of the LCD no. 3182's temperature, instantaneous zonal velocity and instantaneous meridional velocity time series in the South Atlantic Current..... 134
Figure 5.41. Energy preserving spectra of the LCD no. 3185's temperature, instantaneous zonal velocity and instantaneous meridional velocity time series in the South Atlantic Current..... 135
Figure 5.42. Energy preserving spectra of the LCD no. 3187's temperature, instantaneous zonal velocity and instantaneous meridional velocity time series in the South Atlantic Current..... 136
Figure 5.43. Energy preserving spectra of the LCD no. 3189's temperature, instantaneous zonal velocity and instantaneous meridional velocity time series in the South Atlantic Current..... 137
Figure 5.44. Energy preserving spectra of the LCD no. 3190's temperature, instantaneous zonal velocity and instantaneous meridional velocity time series in the South Atlantic Current..... 138
Figure 5.45. Energy preserving spectra of the LCD no. 3191's temperature, instantaneous zonal velocity and instantaneous meridional velocity time series in the South Atlantic Current..... 139
Figure 5.46. Energy preserving spectra of the LCD no. 3192's temperature, instantaneous zonal velocity and instantaneous meridional velocity time series in the South Atlantic Current..... 140
Figure 6.1. Trajectories described by the LCDs in the Brazilian Coastal Current..... 148
Figure 6.2. AVHRR image taken on 29 April 1993..... 149
Figure 6.3. The BC/BCC front at the SBCS in 5 June 1993 and 16 August 1993..... 150
Figure 6.4. One-day sequence of AVHRR images taken in 19 July 1993 and 20 July 1993..... 151
Figure 6.5. Time series of longitude, latitude and temperature for the Brazilian Coastal Current..... 153
Figure 6.6. Energy preserving spectra of the LCD no. 3178's temperature, instantaneous zonal velocity and instantaneous meridional velocity time series in the Brazilian Coastal Current..... 156
Figure 6.7. Energy preserving spectra of the LCD no. 3179's temperature, instantaneous zonal velocity and instantaneous meridional velocity time series in the Brazilian Coastal Current..... 157
Figure 6.8. Energy preserving spectra of the LCD no. 3180's temperature, instantaneous zonal velocity and instantaneous meridional velocity time series in the Brazilian Coastal Current..... 158
Figure 6.9. Extreme position time series for the BCC and BC..... 161
Figure 6.10. MCSST images for February 1984 and August 1983 indicating the minimum and maximum latitudinal position of the BCC for the period of 1984 to 1995.. 161
Figure 6.11. Statistics for the BCC and BC extreme positions per month..... 162
Figure 6.11. Total catch of sardine (*Sardinella brasiliensis*) in the SBB for the period between 1980 and 1990..... 165
Figure 6.12. BCC and BC extreme positions per season in the SBCS..... 166
Figure 6.13. Schematic ilustration of the surface currents in the SBCS and BMC regions..... 167
Figure 7.1. Eddies present in the overall buoy tracks..... 172
Figure 7.2. Distribution of the individual eddies' temperatures in relation to the eddies' diameter..... 173
Figure 7.3. Relationship between the diameter and the internal Rossby radius of deformation for the eddies in class 1 and 2..... 175

Figure 7.4. Relationship between the Rossby number and the eddies' diameters for the BC, the BCC and the SAC..... 177
Figure 7.5. Linear regressions between the diameter, rotational period and tangential velocities for the class 1 eddies..... 179
Figure 7.6. Linear regressions between the diameter, rotational period and tangential velocities for the class 2 eddies..... 179
Figure 7.7. Eddies present in the high-resolution AVHRR images..... 181
Figure 7.8. Distribution of the individual eddies' temperatures in relation to the eddies' diameter: mean and standard deviation..... 182
Figure 7.9. Relationship between the diameter and the internal Rossby radius of deformation for the eddies found in the AVHRR images..... 184
Figure 7.10. AVHRR image of 27 April 1993 showing the 'pinching off' of three cold core (cyclonic) eddies from the cold (MC) part of the western subtropical front..... 185
Figure 7.11. Two day sequence of AVHRR images taken in 27 January 1994 and 29 January 1994 at the western subtropical front..... 186
Figure 7.12. AVHRR image of 20 May 1994 showing a mushroom-like feature extending from the BCC towards the BC in the BC/BCC front..... 187
Figure 8.1. Linear regressions between AVHRR brightness temperatures and SSTs and bulk temperatures from COADS..... 195
Figure 8.2. Linear regressions between AVHRR brightness temperatures and SSTs and bulk temperatures from COADS (discarding the bulk temperatures measured in the Malvinas Current)..... 196
Figure 8.3. Linear regressions between AVHRR brightness temperatures and SSTs and buoy temperatures..... 199
Figure 8.4. ATSR SST mosaic image of 8 November 1993..... 203
Figure 8.5. ATSR SST mosaic image of 9 November 1993..... 204
Figure 8.6. ATSR SST mosaic image of 5 May 1994..... 205
Figure 8.7. DeltaT AVHRR minus ATSR images..... 206
Figure 8.8. Frequency histograms of representative cloud free sub-scenes of the deltaT AVHRR minus ATSR images..... 214
Figure 8.9. DeltaT ATSR daytime minus ATSR night time images..... 216
Figure 8.10. Frequency histograms of representative cloud free sub-scenes of the deltaT ATSR daytime minus ATSR night time images..... 218

List of Tables

Table 3.1. Satellites and sensors operating between 1993-94..... 30
Table 4.1. Lifetime and number of observations (N) for the LCDs after achieving the vicinity of the BMC region..... 42
Table 4.2. Time series used to describe the BC, BCC and SAC..... 45
Table 4.3. High-resolution AVHRR images used in this work..... 56
Table 4.4. Full-resolution ATSR images used in this work..... 66
Table 4.5. Number of match-up points between *in situ* and satellite temperatures..... 69
Table 4.6. DeltaT AVHRR minus ATSR images..... 72
Table 4.7. DeltaT ATSR daytime minus ATSR night time images..... 72
Table 5.1. Period of the major energy peaks for the seasonally averaged MCSST anomalies PC modes 1 to 4..... 92
Table 5.2. Seasonally averaged MCSST anomalies individual contributions to PC modes 1 to 4..... 94
Table 5.3. BC and SAC velocity, kinetic energy and temperature statistics..... 120
Table 5.4. Period of the major energy peaks for the buoys' temperature and instantaneous velocity time series in the BC and SAC..... 122
Table 6.1. BCC velocity, kinetic energy and temperature statistics..... 154
Table 6.2. Period of the major energy peaks for the buoys' temperature and instantaneous velocity time series..... 159
Table 6.3. Statistics for the BCC and BC extreme positions over the year..... 163
Table 7.1. Size and period statistics for the eddies found in the buoys' trajectories..... 173
Table 7.2. Rossby number statistics for the eddies found in the buoys' trajectories..... 176
Table 7.3. Linear regression between the rotational period, tangential velocity, perimeter and diameter for the eddies in class 1..... 178
Table 7.4. Linear regression between the rotational period, tangential velocity, perimeter and diameter for the eddies in class 1..... 178
Table 7.5. Comparison between measured and estimated V_T and T_R of the surface eddies in the Southwestern Atlantic Ocean..... 178
Table 7.6. Size statistics for the eddies found in the AVHRR images..... 183
Table 8.1. Linear regressions between the bulk temperatures from COADS and the AVHRR BTs and SSTs..... 194
Table 8.2. Linear regressions between the bulk temperatures from $COADS_{lessMC}$ and the AVHRR BTs and SSTs..... 197
Table 8.3. Linear regressions between the buoy temperatures and the AVHRR BTs and SSTs..... 198
Table 8.4. DeltaT between *in situ* temperatures and ATSR SSTs..... 200
Table 8.5. Statistics for the deltaT AVHRR minus ATSR images..... 213
Table 8.6. Statistics for the deltaT ATSR daytime minus ATSR night time images..... 218

Acknowledgements

Tatiana for being my wife, my sister soul, my inspiration and the proof that dreams can come true. Isabela for being part of all. Ian Robinson for being my supervisor, friend and the one who guided me all the way through this work. CNPq for the funding and support for this research. INPE for the COROAS data and background. CNPq and the other Brazilian funding agencies FAPESP and CIRM for supporting COROAS. JPL/NASA for the MCSST data set. ESA for providing the ATSR images through the AO3-128 project. SOC/SOES for providing the support and facilities for the completion of this work. Kelvin Richards for the suggestions in the upgrade. David Cromwell, Paolo Cipollini, Peter Challenor and Neil Wells for the discussions and ideas. Kate Davis, Luciane Veeck and Luciano Pezzi for the technical support to produce some of the figures. Ian Robinson, Valborg Byfield, David Cromwell, Robert Potter and Kate Delaney for the help in the English review of this document. Merritt Stevenson, João Lorenzzetti, Sydnéa Maluf and José Carlos Stech for the support from INPE and friendship. Osmar Möller, Carlos Garcia, Maurício Mata, Renato Ghisolfi and Ivan Soares for the support from FURG and friendship. Edmo Campos and Yoshimine Ikeda for the support from IOUSP and friendship. Raul Guerrero and Maria Gabriela of INIDEP in Argentina for providing important references about the Southwestern Atlantic Ocean. For the discussions and friendship: Alexandre Cabral, José da Silva, Paulo Sumida, Antônio Caetano Caltabiano, Simon Keogh, Luis Felipe Navarro-Olache, Alessio Bellucci, Anita Grezio, Carlos Lentini, Asdrubal Martinez, Daniel Ballestero, Luca Centurioni, Robert Potter, Andreas Thurnherr and Craig Donlon. For the friendship: José Antônio Soares, Leoni Dransfield, Susanne Ufermann, Stuart Brentnall, Nelson Violante, Ana Paula Telles, Silvia Lucato, Eva Ramirez, Francisco Salís Marín, Maria Baker, Dawn Powell, Miguel Tenório and Brigitte, Manolis and Virginie, Daniel and Sandra, Toby Wicks and Kate Delaney, Boris and Tamaris, César and Sílvia, Phillipe and Elisabeth, Silvia and Carvalho, Roberto and Cristiane, André and Adriene, Rafael Sperb, Carol Jones, Valeria Salvatori. Marcelo Travassos, Regina Rodrigues, Sérgio Faria, Lúbia Vinhas, Jaqueline Madruga, Mantovani and Angélica, Marco and Vera, Guga and Marilne, Helder and Fabiana, Osman and Evania, Ney and Marley, Luis Felipe and Lucy, Gilberto and Elisa, Marisa and Luciano, Rodrigo and Dhesireé, Nico and Luciane, Marcos and Tatiana, Jaime, Claudia, Florencia and Santiago for being more than friends. My mother, father, sister, Alvimar, André, Lucas, Dinha, Nádia and Vanessa for always believing in what I have chosen to do. For Jorge. For those who question God and God for being the eternal question.

Acronyms

AABW..... Antarctic Bottom Water
AAIW..... Antarctic Intermediate Water
AATSR..... Advanced Along Track Scanning Radiometer
ACC..... Antarctic Circumpolar Current
ADEOS..... Advanced Earth Observing Satellite
AGCM..... Atmospheric General Circulation Model
ATS..... Advanced TIROS-N
ATSR..... Along Track Scanning Radiometer
AVHRR..... Advanced Very High Resolution Radiometer
BC..... Brazil Current
BCC..... Brazilian Coastal Current
BgC..... Benguela Current
BMC..... Brazil-Malvinas (Falklands) Confluence Zone
BT..... Brightness Temperature
CCT..... Computer Compatible Tape
CDA..... Command and Data Acquisition
CEOS..... Committee on Earth Observation Satellites
CIRM..... Comissão Interministerial para os Recursos do Mar
CLIVAR..... Climate Variability and Predictability
CNES..... Centre National d'Etudes Spatiales
CNPq..... Conselho Nacional de Desenvolvimento Científico e Tecnológico
COADS..... Comprehensive Ocean-Atmosphere Dataset
COROAS..... Oceanic Circulation in the Western Region of the South Atlantic
CPSST..... Cross Product Sea Surface Temperature
CW..... Coastal Waters
CZCS..... Coastal Zone Color Scanner
EKE..... Eddy Kinetic Energy
ENVI..... Environment for Visualizing Images®
EODC..... Earth Observation Data Centre
EOF..... Empirical Orthogonal Function
ERS..... European Remote Sensing Satellite
ESA..... European Space Agency
FAPESP..... Fundação de Amparo à Pesquisa do Estado de São Paulo
FGGE..... First GARP Global Experiment
FOV..... Field of View
FURG..... Fundação Universidade Federal do Rio Grande
GAC..... Global Area Coverage
GPS..... Global Positioning System
HRPT..... High Resolution Picture Transmission
IDL..... Interactive Data Language®
INIDEP..... Instituto Nacional de Investigación y Desarrollo Pesquero
INPE..... Instituto National de Pesquisas Espaciais
IOUSP..... Instituto Oceanográfico da Universidade de São Paulo
IRR..... Infrared Radiometer
ISRO..... Indian Space Research Organization
ITOS..... Improved TIROS Operational Satellites
JPL..... Jet Propulsion Laboratory
JRD..... James Rennell Division for Ocean Circulation and Climate
LAC..... Local Area Coverage
LCD..... Low Cost Drifter
LST..... Local Solar Time

MC..... Malvinas (Falklands) Current
MCSST..... Multi-Channel Sea Surface Temperature
MKE..... Mean Kinetic Energy
NADW..... North Atlantic Deep Water
NASA..... National Aeronautics and Space Administration
NCAR..... National Center for Atmospheric Research
NCEP..... National Center for Environmental Prediction
NESDIS..... National Environmental Satellite, Data and Information Service
NOAA..... National Oceanic and Atmospheric Administration
Nsp..... Radiance of Space
OCM..... Ocean Colour Monitor
OCTS..... Ocean Color and Temperature Scanner
PC..... Principal Component
PNBoia..... Programa Nacional de Bóias – National Buoy Programme
PTT..... Platform Transmit Terminal
RSMAS..... Rosenstiel School of Marine and Atmospheric Sciences
SAC..... South Atlantic Current or Brazil Current Extension
SACW..... South Atlantic Central Water
SAF..... Subantarctic Front
SAR..... Synthetic Aperture Radar
SBCS..... Southern Brazilian Continental Shelf
SEC..... South Equatorial Current
SOC..... Southampton Oceanography Centre
SOES..... School of Ocean and Earth Science
SOI..... Southern Oscillation Index
SOS..... Southern Ocean Studies
SST..... Sea Surface Temperature
STF..... Subtropical Front
STW..... Subtropical Water
SVP..... Surface Velocity Program
SZA..... Satellite Zenith Angle
THIR..... Temperature Humidity Infrared Radiometer
TIROS..... Television Infra Red Observational Satellites
TKE..... Total Kinetic Energy
TOGA..... Tropical Oceans Global Atmosphere
TOPEX..... Ocean Topography Experiment
TOS..... TIROS Operational Satellites
T/P..... TOPEX/Poseidon
TW..... Tropical Water
UHF..... Ultra High Frequency
VHRR..... Very High Resolution Radiometer
WOCE..... World Ocean Circulation Experiment

CHAPTER 1

INTRODUCTION

1.1. Preface

The southwestern region of the Atlantic Ocean (Figure 1.1) comprises one of the most dynamically active regions of the World Ocean, the Brazil-Malvinas (Falkland) Confluence (BMC) region. The BMC comprises territorial waters of Brazil, Uruguay and Argentina, and is an oceanographic front between the Brazil Current (BC) and the Malvinas (Falkland) Current (MC), where cold waters of subantarctic origin carried by the MC meet warm waters of tropical origin carried by the BC. The BMC is the western part of the Subtropical Front, the region where the subsurface South Atlantic Central Water is formed and where the South Atlantic Current flows as part of the South Atlantic subtropical gyre.

A complete understanding of the physical aspects of the Brazil-Malvinas confluence is far from being achieved. Reasons for that lie in the fact that the South Atlantic remained for many years one of the regions of the World Ocean where there was a remarkable lack of *in situ* measurements, especially current measurements. The complex physical processes of water mass mixture occurring in the BMC region and its vicinity, together with a strong seasonal oscillation of the BMC, make the situation even more complicated.

Nevertheless, since primary production and other levels of the trophic chain including fishes are directly linked with the water masses in the Southwestern Atlantic (Castello et al., 1997; Boltovskoy et al., 1999), classical measurements of temperature and salinity are fairly common. These measurements are, however, usually made in relation to specific regional purposes and unfortunately fail to provide a general view of the scale of the major phenomena occurring over larger areas.

At the same time that most of the fisheries and subsequent economical interests of Brazil, Uruguay and Argentina depend directly upon the BMC, these countries never joined efforts to study this region in an integrated way. To the present, when *in situ* data are needed, most

of the studies in the BMC region are restricted to the continental waters of the individual countries. Unfortunately the present situation is that, apart from individual collaborations among scientists, Brazil, Uruguay and Argentina do not have a joint programme to study or monitor the convergence.

Figure 1.1. The Southwestern Atlantic Ocean: bathymetry (metres) and main features.

Because of the lack of integration between the countries and the difficulty in obtaining direct measurements in the currents present in the BMC region, several primary questions regarding the kinematics and dynamics of this region remain to be answered. For instance, questions remain about the mechanisms involved in the BMC oscillation, its interconnections with the large-scale South Atlantic atmospheric systems and with current systems like the Antarctic Circumpolar Current and the South Equatorial Current. More basic still, a good description of the fronts and other mesoscale features like meanders and eddies in the BMC is far from complete.

Three major currents occur at the surface in the BMC region: the Brazil Current (BC), its extension towards the open Atlantic Ocean, the South Atlantic Current (SAC) and the Malvinas (Falkland) Current (MC). Using data from drifting buoys and satellite imagery, this thesis provides some new insights about the surface signature of the BC and of the SAC. The data presented and discussed here are also used to characterise the Brazilian Coastal Current (BCC), a newly described coastal extension of waters from the BMC region which was found to dominate the South American coast at latitudes of about 35°S to 25°S in wintertime. Unfortunately, owing to lack of *in situ* data, the MC is not studied in this work.

Questions regarding the speed, direction, oscillations, typical temperatures and kinetic energies of the BC, SAC and BCC are partially answered in this thesis. Some of the characteristics of the mesoscale features present in these currents or in the oceanographic fronts present in the Southwestern Atlantic Ocean are also investigated here. For example, Chapter 7 of this thesis offers new insights on the eddy field of the BMC and the South Brazilian Continental Shelf (SBCS) regions. We ought to answer, for instance, how the eddies are distributed, which are their typical sizes and rotational periods. We also investigate, for example, which will be the possible forming mechanisms of the eddies in the BMC region and how they differ from the eddies present in the SBCS.

To achieve the objectives of this research we used a combination of *in situ* and satellite data collected in the Southwestern Atlantic Ocean. The effectiveness of remote sensing for studying the BMC region has been evident since the pioneer works by Tseng (1974) and Legeckis (1978). More recently, Podestá (1997) emphasised this effectiveness adding that satellite data can in future be used in a programme for fisheries forecasting of the region. However, much descriptive work is still lacking on the behaviour of the fronts and associated mesoscale activity in the Southwestern Atlantic Ocean. This thesis aims also to bring about some new insights in this subject.

The importance of the seasonal oscillation of the BMC region in the Argentinean, Uruguayan and Southern Brazilian weather is still unknown. The same applies to the penetration of the cold waters from the BMC region in low latitudes of the SBCS, which is proved in this thesis to occur seasonally every year. Teleconnections are reported to occur between the precipitation regime in Southern Brazil and Uruguay and the discharge of the La Plata River with the El-Niño Southern Oscillation in the Pacific (Ciotti et al., 1995; Diaz et al., 1998; Grimm et al., 1998) and with the SST fields in the Southwestern Atlantic (Diaz et al., 1998).

The question remains on the local connections between the former variables and the presence of cold water intrusions alongshore the SBCS in wintertime.

Finally one could ask: if remote sensing is to be used as a major tool for descriptive studies of the BMC surface phenomena, how accurate are the present retrievals of sea surface temperature (SST) that the current satellites offer? Briefly, what is the relation between *in situ* and satellite SST in the Southwestern Atlantic Ocean? The question is worthwhile, since the majority of the algorithms for atmospheric correction of remote sensing images are global and, especially for the South Atlantic where few *in situ* data are available, a regional bias could occur. If some bias exists, will it make our interpretations of the SST fields in the Southwestern Atlantic still valid? These questions are addressed in this thesis as well.

1.2. Objectives

The main objectives of this thesis are:

- To describe some of the mesoscale surface processes occurring in the Southwestern Atlantic Ocean by utilising a combination of sea surface temperature images and Lagrangian (buoy) data for the period of 1993 to 1994;

- To describe and characterise the eddy activity in the area and period of study by using the satellite and buoy data;

- To compare *in situ* sea surface temperature measurements obtained by drifting buoys and by ships of opportunity in the Southwestern Atlantic Ocean with estimates derived from the AVHRR and ATSR sensors.

In order to achieve the general objectives indicated above, some specific objectives were drawn in the context of the distinct processes occurring in the Brazil-Malvinas Confluence (BMC) region and in the region of the Southern Brazilian Continental Shelf (SBCS). Moreover, a general description of the South Atlantic Ocean as a whole was made for the period between 1982 and 1995 aiming to support our understanding of the processes occurring in the BMC and SBCS during 1993 and 1994. For that, specific objectives follow:

- To describe the SST fields in the South Atlantic by using a set of low-resolution, monthly-averaged AVHRR images for the period between January 1982 and December 1995;

- To describe the variability of the South Atlantic SST mean and anomaly fields by using Principal Components analysis.

The high-resolution AVHRR images were used for describing the thermal surface fronts occurring in the Southwestern Atlantic and the eddy activity during the period from March 1993 to July 1994. The penetration of waters from the BMC region inside the SBCS was noticed from the AVHRR images and the current associated with this phenomenon was studied by a combination of the low and high-resolution images and buoy data. For the BMC and SBCS regions, the buoy data were used with the following specific objectives:

- To describe the spatial Lagrangian signature, mean direction and speed of the Brazil Current (BC), the South Atlantic Current (SAC) and the Brazilian Coastal Current (BCC) in the BMC and SBCS regions between 1993 and 1994;

- To describe the kinetic energies and oscillations present in the BC, SAC and BCC during the period of this study;

- To evaluate, together with high-resolution AVHRR data, the rotational periods, tangential velocities and sizes characteristic of the eddies present in the study area from March 1993 to July 1994.

In situ SST data for the period and area of this study were available from buoy measurements and from ships of opportunity. Furthermore, skin SST fields were also available from ATSR images. The availability of several distinct measurements and estimations of SST for the same period and area provided the opportunity of further investigation aiming:

- To assess the correlation between *in situ* SST data and estimates made by the AVHRR and ATSR sensors;

- To assess the temperature difference (deltaT) between skin and 'bulk' measurements and its spatial patterns in the study area;

- To investigate the importance of deltaT in mesoscale studies in areas of strong thermal gradients such as the Southwestern Atlantic Ocean.

1.3. Structure of the thesis

This thesis is organised as follows: Chapter 1 presents an introduction and the main objectives of the research. Chapter 2 presents the background knowledge in the surface circulation of the Southwestern Atlantic Ocean. A review of the history and methods associated with the satellite observations of the ocean is presented in Chapter 3. Chapter 4 describes the data and methods employed in this work.

The new knowledge obtained in this research is presented in chapters 5 to 8. Each of these chapters are organised with a particular introduction, results, discussions and conclusions. Chapter 5 describes some of the mesoscale surface processes ocurring in the Brazil-Malvinas Confluence region. Chapter 6 presents a study of the Brazilian Coastal Current (BCC), where new evidences suggest that this current is seasonal and an important feature present in the South Brazilian Continental Shelf. Very few measurements and descriptions of the BCC are available in the scientific literature to the present. Chapter 7 is related to the characterisation of the eddies present in the Southwestern Atlantic Ocean, as measured by both drifting buoys and SST images. Chapter 8 presents an analysis of the relationships between *in situ* and satellite SST data for the area and period of this study.

Finally, Chapter 9 summarises the main conclusions of this research and presents some suggestions for future work.

CHAPTER 2

SURFACE CIRCULATION OF THE SOUTHWESTERN ATLANTIC OCEAN

2.1. Currents and water masses

Early oceanographic surveys looking for the comprehension of the water mass composition and circulation in the South Atlantic began with the German expedition of the Meteor, in the twenties (Wust, 1935; Defant, 1936; both cited by Peterson and Stramma, 1991). Clowes (1933), Deacon (1933, 1937) and Defant (1941; cited by Olson et al., 1988) made the first descriptions of the Brazil-Malvinas Confluence region.

Figure 2.1 is a simplified large-scale, upper-level geostrophic scheme for the South Atlantic circulation presented by Peterson and Stramma (1991). In a general sense, the upper layer circulation in this ocean is dominated by a system of anticyclonic (anticlockwise in the southern hemisphere) subtropical gyres and by the Equatorial and Circumpolar Current systems (Reid, 1989; Peterson and Stramma, 1991). The major surface currents occurring in these systems are:

- South Equatorial Current (SEC);
- Brazil Current (BC), the southward western boundary current;
- Malvinas or Falkland Current (MC), the northward western boundary current;
- South Atlantic Current (SAC) or Brazil Current Extension; and
- Benguela Current (BgC).

In opposition to this simple classical description, however, the South Atlantic subtropical gyre is not a closed system. Transport is known to be lost at the northern limit of the gyre, which feeds the equatorial countercurrents and some of the northern hemisphere currents (Stramma et al., 1990).

The limit of the South Atlantic with the Southern Ocean is marked by the Polar Front. There, surface waters are transported eastward by a system of currents (Sarukhanyan, 1987) called

the Antarctic Circumpolar Current (ACC). As this system crosses the Drake Passage, a northward component feeds the formation of the Malvinas (Falkland) Current (MC), which is originated as a branch of the Subantarctic Front, the northernmost front associated with the ACC in the Drake Passage (Olson et al., 1988).

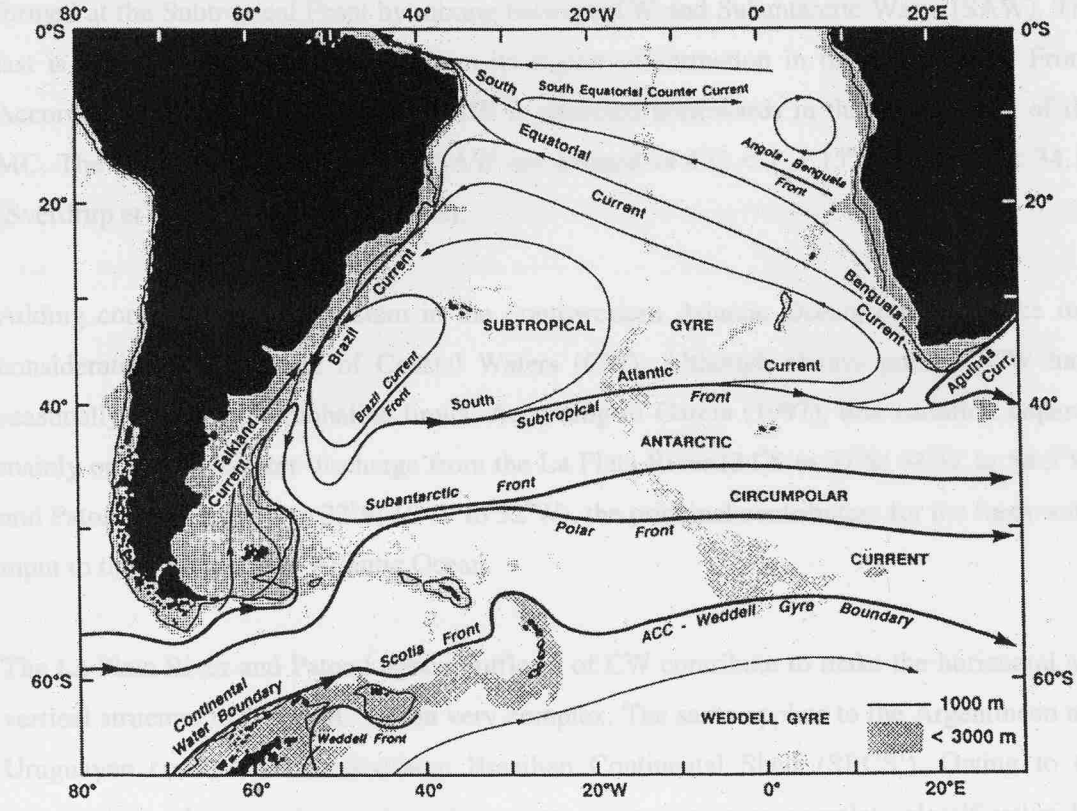

Figure 2.1. Surface circulation in the South Atlantic. Source: Peterson and Stramma (1991).

According to Sarukhanyan (1987), the Polar Front (also called Antarctic Front) is not narrow, but a complex band, with a relatively large eastward velocity component, delimiting the region of transition between Antarctic and Subantarctic waters. The northern axis of the ACC system marks the northern Subantarctic boundary of the Antarctic Front or, simply, the Subantarctic Front. The southern axis of the ACC limits the southern Antarctic boundary, traditionally known as the Polar Front (Peterson and Stramma, 1991).

Sverdrup et al. (1942) established the thermohaline characteristics of the surface waters carried by the Brazil Current (BC), known as the Tropical Water (TW). Emilson (1961) and Thomsen (1962) later proposed new thermohaline limits, being the values of $T > 20^{\circ}C$; $S > 36$

(Emilson, 1961) the most used in the current literature. Vertically, the South Atlantic is composed of a set of water masses which includes the South Atlantic Central Water (SACW), the Antarctic Intermediate Water (AAIW), the North Atlantic Deep Water (NADW) and the Antarctic Bottom Water (AABW).

SACW, also known as Subtropical Water (STW), flows immediately below the TW and is formed at the Subtropical Front by mixing between TW and Subantarctic Water (SAW). The last is carried northwards by MC from its region of formation in the Subantarctic Front. According to Bianchi et al. (1993), SAW is advected northwards in the upper 500m of the MC. The thermohaline limits of the SAW are defined as $4^{o}C < T < 15^{o}C$; $33.7 < S < 34.15$ (Sverdrup et al., 1942; Thomsen, 1962).

Adding complexity to the system in the Southwestern Atlantic Ocean, one may take into consideration the presence of Coastal Waters (CW). Although always present, CW have seasonally variable thermohaline limits. According to Garcia (1997), this variation depends mainly on the freshwater discharge from the La Plata River ($34^{o}S$ to $37^{o}S$; $54^{o}W$ to $58.5^{o}W$) and Patos Lagoon ($30^{o}S$ to $32^{o}S$; $50^{o}W$ to $52^{o}W$), the principal contributors for the fresh water input to the Southwestern Atlantic Ocean.

The La Plata River and Patos Lagoon outflows of CW contribute to make the horizontal and vertical structure of the BMC region very complex. The same applies to the Argentinean and Uruguayan coasts and the Southern Brazilian Continental Shelf (SBCS[1]). Owing to the complexity and seasonal variation of its water masses, a more complete classification has been made by Castro and Miranda (1998) for the SBCS region. These authors described two kinds of CW occurring at the SBCS: Coastal Water influenced by Subantarctic Water (CWISb: $S < 34$) and Coastal Water influenced by Tropical Water or Shelf Break Water (SBrW: $34 < S < 36.7$).

According to a seasonal cycle which is so far understood to be related to changes in the local wind regime and in the continental freshwater discharge (Miranda, 1972; Ciotti et al., 1995; Lima et al., 1996; Garcia, 1997; Castro and Miranda, 1998), the thermohaline characteristics of the SBCS change from winter to summer. Changes in the water mass characteristics are also believed to be linked to changes in the regime of the currents in the SBCS.

[1] SBCS in this text denotes the regions named by Castro and Miranda (1998) as Southern Brazilian Shelf (from Arroio Chuí - 33°48'S to Santa Marta Cape - 28°40'S) and South Brazil Bight (from Santa Marta Cape to Cabo Frio - 23°S).

In the Uruguayan continental shelf and in the southern part of SBCS up to Santa Marta Cape (28.5°S; 48.6°W), for instance, the La Plata River outflow is supposed to feed a fresher coastal current coming from the south, which contributes to the major changes in the T-S characteristics of the continental shelf water masses. Strong indication of the presence of a coastal current occurring to the south of Santa Marta Cape in wintertime is inferred from horizontal maps of temperature and salinity derived from hydrographical surveys (e.g. Hubold, 1980; Ciotti et al., 1995; Lima et al., 1996; Castro and Miranda, 1998), since very few direct measurements have been reported for the SBCS so far.

Aiming to get round the problem of the lack of direct measurements in the SBCS, Zavialov et al. (1998) developed an inverse model based upon historical hydrographic and meteorological data to study the currents at the southern part of the SBCS. The authors concluded that a northward current must occur all the year long at the Brazilian continental shelf in the area between 30°S and 35°S.

Studying the La Plata River estuary, however, Guerrero et al. (1997) concluded that a northward drift of fresher waters from the estuary only happens in wintertime, not all the year round as proposed by Zavialov et al. (1998) for the currents to the north of 30°S. According to Guerrero et al. (1997), the northward drift of the La Plata CW only occurs under higher continental drainage, and under a condition of balance between onshore and offshore winds. The authors considered a line perpendicular to the axis of the La Plata River, and divided wind data into onshore (from NE, E, SE and S) and offshore (from NW, W, SW and N) components. Onshore winds act to pile up water in the La Plata estuary while offshore winds increase seaward discharge.

Guerrero et al. (1997) also described that the monthly mean discharge of the La Plata River is higher (about 25000 m^3/s) during the months of April to July, dropping down to about 20000 m^3/s in the rest of the year. Water outflow from the La Plata River is deflected to the north by Coriolis force when entering the continental shelf. The flow generated at the shelf from La Plata River is considered to be barotropic and geostrophic, being driven by the sea surface elevation. This latter is caused by the river discharge and Ekman transport (Zavialov et al., 1998).

A T-S diagram for the SBCS presented by Odebrecht and Garcia (1997) can be seen in Figure 2.2. A similar T-S diagram constructed from historical data sets for the summer and wintertime is presented by Castro and Miranda (1998). From these T-S diagrams it is clear that CW changes its thermohaline characteristics seasonally, reaching very low salinity limits

in spring and winter. Odebrecht and Garcia (1997), for instance, found salinity as low as 26 during spring. Values of the same magnitude were also found for the region of influence of the La Plata River, in Argentina, during summertime (Guerrero and Piola, 1997). Although this is not noticed in Figure 2.2, the T-S diagram presented by Castro and Miranda (1998) also indicates that there is a discontinuity of T-S points between CW and SACW in winter at the SBCS. This implies that the mixing between these two water masses is minimal or non existent in this region during wintertime.

Figure 2.2 also indicates that the distinct water masses of the SBCS have different chlorophyll patterns. CW and SAW are considered eutrophic waters, with higher chlorophyll content than the TW (Ciotti et al., 1995). Since a coastal current flowing northwards would carry eutrophic waters from the south to the SBCS, the investigation of this current can be very important for assessing the biological characteristics of this area.

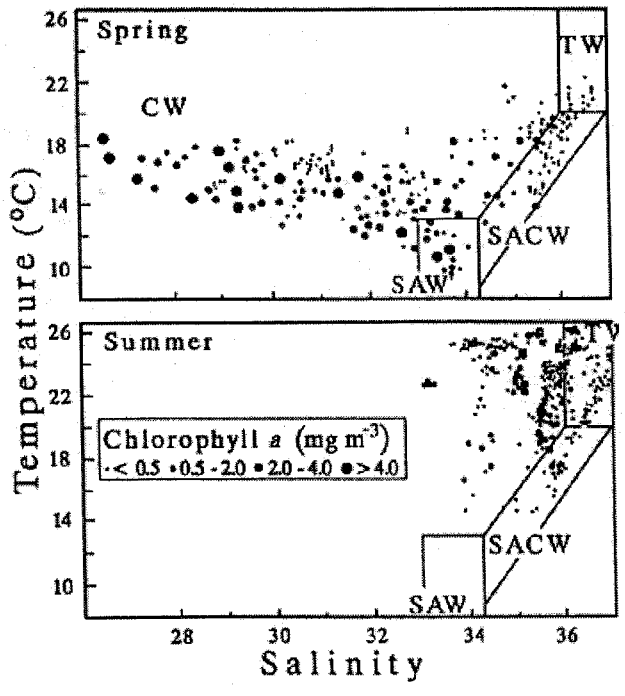

Figure 2.2. T-S diagram for the Southwestern Atlantic Ocean. Source: Odebrecht and Garcia (1997).

At the subsurface in the BMC region, the mixing between TW and SAW forms SACW which spreads itself over the entire South Atlantic from the Subtropical Front. Along the SBCS

slope, part of the SACW is also transported by the BC as it flows to the south (Garfield, 1990). This process is believed to support the increase of the BC transport along its southwestward flow. The thermohaline limits for the SACW are: $6^{\circ}C < T < 18^{\circ}C$; $34.5 < S < 36$ (Sverdrup et al., 1942). Moving towards higher depths in the South Atlantic, AAIW is present flowing northward below the SACW. In the sequence towards the bottom we find NADW and, deeper still, AABW.

2.2. Brazil Current transport and coastal interactions

In the Southwestern Atlantic, the western boundary BC is formed near 10°S, being fed by a small part (about 4 Sv) of the westward SEC which bifurcates southward. The BC is a weak current compared to other western boundary currents, like the Gulf Stream, the Kuroshio or the Agulhas Current (the East Australian Current is another weak western boundary current). Peterson and Stramma (1991) explain this by the loss of transport from the South Atlantic Subtropical Gyre to the northern hemisphere and to equatorial countercurrents. Supported with results from Stramma et al. (1990) obtained for the region between 10°S and 20°S, Peterson and Stramma (1991) maintain the idea that the BC transport remains relatively small (about 11 Sv or less) along its southward flow between 19°S to 25°S.

Garfield (1990), however, pointed out that previous calculations of the BC transport, made by geostrophic computation, can vary depending on the choice of an adequate reference level. Lists of the previous attempts to measure the BC transport can be found in Garfield (1990), Peterson and Stramma (1991) and Garzoli (1993). Estimates in these lists vary among 0 Sv at 20°S (Fu, 1981), 28 Sv at 38°S (Peterson, 1992) and 22.5 Sv at 43°S (Gordon, 1989). An extremely high value of 76 Sv was found at 37°S by McCartney and Zemba (1988, cited by Garzoli, 1993).

Pegasus measurements and NOAA satellite images used by Garfield (1990) have shown that an important part of the BC is transported on the shelf, at depths less than 500 m, the shallowest reference level found in the literature in order to compute BC transport. Inshore transport of the BC and its interactions with the bathymetry or northward coastal currents is far from being completely understood. In disagreement with Peterson and Stramma's (1991) ideas that the BC transport does not increase very much southward (at least down to 25°S), Garfield (1990) remarked that the BC transport is indeed amplified to the south of Cabo Frio,

Brazil, at 23°S. Gordon and Greengrove (1986) agree with this idea, adding that the rate of intensification of the BC transport is about 5 % per 100 km to the south of 24°S.

Campos et al. (1996a) also emphasised the idea of the southward BC transport increment. These authors, discussing early current meter results from the COROAS project, presented an estimate of 2 Sv for the BC transport between the 200 m and 1000 m isobaths offshore Santos, Brazil (24°S, 47°W).

Garfield (1990) described the BC at the latitude of 24°S as a narrow and shallow current, carrying TW and SACW in depths shallower than 400 m. At 31°S, the BC is wider and deeper, and the driving mechanisms of this increase could be related to the contribution of coastal waters and the incoming of SACW from the subtropical gyre. As a matter of fact, the BC remains closely linked to the shelf break between 24°S and 31°S, and a significant part of the BC transport occurs in depths less than 500 m. This leads to geostrophic calculations underestimating the real BC transport.

Further evidence of inshore transport of the BC can be found in Evans and Signorini (1985). These authors took Pegasus measurements at 24°S and found a transport of 5 Sv inshore the 200 m isobath. Added to this 5 Sv, a value of 6 Sv was found offshore, contributing to a BC total transport of 11 Sv in that region.

2.3. Mesoscale processes and features

Two concentric anticyclonic recirculation cells are cited by Peterson and Stramma (1991) to exist offshore Southern Brazil, Uruguay and Argentina, feeding the downstream intensification of the BC transport by its poleward ends. The first cell appears to be placed south of 30°S and is evident from hydrography, infrared sea surface temperature imagery and Lagrangian data. To the north of 30°S, a second cell is located from 20°S to 40°S. This cell was also observed by Reid (1989).

Stevenson and Souza (1994) and Stevenson (1996) described a cyclonic, inshore recirculation scheme of the BC south of 20°S. With periods varying from 115 to 161 days, this recirculation mode of the BC can transport CW mixed with SAW (MC carried) northwards up to the latitudes of the tropical Rio de Janeiro city, nearly 23°S. Campos et al. (1996b), describing the presence of low salinity, cold waters from the BCM region up to 23°S during

the winter of 1993, pointed out the necessity of further work to establish the long-term variability of the presence of this intrusion of cold waters over the Brazilian continental shelf.

The presence of upwelling in the Brazilian coast is well documented in the literature. The best known case of upwelling occurs at Cabo Frio (23°S; 42°W), where the prevailing northeastly winds force the extrusion of coastal waters offshore and, by continuity, SACW is upwelled in the coast. Lorenzzetti and Gaeta (1996) call attention to some speculation among Brazilian researchers who have correlated the seasonality of the Cabo Frio upwelling with the cross-shore fluctuation of the SACW.

According to Garcia (1997), the upwelling phenomenon is also common in the SBCS region. This upwelling can be divided into two types, one occurring at the coast and another attached to the shelf break. The first case is more likely to happen in the spring and summertime, due to the presence of the same northeastly winds driving the Cabo Frio upwelling. This coastal upwelling can occur between 28°S and 32°S, according to Miranda (1972, cited by Garcia, 1996) and Hubold (1980). In the spring and wintertime, lateral mixing between BC and a coastal branch of the MC can form frontal cyclonic eddies (cold in the southern hemisphere), which can cause upwelling of SACW.

Evidences for the presence of a semi-permanent eddy located in the southern Brazilian coast near Santa Marta Cape were presented by Lorenzzetti et al. (1994). By using a set of AVHRR (Advanced Very High Resolution Radiometer) images and data from drifting buoys, the authors described a cyclonic (cold) eddy present in the area from March to June 1993. Buoy tracks along the eddy indicated diameters ranging from 70 km to 275 km. Analysing their satellite images, the authors suggested a typical diameter of 200 km for this feature. Lorenzzetti et al. (1994) also observed the advection of the eddy southwestward, at a rate which could be computed to be about 3 cm/s.

2.4. Measurements of the Brazil-Malvinas Confluence variability

The seasonal variability and characteristics of the Brazil-Malvinas Confluence zone (BMC) have been studied since Deacon (1937) and Defant (1941; cited by Olson et al., 1988). In the seventies and eighties the BMC region was investigated by authors like Reid et al. (1977), Gordon and Greengrove (1986), Piola et al. (1987), Olson et al. (1988), Gordon (1989) and

Garzoli and Garraffo (1989), for example. More recently, Garzoli and Simionato (1990), Provost et al. (1992), Garzoli (1993), Bianchi et al. (1993), Goni et al. (1996), Seeliger et al. (1997), among others, can be cited as authors studying the physical aspects of the BMC region.

One of the more remarkable features of the BMC region evident from these works is that the position of the confluence oscillates seasonally, with the BC reaching the southernmost limits in the Austral summer, and the MC achieving its northernmost limits in the wintertime.

Nevertheless, the complete reasons for the BMC oscillation through the year are still unknown (Peterson and Stramma, 1991). Speculations include relations with the seasonal cycles elsewhere in the South Atlantic. The subtropical atmospheric pressure system, for example, moves its centre of high pressure northward in the winter, intensifying at the same time. Furthermore, the South Equatorial Current (SEC) is also strengthened and displaced to the north in the wintertime, and the zero-line of the wind stress curl is shifted 5° in latitude north from its mean position in the summer. As pointed out by Garzoli and Garraffo (1989), the spatial variation of the BMC can also be linked to the large scale variability of the winds and of the SEC which feeds the BC.

To illustrate the meteorological aspects of the South Atlantic ocean with respect to the seasons, Figures 2.3 to 2.6 show the climatological atmospheric pressure and wind patterns at reduced sea level and surface (1000 hPa), respectively, for the Austral summer and winter. The maps were generated using selected data from the NCEP (National Center for Environmental Prediction) / NCAR (National Center for Atmospheric Research) Reanalysis Project (Kalnay et al., 1996), which contains the so-called "13-year base period monthly means" valid for 1982 through 1994.

As described by Peterson and Stramma (1991), Figures 2.3 and 2.4 show the displacement of the subtropical high pressure centre towards the north in wintertime. At the same time in winter, the centre of this high increases in magnitude to about 1023 mb, whereas in summer the highest pressure is about 1019 mb. The winds (Figures 2.5 and 2.6) are governed by the distribution of the atmospheric pressure systems. In the BMC region the dominant winds are from NW to W. Westerly winds achieve lower latitudes in wintertime. At the SBCS, on the other hand, the dominant winds are coming from the NE and are weaker in the winter.

According to Olson et al. (1988), the local wind stress curl may also play a role in the position where the BC separates from the coast (position sometimes interpreted as the BMC location).

The authors, however, report that the local winds are unlikely to be uniquely responsible for the BMC oscillation. Another alternative proposed by Olson et al. (1988) is the variation in the MC forced by variations in the ACC system. Pressure changes in the Subantarctic Front, where MC is fed by a branch of the ACC, could reach the BMC region by Kelvin waves. Wind induced advective changes in the MC could also link the Antarctic sector with the BMC region.

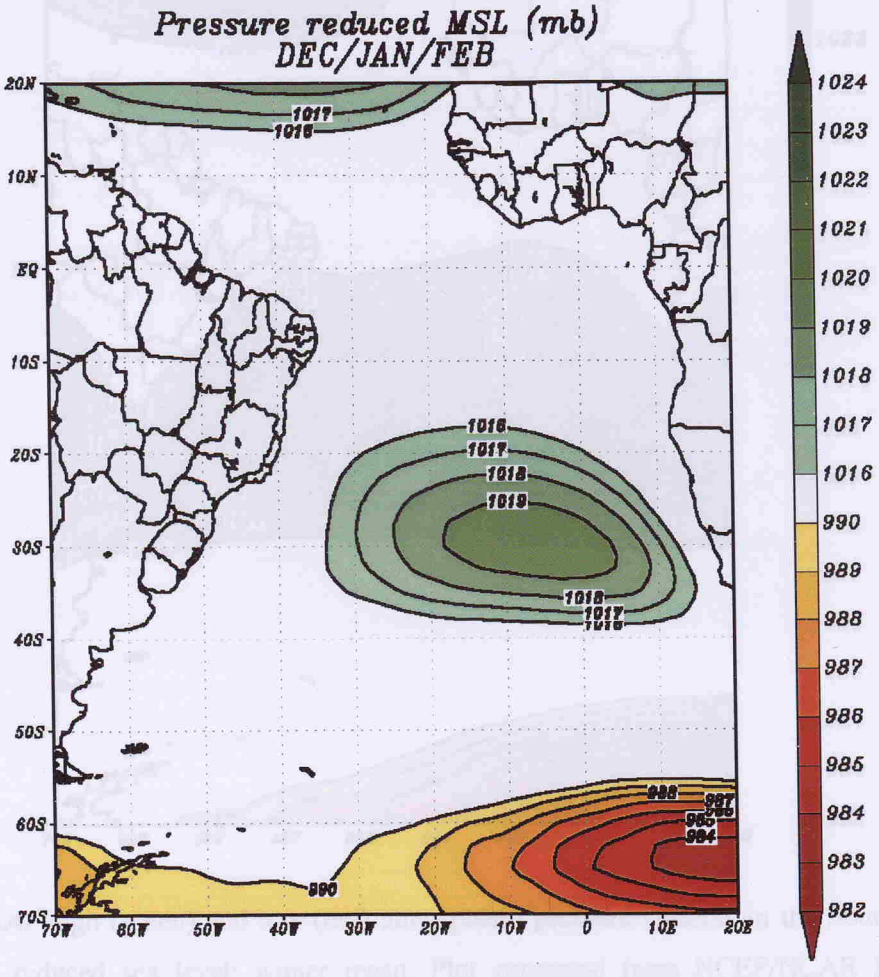

Figure 2.3. High (green) and low (red) atmospheric pressure systems in the South Atlantic ocean at reduced sea level: summer mean. Plot generated from NCEP/NCAR Reanalysis Project data (Kalnay et al., 1996).

The location of the BMC is believed to range from 36°S to 39°S in mean (Reid et al., 1977). The position in which the BC reverses its direction, however, is further south between 40°S and 46°S. After meeting the MC in the BMC region, the BC separates from the shelf break and penetrates the Atlantic Ocean interior, forming a series of large amplitude meanders.

Legeckis and Gordon (1982) found the variable limit of 38°S to 46°S as the maximum latitude of warm water related to the BC. The variability of this limit was found to be bi-monthly and accompanied by intermittent formation of warm-core anticyclonic eddies.

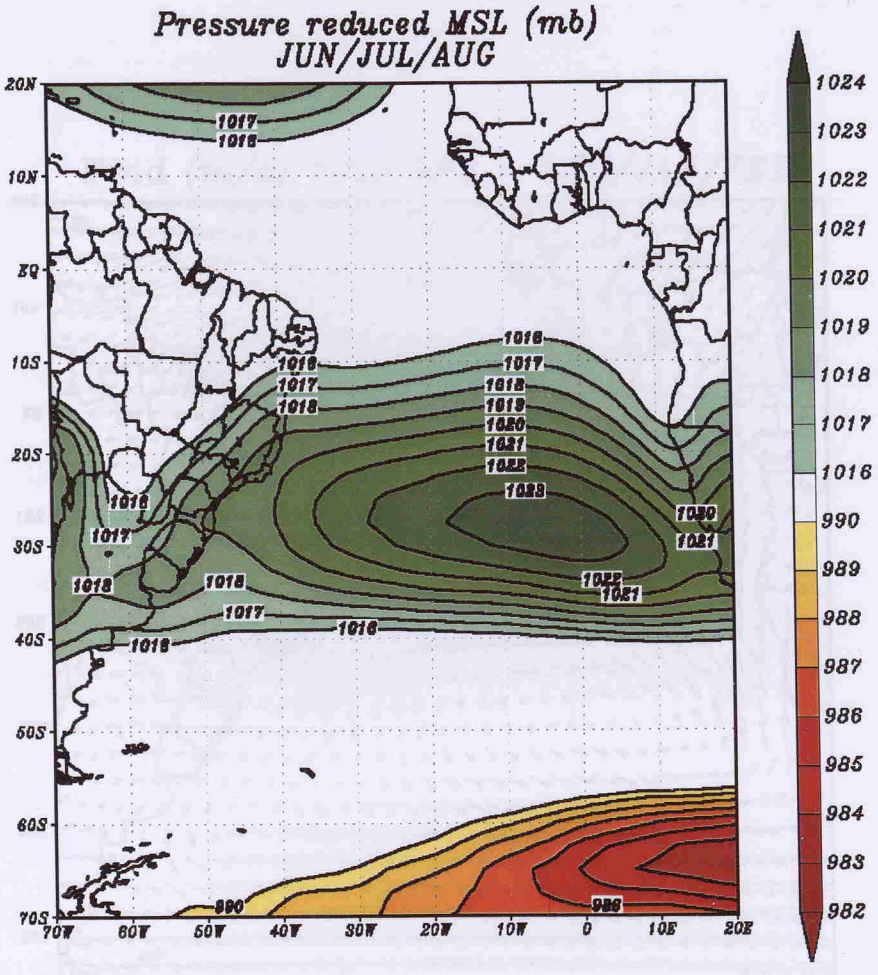

Figure 2.4. High (green) and low (red) atmospheric pressure systems in the South Atlantic ocean at reduced sea level: winter mean. Plot generated from NCEP/NCAR Reanalysis Project data (Kalnay et al., 1996).

Peterson and Stramma (1991) also compared the southward excursions of the BC with the analogous semi-periodic westward penetrations of the Agulhas Current into the South Atlantic. They pointed out the same bi-monthly time scales for both these current excursions.

Working with AVHRR data collected between July 1984 to June 1987, Olson et al. (1988) established the statistical characteristics of the separation region from the continental shelf

(position of the crossing with the isobath of 1000 m) for both the BC and MC. Following these authors, the BC separates from the shelf in the mean latitude of 35.8°S, with a standard deviation of 1.1°, or about 210 km (the total range of latitudes was found to be 4.8°, or 920 km). The MC, on the other hand, separates from the shelf at a mean latitude of 38.8°S, with a standard deviation of 0.9°, or 170 km (the width of maximum separation is 4.4°, or 850 km). The band of separation between BC and MC was found to vary from zero to 6° in latitude.

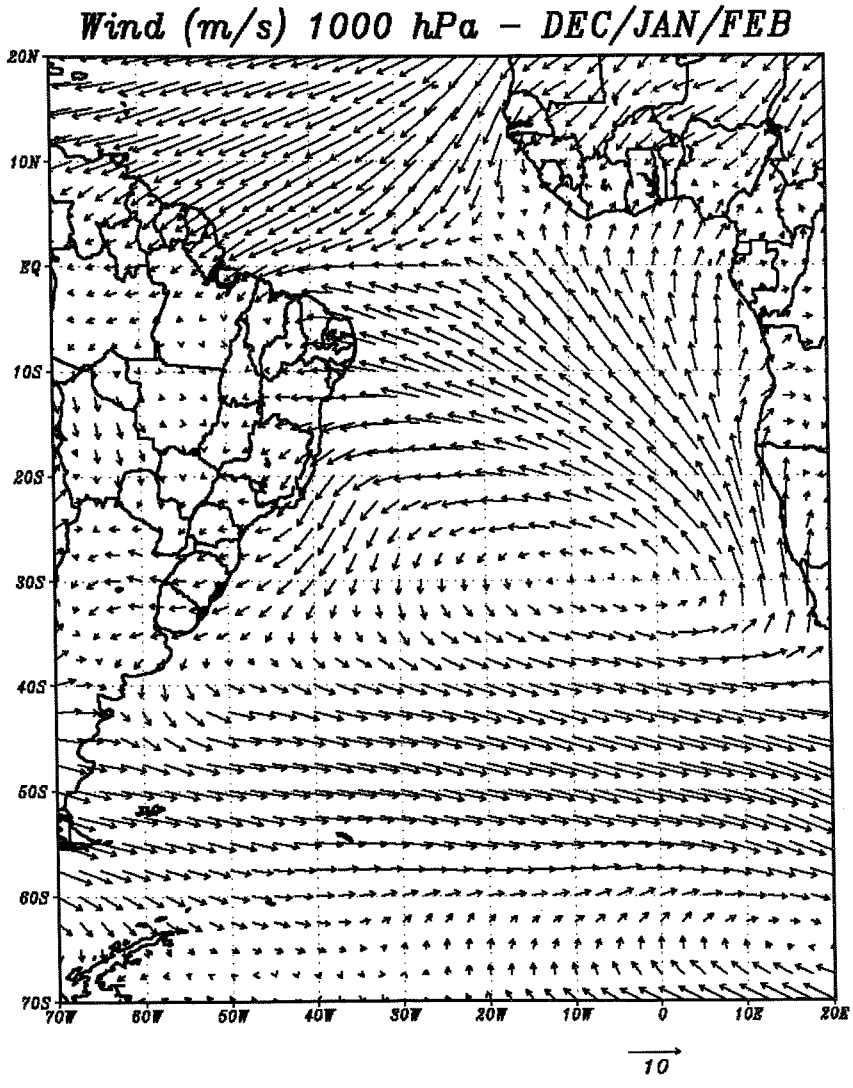

Figure 2.5. Surface winds in the South Atlantic ocean: summer mean. Plot generated from NCEP/NCAR Reanalysis Project data (Kalnay et al., 1996).

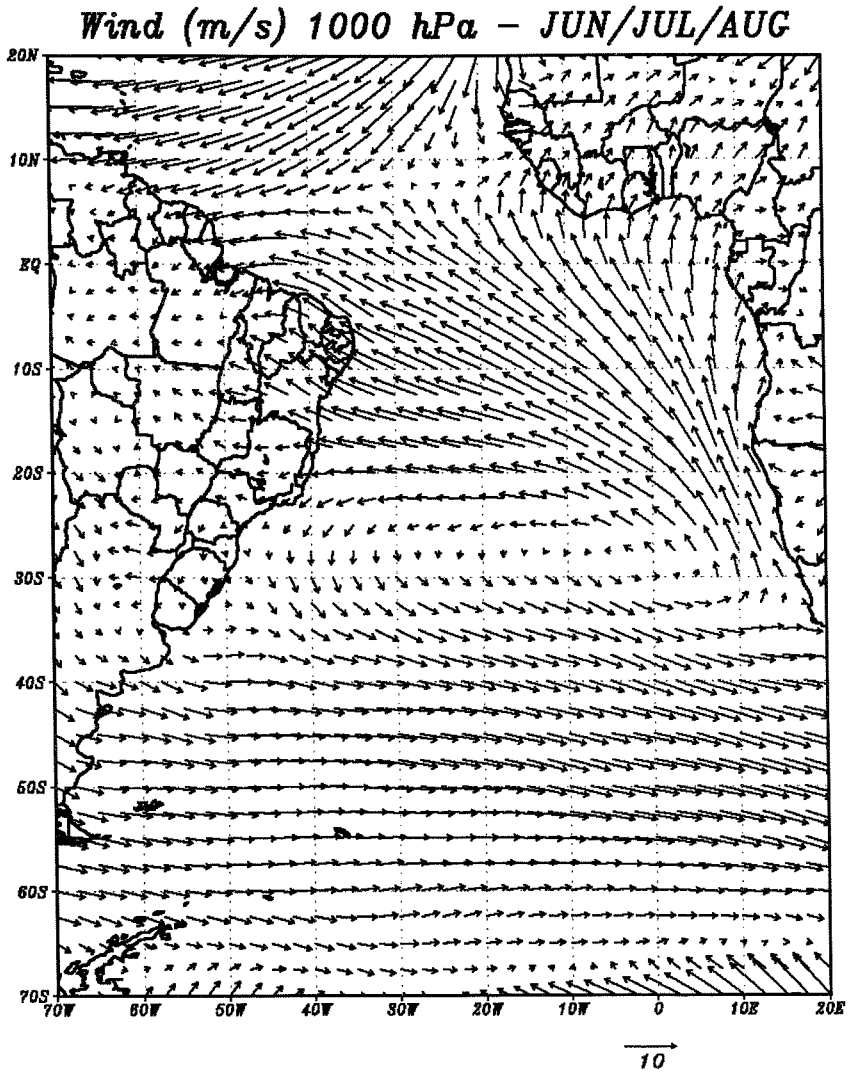

Figure 2.6. Surface winds in the South Atlantic ocean: winter mean. Plot generated from NCEP/NCAR Reanalysis Project data (Kalnay et al., 1996).

2.5. Lagrangian measurements of currents and kinetic energies

Several authors used drifting buoy measurements to describe either the large scale variability of the Southern Hemisphere oceans or the mesoscale variability of the BMC region (e.g. Patterson, 1985; Piola et al., 1987; Olson et al., 1988; Figueroa and Olson, 1989; Shafer and Krauss, 1995). Satellite-tracked, drifting buoy data presented by Olson et al. (1988) show a large anticyclonic circulation in the BMC region, believed to exist for long periods of time. This anticyclonic cell is the one discussed earlier in this document (Section 2.3), which is believed to participate in the process of intensification of the BC transport to the south of 30°S

(Peterson and Stramma, 1991). One of the drifters presented in Olson et al. (1988) spent 8 months describing an anticyclonic circulation in the BMC area.

Schafer and Krauss (1995) presented statistics for the major ocean currents in the Southwestern Atlantic and in the ACC. The authors deployed more than 130 satellite-tracked drifting buoys in the South Atlantic between 1990 and 1993, the majority of them drogued at 100 m depth. The BC mean velocity was found to be weak between 7°S to 20°S (4 cm/s [2]), increasing to 40 cm/s in the vicinity of the BMC region. The BMC region presented large variability, with zonal and meridional r.m.s. (root mean square) currents of about 40 cm/s.

The South Atlantic Current (SAC) was found to be almost zonal, with less variability than the BMC region, and presenting a mean velocity of 12 cm/s. The ACC in the Drake Passage and Scotia Sea presented a mean eastward velocity of 16 cm/s, with high r.m.s. velocities comparable to those from the BMC region. Following Schafer and Krauss (1995), the BC shows typical Eddy Kinetic Energy (EKE) varying between 200-400 cm^2/s^2. The MC reaches more than 500 cm^2/s^2. EKE values in the BMC region reach 1600 cm^2/s^2, decreasing again in the SAC farther east.

Piola et al. (1987), Stevenson and Souza (1994) and Stevenson (1996) also presented EKE values for the BC derived from drifting buoy data. While Piola et al. (1987) worked with FGGE (First GARP Global Experiment) buoys, the last authors used WOCE standard LCD drifters. EKE dominated the BC flow in both cases, but Stevenson and Souza (1994) and Stevenson (1996) found these values to range between 1332 cm^2/s^2 and 4207 cm^2/s^2, while Piola et al. (1987) found 500 cm^2/s^2. The Mean Kinetic Energy (MKE) in the BC was estimated to vary between 114-171 cm^2/s^2 by Stevenson and Souza (1994), values in good agreement with 200 cm^2/s^2 found earlier by Piola et al. (1987). The value of 200 cm^2/s^2 was also estimated for the MKE in the BMC region by Piola et al. (1987), but the EKE found in this region was 1200 cm^2/s^2, much higher than in the BC.

[2] Note that, despite recommendations for the utilisation of the International System of Units (SI), which indicates m/s as the unit for expressing the speed, current speeds denoted in this thesis are in cm/s. The units were previously used in the scientific literature described here and are kept for expressing our results for the sake of a direct comparison with previous works. The same applies to the units of energy which are here expressed in cm^2/s^2 instead of the SI unit J.

2.6. Brazil-Malvinas Confluence eddies

Eddies in the BMC region were first described by Legeckis and Gordon (1982) when analysing the BC and MC in 1975, 1976 and 1978 from satellite infrared images. The authors describe that the warm core eddies found at the BMC are formed during the retraction of the BC from the confluence at intervals of a week. The eddies described by Legeckis and Gordon (1982) for the BMC region are elliptical, with diameters of 180 km and 120 km for the major and minor axis, respectively. Advection to the south is described to occur at velocities of 4 km/day to 35 km/day, the higher the velocity the younger the eddy would be.

Olson et al. (1988) described that the frontal region between BC and MC is filled with eddies and high amplitude meanders. The authors have presented a very classical satellite image of the BMC region (Figure 2.7), where a large elliptical warm core eddy (anticyclonic in the southern hemisphere) of about 400 km by 200 km (major and minor axis respectively) is noticed detached from the BC southward extension. Olson et al. (1988) also presented some drifting buoys trajectories superimposed with AVHRR images in the BMC region to illustrate the nature of an eddy and meanders of the MC/BC front.

Garzoli (1993), using inverted echo sounders at the BMC region, observed both cyclonic and anticyclonic eddy circulation in the area. The author attributed the variability of the dynamic height field of the BMC region to the variation of the front position, its meandering and to eddy generation. Eddy diameters, as observed by Garzoli (1993), varied from 100 km to 150 km. These sizes were considered to be two to three times bigger than the expected Rossby radius of deformation for the area.

By using the chemical tracer CFC-113, Smythe-Wright et al. (1996) identified an eddy formed in the BMC region in the vicinity of Cape Basin, Africa (36.3°S; 3.9°E). Older than 4 years, approximately 600 m deep and measuring 150 km in diameter, the observation of this eddy would have marked the first evidence of such a structure so far east in the South Atlantic Ocean. Smythe-Wright et al. (1996) argue that this eddy should have travelled eastward in isolation from the surface since November 1988, assuming a 5500 km long trajectory along 40°S to 13°E before turning northward in the far east part of the subtropical gyre. Although the nature of this particular eddy has been recently claimed by McDonagh and Heywood (1999) to be related to the Agulhas Current rather than to the BC, the final conclusions drawn by Smythe-Wright et al. (1996) are still worth mentioning.

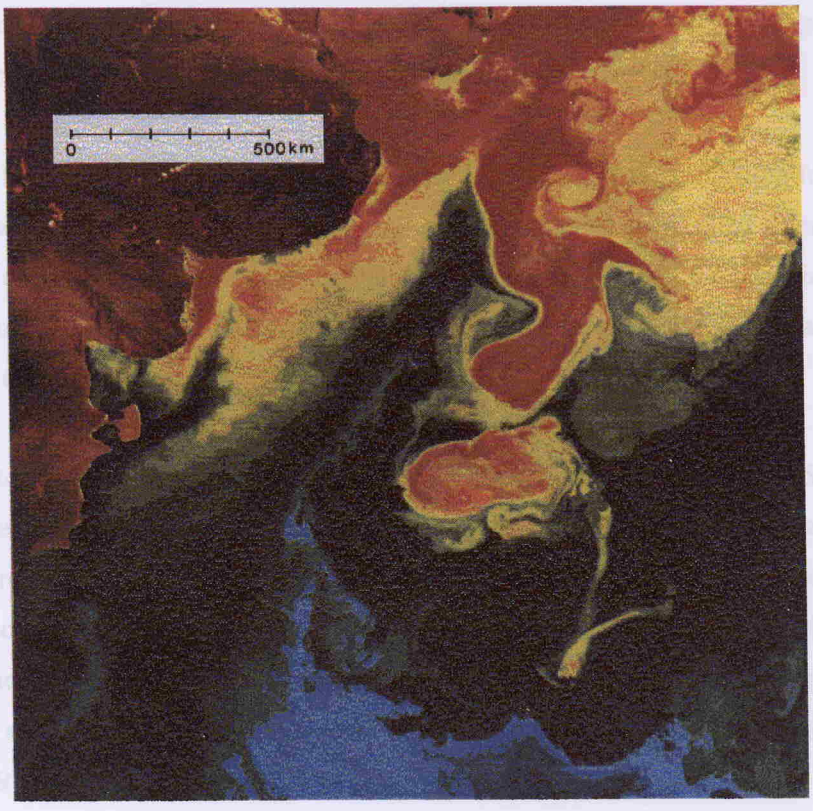

Figure 2.7. AVHRR image of the Brazil-Malvinas Confluence zone obtained in February 1985. The image illustrates the formation of a large anticyclonic (warm) eddy which had detached from the Brazil Current (in red) at its southward extension. Malvinas Current waters are seen in green to blue tones. Source: Olson et al. (1988).

Following the suggestion made by Gordon (1989) that at least 6 eddies are formed at the BMC each year, and considering that some of these structures can reach the far east part of the subtropical gyre, Smythe-Wright et al. (1996) suggested that the transport of multiple eddies generated in the BMC region by the SAC serves to retain salt within the gyre. This phenomenon would reduce the warm salty Indian Ocean water inflow required to balance the overall salt budget of the subtropical South Atlantic. Smythe-Wright et al. (1996) also point out the necessity of a systematic study of the characteristics of both the eddies formed at the BMC region and at the SAC itself.

Hooker and Brown (1996) discussed the nature of BC eddies formed in the BMC region. For the first time in the literature, the authors suggested that some of the BMC eddies are not isolated monopole vortices, but have sometimes a dipole configuration for both warm and cold rings. Hooker and Brown (1996) also observed a coalescence mechanism originated from the interaction between a monopole (solitary) and a dipole eddy, pointing out the

importance of such a process since coalescence between two rings of opposite vorticities cannot occur if they are both monopoles (one of them must be a dipole).

Hooker and Brown (1996) described dipoles formed in the BMC region lasting for 2 months, rotating at a rate of about 12 degrees per day. The authors also called attention to the importance of the use of infrared satellite imagery for studying the oceanic mesoscale variability, and to the application of new methods of visualisation of AVHRR images to better enhance the existence of dipoles in the ocean.

According to Podestá (1997) the present knowledge of the eddies in the Southwestern Atlantic Ocean is still lacking in basic aspects such as the frequency of formation, typical sizes, movements, lifetime and destination of these structures. Podestá (1997) hints that the number of eddies expelled from the BC is lower than that of other western boundary currents, but offers no proof for his affirmation. The energy contained in the BC eddies, however, seems to be similar to that of eddies formed in more energetic currents (Olson, 1991; cited by Podestá, 1997).

Podestá (1997) also reports that most of the studies based upon satellite data in the Southwestern Atlantic are in fact related to the open ocean BMC region. The author points out that, although there are many processes associated with the SST fields in the coastal regions of the Southwestern Atlantic, the utilisation of satellite information for the monitoring of these processes is not very frequent.

The results to be shown in this thesis offer an improvement to the present knowledge of the mesoscale processes in the Southwestern Atlantic by combining satellite information with drifting buoy data. Together with a study of the BMC region, a study of the SBCS and of the eddy field of both these regions is offered here. Before presenting these results, however, the next Section of this thesis will describe the basic concepts and historical development of the SST observation and estimation through sensors onboard satellites.

BLANK PAGE

CHAPTER 3

SATELLITE OBSERVATIONS OF THE OCEAN

3.1. Historical perspective

Satellites have been used for several decades to observe physical processes in the upper layer of the oceans. Remote Sensing offers synoptic views and regular temporal sampling of the ground. Not considering the instrument and spacecraft conception and launching, Remote Sensing data can be available at relatively low cost for the user. Remotely sensed data are used to monitor small to large scale processes in the ocean, from coastal, shallow waters, to deep ocean basins.

In comparison to the rest of the World Ocean, the Southwestern Atlantic is a region where there is a huge lack of *in situ* measurements, specially those referring to currents (Campos et al., 1996a; Peterson et al., 1996; Müller et al., 1998). As this is a chronic problem several authors have used Remote Sensing data and techniques to increase their understanding of the physical processes happening in that area.

Olson et al. (1988), for instance, report that the region of the Brazil-Malvinas (Falklands) Confluence (BMC), inside the Southwestern Atlantic Ocean is particularly suited for studies involving Remote Sensing techniques. The reason for this is the synoptic monitoring needed to describe the spatial mesoscale variability of the BMC, and the strong thermal signal found at the surface in that region.

Podestá (1997) points out that the strong thermal gradients between the Brazil and Malvinas currents is the reason why the BMC region has been studied by remote sensing techniques since the seventies. Tseng (1974) was pioneer on describing the BC fluctuations using Remote Sensing. This author used infrared data from the infrared radiometer THIR (Temperature Humidity Infrared Radiometer), which flew on the American satellite Nimbus-5.

The development of operational orbital platforms for studying the ocean derived mainly from the American experience with the Mercury mission, in the sixties, and with the establishment of the first series of Nimbus and NOAA (National Oceanic and Atmospheric Administration) series of meteorological satellites, in the seventies. The NOAA series supported the development of the Very High Resolution Radiometer (VHRR), an instrument designed to assess the Sea Surface Temperature (SST) of the oceans. Further development of the VHRR gave way to the modern AVHRR (Advanced Very High Resolution Radiometer), a present day five channels instrument widely used to generate SST charts.

Meanwhile, in the nineties, an initiative of the European Space Agency (ESA) put in orbit the ERS-1 (European Remote Sensing Satellite). Among other instruments, the ERS-1 satellite carried onboard the ATSR (Along-Track Scanning Radiometer), which was designed to measure the sea "skin" temperature, which is related to the first molecular layer of the sea at the sea-air interface. In April 1995, the launching of the ERS-2 put in orbit the ATSR-2 instrument.

In August 1996, the Japanese Space Agency NASDA launched the ADEOS (Advanced Earth Observing Satellite), carrying onboard the OCTS (Ocean Color and Temperature Scanner), designed for coastal and oceanic investigation. ADEOS stopped transmitting data from 30 June 1997 onwards due to an operational failure. While the satellite was still operational, however, OCTS was able to provide very good observational data for the oceanographic community. OCTS was a 12 band, multi-spectral scanner, able to determine the Sea Colour and SST at a spatial resolution of 700 m, better than both AVHRR and ATSR.

The study of ocean colour from space started in the late seventies with the deployment of the Coastal Zone Colour Scanner (CZCS) onboard the NOAA Nimbus-7 satellite. This instrument consistently recorded data in the World Ocean in order to achieve a measure of the concentration of phytoplankton and to establish global seasonal levels of primary productivity.

Following the success of the CZCS, NASA (National Aeronautics and Space Administration) was planning for many years to launch another radiometer designed to measure the sea colour. After years of expectations by the scientific community, the Sea-WIFS sensor was finally launched in August 1997 onboard the SeaStar satellite. Although Sea-WIFS was placed in orbit a little later than OCTS, the malfunction of the ADEOS satellite made Sea-WIFS the only sea colour orbital scanner in operation until May 1999.

Owing to the general interest of the scientific community in the sea's primary production estimated from sea colour data, the Indian Space Research Organization (ISRO) launched its own sea colour orbital sensor, the OCM (Ocean Colour Monitor) on 26 May 1999. This instrument is a solid state camera operating in eight spectral bands flying onboard the IRS-P4 (Oceansat-1) satellite.

During the last decades both the end of the cold war and the necessity for new variables to be monitored in the oceans allowed civil space enterprises to develop and to launch other kinds of sensors into space. The use of radar imagery or altimetry in oceanography, for example, is nowadays widely applicable to the study of surface and internal waves, surface slicks, bottom topography, surface winds, geostrophic currents and sea level. The first orbital radar images produced over the ocean were obtained by the Seasat satellite, launched in 1978 and alive for about 100 days. The results of its Synthetic Aperture Radar (SAR) were very remarkable, and it was used later as the base of the modern SARs.

Seasat was also designed to establish the "proof of concept" for ocean circulation measurements by a radar altimeter (Yamarone Jr. et al., 1995). Due to its good results and to the results of other missions (e.g. the Skylab, GEOS-3 and Geosat), the United States and France established plans for what became the joint mission TOPEX (Ocean Topography Experiment) / Poseidon (T/P). Since its launching on 10 August 1992, the T/P satellite has been measuring the height of the sea surface relative to the Earth's centre of mass, which allows the mapping of the ocean's topography. Other geophysical parameters like geostrophic currents, tides and waves, for example, can also be studied by utilising T/P measurements. Following the same principles of T/P, ESA is currently also running its own altimetry mission onboard ERS satellite series.

As discussed, the satellite and instruments designed to retrieve physical parameters of the ocean in a global or local basis are many. In the context of this thesis, where the AVHRR and ATSR instruments are used to provide SST estimates over the study region, the characteristics of these sensors and their carrying platforms will be better described in the next sections.

3.2. Thermal infrared imagery

3.2.1. Satellites and sensors

The establishment of a series of procedures leading to the estimation of SST from satellite measurements began in the early sixties with the operation of the Television Infra Red Observational Satellites (TIROS). The meteorological TIROS Operational Satellites (TOS) operated between 1966 and 1969, leading to the Improved TIROS Operational Satellites (ITOS) series in the early seventies.

The ITOS series of satellites were taken over afterwards by NOAA, being renamed as the TIROS/NOAA series. From 1978, NOAA started the Advanced TIROS-N (ATN) series, which has been in continuous operation until the present (Forrester, 1991; Kidwell, 1995). The last version of the radiometer carried by the NOAA satellites is the AVHRR/2, referred to here simply as AVHRR, although AVHRR/3 is expected by the beginning of this decade.

In 1991, ESA launched the ERS-1, which carried the ATSR sensor. This instrument is composed of a passive Infrared Radiometer (IRR) and a two-channel (23.8 and 36.5GHz) Microwave Sounder, aiming to provide atmospheric total water vapour content. Further references in this text to the ATSR are actually relative to the IRR. The nature of the SST estimate performed by the ATSR is intrinsically different from that of AVHRR, since the ATSR instrument is designed to make conical scans over the scene, in two distinct angles of view (discussed later in this section). Based upon the success of the ERS-1 mission, ESA launched the ERS-2 satellite in 1995, putting the ATSR-2 sensor in orbit. Following this, ESA plans to launch the AATSR (Advanced ATSR) on Envisat early this decade.

All NOAA series and ERS satellites fly sun-synchronous (quasi-polar) orbits around the earth, approximately at an altitude of 800 km. NOAA manages to operate 2 satellites simultaneously, separated by about 90° in longitude (about 6 hours), which means there are at least four overpasses at each location daily, a much better temporal resolution than ATSR. The ascending node for NOAA-11, 13 and 14 satellites was set to 13:40 LST (Local Solar Time), while the descending node was set to 01:40 LST. NOAA-12 is orbiting its ascending node at 19:30 LST and its descending node at 07:30 LST. This satellite is nowadays operating simultaneously with NOAA-14, but some years ago NOAA-12 used to operate with NOAA-11.

The temporal resolution of ATSR images depends mainly on the ERS orbit phase and cloud coverage. Jones (1997) shows the sampling density of ATSR data in the South Atlantic ocean for the period between January 1992 and December 1994. Due to the increase of cloud coverage towards the pole, Jones (1996) found a typical sampling density of two measurements every 10 days in the tropics, and of 1 measurement every 20 days at higher latitudes. All the polar-orbiting satellites with sensors able to estimate SST in operation during the years of 1993 and 1994 (the period when the drifters used in this study were at the sea) are shown in Table 3.1.

The spectral channels for AVHRR and ATSR sensors are centred at the following wavelengths:

- 0.63 μm (AVHRR channel 1);
- 0.91 μm (AVHRR channel 2);
- 1.6 μm (ATSR-1 channel 1);
- 3.7 μm (AVHRR channel 3; ATSR-1 channel 2);
- 10.8 μm (AVHRR channel 4; ATSR-1 channel 3);
- 12 μm (AVHRR channel 5; ATSR-1 channel 4).

The AVHRR instrument has its first two channels centred at visible (suitable for cloud identification) and near infrared (suitable for land/sea discrimination) bands of the electromagnetic spectrum. Aiming to improve daytime cloud identification over snow and ice, the ATSR instrument has an unique channel in the near-infrared substituting both AVHRR channels 1 and 2 (Závody et al., 1994). ATSR-2, on the other hand, has added three visible channels in comparison to ATSR-1, those centred at 0.56 μm, 0.67 μm and 0.87 μm.

The AVHRR sweeps out a swath of about 3000 km wide on the earth's surface, the product of a cross-track field of view (FOV) of ± 54° off nadir. Full-resolution (1.1 km at nadir) data are automatically downloaded to the ground stations in the HRPT (High Resolution Picture Transmission) mode. From the total time of about 102 min of each satellite orbit, 10 min of full-resolution data can also be recorded onboard and later downloaded to one of CDA (Command and Data Acquisition) ground stations managed by the NOAA NESDIS (National Environmental Satellite, Data and Information Service). This mode of acquisition is named LAC (Local Area Coverage).

Table 3.1. Satellite and sensors operating between 1993-94

satellite	*satellite lifetime*	*sensor*	*sensor lifetime*
NOAA-11	24 September 1988 - 11 April 1995	AVHRR	8 November 1988 - 11 April 1995
NOAA-12	14 May 1991 - present	AVHRR	same as the satellite
NOAA-13	9 August 1993 - 21 August 1993	AVHRR	same as the satellite
NOAA-14	30 December 1994 - present	AVHRR	11 April 1995 - present
ERS-1	17 July 1991 - 2 June 1996	ATSR-1	3.7 μm channel failed on 26 May 1992

When NOAA satellites dump the full-resolution data to the ground, an internal recorder also re-samples this acquired data from 1 km × 1 km to 4 km × 4 km resolution. By doing that, the system allows the CDA stations to receive the complete (re-sampled) set of data registered at each entire satellite orbit. This acquisition mode is known as GAC (Global Area Coverage), and is the basis of NOAA's global operational SST charts, such as the NOAA MCSST products and, more recently, the NOAA AVHRR Oceans Pathfinder (Forrester, 1991, Vazquez et al., 1998).

The modes of acquisition and downloading of ATSR images are slightly different from NOAA's . ATSR is a radiometer with a conical scan (Figure 3.1), inclined at angles varying from 0° to 24° in the nadir view, and from 53° to 55° in the forward view (Saunders et al., 1993; Mutlow et al., 1994; Jones, 1997). Pixel resolution ranges from 1 km × 1 km at nadir to 1.5 km × 2 km at 55°. The ATSR curved swath is nominally 500 km wide, with 555 pixels across the nadir swath and 371 pixels across the forward swath (Mutlow et al., 1994).

Due to its telemetry bandwidth, the ATSR data need to be compressed onboard the satellite before its downloading to the ground. This compression procedure allows three out of the four ATSR channels to be transmitted simultaneously. Two of the three telemetry slots are always occupied by ATSR channels 3 and 4. The third telemetry slot transmits either channel 1 or channel 2 data, depending on an automatic selection based on the scene radiance levels measured by channel 1. The automatic selection generally results in the transmission of channel 1 data in the daytime, and of channel 2 data at night. Nevertheless, bright spots in the scene at night produced by forest fires, as an example, can trigger the transmission of channel 1 data (Mutlow et al., 1994).

Závody et al. (1994) discuss the ATSR processing scheme developed at the UK Earth Observation Data Centre (EODC), including the modes of decodification of telemetry data, geolocation of the images and derivation of scientific products, such as the SST images. According to Závody et al. (1994), geolocation is by far the most complex part of the ATSR processing scheme. Images produced by the ATSR conical scan are mapped into 1 km × 1 km pixels in two-dimensional 512 × 512 arrays, and collocation accuracy of both nadir and forward view 512 km × 512 km images is about 1 km in the worst case. SST products available from ATSR measurements include the full-resolution (512 × 512 array, 1 km × 1 km pixel resolution) data, and a high precision, global, spatially averaged SST field (Mutlow et al., 1994). This last product, called ASST, is produced by cloud clearing and the averaging of full-resolution data into sample bins of 0.5 degrees × 0.5 degrees in latitude/longitude.

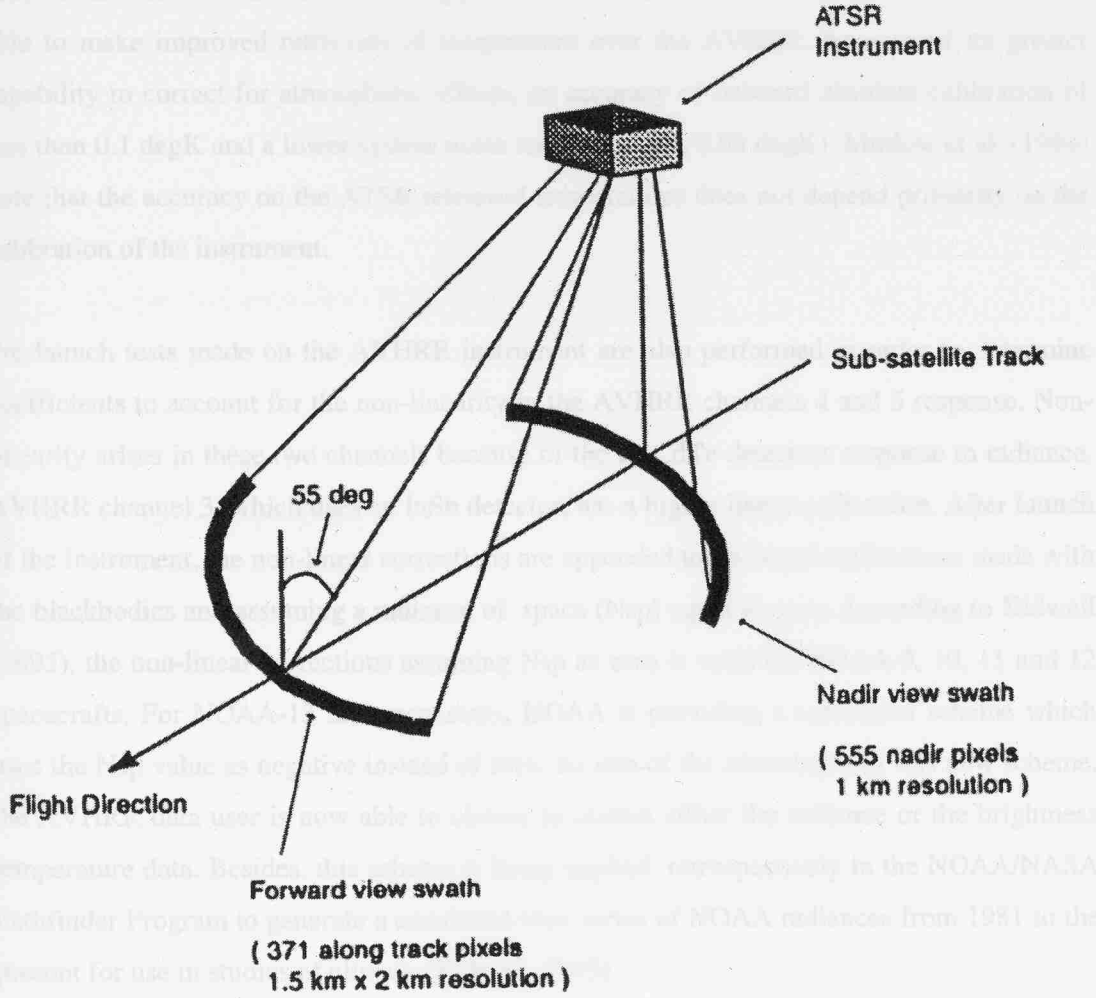

Figure 3.1. ATSR scan geometry. Source: Mutlow et al. (1994).

Infrared radiometer measurements are expected to be accurate, requiring the sensors to be well calibrated and stable. Following Planck's Law (see Section 3.2.2), small errors in radiance measurements made by the sensors can generate large errors in retrieving the actual temperature of the scene (Robinson, 1985). Long-term, onboard calibrations of the ground radiance measurements are often made by taking onboard blackbody radiance measurements as well. Both AVHRR and ATSR are designed to make measurements on temperature-stable (warm) internal blackbodies and on the (cold) space every scan cycle. The use of linear extrapolation between digital counts of blackbody or space radiance, and ground radiance is used to retrieve ground digital counts.

Robinson (1985) reports that AVHRR in-flight calibration errors can produce temperature uncertainties of about 0.3 degK. This arises from errors in the assumed emissivity of the blackbody, and from the accuracy and resolution of the platinum resistance thermometers used to monitor the blackbodies' temperatures. Saunders et al. (1993) consider the ATSR able to make improved retrievals of temperature over the AVHRR, because of its greater capability to correct for atmospheric effects, an accuracy of onboard absolute calibration of less than 0.1 degK and a lower system noise temperature (< 0.05 degK). Mutlow et al. (1994) note that the accuracy on the ATSR retrieved temperatures does not depend primarily on the calibration of the instrument.

Pre-launch tests made on the AVHRR instrument are also performed in order to determine coefficients to account for the non-linearity in the AVHRR channels 4 and 5 response. Non-linearity arises in these two channels because of the HgCdTe detectors response to radiance. AVHRR channel 3, which uses an InSb detector, has a highly linear calibration. After launch of the instrument, the non-linear corrections are appended to on-board calibrations made with the blackbodies and assuming a radiance of space (Nsp) equal to zero. According to Kidwell (1995), the non-linear corrections assuming Nsp as zero is valid for NOAA-9, 10, 11 and 12 spacecrafts. For NOAA-13 and successors, NOAA is providing a correction scheme which uses the Nsp value as negative instead of zero. As one of the advantages of this new scheme, the AVHRR data user is now able to choose to correct either the radiance or the brightness temperature data. Besides, this scheme is being applied retrospectively in the NOAA/NASA Pathfinder Program to generate a consistent time series of NOAA radiances from 1981 to the present for use in studies of climate (Kidwell, 1995).

3.2.2. Sea surface temperature estimates

Infrared radiometers are instruments designed to measure the infrared radiation reflected or emitted by the earth surface towards the direction of the sensor. Although the sun emits radiation at shorter wavelengths peaking in the visible (0.4 μm to 0.7 μm), the earth emits radiation peaking around 10 μm, which is thermal infrared. The amount of energy emitted by the sea surface towards the direction of an infrared radiometer mounted on a satellite orbiting the earth is the basis for computing the SST.

Robinson (1985), Maul (1985) and Fiúza (1992) offer excellent texts regarding the physics of the infrared radiation and its relation to the "real" temperature of a "grey" body. The relationship between Spectral Exitance (or Spectral Emmitance, M_λ) and Temperature (T) of a perfect emitter blackbody is given by Planck's Law:

$$M\lambda = L\lambda\pi = \frac{C_1}{\lambda^5\left[exp(C_2 / \lambda T) - 1\right]} 10^{-6} \tag{3.1}$$

where:

M_λ: Spectral exitance in $W.m^{-2}.\mu m^{-1}$;

L_λ: Spectral radiance in $W.m^{-2}.\mu m^{-1}$;

λ: Wavelength in μm;

C_1: $3.74.10^{-16}$ $W.m^{-2}$;

C_2: $1.44.10^{-2}$ m.degK;

T: Temperature in degK.

Planck's Law assumes that the blackbody is a Lambertian surface (emits radiation equally in all directions). The relation between the Spectral Exitance of a blackbody (perfect emitter) and a grey body (natural surfaces) is given by the Spectral Emissivity (E_λ):

$$\varepsilon_\lambda = \frac{M\lambda\, natural\ surface}{M\lambda\ blackbody} \tag{3.2}$$

The emissivity does vary weakly in relation to the body's temperature, but major variations are caused by varying the wavelength. Sea surface emissivity is about 0.98, varying very little with wavelengths between 3 μm to 14 μm (range of infrared sensors), temperature and surface roughness, although affected by surface slicks (Robinson, 1985). Satellite Zenith Angle (SZA) also plays an important effect in the sea surface emissivity and, at SZA equal or greater than 50°, waves are likely to produce some effect as well. Sensors measuring the 3.7 μm channel (AVHRR channel 3 and ATSR channel 2) were found to have daily infrared radiance measurements contaminated by direct solar irradiance reflected at the sea surface. As a result of this, AVHRR channel 3 and ATSR channel 2 are only used in night algorithms to produce SST estimates.

Having measured L_λ by different channels of each infrared radiometer, Equation 3.1 enables one to compute the scene temperature as if the emitter was a blackbody. This wavelength dependent temperature is called "apparent" or "brightness" temperature (BT), and it forms the basis of empirical or experimental algorithms to generate SST.

Although the infrared radiometers are designed to operate in certain bands (channels) of the electromagnetic spectrum where the influence of the atmosphere is lower ("atmospheric windows"), the pathlength of atmosphere between the ground and the orbital sensor still influences the level of radiance detected by the sensor. Robinson (1985) observes that absorption of incoming radiation and later re-emission of it in different wavelengths is the main problem in the spectral range of 3 μm to 14 μm. In opposition to the visible, infrared radiation is less affected by molecular or aerosol scattering. Robinson (1985) also refers to ozone, carbon dioxide and water vapour as the main absorbers of infrared radiation in the atmosphere. Závody et al. (1995) also consider the following gases as minor contributors to the absorption in the atmosphere: nitrogen, nitric acid, ammonia, carbonyl sulphide, nitrous oxide, methane, trichloromethane (FC11) and dichlorofluoromethane (FC12).

The actual absorbance of the atmosphere varies both spatially and temporally, and the distribution of its absorbing molecules through the atmosphere varies in an even more complicated manner. The result, however, is that the atmosphere (being cooler than the ground or sea) emits infrared radiation representing lower temperatures than the ground or sea.

The AVHRR and ATSR programmes have different approaches to solve or diminish the effect of atmospheric absorption. From the development of the AVHRR sensor, the approach

to estimate SST from infrared measurements was a multi-channel or multi-window technique, where different BT measurements taken on different channels in the infrared are combined in a specific algorithm. The first AVHRR/2 (5 channels) instrument launched onboard NOAA-7 allowed the establishment of the MCSST (Multi-Channel Sea Surface Temperature) procedure.

The MCSST procedure, obtained by regressing different pairs of combinations between two or three AVHRR infrared channels, resulted in simulation equations with very small errors of SST prediction (McClain et al., 1985). When compared with *in situ* SST data, however, the equations proved to have a consistent bias. In order to reduce this bias, NOAA started to use sets of closely matched buoy and satellite measurements. As a result, NOAA's algorithms evolved to estimate subsurface "pseudo-bulk" temperatures (close to those measured by buoys or ships of opportunity), rather than the "skin" temperatures from which the radiance is directly emerging towards the sensor. McClain et al. (1985) also indicate that the addition of terms depending upon the Satellite Zenith Angle (SZA) gave better performance to the nighttime MCSST algorithms. The authors also indicate that SST estimates retrieved by the MCSST scheme have accuracies of 0.5-0.6 degK. An extensive description of all atmospheric correction algorithms used so far at NOAA since the launching of the TIROS-N spacecraft in 1978 can be found in Kidwell (1995).

ATSR measurements, on the other hand, can be combined in terms of different angles of viewing the same scene. This technique, known as the multi-view technique, allows correction for the atmospheric effect by estimating the influence of the absorbers through different atmospheric paths. The way of combining different channels in different views are similar to NOAA's "dual-window", "split-window" or "triple-window" techniques, although the retrieved temperature refers to the "skin" or molecular surface of the sea. Differences between "bulk" and "skin" temperatures are still under investigation, and some discussions on this subject can be found in Robinson (1985), Hepplewhite (1989), and Mutlow et al. (1994), among others. Závody et al. (1994) report this problem as a work in progress to provide further enhancements of the ATSR data products.

BLANK PAGE

CHAPTER 4

DATA AND DATA PROCESSING METHODS

4.1. Low Cost Drifters

4.1.1. Characteristics of the buoys and associated data

The drifting buoys used in this work were built at INPE (Instituto Nacional de Pesquisas Espaciais - National Institute for Space Research), Brazil, for use in the COROAS project, the Brazilian counterpart to the WOCE project (Campos et al., 1996). Like all the surface drifters in use within the WOCE Surface Velocity Program (SVP), the COROAS LCDs were fabricated following the design proposed by Sybrandy and Niiler (1991).

The principal components of the LCDs are the surface float, the wire tethers, the subsurface float or balance element and the holey-sock drogue (Figures 4.1 and 4.2). The surface float houses the antenna, the Platform Transmitter Terminal (PTT, the ARGOS transmitter plus the data processor), batteries and the SST and drogue-loss (immersion) sensors. The holey-sock drogue provides the drag for the LCDs surface float. The LCD is designed to follow water parcels vertically averaged over the holey-sock height of about 6-7 m, centred 15 m below the surface (Niiler et al., 1991).

According to Niiler et al. (1991), the LCD design was developed to meet two principal objectives:

To have known water-following characteristics or to have a predictable slip of the drogue centre through the water (for the water-following capability of the holey-sock drogue refer to Niiler et al. (1995));

To last for many months in the rugged open ocean environment.

A third objective of the design, as the name of the drifter indicates, is the low cost of its fabrication (around US$ 2000 in 1991). The facility of deployment was also desirable.

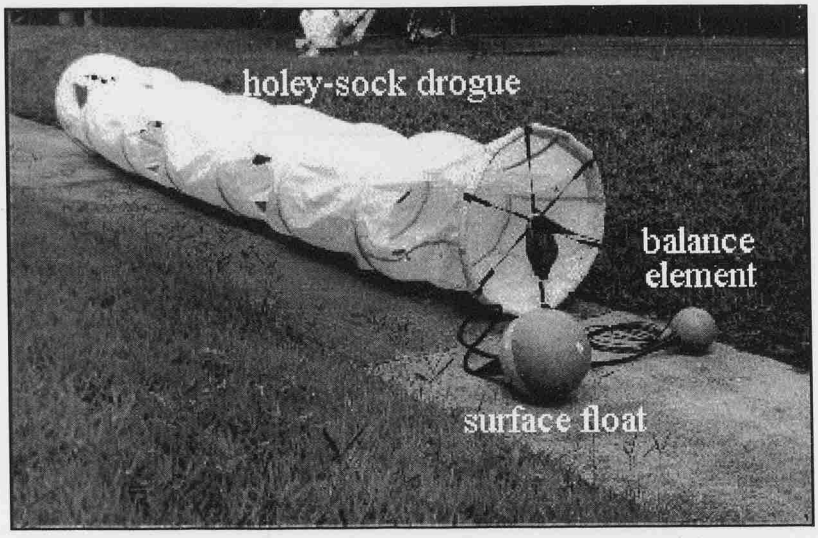

Figure 4.1. Photograph of the WOCE standard Low Cost Drifter (LCD) fabricated at INPE.

The drifter design adopted by the SVP/WOCE attempted to minimise the effects of wind and waves in the surface float, the contamination of the current signal by aliasing of wave-induced and tether forces, and slippage of the drogue. To achieve that, the LCDs have some distinct mechanical characteristics (Sybrandy et al., 1995):

- The surface float is spherical in order to minimise the rectification of surface waves into net horizontal forces;

A subsurface float is present to reduce the mean tension between the surface and subsurface components. This also reduces the aliasing of vertical forces into slip-producing horizontal forces;

- The wire tethers are thin and stiff in order to minimise drag-induced slip and to reduce looping and kinking caused by wind waves;

The drogue is dimensionally stable with a design resistant to kiting under normal load conditions. The holey-sock gives a drag area ratio (drogue:tether + floats) of about 37.

The ARGOS PTTs contained in the COROAS drifters were programmed to report geophysical parameters to the NOAA satellites at 90 second intervals. In order to save energy and costs, the PTTs were also programmed to work only for 8 hours per day.

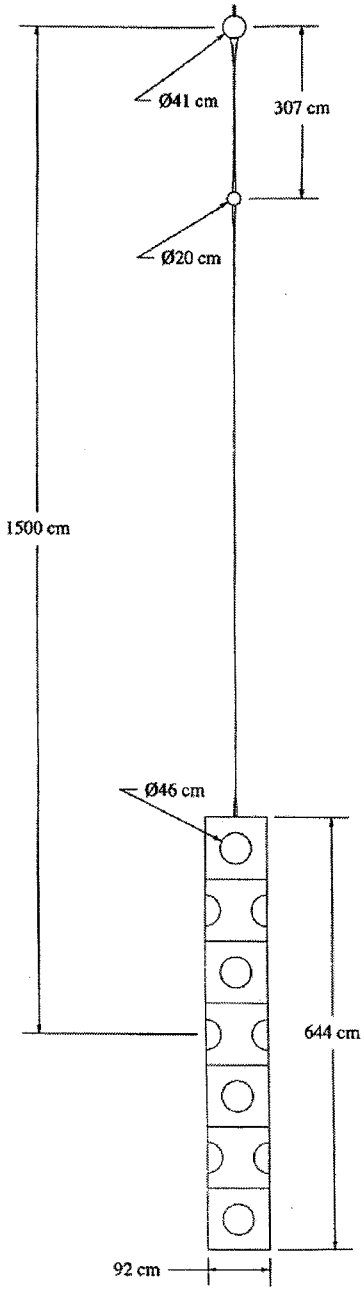

Figure 4.2. Squematic of the LCD. Source: Sybrandy and Niiler (1991).

To be able to measure SST, each LCD had a thermistor attached to the hull. The thermistor measured temperatures at 12 cm beneath the mean water line of the buoy to a precision of about 0.05°C (Stevenson et al., 1998). The buoys' positions, together with the temperature measurements and other geophysical parameters (such as the battery level and an empirical

measurement of whether the buoy still had its drogue, for instance) were assessed through the ARGOS System at CNES (Centre National d'Etudes Spatiales) in Toulouse, France.

The drifters' positions were computed in the ARGOS centre in Toulouse. At the time our data were acquired, ARGOS used to compute the location of moving PTTs by using the measurement of the Doppler effect on the transmitters' signals to the satellites during their passage above the transmitters' horizon (ARGOS, 1988).

The accuracy of the location estimates made at ARGOS in the past were divided into three different classes, where the best, used in our data, was nominally equal to 150 m (ARGOS, 1988). Depending on the quality of data being transmitted and external factors like the sea state, for example, the locations could in fact be accurate to 111 m or $\pm$ 0.001° in latitude (Stevenson et al., 1998). At the time of writing, however, ARGOS-tracked platforms are being configured to transmit GPS (Global Positional System) data together with their geophysical measurements, which has improved the accuracy of the locations to circa 5 m.

Owing to the previous ARGOS methodologies of retrieving the PTTs' locations, only one position for each LCD was computed for each particular NOAA satellite overflight above the transmitter horizon. To assure good quality data as well, ARGOS also only compute a particular location if more than 3 transmissions are received during the overflight (Stevenson et al., 1998). The same is not the case for the geophysical parameters being measured by the buoys, like temperature. Because the measurements are transmitted to the satellite at 90 s, several of them are actually received by the satellite during each overpass. The result is that the user ends up with more temperature measurements than buoy locations in relation to the time.

The duration of a particular NOAA satellite overflight above a transmitter located at the sea surface is about 10 to 15 minutes. The number of NOAA satellite overflights in a particular location, though, increases with latitude. That makes the number of locations obtained by ARGOS for a particular PTT increase with latitude as well. Stevenson and Alonso (1986) have shown that the number of ARGOS locations per day is around 6 between the Equator and $\pm$ 40° in latitude, increasing exponentially to 19 at the latitude of about 70°N or 70°S.

After the collection phase, the LCD data were retrieved from the ARGOS centre in France to INPE, Brazil, through a modem connection. Each LCD time series was recovered and updated at 4 day intervals until the end of the transmission period for each buoy. Once all the time

series were complete, the data were submitted to a test of consistency, which discarded discrepancies in both position and temperature series.

To overcome the problem of receiving more temperature measurements than buoy locations, the temperature data used in this work was always the one closer in time (usually zero to a few seconds) to a particular buoy position computed by ARGOS. No temporal temperature average was performed for a given overflight also because the buoys were most of the time following temperature contours which do not change in the very short period of time typical of a satellite overpass and, by consequence, most of the temperature retrievals were the same. Very few exceptions to that were treated case by case and spurious data were visually discarded from the series.

The drifters used in this work were deployed in the BC in a position close to the shelf break near 24.8°S, 44.3°W off the São Paulo State coast, Brazil. The deployment campaign was conducted by the COROAS project, onboard the R.V. Prof. W. Besnard. The buoys were deployed following a box pattern, five at a time, in February 1993 (buoys number 3178 to 3182), July 1993 (number 3183 to 3187) and January 1994 (number 3188 to 3192). For more information about the LCDs' launching procedure refer to Stevenson and Castro Filho (1996).

Following the general flow of the BC, the 15 buoys launched in this current drifted southwestward covering the COROAS region of interest off the São Paulo coast (~ 23°S to 27°S, 42°W to 47°W). From the second group of buoys launched in the BC, buoys 3184 and 3186 stopped transmitting data immediately after the launching. All the other 13 buoys traversed the COROAS study area. After a variable time which depended on each particular buoy trajectory, all the buoys (apart from buoy 3183) reached the vicinity of the BMC region at about 30°S. The BMC area not being a region of primary interest for COROAS objectives, the Lagrangian dataset collected by the project in that area was kindly made available for this research.

The Lagrangian dataset used in this work, then, consists of positions and temperature time series of 12 LCDs which had drifted into the vicinity of the BMC region in 1993 and 1994. The lifetime period of each LCD depended on both the PTTs electronic programming scheme and on eventual accidental losses. Without counting the time already spent in the COROAS area of study, the buoys used here had lifetimes varying from 2 weeks to about 11 months (Table 4.1.).

Table 4.1. Lifetime and number of observations (N) for the LCDs after achieving the vicinity of the BMC region

buoy	*start (Julian day)*	*finish (Julian day)*	*lifetime (days)*	N
3178	6 Apr 93 (96)	3 Jul 93 (184)	88.03	186
3179	24 Mar 93 (83)	15 Oct 93 (288)	204.29	298
3180	21 May 93 (141)	30 Jul 93 (211)	69.78	224
3181	12 Mar 93 (71)	26 Mar 93 (85)	14.27	21
3182	23 Mar 93 (83)	11 Feb 94 (407)	324.23	1350
3185	1 Set 93 (244)	15 Apr 94 (470)	226.03	747
3187	13 Dec 93 (347)	16 Apr 94 (471)	123.11	371
3188	12 Feb 94 (408)	1 Mar 94 (425)	17.03	65
3189	13 Feb 94 (409)	5 Jul 94 (551)	141.96	513
3190	5 Feb 94 (401)	5 Jul 94 (551)	150.05	474
3191	1 Feb 94 (397)	5 Jul 94 (551)	153.99	576
3192	4 Feb 94 (400)	5 Jul 94 (551)	151.03	585

Note: Julian day 1 = 1 Jan 93; Julian day 366 = 1 Jan 94.

After reaching the area close to the BMC region at about 30°S in the BC, three LCDs turned westward, penetrated the continental shelf and then drifted in a direction opposite to the BC flow. Previous COROAS results suggested a coastal recirculation scheme for the BC (Stevenson and Souza, 1994; Stevenson, 1996), in which the northeastward course followed by these buoys was thought to be a coastal branch of a large BC loop. Further analysis made in this work (Chapter 6) has demonstrated that the buoys actually entered a coastal current which interacts with BC, but which is not part of it. This current is referred to in this work as the Brazilian Coastal Current (BCC).

Seven of the remaining LCDs followed an eastward direction when reaching the BMC region. Carried by the extension of BC called the South Atlantic Current (SAC), these buoys penetrated the open ocean to longitudes up to 36°W. The other 2 LCDs used here had trajectories entirely located in the BC. None of the buoys used here sampled the Malvinas (Falkland) Current. Figure 4.3 shows the overall trajectories of the LCDs in the form of a 'spaghetti diagram'.

The number of locations retrieved for each of the drifters used in this work varied from 0 to 7 per day, being equal to 4 most of the time (39.4 % of the cases). Figure 4.4 displays the frequency histogram of the number of observations per day for the overall set of LCDs used here. 86.7 % of the data were collected at the rate of 2 to 5 locations per day. Considering that the range of latitudes covered by our LCDs was between 23°S and 45°S (Figure 4.3), 2 to 5

locations per day are broadly in agreement with the estimates made previously by Stevenson and Alonso for Service ARGOS retrievals (1986).

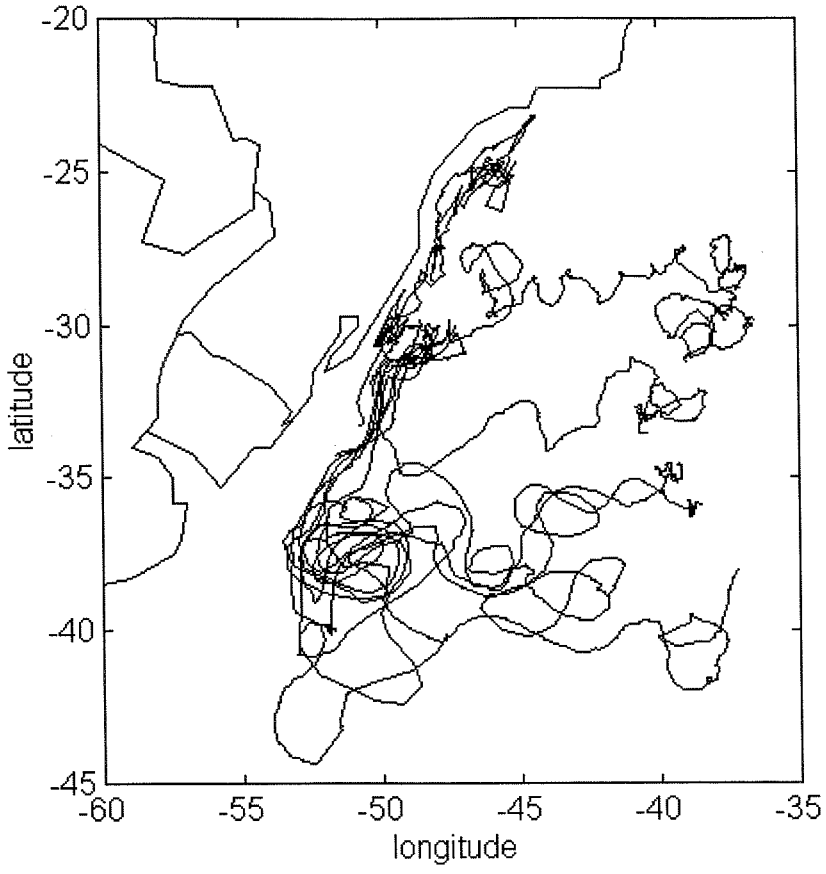

Figure 4.3. Overall trajectories of the LCDs used in this work.

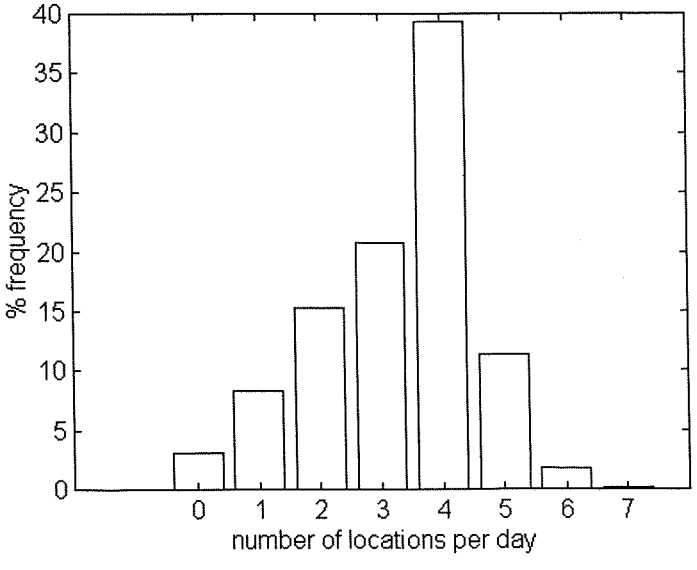

Figure 4.4. Frequency histogram of the locations per day for the LCDs.

4.1.2. Data processing

4.1.2.1. Pre-processing and quality control

As remarked before, the LCD time series were submitted to pre-processing and quality control in order to discard eventual discrepancies in both position and temperature data.

First of all, part of the temperature data, more frequent than the positional data in the original time series, was discarded following the procedure described in Section 4.1.1. Owing to the technology involved in the telemetry link between the PTT and the satellite (transmission of a UHF signal with the PTT identification and geophysical measurements), electronic noise is often encountered. This causes the recording of spurious data. Other factors like the stability of the PTT's internal oscillator (which mantains the transmission signal at a certain frequency) or even its abrupt movement caused by the sea state, for example, can also cause the apperance of bad data in the series. Spiking points in both the temperature and position time series, when caused by bad data, were often several orders of magnitude bigger or smaller than the adjacent points. They were manually discarded from all the time series. This was preferable rather than aliasing of the series because the number of locations per day for the buoys (Figure 4.4) was low and confined to a period of the day which depended on the NOAA's satellites orbit.

4.1.2.2. Time series

After passing the quality control, their time series of latitude, longitude and temperature collected by the LCDs were processed to compute the main characteristics in the Brazil Current (BC), the South Atlantic Current (SAC) and the Brazilian Coastal Current (BCC).

The trajectories described by each particular buoy were described entirely in the BC (buoys number 3181 and 3188), entirely in the BCC (3178 and 3180), in the BC and BCC (3179), or in the BC and SAC (3182, 3185, 3187, 3189, 3190, 3191 and 3192). The data from all buoys were divided into their BC, SAC and BCC components, in order to separately describe these currents.

Since the BC develops its main flow as a western boundary current parallel to the coast (southwestward in the BMC vicinity), the criteria adopted to divide each entire track into its current components was based upon the southernmost location where a major change from

the BC direction occurred in the trajectories. In every case of a buoy leaving the BC and entering the SAC, for instance, the change in direction was about 90 degrees, from SW to SE. In the case of the buoy entering the BCC from BC, the change in direction was about 180 degrees, from SW to NW. Table 4.2 shows the time intervals and geographical positions of the beginning and end of the series used to describe the BC, BCC and SAC.

4.1.2.3. Mean current and kinetic energies

To estimate the current speed and direction, all the buoy positions for a particular current were transformed from longitude and latitude into zonal and meridional displacements, respectively. Units were converted from the original degrees per day into cm/s. While the international recommendation is to use the International system (SI) units, the CGS units were used here in order to facilitate direct comparison with previously published results, essentially all of which are in CGS units.

Table 4.2. Time series used to describe the BC, BCC and SAC

(a) Brazil Current

	date (Julian day)		*latitude (S)*		*longitude (W)*	
buoy	***start***	***finish***	***start***	***finish***	***start***	***finish***
3179	24 Mar 93 (83)	27 Apr 93 (117)	47.60	49.73	29.52	31.09
3181	12 Mar 93 (71)	26 Mar 93 (85)	47.85	50.36	29.82	32.53
3182	23 Mar 93 (83)	28 Mar 93 (87)	47.90	48.36	30.15	31.05
3185	1 Set 93 (244)	24 Oct 93 (297)	47.85	50.13	29.98	33.30
3187	13 Dec 93 (347)	4 Jan 94 (369)	48.55	52.07	29.82	36.66
3188	12 Feb 94 (408)	1 Mar 94 (425)	47.91	51.62	29.79	34.19
3189	13 Feb 94 (409)	15 Mar 94 (439)	48.29	53.25	29.95	36.80
3190	5 Feb 94 (401)	1 Mar 94 (425)	47.55	53.46	29.79	37.51
3191	1 Feb 94 (397)	27 Feb 94 (423)	47.19	52.93	29.62	37.50
3192	4 Feb 94 (400)	26 Feb 94 (422)	47.49	53.58	29.95	37.07

(b) Brazilian Coastal Current

	date (Julian day)		*latitude (S)*		*longitude (W)*	
buoy	***start***	***finish***	***start***	***finish***	***start***	***finish***
3178	6 Apr 93 (96)	3 Jul 93 (184)	28.59	23.10	48.02	44.37
3179	28 Apr 93 (118)	15 Oct 93 (288)	30.93	25.60	49.87	46.48
3180	21 May 93 (141)	30 Jul 93 (211)	33.30	24.59	50.79	45.02

(c) South Atlantic Current

	date (Julian day)		*latitude (S)*		*longitude (W)*	
buoy	***start***	***finish***	***start***	***finish***	***start***	***finish***
3182	28 Mar 93 (87)	11 Feb 94 (407)	48.34	38.95	31.06	31.19
3185	24 Oct 93 (297)	15 Apr 94 (470)	50.12	40.08	33.32	33.51
3187	5 Jan 94 (370)	16 Apr 94 (471)	52.06	37.24	36.69	37.96
3189	15 Mar 94 (439)	5 Jul 94 (551)	53.25	39.27	36.80	34.58
3190	2 Mar 94 (426)	5 Jul 94 (551)	53.44	47.43	37.85	39.67
3191	28 Feb 94 (424)	5 Jul 94 (551)	52.87	41.93	37.83	38.99
3192	27 Feb 94 (423)	5 Jul 94 (551)	53.34	38.46	37.70	35.81

Having the zonal and meridional displacements (x_i, y_i), and knowing the time interval (t) between two consecutive position measurements (i, i+1), the zonal (u_i) and meridional (v_i) instantaneous velocities (cm/s) were computed as follows:

$$ui = \frac{x_{i+1} - x_i}{t_{i+1} - t_i} \quad ; \quad vi = \frac{y_{i+1} - y_i}{t_{i+1} - t_i} \tag{4.1}$$

The mean zonal ($\overline{U}$) and meridional ($\overline{V}$) velocity components for each time series were given by:

$$\overline{U} = \frac{1}{n-1}\sum_{i=1}^{n-1} ui \quad ; \quad \overline{V} = \frac{1}{n-1}\sum_{i=1}^{n-1} vi \tag{4.2}$$

where n is the number of points in each positional time series.

The overall mean current velocity (V_m) and the mean current direction (θ_c) were obtained from:

$$Vm = \sqrt{\overline{U}^2 + \overline{V}^2} \quad ; \quad \theta c = arctan\left(\frac{\overline{V}}{\overline{U}}\right) \tag{4.3}$$

where V_m is in cm/s and θ_c is in degrees. The final mean current direction, however, was transformed into the appropriate geographic bearing.

In order to examine the influence of time dependent, mesoscale perturbations present in each trajectory within the BC, SAC and BCC, the time series were also used to compute the mean, eddy and total kinetic energies (MKE, EKE and TKE, respectively) as defined below. These

energies were computed on a temporal basis, in contrast with some methodologies which use spatial averages (e.g. Figueroa and Olson, 1989; Zambianchi and Griffa, 1994; Schäfer and Krauss, 1995). This approach has the advantage of computing energies for each buoy time series, and is especially useful when one has a small number of tracks over a specific area or if the study area is not regularly covered by the tracks.

For the computation of the kinetic energies, it was assumed that the velocity of a fluid parcel, at a particular moment along its trajectory, was equal to the summation of the velocity of a mean current (V_m) and of a perturbation. The instantaneous zonal (u'_i) and meridional (v'_i) perturbation velocities were represented by the successive buoy detrended (demeaned) instantaneous velocities.

The mean kinetic energy (MKE) was then computed from the mean current velocity (V_m) by:

$$MKE = m \frac{Vm^2}{2} \tag{4.4}$$

where the fluid mass (m) is considered equal to unity, i.e. energy per unit mass. While V_m is given in cm/s, MKE is given in cm^2/s^2.

The eddy kinetic energy (EKE) is given by:

$$EKE = \frac{U_{EKE} + V_{EKE}}{2} \tag{4.5}$$

where U_{EKE} and V_{EKE} represent the time-averaged instantaneous zonal and meridional kinetic energy associated with the components of the detrended velocities, given by:

$$UEKE = \frac{1}{n-1} \sum_{i=1}^{n-1} u'i^2 \quad ; \quad VEKE = \frac{1}{n-1} \sum_{i=1}^{n-1} v'i^2 \tag{4.6}$$

The total kinetic energy (TKE) was computed by adding the MKE and the EKE terms for each time series. All kinetic energies were estimated in CGS units (i.e. cm^2/s^2), since the currents were in cm/s units.

4.1.2.4. FFT analysis

Fast Fourier Transform (FFT) analysis was performed on each particular time series of detrended instantaneous zonal (u'_i) and meridional (v'_i) velocities for each of the currents studied here. Detrended temperature time series were also subject to the same procedure. In order to perform the analysis, all the series were interpolated to a fixed interval of 2.4 hours (0.1 days). The FFT was performed utilising Matlab® routines that computed the discrete Fourier transform with a radix-2 for time series of a power of two length (Little and Shure, not dated).

The function that implements the transform is given by (Little and Shure, not dated):

$$X(k+1) = \sum_{N=0}^{N-1} x(n+1) W_N^{kn} \tag{4.7}$$

where $W_N = e^{-j(2\pi/N)}$, N is the number of points and X is the discrete FFT transform of the detrended and interpolated buoy time series . The series are denoted in Equation 4.7 running over n+1 because Matlab® vectors (k) run from 1 to N instead of from 0 to N-1.

From Equation 4.7 it is possible to perform a periodogram estimate of the discrete power spectrum X at N/2+1 frequencies. A complete description of the power spectrum estimation can be found in Jenkins and Watts (1968) and in Section 13.4 of Press et al. (1992).

According to Press et al. (1992), when performing the periodogram estimate the effect of *leakage* is very common. Data windowing is the solution to this problem. Data windowing modifies the relationship between the spectral estimate at discrete frequencies and its continuous (periodogram) spectrum at nearby frequencies. Press et al. (1992) reports that there are many window functions used to prevent spectral *leakage*, most of them rising from zero to a peak and then falling again. The windows are named after someone and the most common are: 'Tukey', 'Bartlett', 'Parzen', 'Hanning', 'Hamming' and 'Welch'.

The Matlab® routines employed in this thesis to generate the power spectra made use of both 'Hanning' and 'Hamming' windows. The first was used to prevent *leakage* while the last was used to smooth the resulting spectra. The 'Hanning' and the 'Hamming' window coefficients are, respectively, given by (Little and Shure, not dated):

$$w(n) = 0.5\ \{1 - cos\ [2\pi\ (n/N\text{-}1)]\},\ n = 1...N \tag{4.8}$$

$$w(n) = 0.54 - 0.46\ cos\ [2\pi\ (n/N\text{-}1)],\ n = 1...N \tag{4.9}$$

The smoothing of the power spectrum is employed to reduce the variance and to increase statistical confidence, or reduce confidence limits. A compromise must be found between strong smoothing (more confidence but stronger bias) and weak smoothing (less confidence but less bias). In this work, we opted to run the smoothing using the 'Hamming' window at a variable length. According to Afonso Paiva (author of the Matlab® routine specs.m used here, not published), the idea of using a variable length window is to have smaller size for low frequencies where we have less points, and progressively increase the window size towards higher frequencies. The effect will be a weaker smoothing at lower frequencies where we have less statistical confidence, but no information is lost. The defaults used over all the distinct spectra estimated in this thesis were: window width (*smo*) equal to 22 increased by 1 at each 10 intervals.

The inferior and superior confidence limits for the spectra are, respectively, given by:

$$C.L._{(inf)} = df\ /\ [\chi\ (df,\ a/2)] \tag{4.10}$$

$$C.L._{(sup)} = df\ /\ [\chi\ (df,\ 1 - a/2)] \tag{4.11}$$

where:

χ is the Chi square distribution;

df is the number of degrees of freedom;

$a = 1 - p/100$;

p is the confidence level (e.g. 90 %, 95 %).

The degrees of freedom were computed as follow:

$$df = 2 \times smo \times wffac \times tap \tag{4.12}$$

where:

smo = 22 (window width);

$wffac$ = 0.63 (correction for the effective size of Hamming window)

tap = 2.6 (correction for the time windowing)

All the spectra were computed to a confidence level of 95 %. The FFT spectra plots were scaled in the *x* axis to a log scale of frequencies (inverse of the period). The most prominent peaks in periods bigger than a day were accounted as indicative of the oscillations present in a particular current for the time when the buoys were in the water (see Table 4.2).

4.1.2.5. Eddy observations

Time series of position and temperature for particular eddies or rings found in each of the currents were manually extracted from the original latitude and longitude time series. The eddies or rings were identified as closed or almost closed tracks found in the total trajectory of a particular buoy. From the positional time series, the displacement time series were computed as described in Section 4.1.2.3. Having the start date (d_i) and finish date (d_n) of occurrence of a particular eddy, the period of rotation (T_R) is simply $d_n - d_i$. Using T_R together with the measurement of the buoy displacement along the eddy perimeter (P), it was possible to compute the tangential velocity (V_T) for each eddy:

$$V_T = P/T_R \tag{4.13}$$

From the time series it was also possible to compute each eddy's mean position, mean temperature, temperature standard deviation and to report its direction of rotation (cyclonic or anticyclonic).

An empirical estimate of the eddies' typical diameter was made assuming that all the eddies were circular in shape, which is approximately correct for the biggest eddies. It was also assumed, although not necessarily correct, that the buoys were always surrounding the edge of the eddies. Hence, the eddy diameter (D) is simply the eddy perimeter (P) divided by π. This estimate of the eddy diameter from the buoys' trajectories is useful for future comparisons with eddies found in the satellite images.

Using the methodology of extracting the eddies as closed tracks directly from the original drifters' time series, it was possible to resolve eddies in the range of a couple of hours to a maximum rotational period of about 40 days. A total number of 126 eddies were detected during the period of this study. However, in the case when the eddies were tracked for periods longer than their rotational period they were counted more than once.

As expected, there is a direct relation between the eddy rotational period (T_R) and its perimeter (P). This relation, however, changes from small-scale eddies to mesoscale ones. Small-scale eddies of T_R lower than 5 days and P lower than 100 km were found to dominate the spectrum of eddies sampled by the buoys (about 65 % of the frequency), although they are more difficult to be spotted directly in the trajectories. Figures 4.5 and 4.6 show the frequency histogram of the rotational periods and perimeters for all the eddies found in the LCDs' trajectories.

Knowing that the majority of the eddies identified through this methodology were small scale ones, future analysis will separate them from the mesoscale ones. Small scale eddies found here include several examples of shelfbreak eddies present in the BC/BCC front along the Brazilian shelfbreak. This work presents the first description of this kind of eddies in the known literature for this region.

In summary, the eddies found in the buoys' trajectories can be divided in two classes:

- Class 1: small-scale eddies, $T_R < 5$ days and $P < 100$ km;
- Class 2: meso-scale eddies, $T_R \geq 5$ days and $P \geq 100$ km.

According to Pond and Pickard (1983) and Knauss (1997), the scaling of the non-linear and Coriolis (f) terms of the equation of motion is useful when trying to find out the relative importance of these terms in different types of motion in the sea. For instance, the Rossby number (Ro) is the non-dimensional ratio between the non-linear (acceleration) and the Coriolis terms of the equations of motion. Ro is expressed in the form $Ro = U / fL$, where U is the typical speed of the motion and L is the length scale often associated with the radius of curvature. Considering eddies or rings in the ocean, a common practice is to scale them in relation to their maximum rotational velocities and radius (Olson, 1980; cited by Chassignet et al., 1990).

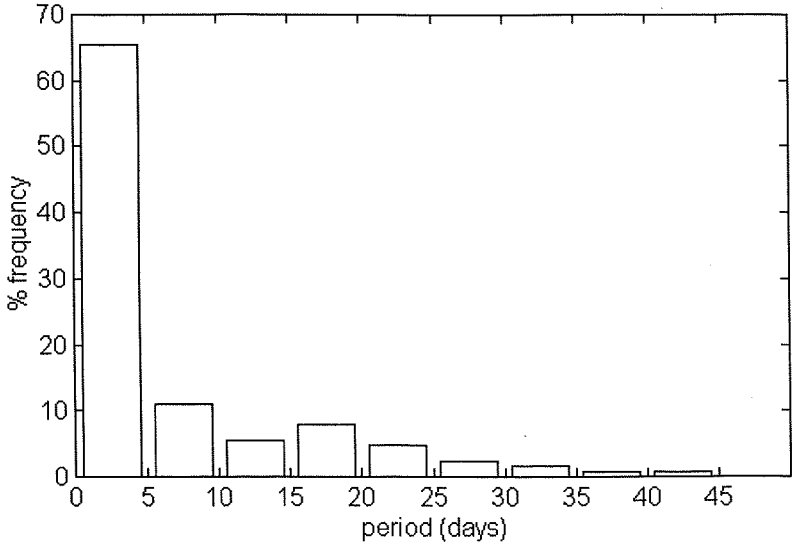

Figure 4.5. Frequency histogram of the eddies rotational periods.

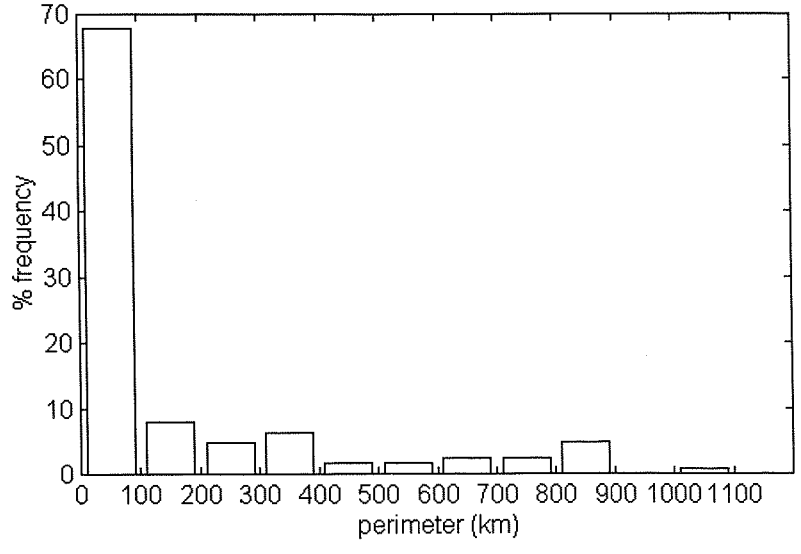

Figure 4.6. Frequency histogram of the eddies perimeters.

From the measurements of the radius (radius = D / 2), tangential velocity (V_T) and average latitude (remembering that $f = 2\omega\sin\phi$) of each eddy found in the buoys trajectories, the Rossby number was computed to indicate the relative importance of the aceleration and Coriolis forces in the particular eddies. Statistics for Ro were computed for the eddies in the particular currents BC, BCC and SAC and also in the classes 1 and 2 defined above.

Considering an idealised two layer density ocean in the front between the BC and MC (the western subtropical front) and in the BC/BCC front, the internal Rossby radius of deformation (Rd) was also computed for the range of latitudes where the eddies were present. This property gives a length scale at which the rotational (f) forces become comparable to the buoyancy forces (pressure gradient) in the equation of motion (Richards and Gould, 1996). Rd is defined as $Rd = (g' H_o)^{1/2} / f$ (Pond and Pickard, 1983) where the reduced gravity (g') is the gravity (g) times the density difference between layers ($g' = g\ (\Delta\rho/\rho)$) and H_o is the upper layer depth.

In the western STF, BC was considered to carry tropical waters with density (ρ) of 1025 Kg/m^3 in a 200 m water column above SACW, whose typical density was assumed to be 1027 kg/m^3. In the BC/BCC front, the BCC density was assumed to be 1023 kg/m^3 (coastal waters) extending in a water column of 100 m above TW carried by BC with density of 1026 kg/m^3. These numbers were based on the T-S diagrams and vertical profiles of temperature and salinity presented by Castro and Miranda (1998) and Ciotti et al. (1995) for the SBCS.

According to Richards and Gould (1996), wavelengths of about 4 to 6 times the Rossby radius of deformation dominate a fully developed eddy flow. The characterisation of the eddies present in the buoy trajectories, which will be presented in Chapter 7 of this thesis, included the statistics of the ratio D / Rd for the particular currents and for classes 1 and 2. Other analyses made of the eddy properties included the linear correlation between eddy size (represented, for instance, by P or D) and eddy rotational period (T_R) or tangential velocity (V_T) for classes 1 and 2. The linear relationships can be used as empirical models for the prediction of T_R or V_T of eddies present in satellite images of the study region, where only eddy dimensions can be assessed in particular images.

4.2. AVHRR images

4.2.1. High-resolution images

The high-resolution AVHRR images used in this work were provided by the Brazilian National Institute for Space Research, INPE. This institution operates an HRPT antenna in Cachoeira Paulista, Brazil (22°41'S, 45°W). Although this antenna is able to record four AVHRR HRPT images per day (one image at approximately 12 h for each of the two operational NOAA satellites), problems of storage space and lack of personnel involved in the acquisition phase consistently caused loss of acquisition.

Because of the perceived importance of the COROAS project, however, the oceanographers of INPE managed to guarantee the consistency of AVHRR image recording since 1992. Because of a shortage of recording media (CCT tapes), just one single image was recorded at INPE per day although this was adequate for the COROAS objectives. During the months of Austral winter (June to August), the cloud coverage in the Southwestern Atlantic Ocean tends to increase dramatically, leaving sometimes the entire COROAS area of study without any useful information. In this case, the COROAS AVHRR scenes were simply not recorded and stored at Cachoeira Paulista. The AVHRR scenes, 5 channels, were stored in NOAA's 1b format.

After the acquisition and storage, the AVHRR images were transferred to the Remote Sensing Division of INPE, in São José dos Campos, Brazil. There, the tapes were stored for further processing according to COROAS objectives and timetable. COROAS researchers extract their AVHRR data by using a personal computer based software called SEAPAK, which was developed at NASA/Goddard Space Flight Center, USA (McClain et al., 1992).

The distribution of the AVHRR data from COROAS project to external users is very limited, mainly because of lack of personnel and equipment to extract the data. Because of a personal visit made to INPE in November 1996, COROAS AVHRR scenes could be selected and extracted by the author for use in this work. The data were kindly provided by the Remote Sensing Division, INPE.

After the selection of the interesting scenes (mainly the ones corresponding to the same period of time when the LCDs were in the water, March 1993 to July 1994), the NOAA 1b format AVHRR scenes stored in the CCT tapes were extracted using the SEAPAK software. According to SEAPAK's procedures of extraction, it is possible to select both the atmospheric correction algorithm to generate the SST image and the resample rate to be applied to the extracted images. The algorithms chosen to generate the SST images were the following (Kidwell, 1995):

- NOAA-11 images, daytime: Cross Product Sea Surface Temperature (CPSST) Day Split-Window NOAA Operational Algorithm:

$$SST = (T_4\text{-}T_5 + 0.789)(0.19069T_5 - 49.16) / (0.20524T_5 - 0.17334T_4 - 6.78) + 0.92912T_5 + 0.81(T_4\text{-}T_5)(sec(SZA) - 1) - 254.18 \quad (4.14)$$

- NOAA-11 images, night-time: Cross Product Sea Surface Temperature (CPSST) Night Triple-Window NOAA Operational Algorithm:

$$SST = (T_3-T_5 + 14.86)(0.16835T_4 - 34.32) / (0.20524T_5 - 0.07747T_3 - 20.01) + 0.9712T_4 + 1.87(sec(SZA) - 1) - 276.59 \quad (4.15)$$

- NOAA-12 images: Multi-Channel Sea Surface Temperature (MCSST) Day Split-Window NOAA Operational Algorithm:

$$SST = 0.963563T_4 + 2.579211(T_4-T_5) + 0.242598(T_4-T_5)(sec(SZA) - 1) - 263.006 \quad (4.16)$$

where:

SST: sea surface temperature (degC);

T_3: temperature of the AVHRR channel 3 (degK);

T_4: temperature of the AVHRR channel 4 (degK);

T_5: temperature of the AVHRR channel 5 (degK);

SZA: satellite zenith angle (degrees).

In order to diminish the possibility of cloud contamination on the SST estimates, an albedo threshold test was also applied to channel 1 (visible) during the data extraction. All the SST estimates retrieved from the application of the CPSST and MCSST algorithms used here (Equations 4.14 to 4.16) successfully passed a 10 % visible albedo threshold test which was established during the extraction. Calibration procedures (specific for each channel in each NOAA satellite AVHRR sensor) were also applied to the different AVHRR channels during the process of data extraction in SEAPAK.

SEAPAK is designed to extract 512 × 512 pixels from the original AVHRR image stored in the CCT tape (nominal resolution of 1 km × 1 km), which imposes a limitation when an area bigger than 512 km by 512 km is needed. Typically, a full-scene AVHRR image has 2048 columns by about 4000 lines. The resample rate, however, allows the user to expand the area of interest in each extracted image to more than just a 512 km × 512 km area.

During the process of extraction, the images used in this work were resampled by the rate of 4, which means that a spatially coherent area of 512 × 512 pixels (2048 km × 2048 km) was recorded for each of the selected scenes. However, the resampling process, rather than

averaging a 4 × 4 pixel's grey level into a single pixel, reads one pixel in a row and jumps the next three pixels. Although the spatial resolution of each pixel is not changed in this process, the process results in an acceptable resolution of about 4 km × 4 km for each pixel. The AVHRR images obtained in this form are referred to in this thesis as the high-resolution AVHRR images.

The total number of images extracted at INPE were 81, all of them listed in Table 4.3. They cover the period between 10 March 1993 and 11 July 1994. Table 4.3 also displays the individual dates of acquisition for each image and the NOAA satellite responsible for the data collection. The time of data collection is in GMT. Local time was 2 to 4 hours later than GMT, depending on the season of the year.

All the 4 km × 4 km images extracted at INPE (5 channels plus SST) were geolocated to the Mercator projection at the SOC by using a version of SEAPAK available for Unix systems. All the images were projected over a coherent area in the vicinity of the BMC region (26.4°S to 42.7°S; 38.8°W to 58.8°W).

The geolocation technique employed in SEAPAK corrects the entire image by the coordinates of 2 known control points, which usually refer to notable points in the coast. This process was found to have an accuracy ranging from 1 to about 5 pixels in both zonal and meridional directions. Further improvements were made by translating the image in the zonal and meridional directions until exact correspondence between the line of the coast in the image and a coastal line drawn by SEAPAK from its geographical data bank.

Table 4.3. High-resolution AVHRR images used in this work

image number	*date*	*time (GMT)*	*Julian day*	*NOAA satellite*
1	10 Mar 93	10:19	69.43	12
2	27 Mar 93	10:55	86.45	12
3	28 Mar 93	19:58	87.83	11
4	29 Mar 93	10:11	88.42	12
5	21 Apr 93	10:22	111.43	12
6	26 Apr 93	10:11	116.42	12
7	27 Apr 93	19:26	117.81	11
8	28 Apr 93	06:41	118:28	11
9	29 Apr 93	06:28	119.27	11
10	30 Apr 93	06:18	120.26	11
11	10 May 93	18:29	130.77	11
12	19 May 93	10:18	139.43	12
13	24 May 93	10:11	144.42	12
14	5 Jun 93	19:55	156.83	11

15	22 Jun 93	09:49	173.41	12
16	23 Jun 93	19:37	174.82	11
17	24 Jun 93	10:46	175.45	12
18	27 Jun 93	19:49	178.83	11
19	29 Jun 93	20:04	180.84	11
20	30 Jun 93	10:17	181.43	12
21	4 Jul 93	19:03	185.79	11
22	5 Jul 93	18:50	186.78	11
23	6 Jul 93	09:48	187.41	12
24	11 Jul 93	19:17	192.80	11
25	19 Jul 93	19:20	200.80	11
26	20 Jul 93	19:09	201.80	11
27	21 Jul 93	18:58	202.76	11
28	22 Jul 93	18:45	203.78	11
29	3 Aug 93	19:40	215.82	11
30	6 Aug 93	19:03	218.79	11
31	7 Aug 93	18:51	219.78	11
32	10 Aug 93	10:36	222.44	12
33	11 Aug 93	19:43	223.82	11
34	16 Aug 93	10:06	228.42	12
35	18 Aug 93	19:58	230.83	11
36	19 Aug 93	19:47	231.82	11
37	20 Aug 93	19:33	232.81	11
38	26 Aug 93	20:01	238.83	11
39	27 Aug 93	19:49	239.83	11
40	28 Aug 93	19:36	240.82	11
41	29 Aug 93	19:23	241.81	11
42	30 Aug 93	19:12	242.80	11
43	6 Sep 93	19:28	249.81	11
44	7 Sep 93	19:15	250.80	11
45	28 Sep 93	20:01	271.83	11
46	7 Oct 93	19:52	280.83	11
47	8 Oct 93	19:38	281.82	11
48	11 Oct 93	19:02	284.79	11
49	8 Nov 93	20:04	312.84	11
50	9 Nov 93	19:51	313.83	11
51	2 Dec 93	20:12	336.84	11
52	18 Dec 93	20:17	352.84	11
53	11 Jan 94	20:26	376.85	11
54	27 Jan 94	20:31	392.85	11
55	28 Jan 94	20:19	393.85	11
56	29 Jan 94	20:06	394.84	11
57	6 Feb 94	20:09	402.84	11
58	9 Feb 94	19:31	405.81	11
59	2 Mar 94	20:17	426.84	11
60	3 Mar 94	20:03	427.83	11
61	11 Mar 94	20:06	435.84	11
62	26 Mar 94	20:24	450.85	11
63	27 Mar 94	20:16	451.84	11
64	2 Apr 94	20:39	457.86	11
65	12 Apr 94	20:16	467.84	11
66	13 Apr 94	20:03	468.83	11
67	22 Apr 94	19:53	477.83	11
68	5 May 94	20:36	490.86	11
69	6 May 94	20:24	491.85	11

70	9 May 94	19:46	494.82	11
71	12 May 94	20:51	497.87	11
72	20 May 94	20:54	505.87	11
73	8 Jun 94	20:21	524.85	11
74	10 Jun 94	19:57	526.83	11
75	12 Jun 94	19:32	528.81	11
76	17 Jun 94	20:11	533.84	11
77	18 Jun 94	19:59	534.83	11
78	26 Jun 94	20:01	542.83	11
79	28 Jun 94	09:56	544.41	12
80	1 Jul 94	20:41	547.86	11
81	11 Jul 94	20:17	557.84	11

4.2.2. MCSST global dataset

The principle of having a long term data set of AVHRR Multi-Channel SSTs lies in the fact that, although the algorithms and sensor calibrations used to derive the MCSSTs change with every new satellite (Kidwell, 1995), all the estimates are tuned with respect to global sets of close match-ups with buoys. This would provide continuity and consistency from satellite to satellite and give a potential source of global SST data for large periods of time. Based upon this principle and aiming to provide data for climate studies and large to mesoscale oceanography, the MCSST program was established by NASA in the eighties.

In order to investigate the spatial and temporal pattern of the SST variability in the South Atlantic Ocean in support of this study in the Southwestern Atlantic, a global series of 14 years of monthly-averaged MCSST images was obtained from JPL/NASA to be used in this work (Smith, 1992). The dataset covers the period between January 1982 and December 1995, totalling a number of 168 images.

Although NASA is conducting a re-analysis of all its MCSST products in an attempt to homogenise SST estimates made in the past by different MCSST algorithms (the NOAA/NASA AVHRR Oceans Pathfinder project: http://podaac.jpl.nasa.gov/sst), at the time of this study the Pathfinder data is less abundant than the 14 years long MCSST time series. Given its greater temporal coverage and to be consistent with other authors' results, the MCSST dataset was chosen for use in this work in spite of the Pathfinder dataset supposedly being of a better quality.

Each monthly MCSST image in this global dataset is an equal-angle grid which consists of 2048 samples from east to west (180°E to 180°W) and 1024 lines from north to south (90°N to

90°S). The height and width of each element in the grid is the same in degrees, i.e. 360/2048 or 0.1757812 degrees. This represents 18 km × 18 km at the Equator, considered to be the nominal spatial resolution of the dataset.

To be consistent with the high-resolution SST images used in this work, most of which derived from daytime atmospheric correction algorithms (Equations 4.14 and 4.16), the MCSST dataset used here is also a daytime retrieval. The original AVHRR data on which the MCCST grid is based was derived from the NOAA-7, NOAA-9 and NOAA-11 satellites. The claimed accuracy of the MCSST estimate is within 0.5°C.

McClain et al. (1985) describes the cloud filtering techniques and the procedures for atmospheric correction applied to the MCSST dataset. Kidwell (1995) describes the individual MCSST algorithms and their evolution with time and according to the different satellites. The monthly data available from JPL was originally produced by the Rosenstiel School of Marine and Atmospheric Sciences (RSMAS) by averaging all the available cloud-free MCSST estimates made from AVHRR GAC data. Due to cloud coverage and other factors, the final averaged product was not always completely filled. To solve this problem, a Laplacian relaxation technique of interpolation was applied to fill in the gaps.

From each of the interpolated global MCSST images, a subset of 512 × 512 pixels was extracted to cover only the South Atlantic Ocean, from 20°N to 70°S, 20°E to 70°W. For simplicity, these subsets will hereinafter be named the MCSST images. Using all the MCSST images available for a particular month between 1982 and 1995, 12 'climatological' averages were computed, one for each particular month. A total of 168 anomaly charts were produced for particular months taking the average, 'climatological' SST estimate for the month in question from the actual SST for the particular month.

4.2.3. Location of the Subtropical Front and of the BC and BCC extremes

Aiming for a description of the seasonal behaviour of the Subtropical Front (STF) and its consequence on the oscillatory movement of the BMC throughout the year, both the high-resolution AVHRR and the MCSST images were used to locate the 20°C isotherm, which was chosen to indicate the limit between TW and SAW or, in other words, the STF itself.

Considering the classification of the South Atlantic and SBCS water masses (Emílsson, 1961; see Chapter 2), the isoline of 20°C is considered to be the lower thermal limit for TW all the year round. For the SBCS, it is assumed that waters with temperatures higher than 20°C are being carried southwestwards only by the BC flow. Following this idea, CW and SAW are assumed to be carried northeastwards (by BCC) inside the SBCS.

When analysing the general behaviour of the 20°C isotherm in the South Atlantic from the 14 year long MCSST dataset, it was noticed that in the open ocean the isoline is zonally directed, while in the regions close to the American and African continents it is deflected by the influence of the boundary currents. Hoffmann et al. (1997), studying the climatic characteristics of the Southwestern Atlantic Ocean, pointed out that the alteration of the zonal distribution of the isotherms in that area is caused by the surface currents occurring there.

The general shape of the 20°C isoline off the SBCS in MCSST images was found to always imitate a 'Z' shape, with the positions of its two extreme vertices marking the possible limits of penetration of the BC (to the south) and BCC (to the north). These extreme vertices were taken as the northernmost limit of the BCC and the southernmost limit of the BC. In the AVHRR images, owing to cloud coverage, the 'Z' shape of the front is, although still visible, less evident.

Owing to the varying penetration of BCC, the 'Z' shape of the 20°C isotherm through the year changes from being compressed during summer to being more stretched in winter. The latitudinal and longitudinal positions of the BCC and BC extremes for each month from January 1982 to December 1995, as defined by the MCSST data, were treated as a time series. The analysis of the BC/BCC oscillation, as described from the statistics of its extreme position time series from the MCSST dataset, is presented in Chapter 6. Because very high cloud coverage in the vicinity of 30°S resulted in extensive interpolation in the MCSST data covering that area, the extreme positions of BCC and BC were not estimated for June 1988, June 1992, May to July 1993, April to September 1994 and March 1995.

Using the same procedure to track the 20°C isoline in the high-resolution images did not result in a long period time series valid for locating the front extreme positions. Rather, whenever the cloud coverage was low for a particular image, the entire front was located and drawn in a map in order to observe the high-resolution behaviour of the front during 1993 and 1994.

4.2.4. Eddy observations

Individual eddies were visually located in the high-resolution AVHRR images. Typically, the eddies present in the satellite SST images are identified as closed elements with the borders delimited by strong horizontal thermal gradients in relation to adjacent waters. The gradients, however, change in intensity according to the stage of formation or coalescence of a particular eddy. Besides, the absolute temperatures inside and outside the eddies are also not constant, which make very difficult the establishment of a single palette of colours to reveal eddies in a temporal sequence of SST images. Cloud coverage is another crucial problem whenever a particular feature needs to be tracked in satellite images.

In this work, each AVHRR image was processed independently using the Interactive Data Language, IDL® and the Environment for Visualizing Images, ENVI® image processing software to enhance the presence of eddies. Each time one of these features was located, it was treated as an ellipse, and its minor and major axis were measured. From the ellipse's equation, the eddy perimeter (P) was estimated. Still in ENVI, the mean latitudinal and longitudinal position of the eddy was assessed, and the temperature profiles for the eddy's minor and major axes (A_{MIN} and A_{MAX}, respectively) were generated. From these profiles (and discarding the cloud covered pixels when detected), an average temperature was computed for each particular eddy.

Using this procedure, 78 eddies were located in the overall set of high-resolution AVHRR images. From this total a few were double counted when they persisted from one image to the subsequent one. Mainly because of cloud coverage but also advection, unfortunately, the location and tracking of a particular eddy in a sequence of images was rare. This made the estimation of the eddies' lifetime extremely difficult.

The majority of the eddies found in the satellite images have perimeters bigger than 100 km. This contradicts what was found in Section 4.1.2.4, but can be explained by the visualisation technique employed here (in which, of course, bigger eddies are visually easier to detect than smaller ones). The frequency histogram for the eddies' perimeters can be seen in Figure 4.7.

The warm core and cold core eddies present in the AVHRR images were subject to simple statistical analysis in order to assess their typical length scales. Their statistics were compared to the ones found for the eddies present in the buoys' trajectories. The ratio between the

eddies' average diameter ($D = A_{MIN} + A_{MAX} / 2$) and the Rossby radius of deformation was also computed.

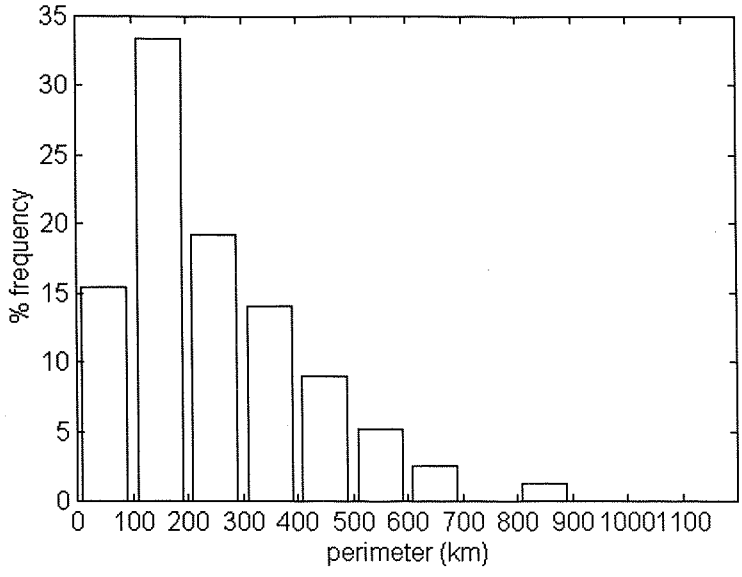

Figure 4.7. Frequency histogram of the AVHRR eddies perimeters.

4.2.5. Principal Component analysis

Principal Component (PC, also known as Empirical Orthogonal Function, EOF) analysis was performed in the MCSST image dataset to describe the 14 years long spatial and temporal variability of the South Atlantic Ocean in support of the study of the mesoscale variability of the Soutwestern Atlantic Ocean during 1993 and 1994.

PC analysis is used to generate new images which are often more interpretable than the original data. It is also used to compress the information content of a series of images (different bands of the same satellite scene or temporal sequences of images over the same scene, for example) into a reduced number of images, called the principal component images (Jensen, 1986). The PC transformation reduces the spectral redundancy of the data (Ready and Wintz, 1973; cited by Schowengerdt, 1997) decomposing space and time-distributed data into PC modes ranked by their variance.

According to Lagerloef and Bernstein (1988), PC analysis is being conventionally applied to oceanographic and meteorological data sets. Practical applications include the study of the

variance associated with fronts, jets or eddies. The PC decomposition procedure is fully described in Preisendorfer (1988) and Lagerloef and Bernstein (1988).

Jensen (1986) points out that the PC transformation generates uncorrelated multispectral data that has ordered variance properties. PC translates the original data axes so that they are reprojected onto a new set of axes or dimensions. The first of this new set of axes is associated with the maximum amount of variance found in the original data set. This is the first principal component or eigenvalue (λ_1 or PC1) and represents the variance of the particular PC mode 1. The second principal component (λ_2 or PC2) is orthogonal to the first and comprises the second largest amount of variance found in the data set. The third, fourth, fifth, and so on, principal components contain decreasing amounts of variance.

The percentage of the total variance explained by each of the PC modes ($\%_i$) is given by:

$$\%i = \frac{\lambda i \times 100}{\sum_{i=1,n} \lambda i} \tag{4.17}$$

In order to assess the relative contribution of each of the original images to the new generated principal components, Jansen (1986) suggests the computation of the correlation between the original images with the principal components by means of what he calls 'factor loadings'. Being k related to the original images and i related to the PC modes, the factor loadings or correlations (F_{ki}) can be computed as follows:

$$Fki = \frac{aki\sqrt{\lambda i}}{\sqrt{Vark}} \tag{4.18}$$

where:

a_{ki} = eigenvector for image k and principal component i;

λ_i = ith eigenvalue (principal component);

Var_k = variance of image k in the covariance matrix.

In practical terms, the factor loadings computed for each of the principal components inform us what image, out of the original set, contributed more to each of the PC modes.

Parada and Cantón (1998) accounted for the errors produced in the estimation of the PC modes owing to a finite number of images used to compute them. These authors considered that a mode is significant only if the sampling error ($\delta\lambda_i$) of a particular eigenvalue is smaller than the spacing between it and a neighbouring eigenvalue. The sampling error is given by:

$$\delta\lambda_i \sim \lambda_i(2/N)^{1/2} \tag{4.19}$$

In this thesis, the PC analysis was performed on two different data sets. Due to computational constraints of the available version of ENVI® used in this work, the whole set of 168 MCSST monthly averaged images could not be utilised. Instead and first, the set of 12 'climatological' average images was used. In this case, the objective of performing the PC analysis was to assess the mean seasonal variability of the South Atlantic. Second, a set of 57 images representing the SST anomalies for the South Atlantic was also used. This set of images was obtained by averaging three at a time the 168 anomalies computed for each month from January 1982 to December 1995 (see Section 4.2.2) all resulting in a time series of seasonally averaged data.

The season average images (four per year from the Austral Summer of 1982 to the Austral Summer of 1996) were obtained averaging the following months for each year:

- Summer: December, January, February;
- Autumn: March, April, May;
- Winter: June, July, August;
- Spring: September, October, November.

The Summer season average was computed using December of the previous year. Since the MCSST dataset starts in January 1982, for the Summer 1982 only 2 months were averaged (January and February 1982). Equally, when arriving in the end of the MCSST anomaly dataset, the month of December 1995 was the only image to represent the so-called Summer 1996. All the other seasonal anomalies were obtained averaging three images as described above. When performing the PC tranform in the seasonally averaged MCSST anomaly data set, the objective was to look for the interannual variability of the South Atlantic Ocean. For that, FFT analysis was performed in the time series of the temporal amplitudes (eigenvectors) derived from the first four PC modes.

4.3. ATSR images

The ATSR images used in this work were obtained from ESA through the AO3-128 project. This project, entitled 'Lagrangian and infrared observations of surface currents in the Brazil-Malvinas Confluence Zone', is a colaboration between SOC, INPE and the Federal University of Rio Grande Foundation (Fundação Universidade Federal do Rio Grande - FURG), Brazil. Part of the results of this project are presented in this thesis, where the differences between *in situ* (retrieved by buoys or ships of opportunity) and satellite (ATSR and AVHRR) temperatures are investigated for the BMC region.

The product used here is the gridded SST (GST) product which consists of 512 × 512 pixels images at a (full) resolution of 1 km × 1 km. The GST images were derived from both nadir-only or nadir/forward views. Each full-resolution ATSR image refers to a single orbit/frame of ATSR data, and was retrieved together with its positional and confidence information.

The selection of the ATSR images was made based upon the availability of high-resolution AVHRR images for the same day and area, with a preference for the less clouded scenes. By extension, it was expected that some buoy SST estimates were coincident in space with the ATSR ones. As a result of this procedure, 37 ATSR images were selected and obtained from ESA for the work presented here. Table 4.4 describes them.

The ATSR images were stored in CEOS (Committee on Earth Observation Satellites) format by ESA and sent to SOC in exabyte tapes. At SOC, the images were read and, using both IDL® and ENVI® softwares, geolocated to the Mercator projection. In the case when more than one image was obtained for consecutive frames of the same satellite track, a mosaic was also generated.

The geolocation procedure used a grid of 5 × 5 latitude/longitude points regularly scattered through the image as ground control points. These points were taken from the ATSR location information which accompanied the SST information in the CEOS format images. Each particular latitude/longitude point in this location grid is accurate to a 1/16th of a kilometre in both along-track and cross-track directions (NRSCL, 1995). The projection of the ATSR images into Mercator made possible future comparisons and superposition with the AVRHH ones, essentially all of them also projected into Mercator (see Section 4.2.1).

Table 4.4. Full-resolution ATSR images used in this work

image number	*orbit*	*frame*	*date*	*time (GMT)*	*Julian day*
1	11513	6525	28 Sep 93	02:27	271.10
2	11520	4185	28 Sep 93	13:39	271.57
3	11520	4275	28 Sep 93	13:40	271.57
4	11642	6435	7 Oct 93	02:43	280.11
5	11642	6525	7 Oct 93	02:44	280.11
6	12100	6435	8 Nov 93	02:37	312.11
7	12100	6525	8 Nov 93	02:38	312.11
8	12107	4275	8 Nov 93	13:51	312.58
9	12107	4365	8 Nov 93	13:52	312.58
10	12121	4365	9 Nov 93	13:21	313.56
11	12121	4455	9 Nov 93	13:22	313.56
12	12443	6435	2 Dec 93	01:43	336.07
13	12443	6525	2 Dec 93	01:44	336.07
14	12450	4275	2 Dec 93	12:57	336.54
15	12450	4365	2 Dec 93	12:58	336.54
16	12672	6435	18 Dec 93	01:40	352.07
17	12672	6525	18 Dec 93	01:41	352.07
18	12679	4275	18 Dec 93	12:54	352.54
19	12679	4365	18 Dec 93	12:55	352.54
20	13389	6435	6 Feb 94	02:24	402.10
21	13389	6525	6 Feb 94	02:25	402.10
22	13396	4275	6 Feb 94	13:37	402.57
23	13396	4365	6 Feb 94	13:38	402.57
24	13733	6435	2 Mar 94	02:24	426.10
25	13733	6525	2 Mar 94	02:25	426.10
26	13740	4275	2 Mar 94	13:37	426.57
27	13740	4365	2 Mar 94	13:38	426.57
28	14650	7795	5 May 94	01:08	490.05
29	14651	6345	5 May 94	02:46	490.11
30	14651	6435	5 May 94	02:47	490.12
31	14651	6525	5 May 94	02:48	490.12
32	15397	6525	26 Jun 94	02:22	542.10
33	15404	4095	26 Jun 94	13:31	542.56
34	15404	4185	26 Jun 94	13:32	542.56
35	15404	4275	26 Jun 94	13:33	542.56
36	15612	6615	11 Jul 94	01:57	557.08
37	15612	6705	11 Jul 94	01:58	557.08

4.4. Bulk temperatures from ships of opportunity

Sea surface (bulk) temperatures were obtained from the Comprehensive Ocean-Atmosphere Data Set (COADS) for the period between March 1993 to July 1994. The data set was available at the James Rennel Division for Ocean Circulation and Climate (JRD) at the Southampton Oceanography Centre (SOC). As described before, during this period a set of buoy, AVHRR and ATSR SST measurements was also available for this study. The COADS

data were obtained in individual monthly records for the region of this study, and included other meteorological measurements such as atmospheric pressure, wind speed and direction and relative humidity, for example. Since preliminary analysis (not shown) did not find a significant relationship between SST and the other meteorological measurements, the last were discarded and not used here.

The COADS dataset available at the JRD is described in Josey et al. (1998) and Woodruff et al. (1993). Essentially, the dataset is an extension of the COADS 1a, which covers the period of 1980 to 1993. The reported meteorological variables have been corrected at the JRD for various observational biases using additional information about measurement procedures which has been blended in from the List of Selected, Supplementary and Auxiliary Ships (the World Meteorological Organisation Report 47, WMO47, cited by Josey et al., 1998).

When information was available reporting that a particular SST was measured using a thermometer located in the ship's engine cooling system, that particular SST was reduced by 0.35°C. If no information was available about the method applied to measure the SST, a reduction of 0.2°C is made in the original measurement, since the WMO47 reports that about 60 % of the ships make engine inlet measurements (Josey et al., 1998).

The SST measured by ships of opportunity is presented together with the position and time where and when it was taken. They were used in this work to assess the relationship between bulk (COADS) SSTs and satellite-retrieved temperatures, which is discussed next.

4.5. Match-ups between *in situ* and satellite sea surface temperatures

Linear regression analysis was performed in order to compare *in situ* temperature measurements (buoy and COADS) with AVHRR and ATSR estimates over the period between March 1993 and July 1994, when the low cost drifters were at sea. AVHRR-retrieved brightness temperatures (BTs) for the AVHRR channels 3, 4 and 5 were also compared to *in situ* measurements. Temperature data for all the buoys were extracted from the time series when they were collected within an interval of ± 3 hours from the image's acquisition time (Kizu and Sakaida, 1996) and inside the area delimited by the AVHRR or ATSR images (see Section 4.2.1). In the case when more than one measurement was made by a particular buoy

within this ± 3 hour period, the temperature used in the regression was the closest in time with the image's acquisition time.

Temperature estimates (BTs and SSTs) were extracted from the satellite images inside ENVI for each of the latitude/longitude co-ordinates of the *in situ* buoy or bulk (COADS) measurements matching the time and space restrictions described above. This co-ordinate will be referred to as the central pixel's co-ordinate, being the geographical co-ordinate of the 4 km × 4 km pixel closest in space to the position where the *in situ* temperature measurement was taken. The BT or SST retrieval for this pixel, when cloud-free, was called 'central pixel's temperature'. The same procedure of temperature retrieval from the AVHRR images was conducted over a matrix of 5 × 5 pixels centred at the central pixel co-ordinate. Inside ENVI, an average temperature was obtained for this 25 pixels matrix (20 km × 20 km area), discarding cloud-covered pixels. This average SST will be referred as the 'average pixel's temperature'.

The maximum time interval of 3 h (before and after the image's acquisition time) was chosen in order to avoid or minimise the effects of the diurnal heating or cooling, which could contaminate the regressions to be performed. As a result of a narrow maximum time interval between the *in situ* and satellite temperatures being compared, fewer points were available for the regressions than if a bigger time interval had been chosen.

For the case of the ATSR SST images, unfortunately, only three match-up points were obtained for comparison with the buoy and bulk measurements for the entire period of time between March 1993 and July 1994. This was mainly caused by the lower number of ATSR images (37) in comparison with the AVHRR (81), but also because the ATSR images cover a much smaller area than the AVHRR images. The ATSR match-up points were obtained for the ATSR mosaic images of 2 March 1994 and 5 May 1994.

A decision was taken not to 'open' the maximum time interval for match-up points in order to prevent the diurnal effects from affecting the analysis, as mentioned before. As a result, the match-up between buoy and bulk SSTs against ATSR SSTs did not result in a regression curve. Rather, a simple evaluation of the deltaT (the temperature difference between the *in situ* and the satellite data) was obtained for four specific situations: buoy against central pixel, bulk against central pixel, buoy against average pixel and bulk against average pixel.

Considering the AVHRR data set, up to 32 points were found to match the *in situ* data in space and time. Table 4.6 shows the number of match-up points obtained for the regressions of buoy and bulk SSTs against satellite temperatures, considering both the 'central pixel' and 'average pixel' situations. DeltaT between AVHRR central and average pixels and COADS and buoy temperatures was also obtained for the entire set of data described in Table 4.5. Simple statistics were used to give an overall view of the differences between *in situ* and AVHRR BTs and SSTs.

When analysing the COADS data set to perform the regressions, it was noted that 6 match-up points, taken in July 1996, were obtained in the core of the Malvinas Current, where there were no drifting buoys sampling the SST. To have consistent results between COADS versus AVHRR temperatures in relation to the buoy versus AVHRR temperatures, the regression analysis between COADS and AVHRR was also performed without the MC match-up points (denoted as the bulk less MC points in Table 4.5). Moreover, when performing the analysis for the bulk temperatures against AVHRR channel 5 BTs, 3 missing points were found for the month of March 1994.

The frequency distribution of the number of match-up points throughout the period of study can be seen in Figure 4.8. The figure indicated that both the buoy and COADS match-ups were well distributed over the overall period of this study. Consequently, there is no seasonal trend or bias in the data set likely to interfere in the results obtained here.

After applying the procedures described above, the match-up points between buoy, bulk and AVHRR BTs and SSTs were taken for the regression analysis. The *in situ* measurements were considered as the independent variables to the linear regression analysis, which was performed to a confidence level of 95 %.

Table 4.5. Number of match-up points between *in situ* and satellite temperatures

satellite temperatures	*in situ temperatures*		
	buoy	*bulk*	*bulk less MC points*
AVHRR BT Ch3	22	32	26
AVHRR BT Ch4	22	32	26
AVHRR BT Ch5	22	29	23
AVHRR SST	22	32	26
ATSR SST	1	1	-

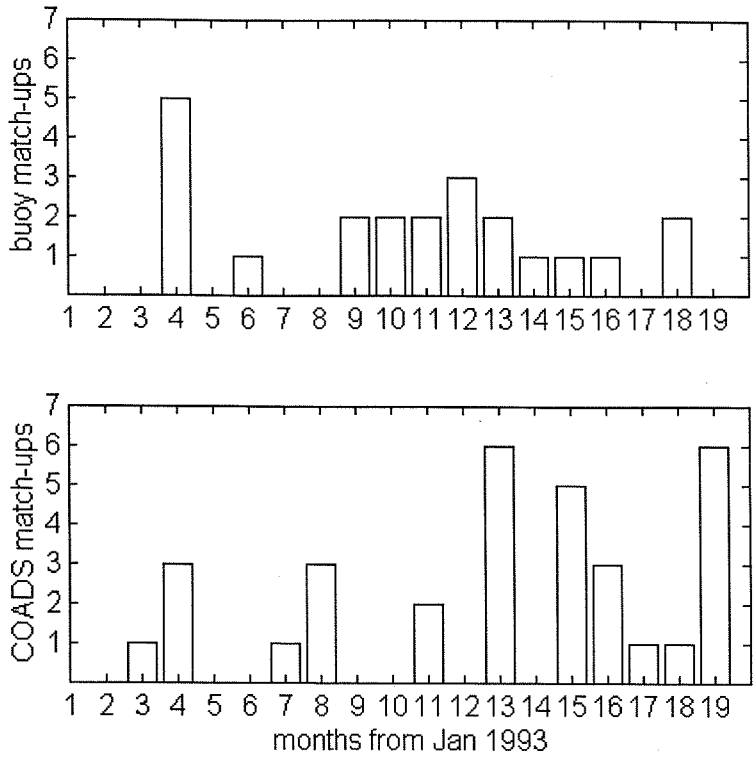

Figure 4.8. Frequency distribution of the number of match-up points between *in situ* and AVHRR temperatures.

4.6. Temperature difference images

AVHRR and ATSR images were used in this thesis to assess the nature and the spatial distribution of the temperature difference (deltaT) between measurements made by these two different instruments. As described in Section 3.2, ATSR performs a measurement of the molecular, 'skin' temperature of the ocean, while AVHRR provides an estimation of the 'bulk' sea surface temperature.

One of the main obstacles for the understanding of the behaviour of the deltaT between AVHRR and ATSR SSTs is actually the difficulty in obtaining a series of images produced by simultaneous overpasses of the NOAA and ERS-1 satellites over the same area. Besides, the geolocation of the images to the same projection and area is not a straight-forward process.

From the set of SST AVHRR and ATSR images available for this work (Tables 4.3 and 4.4), combinations of AVHRR and ATSR pairs from a total of 13 different dates were used to

compute the deltaT over the BMC and SBCS regions (Table 4.6). The deltaT were computed for coincident dates without any time lapse restriction. The deltaT for coincident pixels was computed as follows:

- All the AVHRR images which were coincident in dates with the ATSR ones were transformed from raw binary images to floating point ones, where temperature units were the same as those from the ATSR images (degK times 100);

- Inside ENVI®, the ATSR images, geolocated to the same projection of the AVHRR images, were mosaicked to a mask image (zero in background) with the same size and resolution as the AVHRR ones;

- Each one of the mosaicked ATSR images was subtracted from the coincident AVHRR one, being the temperature units transformed to degC.

The images differerence, therefore, can be expressed as:

$$deltaT_{i,j} = ((AVHRR\_SST_{i,j} - ATSR\_SST_{i,j})/100 - 273.15) \quad (4.20)$$

where:

$deltaT_{i,j}$: temperature difference for image line i, image column j (degC);
$AVHRR\_SST_{i,j}$: SST for AVHRR image line i, image column j (degK × 100);
$ATSR\_SST_{i,j}$: SST for ATSR image line i, image column j (degK × 100).

This process generated a set of 13 images of difference, where each cloud free pixel situated at the sea is a measurement of the deltaT between the AVHRR and ATSR SST estimates. These images are called here deltaT images. All the AVHRR images used in this process were NOAA-11 retrived, daytime SST images generated by the CPSST Day Split Window algorithm (Equation 4.14).

The same procedure described above was used to retrieve the magnitudes of deltaTs between day and night overpasses of the ATSR over the same region. From the set of ATSR images available for this work (Table 4.4), 4 scenes were obtained for nearly the same area during diurnal and nocturnal overpasses of the ERS-1 satellite. They are described in Table 4.7. The magnitude of deltaT computed by the diurnal temperatures minus the nocturnal temperatures

measured by the ATSR is an indicator of the diurnal processes acting on the skin temperature of the ocean in the study area.

Table 4.6. DeltaT AVHRR minus ATSR images

image	*date*	*AVHRR time (GMT)*	*ATSR time (GMT)*
a	28 Sep 93	20:01	02:26
b	28 Sep 93	20:01	13:39
c	7 Oct 93	19:52	02:43
d	8 Nov 93	20:04	02:37
e	8 Nov 93	20:04	13:51
f	9 Nov 93	19:51	13:21
g	2 Dec 93	20:12	12:57
h	18 Dec 93	20:17	12:54
i	6 Feb 94	20:09	13:37
j	2 Mar 94	20:17	13:37
k	5 May 94	20:36	02:46
l	26 Jun 94	20:01	13:32
m	11 Jul 94	20:17	01:57

Table 4.7. DeltaT ATSR daytime minus ATSR night time images

image	*date*	*ATSR daytime (GMT)*	*ATSR night time (GMT)*
a	28 Sep 93	13:39	02:26
b	8 Nov 93	13:51	02:37
c	6 Feb 94	13:37	02:24
d	2 Mar 94	13:37	02:24

4.7. Superimposition of buoy tracks onto satellite images

Aiming to have a visual description of the surface currents in relation to the SST fields present in the study area during the period of this work, buoy trajectories were superimposed to AVHRR images. Several images were selected to be superimposed by the tracks, depending on whether they presented prominent mesoscale features and were reasonably cloud free images. Following Olson et al. (1988), the tracks were superimposed to represent the buoy trajectories in an interval of 40 days long centred in each of the selected image's acquisition time.

CHAPTER 5

MESOSCALE SURFACE PROCESSES IN THE BRAZIL-MALVINAS CONFLUENCE ZONE

5.1. Introduction

In this section we present a study of the mesoscale surface processes in the BMC region for the period between March 1993 and July 1994 inclusive. In order to support our study, the large scale South Atlantic variability was first investigated for the period between 1982 and 1993. The study was conducted by applying Principal Component (PC) analysis to MCSST images for the South Atlantic. Both climatological and anomaly images were analysed and the predominant periodicities found were compared to the ones described in the literature for the Brazil-Malvinas confluence (BMC) region and its vicinity. The results and discussion related to the South Atlantic and BMC region variability are presented here.

This chapter also presents the high-resolution SST fields for the BMC region and vicinities for the period between March 1993 and July 1994, which is coincident with the period when Lagrangian data were obtained for the same region. In subsection 5.3.3, the BMC front spatial distribution is analysed for the period in question and the nature of the front between the Brazil Current (BC) and the Brazilian Coastal Current (BCC) is also investigated. Although some progress has previously been made towards the description of the Brazil-Malvinas confluence, the study of the frontal system between BC and BCC is a new subject of research.

In Section 5.4 we study two of the currents present in the BMC region: the Brazil Current and the South Atlantic Current (SAC). These currents were sampled by WOCE standard Low Cost Drifters. Together with positioning, these buoys also measured the sea surface temperature along their trajectories. The mean current, kinetic energies and temperature statistics are presented for the BC and SAC. Energy (FFT) spectra for the individual buoy's time series indicate the dominant oscillations present in the currents during the period of this study.

5.2. Variability of the SST fields in the South Atlantic Ocean

5.2.1. The climatological SST fields

Large scale sea surface temperature fields for the South Atlantic Ocean were obtained from the MCSST data set described in Section 4.2.2. In total, a set of 168 monthly averaged images was analysed but, for simplicity and also to discard the interannual signal, the seasonal behaviour of the SST fields in the South Atlantic was studied by using the 'climatological' monthly average images described in Section 4.2.2.

Figure 5.1 shows the 12 climatological monthly averaged images representing the period between 1982 and 1995. The Subtropical Front (STF) oscillation is represented by the displacement of the 20°C isoline, which is the thermal limit between tropical and subantarctic waters (Emilson, 1961, Castro and Miranda, 1998). As expected for the global meridional distribution of temperature in the ocean, the isotherms are zonally orientated in the open ocean all the year round. However, from about 5°E and 48°W towards the African and American continents, respectively, the isotherms change orientation reflecting the boundary currents.

The most prominent oceanographic process noticed in the sequence of images seen in Figure 5.1 is the oscillation of the STF. The front reaches its northernmost position in September (early austral spring, Figure 5.1.i), when the mean position of the front, as measured visually from the 20°C isoline in the open ocean, is about 28°S in latitude. The STF retracts to its southernmost position in February (late austral summer, Figure 5.1.b). During February, the mean meridional position of the 20°C isotherm in the open ocean is about 36°S. The mean meridional migration distance of the STF through the year is about 900 km in the open South Atlantic, while in the border to the African Continent the migration range is greater than 2000 km and mostly zonal. In the Brazil-Malvinas Confluence and South Brazilian Continental Shelf regions, the 20°C isotherms take the form of a 'Z', migrating about 1600 km between February and September.

As described by Tomczak and Godfrey (1994), Figure 5.1 also shows the core of the Malvinas Current (MC) as a jet-like northward looping excursion of the Antarctic Circumpolar Current (ACC). In the SBCS region, the coastal extension of MC which feeds the Brazilian Coastal Current is remarkable in wintertime, when cold waters dominate the Brazilian shelf.

During the months of January to March (Figure 5.1.a to c) the Benguela Current (BgC) upwelling system is clearly visible in the African coast, being detached from the STF. Surface temperatures in this upwelling are several degrees lower than in adjacent waters, and the gradients are comparable to those in the BMC region. Tomczak and Godfrey (1994) report that the BgC upwelling is constrained to the shelf, not exceeding 200 km in width. This agrees with the feature seen in Figure 5.1. Still following Tomczak and Godfrey (1994), the upwelling is stronger and restricted to the south in summer and spring when the Trade winds are steady, becoming intermittent and extending itself northwards from July to September. In these months, although the Trade winds are stronger they are not steady, being interrupted by the passage of atmospheric low systems travelling eastwards.

The BMC region is seen oscillating together with the STF, as the confluence is defined as the western extension of the front. The 'Z' form of the 20°C isoline representing the STF is considered in this work as the signature of the Brazil-Malvinas Confluence at the sea surface. The two extreme vertices of the 'Z' in the confluence are believed to be good indicators of the location of maximum penetration of the MC extension towards the north and of the BC towards the south.

The location where the 20°C isotherm reaches its southernmost extreme in the BMC region, as seen in the MCSST climatological images, is varying from about 30°S to 42°S from winter (August-September) to summertime/early spring (February-March), respectively. This location represents the position of maximum penetration of the BC and is related to the BC reversal, the location where the BC shifts its direction towards the east to generate the South Atlantic Current, or BC extension.

The location where the 20°C isotherm reaches its northernmost limit in the BMC region can also be spotted in Figure 5.1 as the upper vertex of the 'Z' in the western boundary of the STF. In the climatological MCSST images, the upper vertex of the 'Z' is related to the penetration of MC. This is clearly visible between January and April (Figure 5.1.a to d), when the jet-like core of MC can be noticed offshore the South American coast. This vertex is, in general, an indication of the position of the BMC, a little further north than the BC reversal position (Reid et al., 1977).

Figure 5.1.e to l show that the upper vertex of the BMC is driven towards the coast in spring, winter and autumn. In this case, this position is not related to the core of MC, but to the coastal current BCC. Chapter 6 will better describe this current. Here we simply note that the

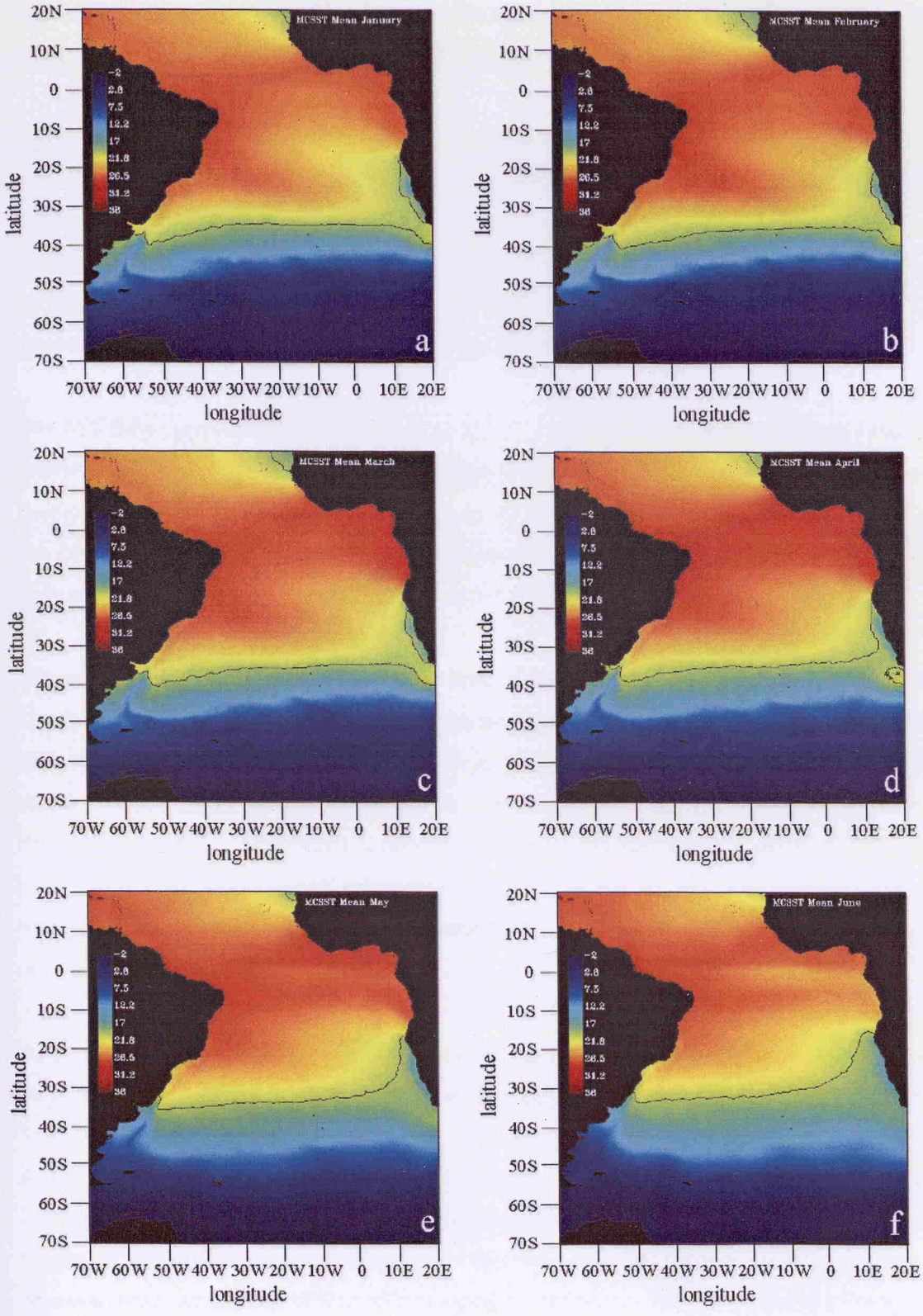

Figure 5.1. Climatological monthly averaged images representing the period between 1982 and 1995. (a) January; (b) February; (c) March; (d) April; (e) May; (f) June. The black line (20°C isotherm) represents the STF.

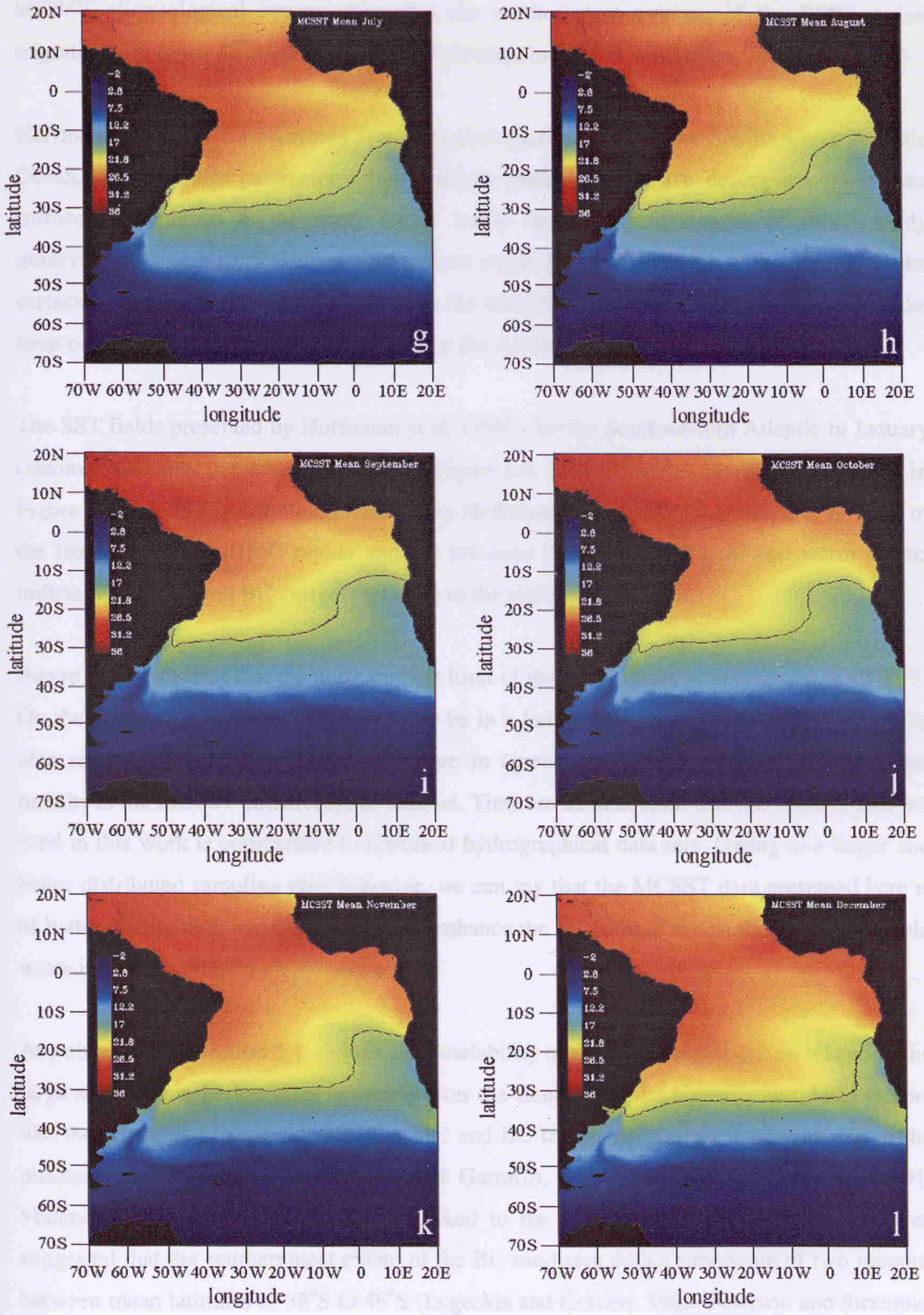

Figure 5.1. (cont.) Climatological monthly averaged images representing the period between 1982 and 1995. (g) July; (h) August; (i) September; (j) October; (k) November; (l) December. The black line (20°C isotherm) represents the STF.

MCSST climatological images show that the northernmost extreme of the BMC region migrates from about 37°S in summertime (February) to 25°S in wintertime (August).

Hoffmann et al. (1997) presented some climatological aspects of the Southwestern Atlantic Ocean. Among other parameters, these authors made an extensive description of the sea surface temperatures in the study region based upon different sources of data, mainly observational and historical ones. The authors report that the temperature distribution at the surface of the ocean is mainly governed by the latitude, season and the currents, while in the deep ocean the temperatures are governed by the circulation.

The SST fields presented by Hoffmann et al. (1997) for the Southwestern Atlantic in January (summer) and July (winter) can be seen in Figure 5.2. In agreement to the results presented in Figure 5.1, the SST distribution presented by Hoffmann et al. (1997) suggests the 'Z' form of the isotherms in the BMC region and the presence of 'tongues' of cold and warm waters indicating the MC and BC currents meeting in the region.

Figure 5.2.a indicates that the northernmost limit of the 20°C isoline in January is about 37°S. On the other hand, for July this limit must be in a latitude lower than 26°S, out of the study area seen in Figure 5.2.b. These values are in agreement to the ones found for the same months in the MCSST climatological data set. They are an indication that the MCSST data set used in this work is comparable to historical hydrographical data sets. Owing to a larger and better distributed sampling grid, however, we can say that the MCSST data presented here is of better quality than hydrography data to enhance the 'Z' form of the isotherms and the cold water intrusion at the South American shelf.

As pointed out in Section 2.4, the seasonal variability of the BMC region can be related to the large scale atmospheric cycles occurring over the South Atlantic. Nevertheless, local factors like the winds and the variation in the MC and BC transports play an important role in the process (Olson et al., 1988; Garzoli and Garraffo, 1989; Peterson and Stramma, 1991; Matano, 1993; Matano et al., 1993). Linked to the oscillation of the BMC, it has been suggested that the southernmost extent of the BC oscillates with a time scale of two months, between mean latitudes of 38°S to 46°S (Legeckis and Gordon, 1982; Peterson and Stramma, 1991; Tomczak and Godfrey, 1994).

In order to account for the temporal and spatial variability of the South Atlantic and particularly of the BMC region, Principal Component (PC) analysis was performed over the

set of MCSST monthly climatological images presented in Figure 5.1. The methods involved in this analysis were described in Section 4.2.5.

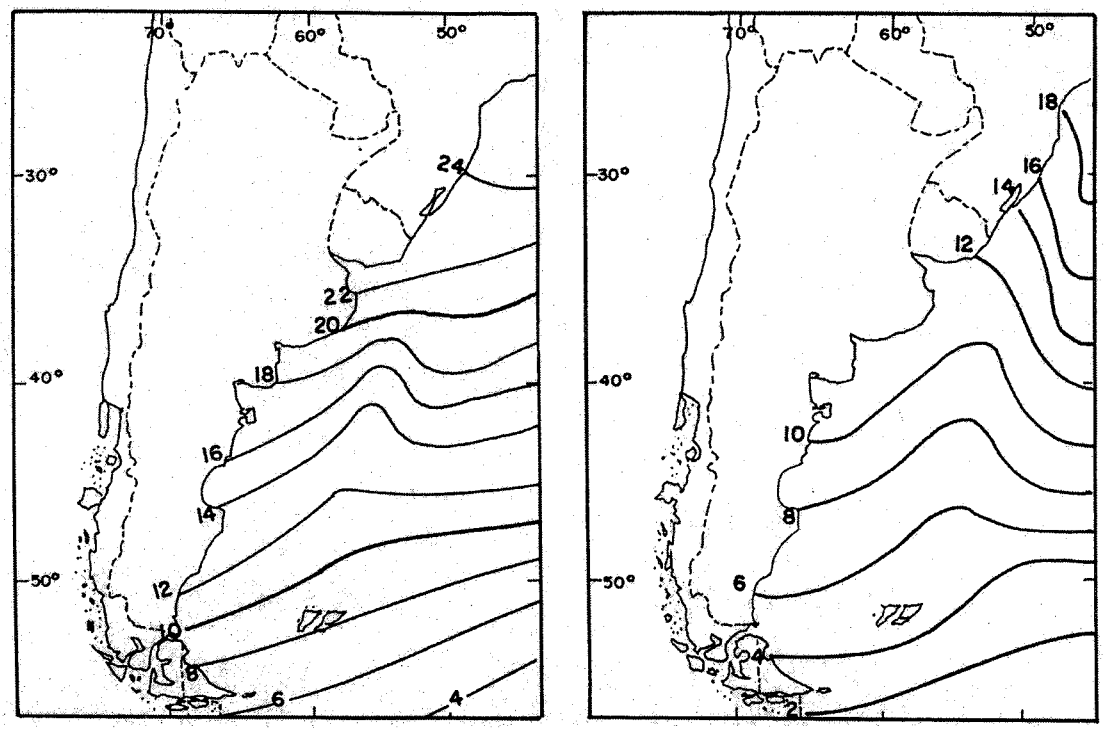

Figure 5.2. SST fields for the Southwestern Atlantic in January (left) and July (right). Source: Hoffmann et al. (1997).

The resulting PC images representing the first, second, third and fourth PC modes of the climatological MCSST images are presented in Figure 5.3.a-d, respectively. PC mode 1 (PC1) explains 99.2 % of the total variance present in the climatological MCSST data set, while PC2, PC3 and PC4 explain 0.5 %, 0.2 % and 0.02 % of the variance, respectively. Together, the first four PC modes represent 99.92 % of the total variance of the data.

The spatial amplitudes of the first PC mode (Figure 5.3.a) are very similar to the temperature patterns of the climatological MCSST image obtained for July (Figure 5.2.g), which roughly represents the temporal mean of all images. Parada and Cantón (1998) have worked with AVHRR monthly maximum images for 1993 in the Alborán Sea (Mediterranean) and also found that the first PC mode computed from the monthly maximums was very similar to the temporal mean of their images.

The orientation and shape of the amplitude zero line in Figure 5.3.a is very similar to those of the 20°C isoline presented in Figure 5.2. This line is dividing warm (Tropical) waters from the cold (Subantarctic, Coastal and Antarctic) waters present to the south of the STF. In the BMC region, the PC1 spatial amplitudes indicate the jet-like characteristics of Malvinas Current, its formation region in the ACC and its extension towards the coast in the southern Brazilian continental shelf (SBCS) region. Looking towards the African continent, the BgC upwelling system is also evident.

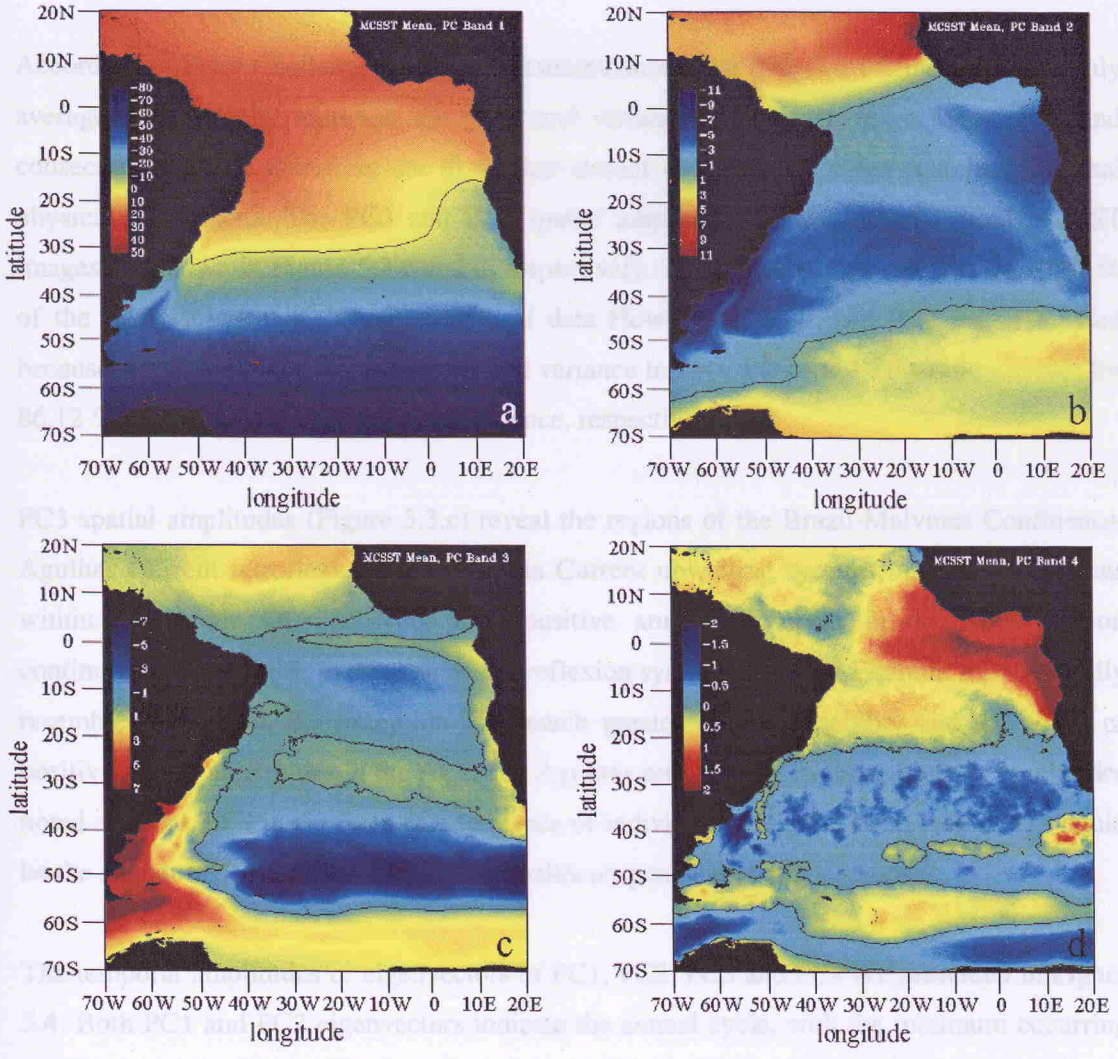

Figure 5.3. PC1 (a), PC2 (b), PC3 (c) and PC4 (d) derived from the climatological MCSST images. The black line represents the line of amplitude zero.

The spatial amplitudes of the second PC mode are shown in Figure 5.3.b. Although accounting for only 0.5 % of the total variance in the climatological data, this mode also

presents a very interesting spatial pattern. The line of amplitude zero is apparently delimiting the entire South Atlantic Ocean Subtropical gyre, where amplitudes are negative in contrast to the positive ones found for the Equatorial Atlantic and Southern Ocean.

The ACC deflection to the north at the east of the Drake Passage, as well as the region of formation of the MC, appear to be contained within the Subtropical gyre in the MCSST climatological mean first PC mode. Like in PC1, PC2 spatial amplitudes still show the MC jet and the BgC upwelling. The SBCS region is dominated by very high negative amplitudes suggesting an extension of MC up to latitudes of about 24°S.

According to Peter Challenor (personal communication), the first two PC modes of monthly averaged data usually represent the mean and variance of the data, respectively. PC3 and consecutive modes, therefore, are those that should be examined when searching for real physical phenomena. The PC3 and PC4 spatial amplitudes of the climatological MCSST images are shown in Figure 5.3.c and d, respectively. They together account for only 0.22 % of the total variance in the climatological data However, if PC1 and PC2 are eliminated because they are representing the mean and variance images, PC3 and PC4 would account for 86.12 % and 7.31 % of the remaining variance, respectively.

PC3 spatial amplitudes (Figure 5.3.c) reveal the regions of the Brazil-Malvinas Confluence, Agulhas Current retroflexion and Benguela Current upwelling systems, as singular regions within the South Atlantic. Very high positive amplitudes occur in the SBCS region continuously up to 24°S, in the Agulhas retroflexion system and in the Equator. PC4 generally resembles PC1, with the exception of a much greater spatial variability and the zones of positive spatial amplitudes in the ACC and Agulhas retroflexion systems. Positive amplitudes noted at about 30°S in the form of a sequence of individually aligned mesoscale circles could be the signature of Rossby waves (Peter Challenor, personal communication).

The temporal amplitudes or eigenvectors of PC1, PC2, PC3 and PC4 are presented in Figure 5.4. Both PC1 and PC2 eigenvectors indicate the annual cycle, with the minimum occurring in February (month 2 in Figure 5.4) and the maximum in September or October (months 9 and 10 in Figure 5.4). PC1 amplitudes are all positive. By multiplying the temporal amplitudes by the spatial amplitudes of the PC modes at any particular location we can assess the anomalies of the mean sea surface temperature for each particular month. For the case of PC1 (Figure 5.3.a), where the temporal amplitudes are all positive, the anomalies are always positive in the tropical region (above the line of zero amplitude) and negative elsewhere. That

is expected, since the line of zero amplitude of Figure 5.3.a represents the spatial mean of the South Atlantic sea surface temperatures.

PC2 temporal amplitudes (Figure 5.4 top right) are negative in the Austral summer/autumn (months 12, 1, 2, 3, 4 and 5) and positive in the winter/spring (months 6, 7, 8, 9, 10 and 11). Considering a particular eingenvalue at the centre of the South Atlantic (negative, as seen in Figure 5.3.b) and its respective temporal amplitudes, we conclude that the temperature anomalies at that point are positive in summer/autumn and negative in winter/spring. This is the behaviour of the entire South Atlantic subtropical gyre, in contrast to that of the tropical Atlantic, ACC and Agulhas systems.

PC3 temporal amplitudes (Figure 5.4 bottom left) also indicate the annual cycle. However, now the amplitudes are negative in autumn/winter and positive in spring/summer. The corresponding temperature anomalies for the BMC and SBCS regions are, consequently, also negative in autumn/winter and positive in spring/summer. PC4 eingenvectors (Figure 5.4 bottom right) indicate a semiannual cycle, with positive peaks in April and October, and negative peaks in January and July.

The presence of an annual cycle in the South Atlantic and in the BMC region has been demonstrated by several authors. Podestá et al. (1991) and Podestá (1997), for instance, report that the annual (or stationary) cycle is responsible for the majority of the SST variability in the Southwestern Atlantic, and that its predominance is even bigger at the continental shelf. The authors suggest that the annual variation of incident solar radiation drives the SST annual cycle in the Southwestern Atlantic Ocean. Other authors like Olson et al. (1988), Garzoli and Garraffo (1989), Provost et al. (1992) and Kampel and Silva Jr. (1996) also demonstrated that the annual cycle is dominant in the Southwestern Atlantic Ocean SST fields.

Analysing SST data for the Tropical Atlantic Ocean, Servain (1991) described the main modes of the interannual climatic variability of that ocean. Based on previous work from other authors, he also reports that the Tropical Atlantic differs widely from the Tropical Pacific with respect to climatic variability, especially in relation to SST. While in the Tropical Pacific Ocean the interannual oscillations are strongest, especially during El Niño episodes, the dominant cycle of the Tropical Atlantic is annual.

Servain (1991) presented results of PC analysis undertaken by others in the Tropical Atlantic region. Like in the results presented here for the climatological MCSST images, Servain (1991) reports that there are two main modes of the SST variability of the Tropical Atlantic.

The first mode describes a heating (cooling or warming) trend in most of the basin, and the second PC mode exhibits an asymmetrical structure close to the Equator. This structure, displayed in Servain's (1991) figure b, is identical to the line of zero amplitude found here for PC2 in the equatorial region of the Atlantic (Figure 5.3.b). This is the limit of the thermal dipole of the Atlantic, which has been the subject of research for many years. The line separating the warm and cold parts of the dipole seen in Figure 5.3.b is also identical to the description offered by Nobre and Shukla (1996).

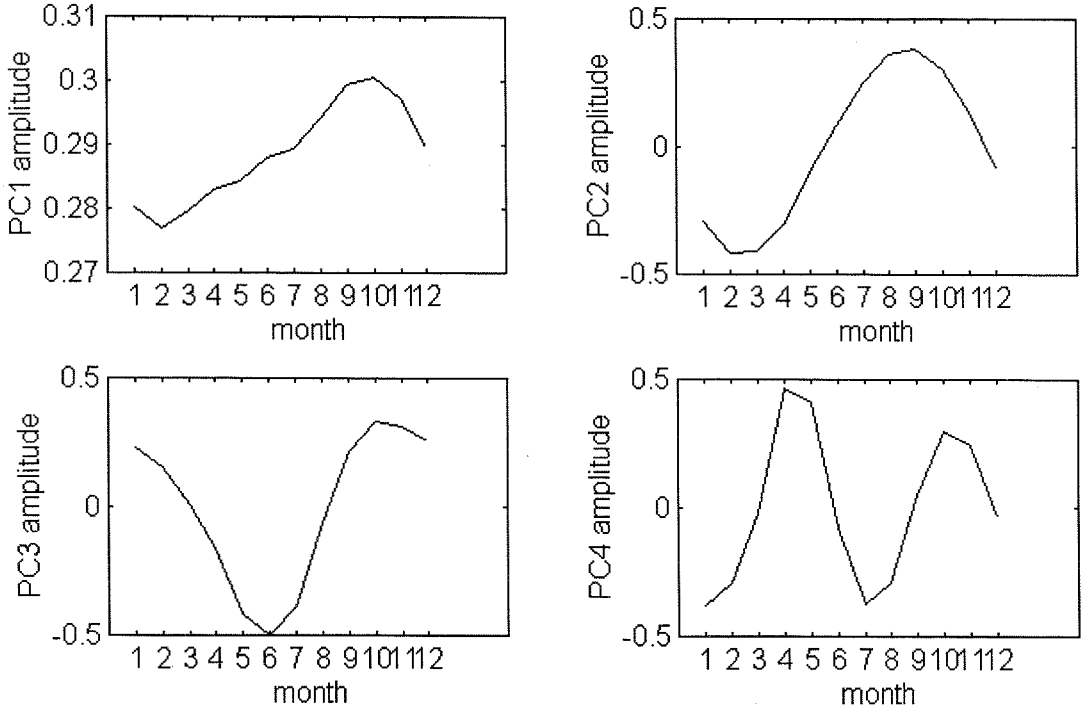

Figure 5.4. Temporal amplitudes or eigenvectors of the MCSST monthly climatological PC1, PC2, PC3 and PC4.

The temporal and spatial behaviour of PC2 obtained in this thesis agrees with the dipole characteristics described by Servain (1991) for the Tropical Atlantic region. According to this author, the northern part of the Tropical Atlantic is coldest in February-March and warmest in September-October. The southern part of that basin is coldest in August-September, and warmest in March-April. The cycle of the Tropical Atlantic meridional dipole is related to the displacement of the axis separating the northern and southern hemisphere trades (e.g. Servain, 1985; cited by Servain, 1991). There are also possible associations with rainfall anomalies in the African Sahel and in the northeast of Brazil, tropospheric circulations over the northern hemisphere and with the Southern Oscillation (e.g. Moura and Shukla, 1981; Déqué and

Servain, 1989; Hastenrath et al., 1987; all cited by Servain, 1991). For more information about the Tropical Atlantic dipole see Nobre and Shukla (1996) and Servain et al. (1998).

Figure 5.5 presents the factor loadings (F) found for the first four monthly climatological MCSST PC modes. As described in Section 4.2.5, the factor loadings give information on the relative contribution of each original image to the new generated PC modes. Figure 5.5 exhibits a pattern very similar to that of the temporal amplitudes seen in Figure 5.4. However, because F is directly proportional to the eigenvalues of each mode, the amplitudes seen in Figure 5.4 are reduced in Figure 5.5. The climatological image of October (spring) is the biggest contributor to the PC1 variability, while February (summer) contributed more to the second PC mode. The major contributors for PC3 and PC4 were July (winter) and April (autumn), respectively.

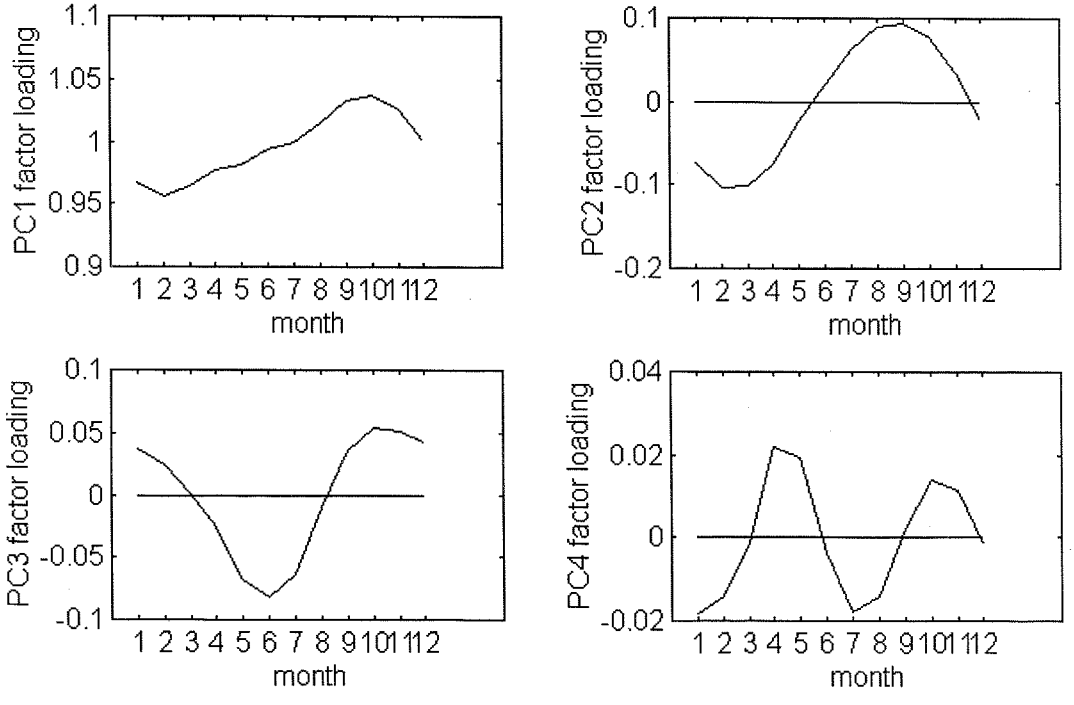

Figure 5.5. Factor loadings of the MCSST monthly climatological PC1, PC2, PC3 and PC4.

5.2.2. The anomaly SST fields

A series of seasonally averaged images of MCSST anomalies from 1982 to 1995, obtained as explained in Section 4.2.5, was utilised here with the objective of accounting for the

interannual oscillations present in the South Atlantic. For that, PC analysis was also performed in the series. Owing to the high number of images utilised in the analysis (57 in total), the overall set of individual anomaly charts are not presented here. The next section in this thesis, however, presents some of the individual anomaly (not seasonally averaged) images computed for the months of March 1993 to July 1994, because these are the months when high-resolution and buoy data were available for this work. These images contributed for the seasonally averaged anomaly images of the spring of 1993 to the winter of 1994. The overall set of seasonally averaged anomaly MCSST charts, as explained in Section 4.2.5, extends itself from the summer of 1982 to the summer of 1996.

However, when performing the PC analysis for the first time, it was noticed that the original resulting seasonally averaged image representing the winter of 1994 was very distinct from the neighbouring images. The image's mean, standard deviation, minimum and maximum values indicated a great deal of inconsistent data, presumably caused by extreme interpolation in the original anomaly images of June, July and August 1994. Combined together to generate the anomaly image of winter 1994, they result in bad data especially in the region of the BMC zone. The subsequent processing was also affected by this problem, resulting in a PC1 strongly dominated by the winter 1994 image as well (not show).

To solve this problem, the previously generated seasonal anomaly images of the winter 1993 and the winter 1995 were used to generate a linearly interpolated image representing the SST anomalies of the winter 1994. This artificial image was used with the other anomaly images for the subsequent PC analysis.

The results of the PC analysis over the seasonally averaged MCSST anomalies demonstrated that 78.04 % of the total variance in the anomaly series is explained by the first 4 PC modes. They are presented in Figure 5.6. The first PC mode accounted for 40.69 % of the variance in the original data, while modes 2, 3 and 4 accounted for 19.09 %, 9.86 % and 8.4 % of the variance, respectively. Figure 5.7 shows the eigenvalues found for PC1, PC2, PC3 and PC4, together with their associated sampling errors. According to Parada and Cantón (1998), an individual PC mode is only significant if its sampling error does not overlap with a neighbouring one. As seen in Figure 5.7, this is not the case for the fourth PC mode.

The spatial distribution of the PC1 amplitudes (Figure 5.6.a) presents a band of positive values zonally centred at the southern part of the open South Atlantic, in a range of latitudes varying from about 40°S to 50°S in the middle of the Atlantic basin. In the BMC region, there is an isolated cell of positive amplitudes centred at about 40°S, 55°W, just below the La Plata

river. By analysing the overall set of seasonally averaged MCSST images (not shown here), it can be noted that this feature is related to the seasonal oscillations of the BMC region, marking the southern excursions of the Brazil Current in summertime.

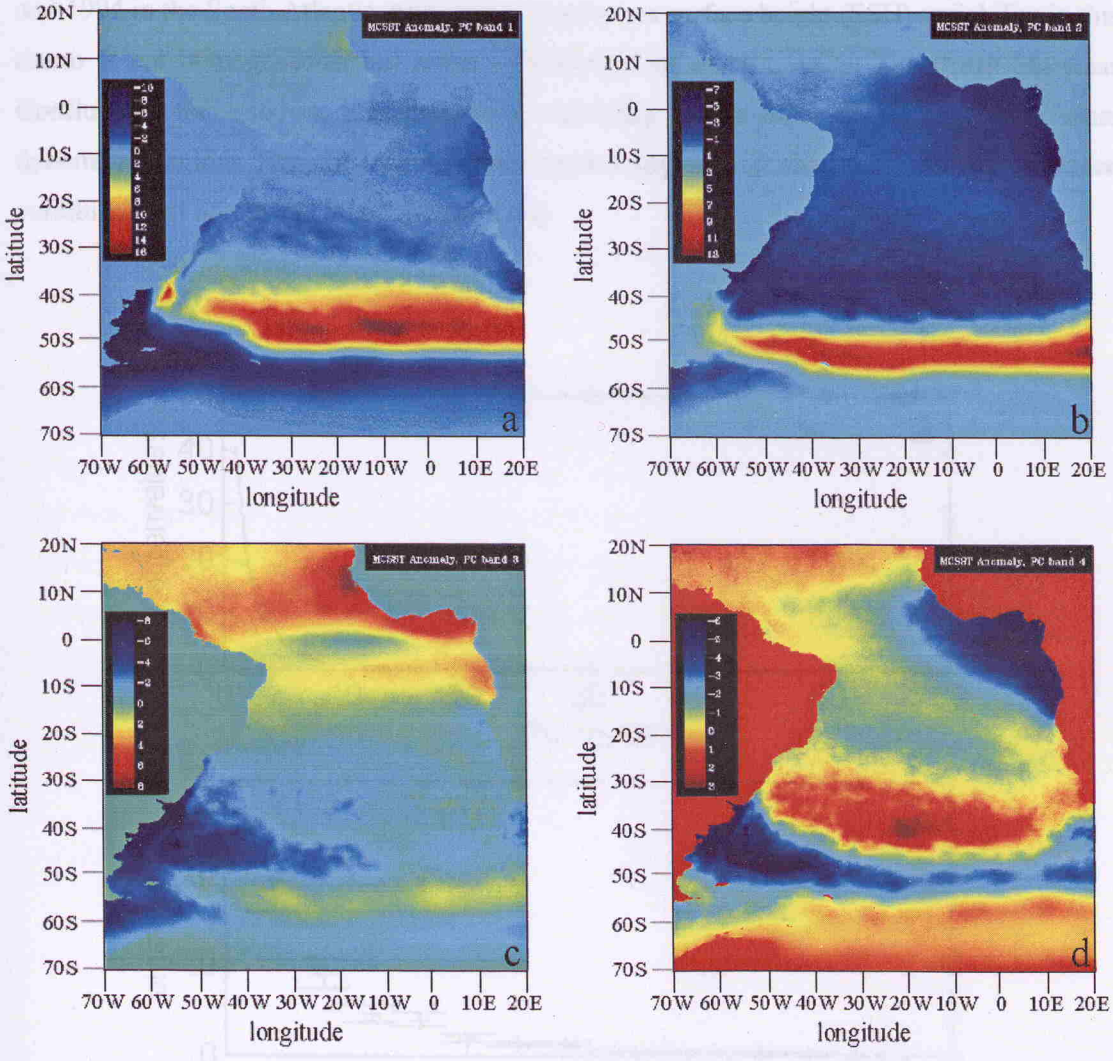

Figure 5.6. PC1 (a), PC2 (b), PC3 (c) and PC4 (d) derived from the seasonally averaged MCSST anomalies.

The shape and distribution of the positive amplitudes of the South Atlantic seen in Figure 5.6.a is coincident with the mean distribution of the region between the Subtropical Front and the Subantarctic Front (SAF), as presented by Peterson and Stramma (1991) and Longhurst (1998). Figures 2.1 and 5.9 show circulation schemes presented by these authors for this region in large and mesoscale resolutions (South Atlantic and Southwestern Atlantic oceans), respectively. As described in Peterson and Stramma (1991), the region between the STF and

the SAF is comprised between the northern and the southern axes of the ACC, being coincident in latitude with the results found here for the first mode seasonally averaged MCSST principal component.

Jones (1997), testing the effects of the orbit error removal in TOPEX/Poseidon data for 1993 and 1994 in the South Atlantic, pointed out that the sea surface height (SSH) variability in this ocean is not homogeneous, but rather concentrated in specific areas. The Brazil-Malvinas Confluence, for instance, presented SSH variability in the order of 40 cm, while other dynamical regions like the Agulhas retroflexion region and the ACC system presented variabilities of 45 cm and 20 cm, respectively.

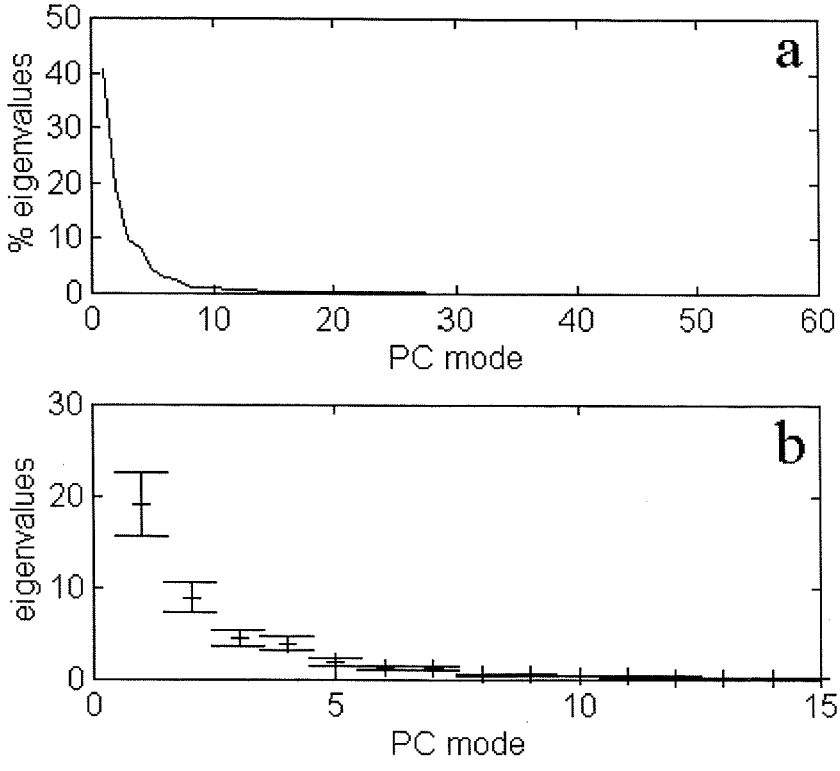

Figure 5.7. Eigenvalues of the seasonally averaged MCSST anomalies. (a) Percentage of the total variance. (b) Absolute values and associated sampling errors for the first 15 PC modes.

The SSH maps presented by Jones (1997) for the South Atlantic (with and without the orbit error removal) indicate that the feature centred at about 40°S, 55°W found here for the seasonal MCSST anomalies first PC is coincident with the region of high SSH variability

found for the BMC region by Jones (1997). Low resolution ATSR variability (standard deviation) maps also presented by this author indicate the BMC region as one of the most energetic in the whole South Atlantic ocean.

Goni et al. (1996), using Geosat and AVHRR data from 1984 to 1989, also indicated the presence of a region of high SSH and SST variability centred at about 40°S, 55°W in the Southwestern Atlantic. The authors report that the frontal movements are one of the processes involved in the generation of this variability. Frontal density fields computed from AVHRR images indicated a preferred position for the fronts off shore the continental shelf and parallel to the South American coast before they retroflex to the northeast direction to follow the BC retroflexion.

SSH and SST anomaly maps showing peaks centred at about 40°S, 55°W are also presented by Provost and Le Traon (1993) and Provost et al. (1992), for example. Olson et al. (1988), using high resolution AVHRR data, mapped the percentage of occupation of both Brazil and Malvinas currents extensions in the Southwestern Atlantic Ocean. By analysing the maps presented by Provost and Le Traon (1993), Provost et al. (1992) and Olson et al. (1988), it can be concluded that the BC and MC extensions to the open South Atlantic are preceded by a frontal activity in a direction parallel to the coast.

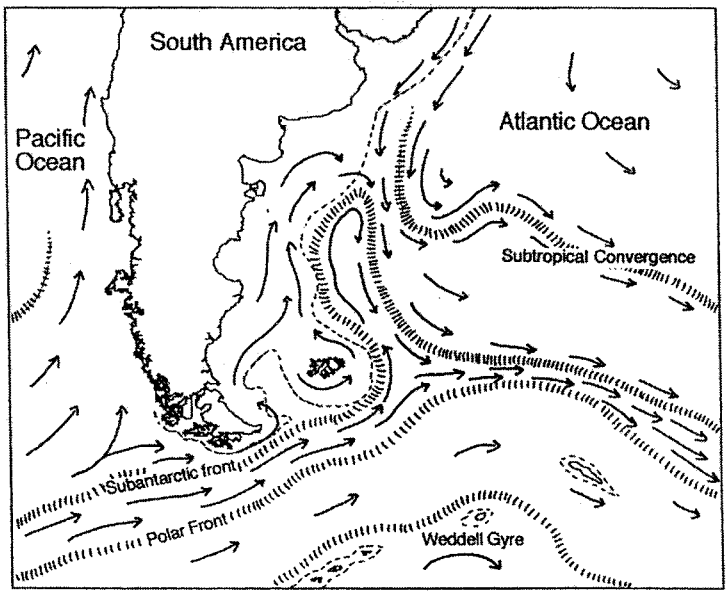

Figure 5.8. Idealised circulation scheme in the Southwestern Atlantic Ocean. Subtropical Convergence stands for the Subtropical Front. Source: Longhurst (1998).

Surface maps of temperature and salinity produced from a conventional hydrographic survey made in October 1984 are presented by Gordon (1989). The maps indicate the front between BC and MC and its associated eddy activity. At the same time that the maps indicate the strong relationship between temperature and salinity signatures in this frontal region, they also show that the front has the same direction indicated by the fronts seen in Olson et al. (1988) and Goni et al. (1996) and the feature seen in the seasonal anomaly MCSST PC1 found in this thesis.

The seasonal anomaly MCSST second, third and fourth PC modes are seen in Figures 5.7.b, c and d, respectively. PC2 presents the subtropical region associated with negative amplitudes, while positive values are strong in the ACC system and weak but present at the equator. PC3 and PC4 have strong positive spatial amplitudes in the Equatorial Atlantic and strong negative amplitudes in the BMC region. PC4, however, has strong positive amplitudes also dominating the southern subtropical region and strong negative amplitudes in the Angola-Benguela region off Africa.

Figure 5.9 presents the temporal amplitudes for the seasonal MCSST anomalies first four PC modes. The anomaly amplitudes displayed a visible annual cycle with PC1 and PC3 generally presenting crests in summer and troughs in wintertime. PC2 behaves the other way round and PC4 behaves broadly like PC1 and PC2, but is less evident. When plotting the spatial mean of each individual MCSST seasonally averaged anomaly images, as seen in Figure 5.10, it can be noticed that the annual signal is very strong in the series. Again, crests are associated with summer and troughs with wintertime.

Figure 5.10 also presents the standard deviation, minimum and maximum temperature anomalies for each of the seasonally averaged images used in the PC analysis. In general, the band of standard deviation is about $\pm$ 1-2°C from the mean.

As described in Section 4.2.5, FFT analysis was performed in the temporal amplitude series in order to account for the dominant periods present in the data. The results of this analysis are presented in Figure 5.11 and Table 5.1. All the peaks described here are significant to the 95 % confidence interval. The dominant peak for PC1 and PC2 was centred at 5.37 years. PC3 had a dominant peak at 10.7 years. This peak was also present in PC4 which had its dominant peak centred at 3 years. Interannual peaks were found at about 2 years, and 1.1-1.4 years.

The annual cycle was present only in PC1. It was centred at 11.6 months. Although the PC analysis performed here has not intended to account for periods lower than an year,

oscillations in the intrannual period band were found to be strong and consistent in all the first four PC bands. Intrannual cycles, as seen in Table 5.1, were centred in periods of 6.6 months to 10 months. The semiannual cycle (6.6 months) was present only in PC3. Intrannual peaks lower than 6 months ($2\Delta t$) were not accounted for.

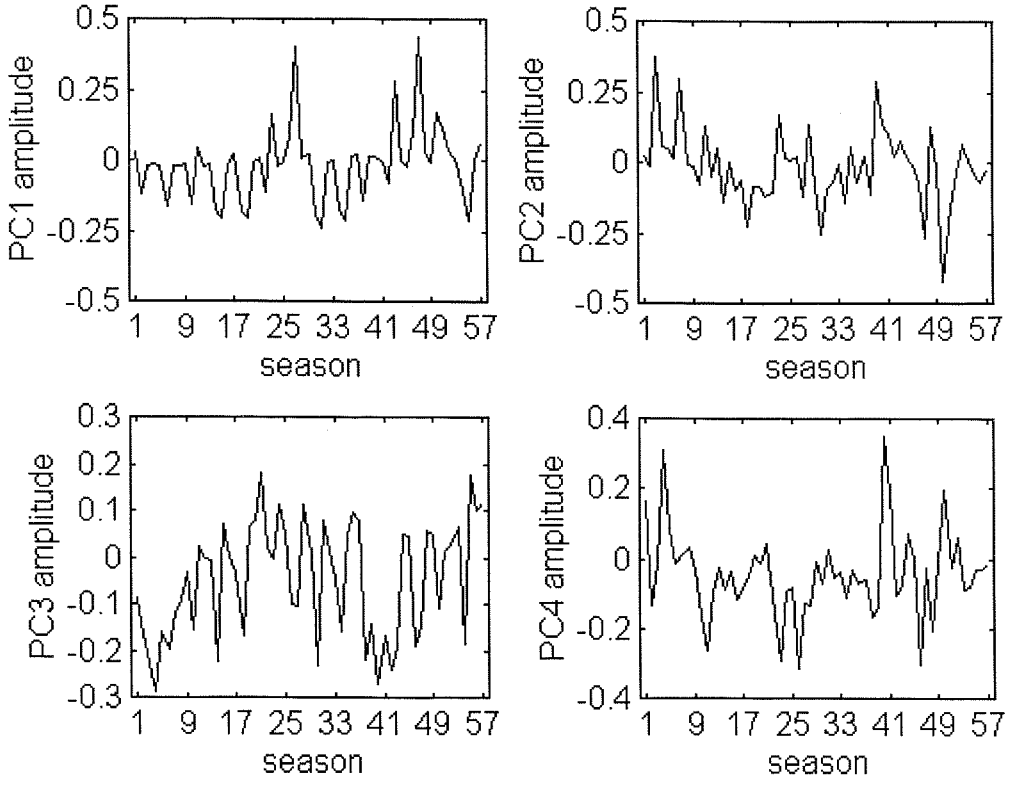

Figure 5.9. Temporal amplitudes for the seasonally averaged MCSST anomalies PC1, PC2, PC3 and PC4. Seasons 1, 9, 17 and so on represent the summers of 1982, 1984, 1986 and so on until 1996.

The importance of the annual cycle in the South Atlantic Ocean was discussed early in this section. The discussion to follow will, therefore, concentrate in the other cycles present in the PC temporal amplitudes series rather than the annual one. For instance, the presence of interannual and intrannual cycles in the Southwestern Atlantic was observed by several authors like Provost et al. (1992), Kampel and Silva Jr. (1996) Campos et al. (1999) and Vivier and Provost (1999a and 1999b), among others.

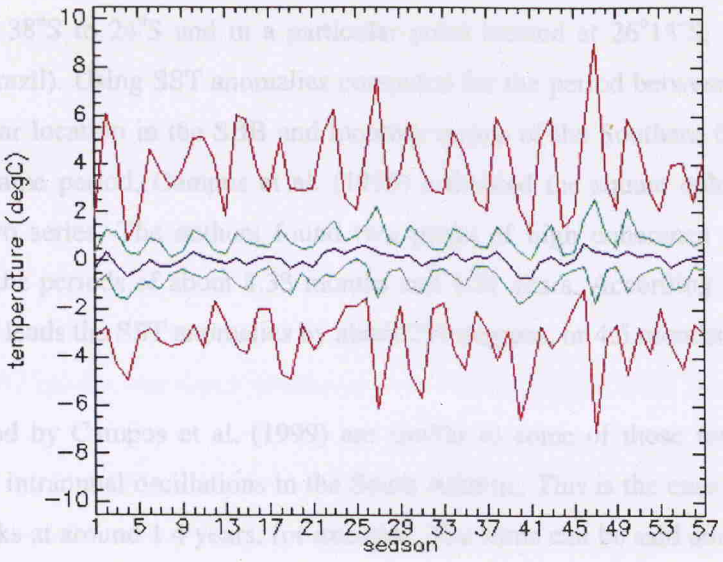

Figure 5.10. MCSST seasonal anomalies in the South Atlantic for the period between January 1982 to December 1995: Spatial mean (blue line), standard deviation (green lines), minimum and maximum (red lines). Seasons 1, 5, 9 and so on represent the summers of 1982, 1983, 1984 and so on until 1996.

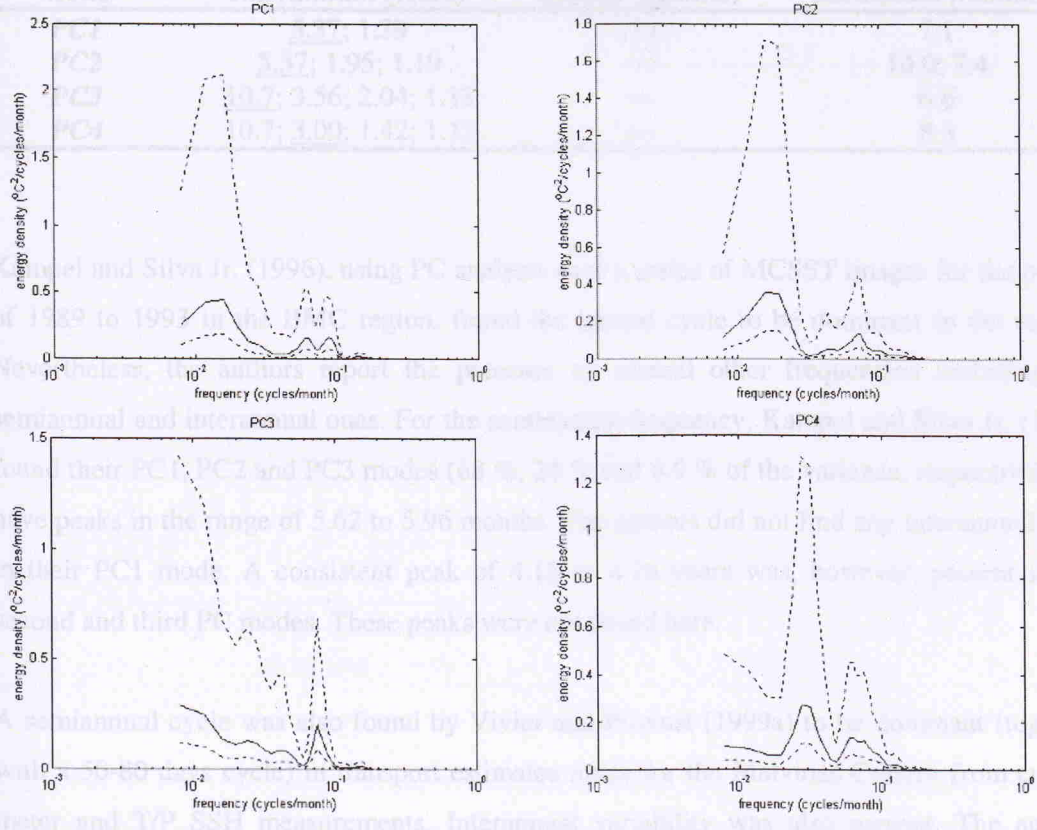

Figure 5.11. Energy preserving spectra for temporal amplitudes of the seasonally averaged MCSST anomalies PC1 (top left), PC2 (top right), PC3 (bottom left) and PC4 (bottom right).

Campos et al. (1999) studied the interannual variability of the SST along the 100 m isobath in the latitudes of 38°S to 24°S and in a particular point located at 26°15'S, 47°43'W (South Brazil Bight, Brazil). Using SST anomalies computed for the period between 1982 and 1994 in their particular location in the SBB and monthly means of the Southern Oscillation Index (SOI) for the same period, Campos et al. (1999) estimated the square coherence spectrum between the two series. The authors found two peaks of high coherence (above 95 % of confidence) in the periods of about 8.33 months and 1.51 years. According to Campos et al. (1999), the SOI leads the SST anomalies by about 270 degrees, or 4.5 months.

The peaks found by Campos et al. (1999) are similar to some of those found here for the interannual and intrannual oscillations in the South Atlantic. This is the case of PC1 and PC4 interannual peaks at around 1.4 years, for example. The same can be said about the PC4 peak centred at 8.3 months.

Table 5.1. Period of the major energy peaks for the seasonally averaged MCSST anomalies PC modes 1 to 4 (dominant period underlined)

Mode	*Interannual (years)*	*annual (months)*	*intrannual (months)*
PC1	5.37; 1.39	11.6	7.1
PC2	5.37; 1.95; 1.19	---	10.0; 7.4
PC3	10.7; 3.56; 2.04; 1.13	---	6.6
PC4	10.7; 3.00; 1.42; 1.13	---	8.3

Kampel and Silva Jr. (1996), using PC analysis over a series of MCSST images for the period of 1989 to 1993 in the BMC region, found the annual cycle to be dominant in the region. Nevertheless, the authors report the presence of several other frequencies including the semiannual and interannual ones. For the semiannual frequency, Kampel and Silva Jr. (1996) found their PC1, PC2 and PC3 modes (68 %, 24 % and 4.9 % of the variance, respectively) to have peaks in the range of 5.62 to 5.96 months. The authors did not find any interannual peak in their PC1 mode. A consistent peak of 4.15 to 4.16 years was, however, present in the second and third PC modes. These peaks were not found here.

A semiannual cycle was also found by Vivier and Provost (1999a) to be dominant (together with a 50-80 days cycle) in transport estimates made for the Malvinas Current from current meter and T/P SSH measurements. Interannual variability was also present. The authors reported that the semiannual peak is compatible with the interpretation that the MC variability responds to a remote forcing mechanism.

Vivier and Provost (1999b) investigated the along-shelf Malvinas Current flow off Argentina. Together with a 50-70 days energy band associated with the incursions of the Brazil Current to the south in the BMC region, they report that a period of 135 days (4.5 months) is significant. However, they add that there is no evidence of an annual or semiannual cycle in the along-shelf data, while in the cross-shelf domain a clear annual cycle is present due to the excursions of the South Atlantic Current.

In order to estimate the contributions of the individual seasonally averaged MCSST anomaly images to the PC modes, the factor loadings (F) for these images were also computed. The factor loading series for PC1, PC2, PC3 and PC4 are presented in Figure 5.12. The first three highest peaks for PC1 to PC4 are presented in Table 5.2. They indicate the highest individual contributions for the first four PC modes of the seasonal MCSST anomalies.

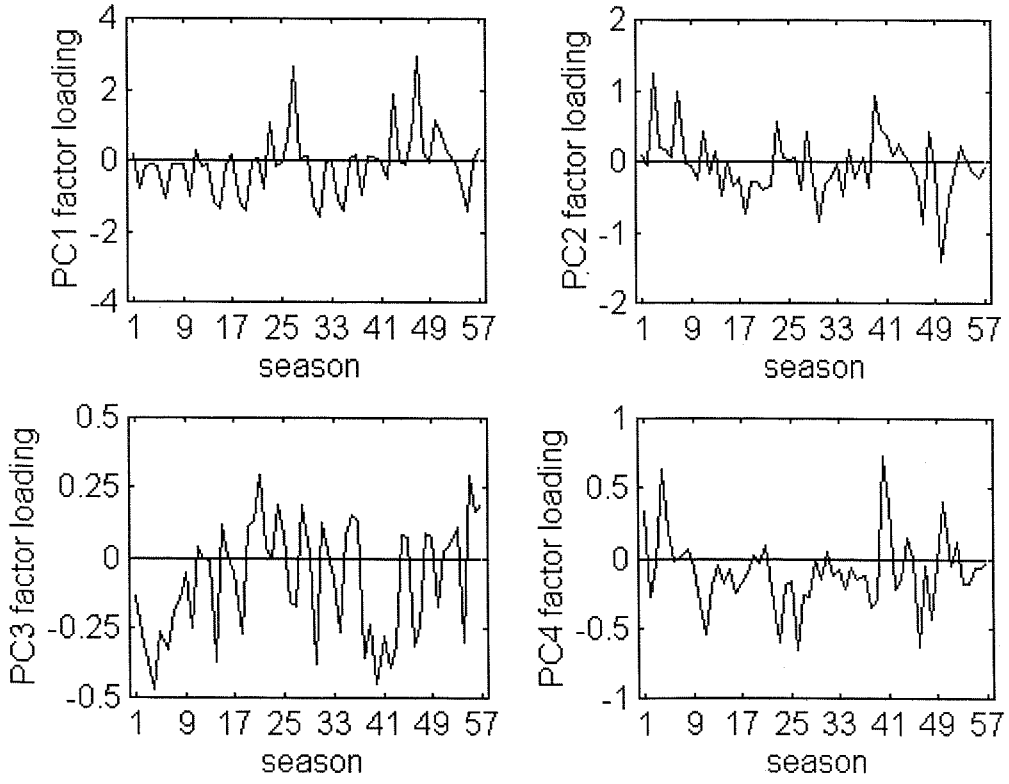

Figure 5.12. Factor loadings for the seasonally averaged MCSST anomalies PC1, PC2, PC3 and PC4. Seasons 1, 9, 17 and so on represent the summers of 1982, 1984, 1986 and so on until 1996.

Table 5.2. Seasonally averaged MCSST anomalies individual contributions to PC modes 1 to 4

	1st highest			*2nd highest*			*3rd highest*		
Mode	***season***	***image***	**F**	***season***	***image***	**F**	***season***	***image***	**F**
PC1	win 93	47	2.91	win 88	27	2.65	win 92	43	1.88
PC2	aut 94	50	-1.40	win 82	3	1.22	win 83	7	0.97
PC3	spr 82	4	-0.47	spr 91	40	-0.45	aut 92	42	-0.40
PC4	spr 91	40	0.73	aut 88	26	-0.65	spr 82	4	0.63

The image representing the winter of 1993 (Figure 5.13.a) is the strongest contributor to PC1 variability, which is dominated by a winter pattern. PC1 second and third highest contributors were the winter of 1988 and the winter of 1992. PC2 is dominated by the variability of the autumn 1994 (Figure 5.13.b) and of the winters of 1982 and 1983, respectively. The spring of 1982 (Figure 5.13.c) and spring of 1991 (Figure 5.13.d) were the major contributors of PC3 and PC4, respectively.

As quoted before, Campos et al. (1999) presented a time series of the Southern Oscillation Index for the period between 1982 and 1993. The most prominent peaks registered in the series occurred in the winter of 1982, winter of 1986, summer of 1988, winter of 1989 and winter of 1991. The peaks of the winter of 1982 and summer of 1988 were, respectively, the effects of the El Niño (high negative SOI) and of the La Niña (high positive SOI) events in the Pacific Ocean. The SOI signature of the (still discussed in the scientific community) extended El Niño of 1990-94 event is not particularly emphasised by Campos et al. (1999), who were searching for an uniform response of the SOI in the time series for the period of 1990 to 1994. Nevertheless, a strong negative SOI peak is clearly visible in their time series for the winter of 1991.

From all the major contributions of the individual seasonally averaged MCSST images to the principal PC modes (Table 5.2), only the winter of 1982 (PC2 second highest contributor) can be directly related to the remote events of the Pacific, in this case the El Niño occurrence of 1982. It has been suggested by Campos et al. (1999) that teleconnections between the Pacific Ocean and the Southwestern Atlantic could occur through the precipitation regime in the South American continent.

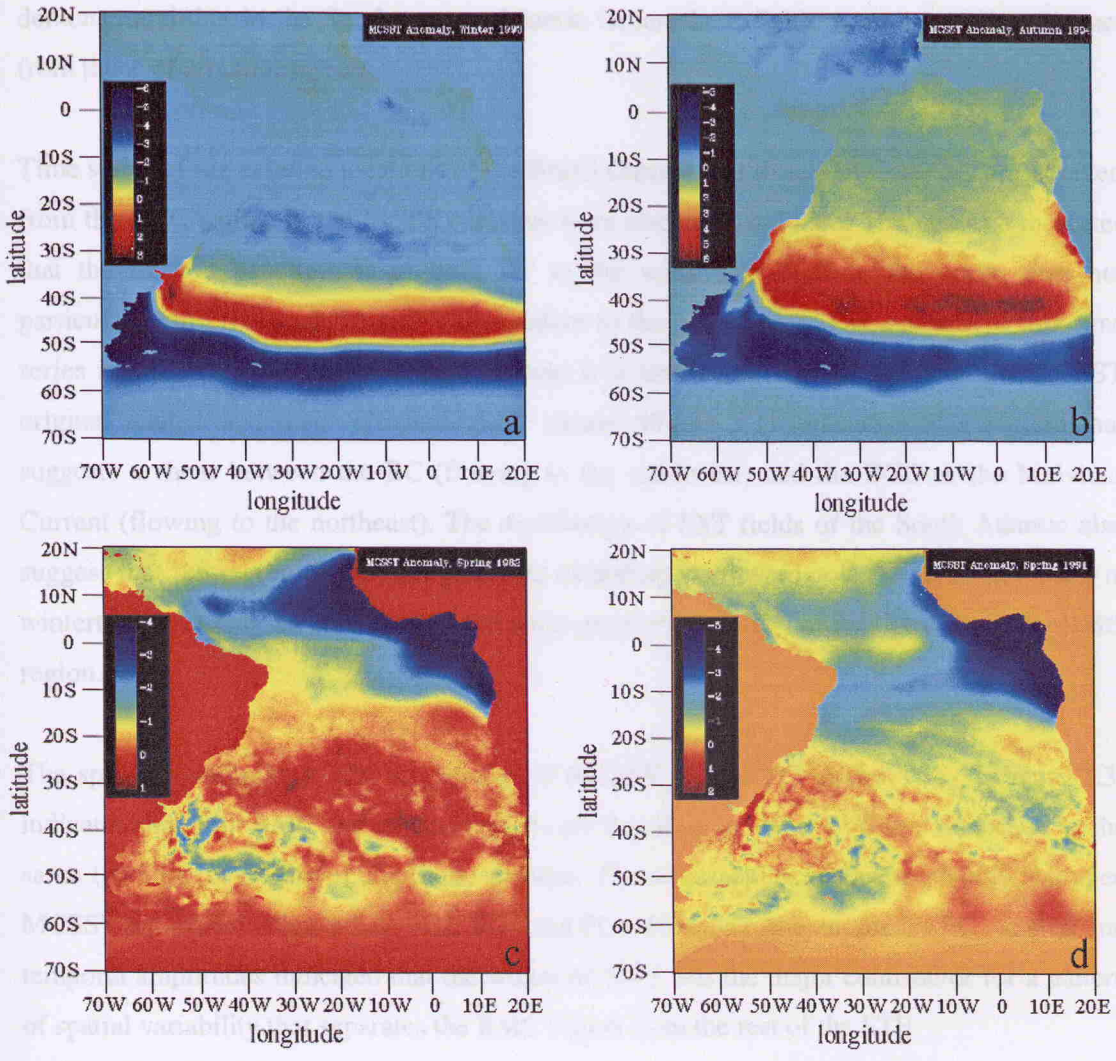

Figure 5.13. Seasonally averaged MCSST anomalies for the winter 1993 (a), autumn 1994 (b), spring 1982 (c) and spring 1991 (d).

5.3. SST fields in the BMC region and its vicinity in 1993 and 1994

5.3.1. MCSST fields

Together with the examination of the PC analysis results described in the earlier section of this document, a visual analysis of the 168 MCSST monthly averaged images covering the South Atlantic in the period between January 1982 and December 1995 was also performed for this work. Owing to the large number of images, they have not been presented here in their entirety. The analysis of the SST fields of the particular years of 1993 and 1994

demonstrated that in the Southwestern Atlantic Ocean these fields were not visibly distinct from those of remaining years.

Time series of the extreme locations of the Brazil Current and Brazilian Coastal Current taken from the 20°C isoline in the MCSST images were also analysed here. The analysis indicates that the relative penetrations of both BC to the south and BCC to the north were not particularly different in 1993 and 1994 relative to the other years. The analysis of this time series is presented in Chapter 7. At this stage it is interesting to note that both the MCSST original images and their 'climatological' means (Figure 5.1) indicate a SST pattern that suggests a shear between the BC (flowing to the southwest) and the BCC or the Malvinas Current (flowing to the northeast). The distribution of SST fields of the South Atlantic also suggest that the region of thermal gradients extending northwards off the Brazilian coast in wintertime is simply an extension of the Subtropical Front (STF) or its signature in the BMC region.

The spatial amplitudes of the climatological MCSST images PC modes 1 to 3 (Figure 5.3) indicated that both BMC and coastal regions off Brazil up to about 24°S are comprised in the same (positive or negative) amplitude domain. The same applies to the seasonally averaged MCSST anomalies (Figure 5.6) PC2, PC3 and PC4. However, the anomalies PC1 spatial and temporal amplitudes indicated that the winter of 1993 was the major contributor for a pattern of spatial variability that separates the BMC region from the rest of the STF.

Three examples of individual MCSST images and their respective anomalies for 1993 and 1994 are shown in Figure 5.14. The figure exemplifies the seasonal behaviour of the STF and its extension towards the coast during March 1993 (early autumn), September 1993 (early spring) and March 1994. In the BMC region and along the southern shelf of Brazil, the MCSST images illustrate the wintertime penetration of the BCC as an extension of the MC or of the waters present in the BMC region. This penetration is not particularly evident in the anomaly images and their PCs, indicating that this is not an anomalous process.

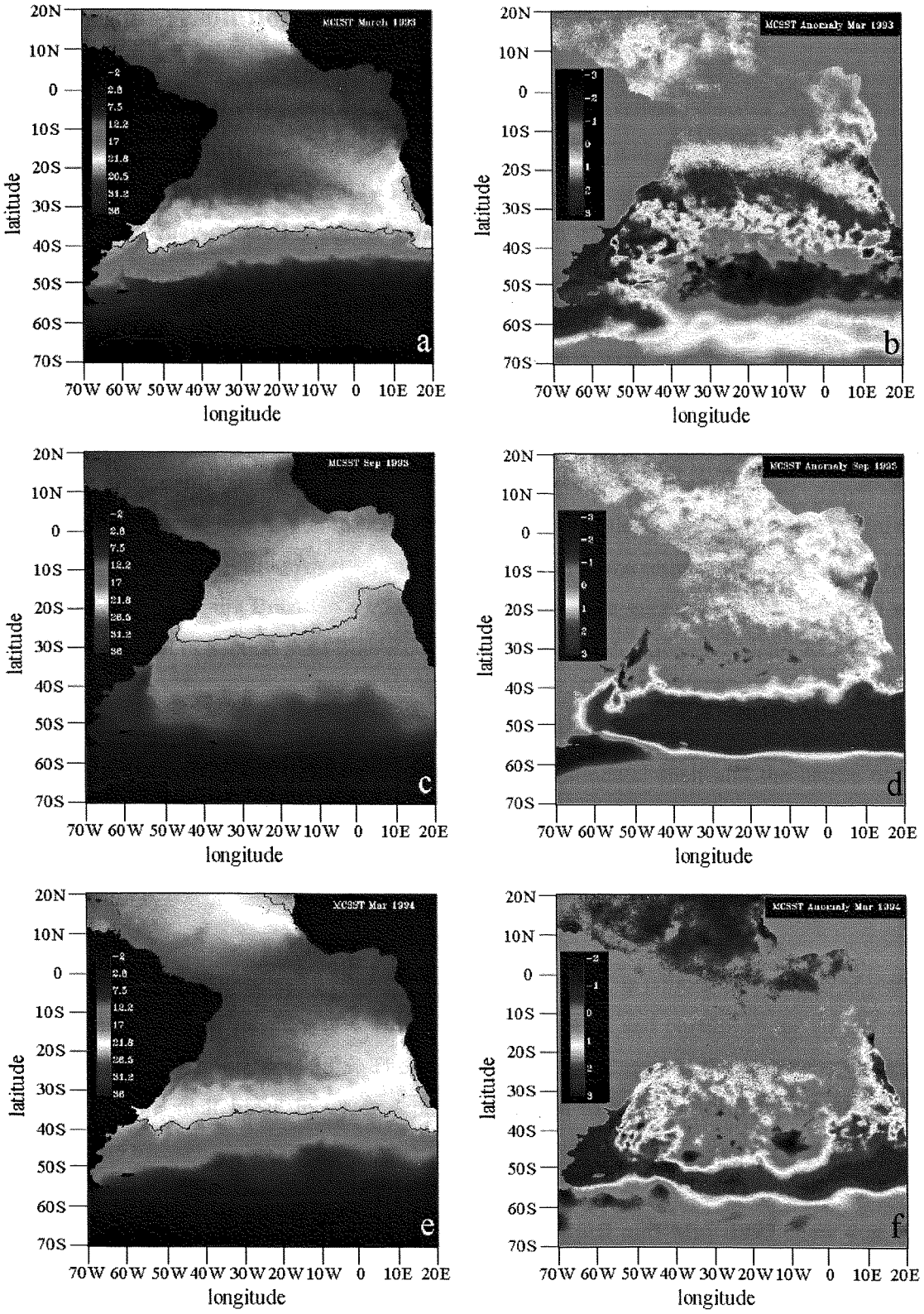

Figure 5.14. (a) MCSST and (b) anomaly images for March 1993; (c) MCSST and (d) anomaly images for September 1993; (e) MCSST and (f) anomaly images for March 1994. The black line (20°C isoline) represents the STF.

5.3.2. High-resolution SST fields

As explained in Section 4.2.1, the COROAS project made available a set of high-resolution AVHRR images which made possible the study of the SST fields in the BMC region for the period between March 1993 and July 1994. The AVHRR images used in this work are listed in Table 4.3. They covered a region between 26.4°S to 42.7°S and 38.8°W to 58.8°W. The temporal changes in the SST fields at the BMC region can be seen in Figure 5.15. For this figure we selected only one image per month to represent each one of the 17 months covered between March 1993 and July 1994. The selected images were usually the most cloud-free ones.

Because of the higher resolution, the AVHRR images could better indicate remarkable mesoscale features, like meanders and eddies. The most noticeable process observed in the sequence of high-resolution AVHRR images, however, was the intrusion of cold waters from the BMC region to the Brazilian continental shelf during the wintertime. This intrusion was already reported in Section 5.3.1 and will given greater consideration in Chapter 7.

Chapters 6 and 7 in this thesis will, respectively, discuss the behaviour of the intrusion of the cold waters from the BMC region in the Brazilian continental shelf and the nature of the eddies formed in both the BMC and in the front between the BC and BCC. In this chapter the discussion will concentrate on the description on a wider scale of the SST fields at the BMC and its vicinity.

Figure 5.15.a shows that on **10 March 1993** the core of MC is noticed as a stream of waters with temperatures lower than 17°C flowing to the northeast and parallel to the Argentinean coast in latitudes lower than 38°S. The signature of the MC core at the surface is observed flowing at the shelf break in water depths of 3000 m to 5000 m (see Figure 1.1 for the bathymetry).

In Figure 5.15.b and 5.16.c, the images representing **April and May 1993** show that cold waters influenced by MC are present at the Argentinean and Uruguayan shelves in latitudes of up to 34°S, at the mouth of the La Plata river. Large meanders are noted at the BMC in April.

On **29 June 1993** (Figure 5.15.d), it is clear that a coastal current is transporting cold waters to the NE direction at the Brazilian shelf in latitudes of up to 28°S, at Santa Marta Cape. Strong gradients can be noticed at the shelf break (for the bathymetry, refer again to Figure

1.1), in a thermal front between BC and BCC. The core of MC, offshore from Argentina at latitudes up to 36°S, is characterised by very low temperatures ranging from 5°C to 7°C.

In the winter images of **19 July and 3 August 1993** (Figure 5.15.e and f), BCC is observed taking the entire Brazilian shelf in the study area. The northern limit of penetration of BCC could not be observed here during these months because the geographical domain of the AVHRR images was restricted to 26.4°S. In the images of **28 September and 7 October 1993** (Figure 5.15.g and h), the BCC domain is diminished by the presence of BC, which resumes occupation of the Brazilian inner shelf from the north.

The period between **8 November 1993 and 27 January 1994** (Figure 5.15.i, j and k) is represented by some of the most cloud-free images available in the overall data set. The BCC is not obvious anymore, for the core of MC is observed retreating from the Uruguayan shelf to the south of 40°S, offshore of Argentina, during this 3 month period. Thanks to the absence of clouds in the region, the meanders formed in the BMC zone are clearly visible from November 1993 to January 1994. In Figure 5.15.i, one of the BMC meanders is forming a warm core eddy (anticyclonic rotation) at a position close to 38°S, 47°W. On 27 January 1994 (Figure 5.15.k), another warm core eddy is noted at the position 39°S, 48.5°W.

February to April 1994 were very cloudy months. The images taken for this period (Figure 5.15.l, m and n), however, still allow us to locate the MC core again heading north. The image taken on 2 March 1994 (Figure 5.15.m), although very cloudy in the southern part, is still able to demonstrate that the MC related waters did not occupy the inner shelf. Moreover, this image also shows the presence of a BC jet interacting with the MC waters in the form of a mushroom-like feature at about 38°S, 53°W.

In **April and May 1994** (Figure 5.15.o and p), the MC reached latitudes of about 36°S, but still did not take the inner shelf as it did in the same months of 1993. On 5 May 1994, another BC dipole feature is present, this time centred at about 35°S, 50°W. The shape of a BMC meander centred at about 38°S, 50°W suggest that dipoles can also develop in the cold part of the convergence.

The image taken on **26 June 1994** (Figure 5.15.p) shows the developing of the BCC and the consequent cooling of the Brazilian shelf. On **11 July 1994** (Figure 5.15.q), the Brazilian continental shelf is again covered by the BCC and the front between this current and BC is once more marked by strong lateral gradients.

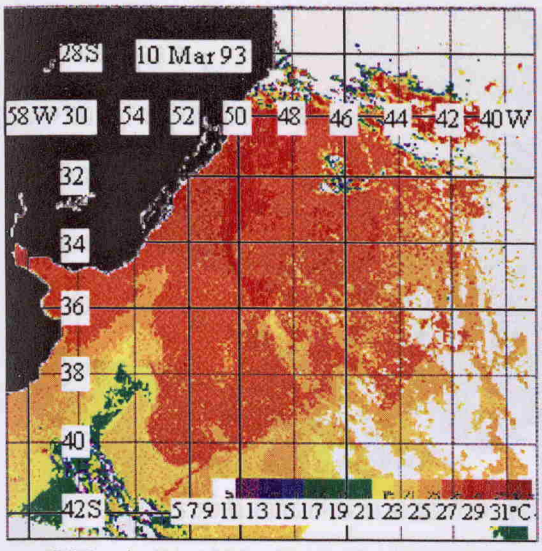

(a) 10 March 1993, NOAA-12, 10:19GMT

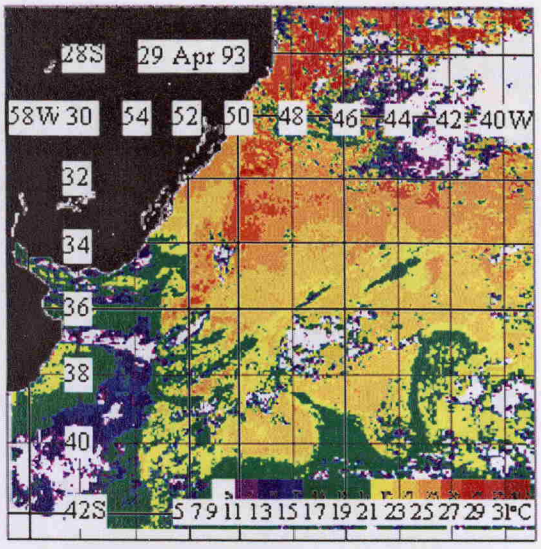

(b) 29 April 1993, NOAA-11, 06:28GMT

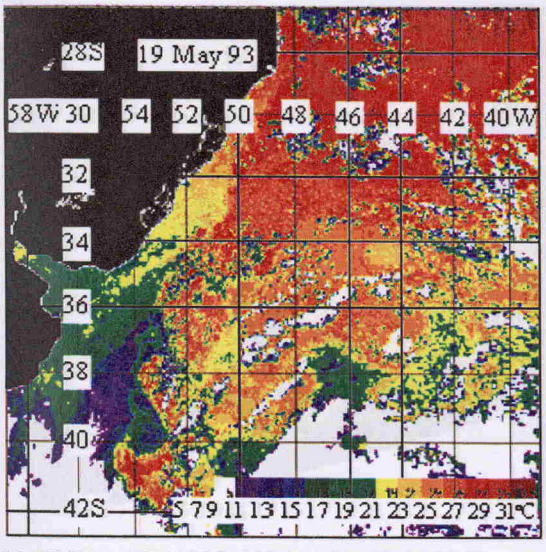

(c) 19 May 1993, NOAA-12, 10:18GMT

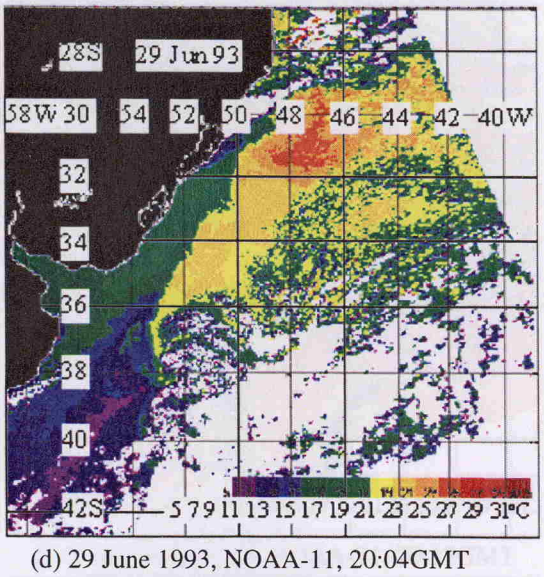

(d) 29 June 1993, NOAA-11, 20:04GMT

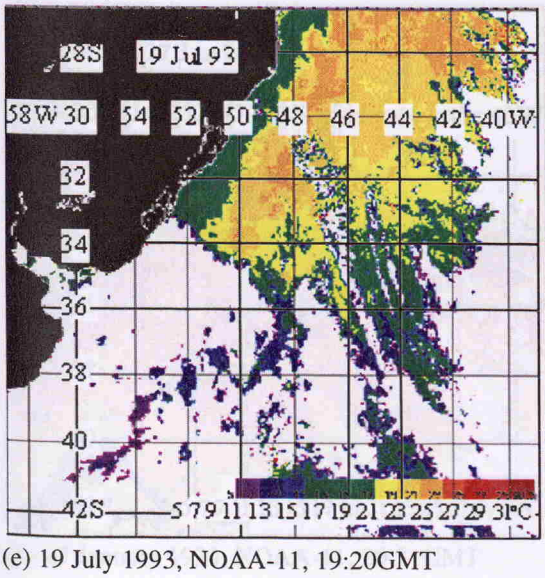

(e) 19 July 1993, NOAA-11, 19:20GMT

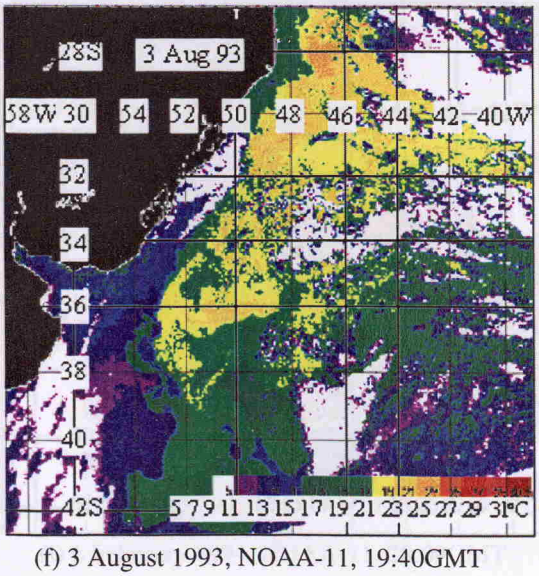

(f) 3 August 1993, NOAA-11, 19:40GMT

Figure 5.15. Temporal sequence of SST in the BMC region and its vicinity.

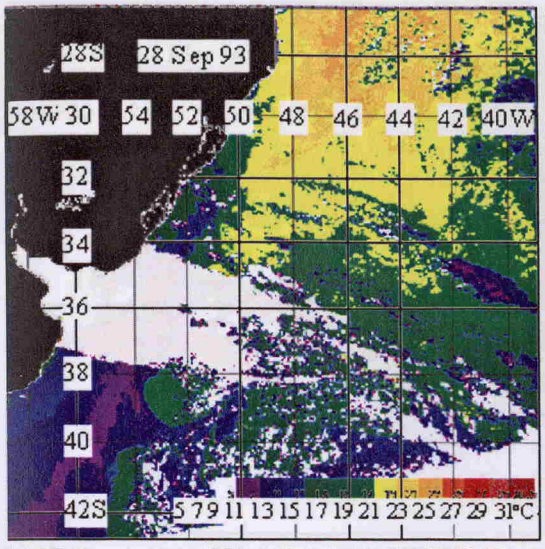

(g) 28 September 1993, NOAA-11, 20:01GMT

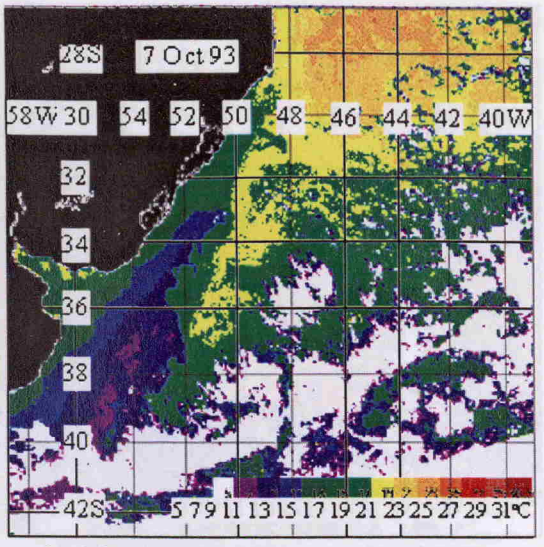

(h) 7 October 1993, NOAA-11, 19:52GMT

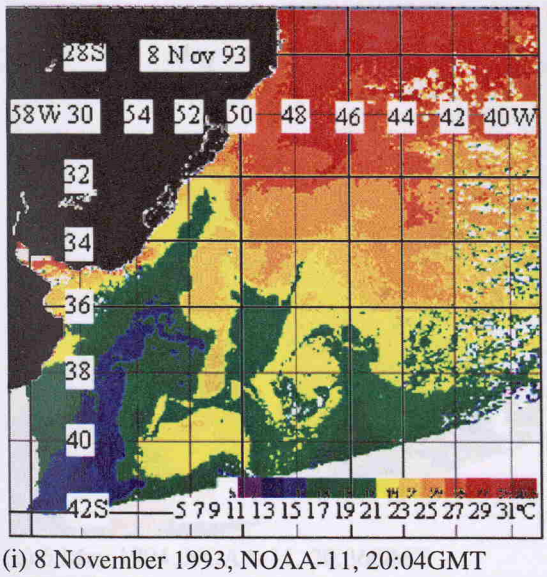

(i) 8 November 1993, NOAA-11, 20:04GMT

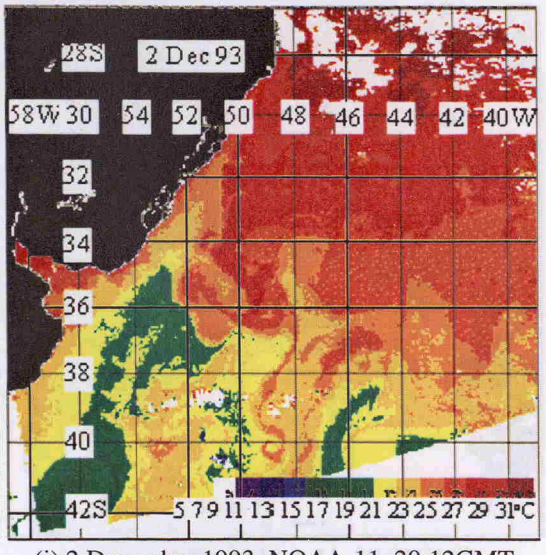

(j) 2 December 1993, NOAA-11, 20:12GMT

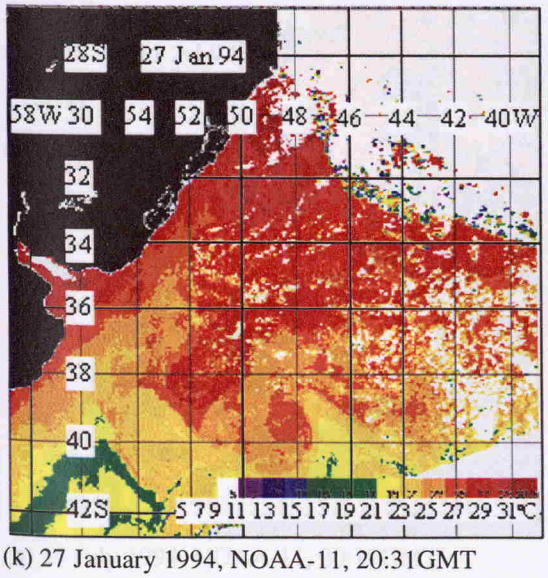

(k) 27 January 1994, NOAA-11, 20:31GMT

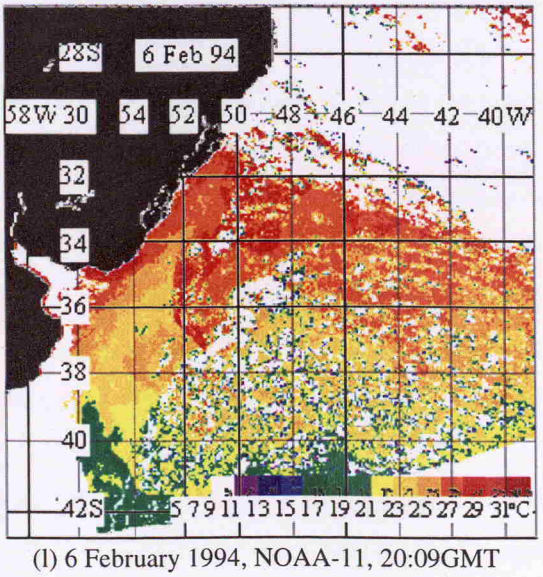

(l) 6 February 1994, NOAA-11, 20:09GMT

Figure 5.15 (cont.). Temporal sequence of SST in the BMC region and its vicinity.

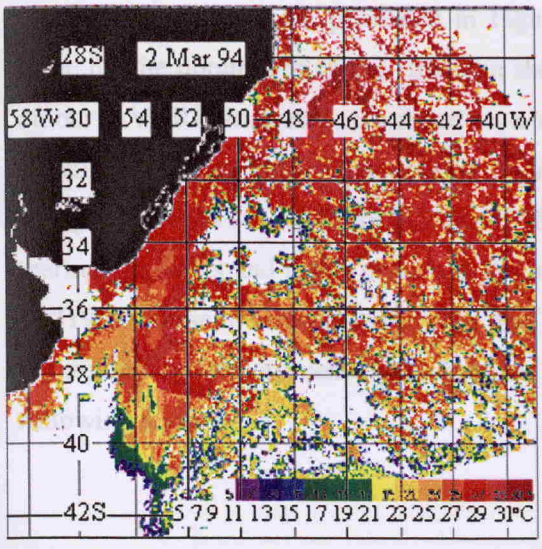

(m) 2 March 1994, NOAA-11, 20:17GMT

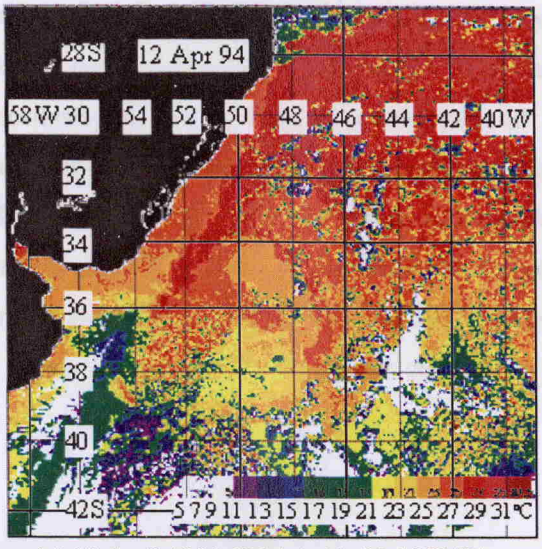

(n) 12 April 1994, NOAA-11, 20:16GMT

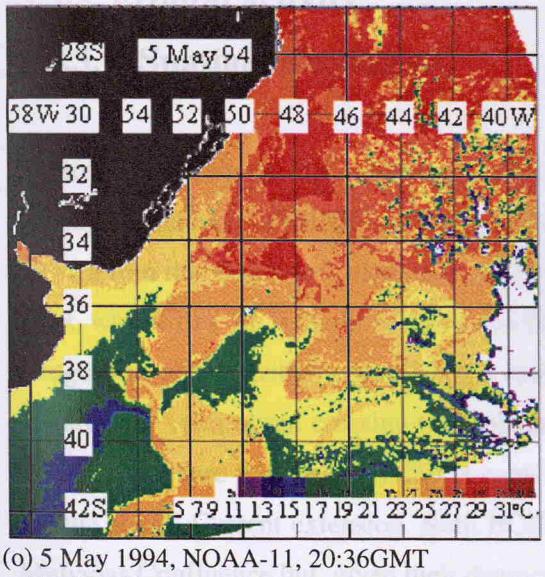

(o) 5 May 1994, NOAA-11, 20:36GMT

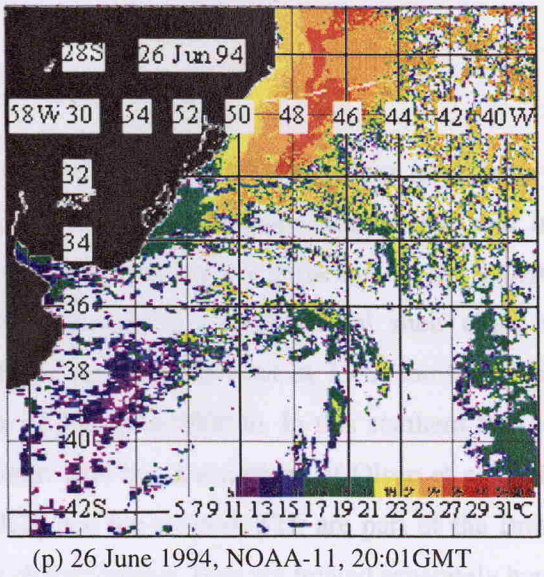

(p) 26 June 1994, NOAA-11, 20:01GMT

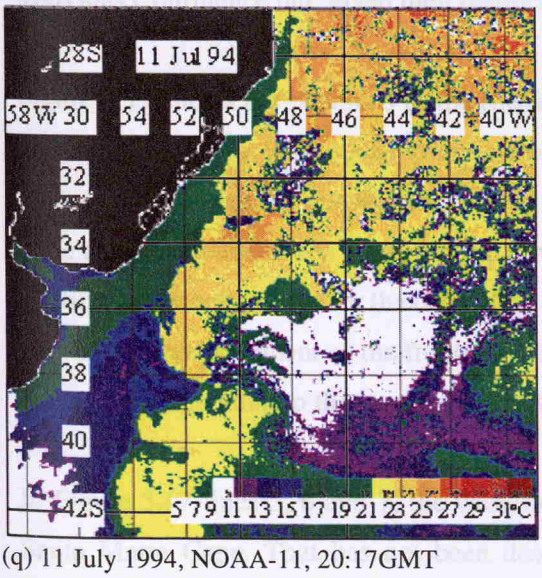

(q) 11 July 1994, NOAA-11, 20:17GMT

Figure 5.15 (cont.). Temporal sequence of SST in the BMC region and its vicinity.

The sequence of images presented in Figure 5.15 demonstrates a very remarkable annual cycle for the domination of the Brazilian shelf by cold (winter) waters. Although the domain of our AVHRR images is restricted to a northern limit of 26.4°S, the domination of the Brazilian shelf by cold waters occurs to latitudes lower than 28°S or 27°S, as previously thought (Campos et al., 1996b; Piccolo, 1998). Remarkable as well is the nature of the surface thermal gradients and fronts present in the images seen in Figure 5.15. According to Olson et al. (1988), these are the characteristics that make the region of the BMC very appropriate to be studied by remote sensing techniques. These characteristics are better studied in the following section.

5.3.3. Frontal activity

5.3.3.1. Spatial distribution

Figure 5.16 shows the 20°C isotherm positions in the BMC and SBCS regions taken from all the high-resolution AVHRR images available for the period between March 1993 and July 1994. From this figure it is clear that the dominant feature noticed in the area is the BC/BCC front, which lies in isobaths of 100 m to 200 m parallel to the continental shelf along the Uruguayan and Brazilian coast. To the south of the La Plata river at 35°S, the front shifts towards the open ocean crossing the isobaths of 200 m to 5000 m. In this southern area, the front (called here the western STF) is consistent with the descriptions of Olson et al. (1988) for the Brazil Current extension. Both BC/BCC and the western STF are part of the Brazil-Malvinas Confluence but, given their distinct characteristics, they are treated separately here.

Figure 5.17 shows the positions of the (meriodinally orientated) BC/BCC and of the (zonally orientated) western Subtropical fronts. The frontal positions were taken from a set of 15 images representing the consecutive months between March 1993 and June 1994. The images were the less clouded ones found for the period in question. In agreement with what has been previously described here for the oscillation of the STF and its western extension, Figure 5.17 shows that the movement of the fronts is related to the season of the year. The BC/BCC front is also seen extending to the north of Santa Marta Cape (~ 28°S).

In Figure 5.17 lines 5, 6 and 7, the western STF is also noticed extending to the latitude of Santa Marta Cape. That has not been described in previous papers using remote sensing techniques to track the frontal systems in the BMC region (e.g. Tseng et al., 1977; Legeckis and Gordon, 1982; Olson et al., 1988; Podestá, 1997). Reasons why these authors have not

previously reported the BMC front to reach latitudes close to 28°S are partly that the area of their study was generally located to the south of Santa Marta Cape and partly the methods involved in their research. Generally, visual interpretation of the major thermal gradients was used to locate the front, whereas here we utilised the 20°C isotherm as a marker of the limit between tropical and subantarctic waters.

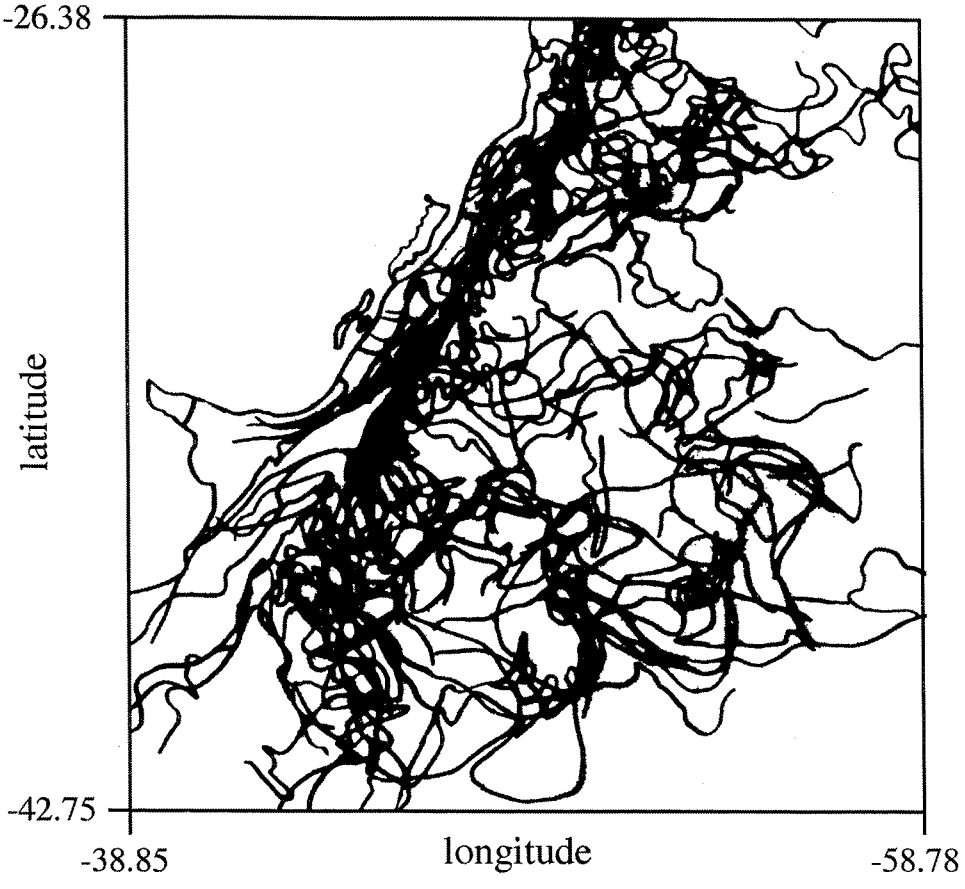

Figure 5.16. BC/BCC and western Subtropical fronts as defined by the 20°C isoline positions taken from all the high-resolution AVHRR images available for the period between March 1993 and July 1994.

The overall trajectories of the COROAS LCDs used in this work (Figure 4.3) also indicate that the buoys followed the general distribution of the fronts in the study area during 1993 and 1994. As the LCDs were launched into the BC in a position close to the shelf break, the buoys drifted to the south and entered either the BCC or the SAC, the MC and BC extensions, respectively. In agreement with the presence of the western STF in latitudes close to 28°S, one of the trajectories seen in Figure 4.3 clearly indicates that SAC (the western STF current) was sampled flowing to the east in this latitude.

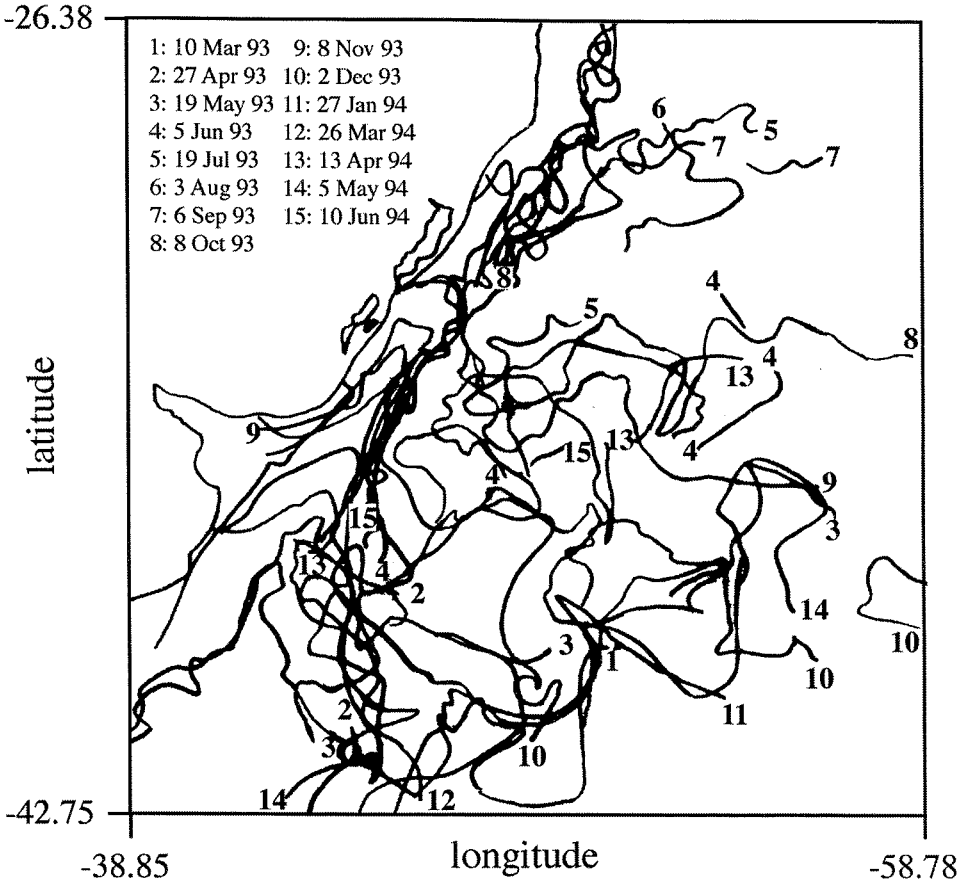

Figure 5.17. BC/BCC and western Subtropical fronts positions as defined by the 20°C isoline taken from a set of 15 images representing the consecutive months between March 1993 and June 1994.

The tendency of surface drifters to concentrate in zones of oceanic fronts was noticed by Hofmann (1985) and Daniaut and Menard (1985) when utilising FGGE (First GARP Global Experiment) buoys in the Southern Ocean. Results from several oceanographic programs like the FGGE, TOGA (Tropical Oceans Global Atmosphere) and WOCE have also indicated that surface buoys can be used to describe frontal motion, meandering and eddies in the sea.

Figure 5.18 shows two examples of AVHRR images with superimposed buoy tracks to ilustrate the tendency of the buoys used in this thesis to follow the major thermal gradients in the BMC region. The image of 11 March 1994 in Figure 5.18 shows a series of buoys drifting south in the BC until the region of the BC reversal, where the current becomes the SAC. A large warm core eddy is seen centred at about 38°S, 51°W. The buoy tracks are associated with the regions of gradients found either between the core of BC and adjacent waters, or in

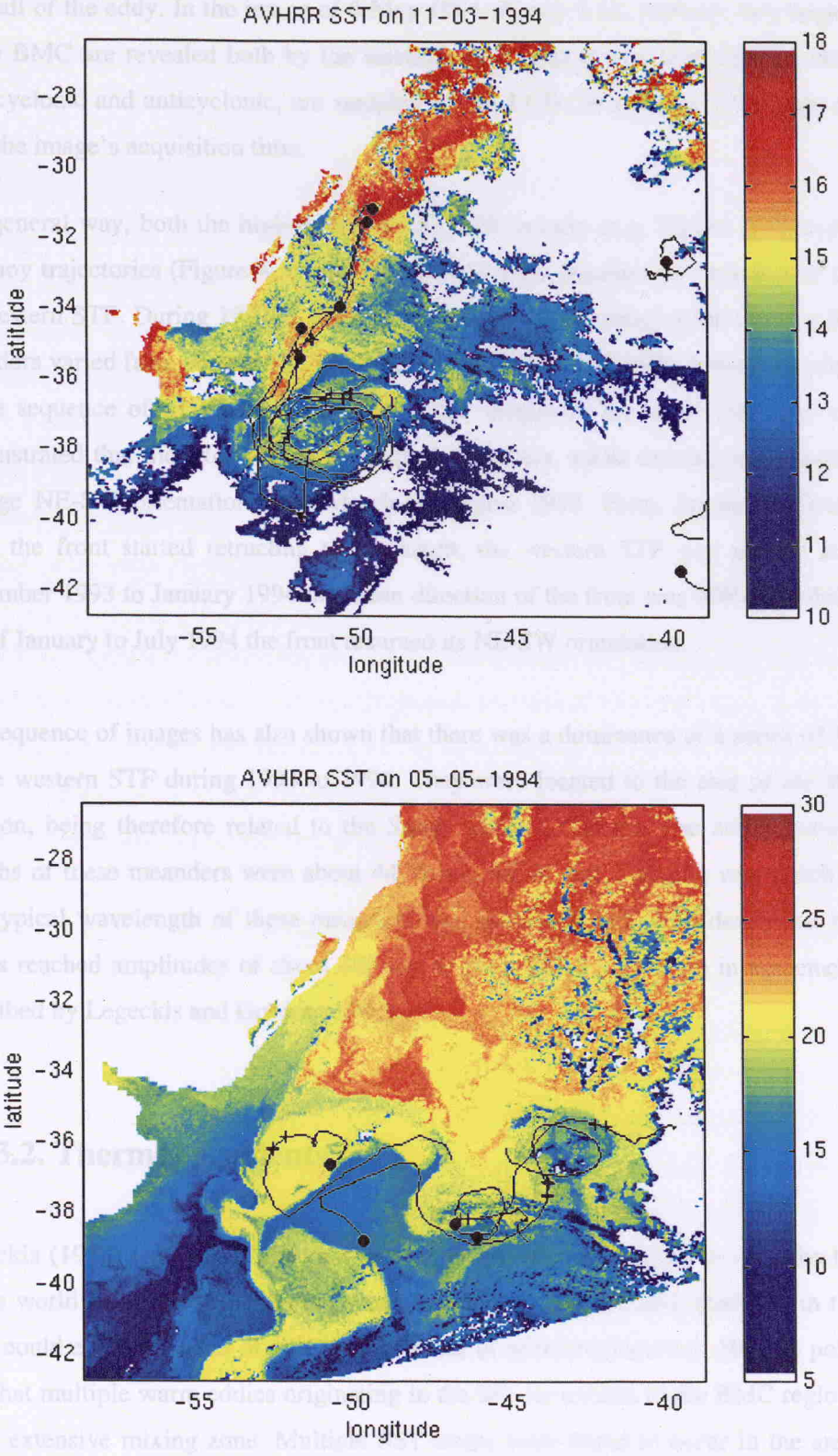

Figure 5.18. AVHRR images of 11 March 1994 (top panel) and 5 May 1994 (bottom panel) superimposed onto buoy tracks in the BMC region. Buoy trajectories are 40 days long, centred at the image's acquisition time. Crosses denote positions of the buoys within ± 12 h of the image's acquisition time. Circles indicate the beginning of the buoys' tracks. Colour bars represent the temperature (degC) in variable ranges to enhance the thermal gradients in the study area.

the wall of the eddy. In the image of 5 May 1994 (Figure 5.18, bottom), two large meanders of the BMC are revealed both by the satellite image and by the buoy tracks. Three eddies, both cyclonic and anticyclonic, are sampled by the LCDs in a period of 20 days before and after the image's acquisition time.

In a general way, both the high-resolution AVHRR images (e.g. Figures 5.16 and 5.18) and the buoy trajectories (Figure 4.3) have demonstrated the presence of meanders of the SAC in the western STF. During 1993 to 1994, the predominant direction of the western STF and its meanders varied from about 45 to 130 degrees (NE-SW to NW-SE). A more detailed analysis of the sequence of 81 high-resolution AVHRR images in the study area (not shown) has demonstrated that the front and its associated meanders, while moving to the north, kept an average NE-SW orientation from March to August 1993. From August to October 1993, when the front started retracting to the south, the western STF was mainly zonal. From November 1993 to January 1994 the mean direction of the front was NW-SE, while from the end of January to July 1994 the front resumed its NE-SW orientation.

The sequence of images has also shown that there was a dominance of a series of 3 meanders in the western STF during 1993 to 1994. They were located to the east of the BC reversal location, being therefore related to the South Atlantic Current. The zonal positions of the troughs of these meanders were about 44°W and 48°W, not changing very much with time. The typical wavelength of these meanders was about 400 km. Well developed meandering waves reached amplitudes of about 400 km as well. These values are in agreement to those described by Legeckis and Gordon (1982).

5.3.3.2. Thermal gradients

Legeckis (1978) was one of the first authors to use satellite images to describe the oceanic fronts worldwide. In his pioneering work, he showed that the SST gradients in the BC/MC front could exceed values of 10°C in a distance of several kilometres. He also points out the fact that multiple warm eddies originating in the BC are present in the BMC region, resulting in an extensive mixing zone. Multiple SST fronts were found to occur in the area as far as 50°S.

Cross-stream gradients in the MC were investigated by Legeckis and Gordon (1982). These authors reported an increase of 1°C in 2 km from the MC core towards its boundaries, and an additional increase of another 1°C in a distance of 10-20 km away from the core towards well-

mixed waters. Extreme temperature changes across the MC/BC front were reported to reach 2.5°C/km in the northern extreme of MC. In the eastern part of the BC reversal zone, Legekis and Gordon (1982) report maximum gradients of 3°C in a distance of 2 km.

The SST gradients found for the MC/BC front in this work are in agreement with those found by Legeckis (1978) and Legeckis and Gordon (1982), although the distances are somewhat broader. As expected, the gradients across well detached eddies towards the neighbouring waters tended to be smaller than those found across the western STF (MC/BC front). The explanation for that lies in the process of coalescence of the individual eddies, where they tend to homogenise their temperatures with those from the surrounding waters over a period of time. From this, knowing the magnitude of the SST gradients at the frontal system that generates a particular eddy, and knowing the across-eddy temperature, the eddy's age could possibly be inferred. At the moment we leave this possibility open for future work.

In order to illustrate the behaviour of the gradients found at the western STF and across eddies formed in this area, Figures 5.20 to 5.25 present a series of transects taken from some of the SST images considered representative of the BMC region. Because in the winter images the MC core contributes to the development of the Brazilian Coastal Current, some of the transects were made across the MC as well.

Figure 5.19 shows the SST image and two transects for **10 March 1993**. In **transect #1**, a gradient of 0.25°C/km (6.1°C in a distance of 24 km) was found between the MC core and BC. The SST gradient of a warm core eddy in relation to surrounding (mixed) waters was of 1.6°C in 24 km (0.06°C/km). Gradients between the MC/BC mixed waters and a MC meander were about 0.1°C/km (2.3°C in 20 km). In Figure 5.19, **transect #2** crosses a cold core eddy at a latitude of about 34°S. This eddy has temperature characteristics of the mixed waters between MC and BC, and is detached from the cold part of the front towards the BC waters. The SST gradient between this eddy and the BC waters (to the west of it) was of 0.02°C/km (2.4°C in 124 km). To the west of this eddy, a cold meander can be noticed in the processes of forming another cold core eddy embedded in the BC.

Transect #1 in Figure 5.20 (**27 April 1993**) was taken across the BC/BCC front and across a MC cold core eddy embedded in the warm part of the MC/BC front. BC/BCC gradient was found to be 0.07°C/km (4.2°C in 56 km), while the gradient between the cold core eddy and surrounding waters was of about 0.1°C/km (8°C in 88 km). Figure 5.20 also shows the coastal waters off La Plata river and the MC core driving the BCC northwards. **Transect #2** in this figure indicated a gradient of 0.11°C/km (4.6°C in 40 km) between coastal waters and the MC

core off the La Plata river, Argentina. The gradient between the MC core and BC in this transect was 0.4°C/km (15.8°C in 40 km).

In the image of **3 August 1993** (Figure 5.21), the BC/BCC front is sampled in 2 transects. In **transect #1**, taken at the Santa Marta Cape (~ 28°S), the frontal gradient was 0.07°C/km (11.9°C in 180 km). This gradient has the same order of magnitude as the one reported by Zavialov et al. (1998) for the BC/BCC front in the area between 30°S and 35°S. To our knowledge, this is the only reference explicit to the gradients of the BC/BCC front available in the literature. It is worth mentioning, however, that the BC/BCC gradients tend to be higher to the south owing to the proximity to the MC core. **Transect #2** taken at about 35°S, for instance, indicated a gradient of 0.32°C/km (6.4°C in 20 km) for the BC/BCC front.

Transect #1 in the image of **8 November 1993** (Figure 5.22) illustrate the gradients between the MC core and the typical MC eddies in relation to BC. In this case, the MC eddy was about 4°C warmer than the MC core but, because of the across transect distances, the gradient between the MC core and BC was smaller than between the MC eddy and BC. The gradients were, respectively, 0.06°C/km (8.7°C in 156 km) and 0.2°C/km (5.1°C in 25 km).

Figure 5.23 shows the image of **27 January 1994** and a particular transect taken along the MC/BC frontal axis. The **transect #1** samples the MC core and two warm core eddies located to the west of two MC meanders at about 40°S. The gradient between the MC core and the warm core eddy to the east of it was about 0.1°C/km (6.7°C in 60 km). Although the second warm core eddy was about 3°C warmer than the first one, the gradient between it and the MC meander to its east was also close to 0.1°C/km.

Another estimate of the gradients across the MC/BC frontal axis is illustrated in **transect #1** of Figure 5.24 (**5 May 1994**). There, like in January 1994, the gradient between the MC core and BC was 0.1°C/km (11.6°C in 116 km). **Transect #2**, in the BC/BCC front, indicated that the SST gradient between these currents was about 0.03°C/km (3°C in 88 km).

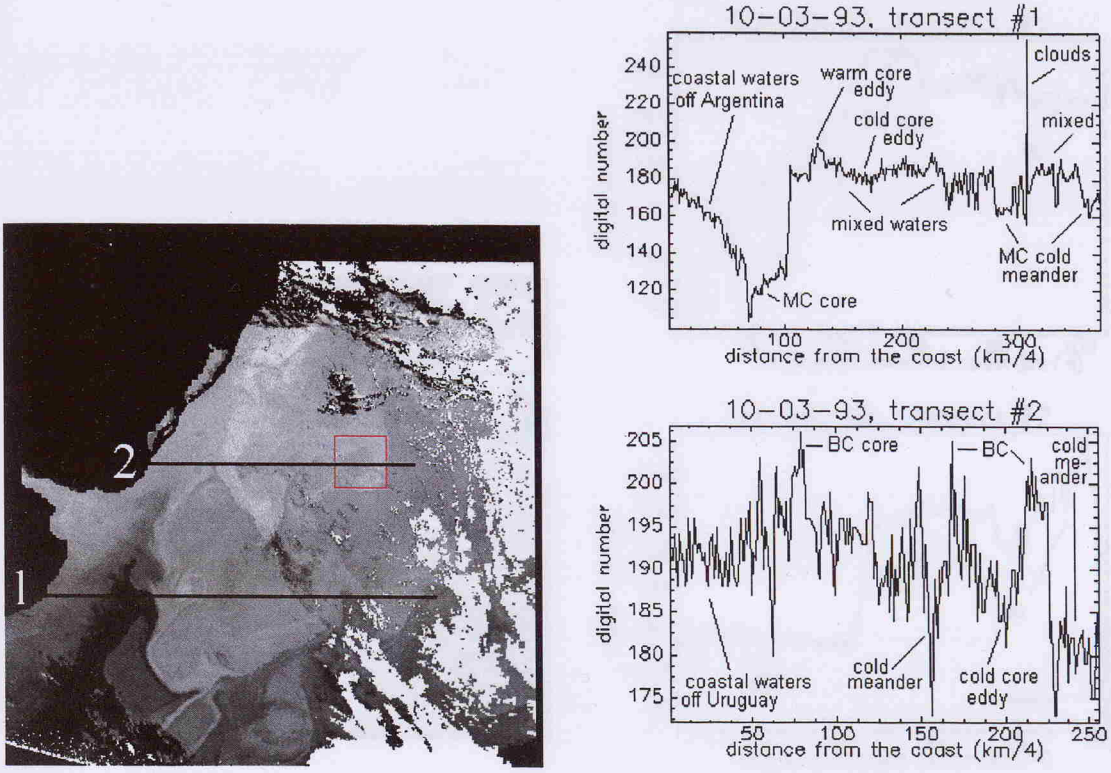

Figure 5.19. AVHRR SST image of 10 March 1993 and the SST profile in 2 particular transects across the image [SST=(Digital Number × 25.5)/255 + 5]. The square seen in the image locates the cold core eddy present in transect #2.

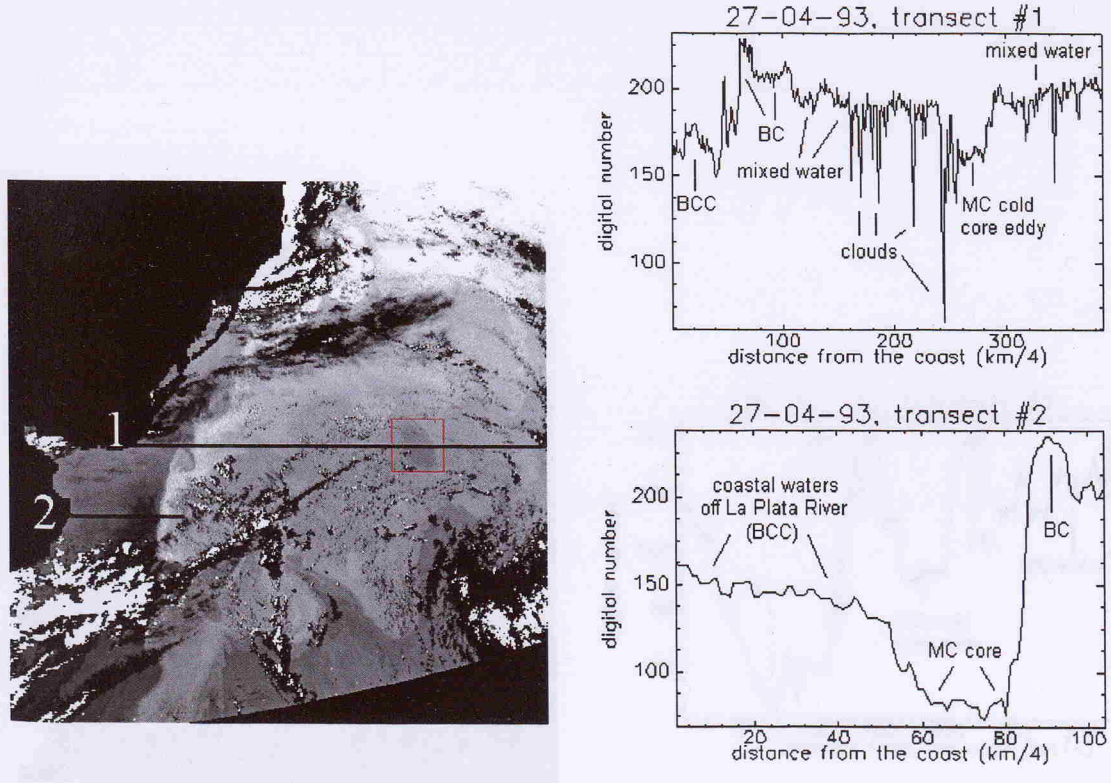

Figure 5.20. AVHRR SST image of 27 April 1993 and the SST profile in 2 particular transects across the image [SST=(Digital Number × 25.5)/255 + 5]. The square seen in the image locates the MC cold core eddy present in transect #1.

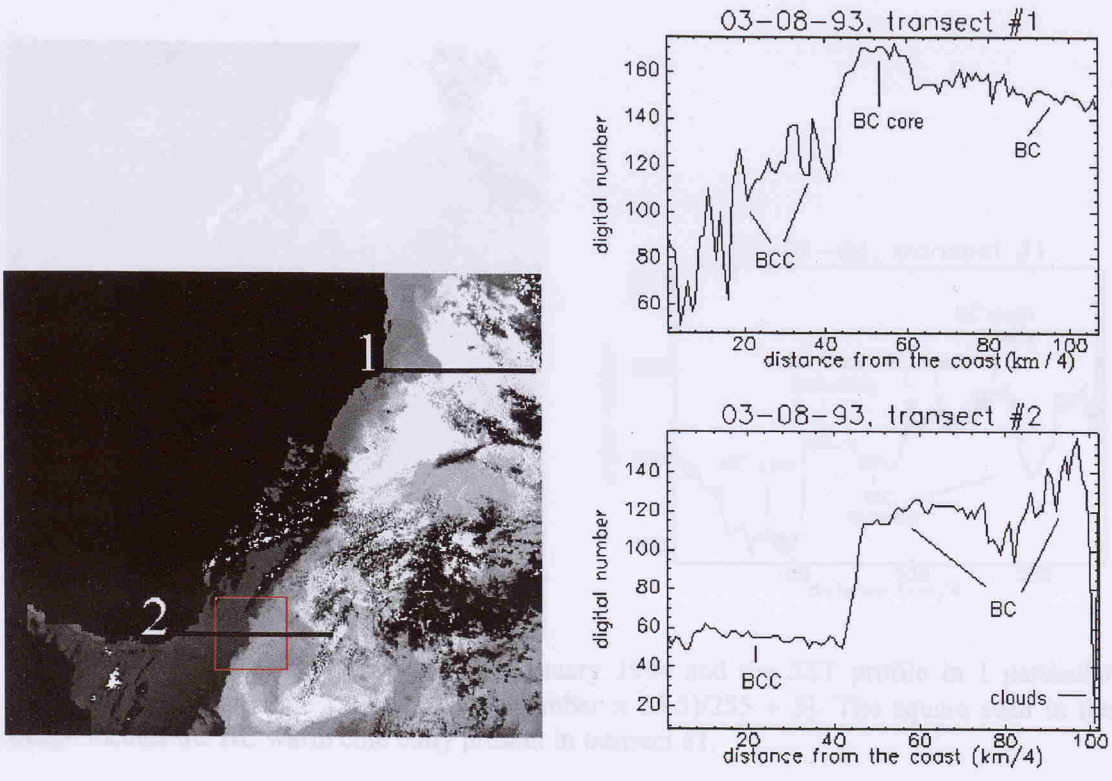

Figure 5.21. AVHRR SST image of 3 August 1993 and the SST profile in 2 particular transects across the image [SST=(Digital Number × 25.5)/255 + 5]. The square seen in the image locates the BC/BCC front present in transect #2.

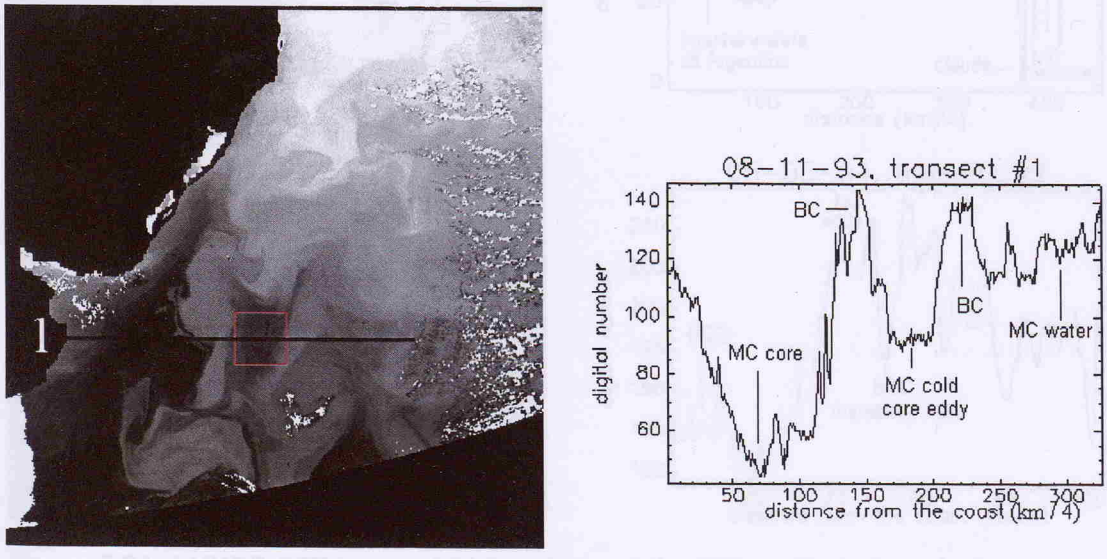

Figure 5.22. AVHRR SST image of 8 November 1993 and the SST profile in 1 particular transect across the image [SST=(Digital Number × 25.5)/255 + 5]. The square seen in the image locates the MC cold core eddy present in transect #1.

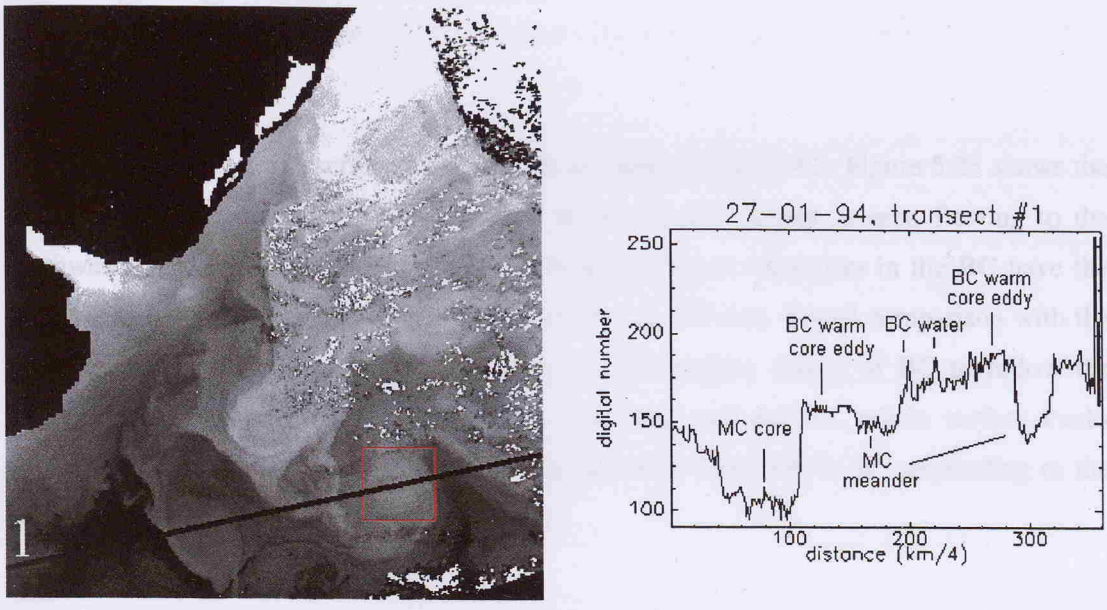

Figure 5.23. AVHRR SST image of 27 January 1994 and the SST profile in 1 particular transect across the image [SST=(Digital Number × 25.5)/255 + 5]. The square seen in the image locates the BC warm core eddy present in transect #1.

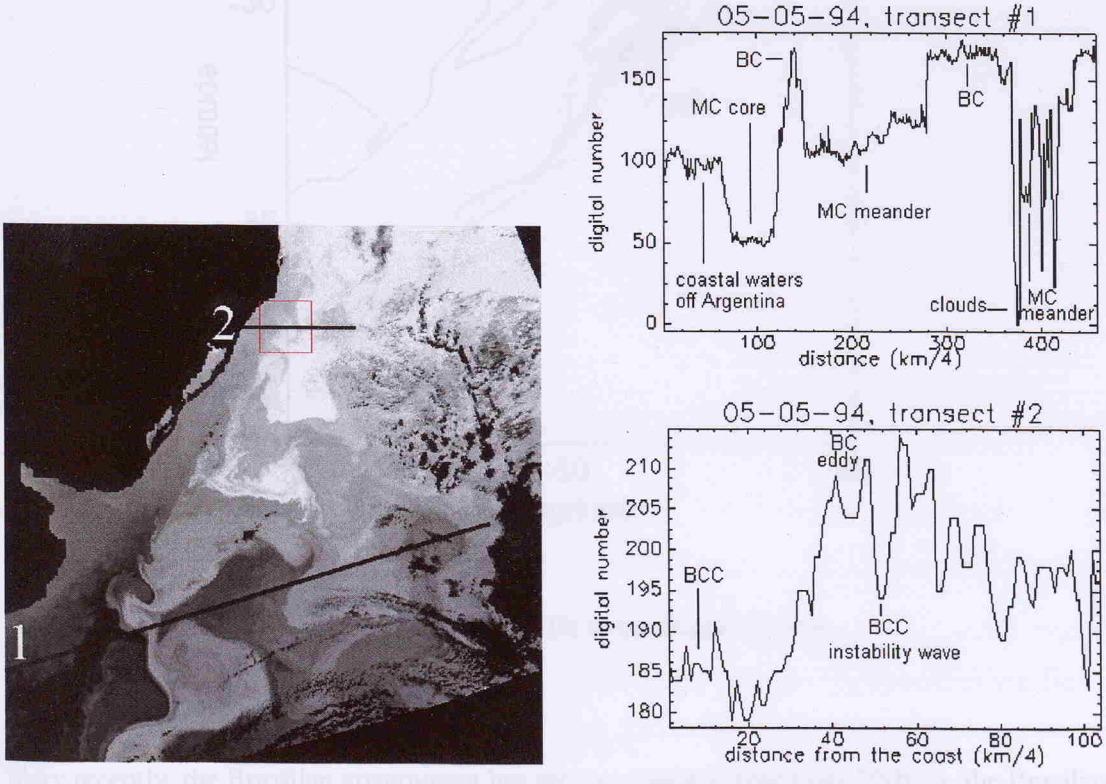

Figure 5.24. AVHRR SST image of 5 May 1994 and the SST profile in 2 particular transects across the image [SST=(Digital Number × 25.5)/255 + 5]. The square seen in the image locates an instability wave at the BC/BCC front present in transect #2.

5.4. Lagrangian measurements

5.4.1. Trajectories

The overall trajectories described by the LCDs are seen in Figure 4.3. Figure 5.25 shows the overall trajectories only for the BC. In this figure, Brazil Current is seen flowing to the southwest, meandering parallel to the South American coast. Meanders in the BC have the same scale as those described for the western STF, e.g. 400 km. Visual comparison with the bathymetry (Figure 1.1) suggests the tendency of the surface waters of BC to follow the isobaths. In the vicinity of 31°S this tendency is very well defined, where surface tracks showed a major change in the direction of the BC flow from SW to W, responding to the orientation of the isobaths of 200 m to 3000 m.

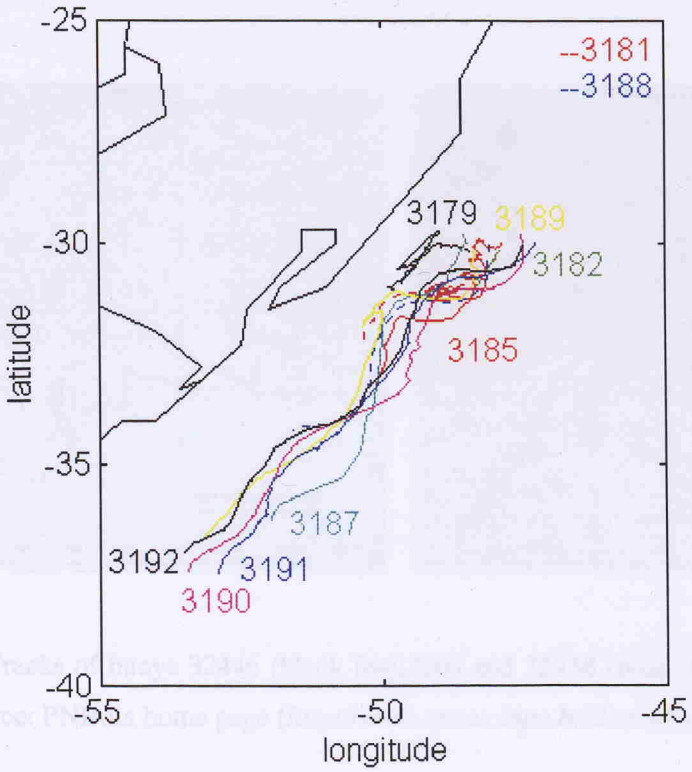

Figure 5.25. Trajectories described by the LCDs in the Brazil Current.

Very recently, the Brazilian government has set up a national plan (alas PNBoia, the Brazilian National Buoy Programme) for the observation of surface currents using WOCE standard Low Cost Drifters. Following the PNBoia, the INPE and the Brazilian petroleum company

Petrobrás had also set up another programme for the Lagrangian observation of surface currents in the areas of interest for the petroleum industry in Brazil. The programme is known as the SATBoia programme. Although the data set is not freely available yet, the updated trajectories of the drifters already deployed by the PNBoia and SATBoia are available in the world wide web at *http://www.atsme.inpe.br/dsr/satboia*. Figure 5.26 shows 2 maps where PNBoia buoys number 32446 (launched on 14 April 1998) and 32458 (launched on 2 August 1998) developed trajectories which followed the bathymetry at the Brazilian shelf break.

As the BC trajectories show in this work, the PNBoia drifters have also followed the major change in bathymetry at about 31°S, just south of Santa Marta Cape. The comparison of the PNBoia tracks with the ones presented by the LCDs used in this work also suggest that the interaction of the BC with bathymetry at latitudes close to 31°S is probably independent of season and, therefore, of possible changes in the BC transport.

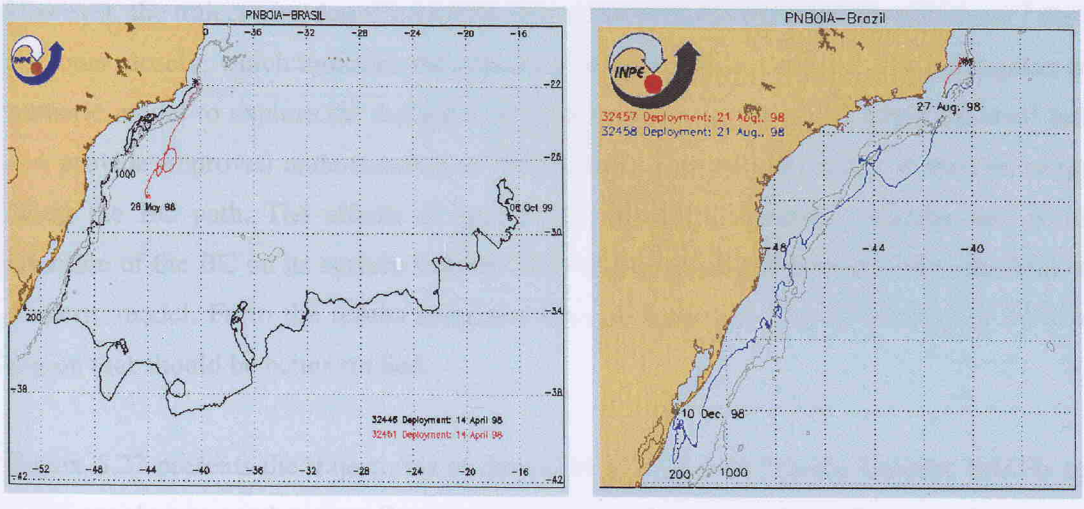

Figure 5.26. Tracks of buoys 32446 (black line, left) and 32458 (blue line, right) in the BC and SAC. Source: PNBoia home page (*http://www.atsme.inpe.br/dsr/satboia*).

Studying the BC path from 20°S to 33°S in 1985, Garfield (1990) verified that the regions close to Cabo Frio and south of Santa Marta Cape were the regions containing the higher variabilities of this current. To the south of Santa Marta Cape, Garfield (1990) suggests that the change in the bathymetry would be enough to increase the variability in the front between BC and coastal waters. Making an analogy with the interaction of the Gulf Stream with the

Charleston bump, the author suggests that the interaction of boundary currents with bathymetry is critical to their stability.

The adjustment of a stable flow drifting across the *f*-plane into a major change in bathymetry is explained by the conservation of potential vorticity. Owing to their design, the surface floats used in this work and in the PNBoia program follow the waters at the average depth of 15 m. Changes in the relative vorticity of a flow are easier to be understood if the flow is barotropic. However, for the eastern side of the BC/BCC front (along which our surface LCDs drifted to the south) the isopicnal gradients are large. Below the BC, hydrographical data have demonstrated (e.g. Castro and Miranda, 1998) that the vertical gradients are also considerable.

Preliminary investigations with the data of the LCDs in the Brazil Current at 31°S (Souza and Cabral, 1996) have indicated that the buoys used in this work did not significantly change their instantaneous velocities when changing direction because of the bathymetric effect. However, the trajectories described by the buoys followed the *f*/D (Coriolis parameter / depth) contours closely, which indicates the conservation of potential vorticity. The conception of a numeric model to explore the surface Lagrangian behaviour of the BC along the shelf break can provide improved understanding of the physical processes occurring at specific regions along the BC path. The effects of specific conditions of transport, velocity and vertical structure of the BC on its surface velocity field could be better understood with the help of a numeric model. From the results presented here, it is evident that the vicinity of 31°S is a region that should be better studied.

Figure 5.27 presents the trajectories of the LCDs in the South Atlantic Current. SAC is seen as a meandering zonal current flowing eastward in a band of latitudes that varied on average from 29°S to 40°S. The size of meanders and eddies in this current varied from about 200 km to 500 km. Eddies were much more present in the SAC than in the BC, being either cyclonic or anticyclonic. Remarkable eddy activity occurred at 37.5°S, 52°W.

Figueroa and Olson (1989) analysed the eddy diffusivity due to mesoscale motions in the South Atlantic Ocean based upon FGGE and SOS (Southern Ocean Studies) drifter data sets. Although still having a poor coverage of the boundary currents, the buoy measurements improved the spatial coverage of velocity measurements in the South Atlantic, which was considered to be very poorly observed. The buoy observations were almost entirely made in the South Atlantic Current. SOS buoys were drogued at about 10 m, while FGGE buoys, when drogued, had several distinct drogue designs and depths. Trajectory maps shown by

Figueroa and Olson (1989) were among the first Lagrangian descriptions of the SAC, and indicate its general zonal orientation.

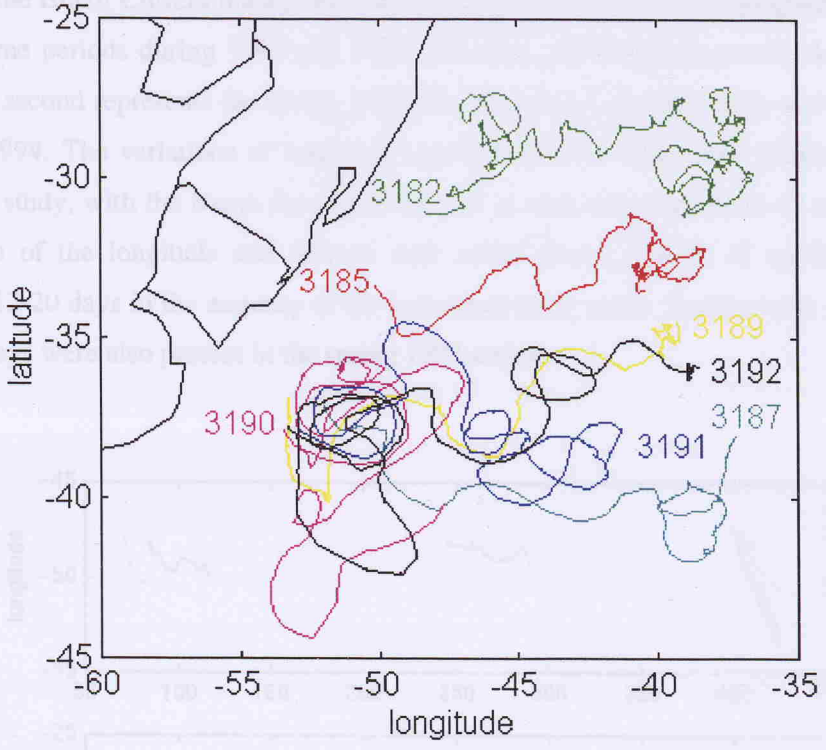

Figure 5.27. Trajectories described by the LCDs in the South Atlantic Current.

Zambianchi and Griffa (1994) applied a stochastic model for particle motion to drifter data in the South Atlantic Current. The authors used data from four SOS drifters deployed in 1984, reporting that their buoys lay in two frontal regions between Brazil and Malvinas currents in the open ocean. The first front, located at about 32°S, was related to the Brazil Current waters, while the second front (at 40°S) corresponded, according to the authors, to the northern edge of MC. The SAC, as derived from the Zambianchi and Griffa (1994) descriptions, had a northeastern direction and was characterised by strong meanders of about 400 km in wavelength and 200 km in amplitude. The meanders sizes described by Zambianchi and Griffa (1994) are compatible with those measured by the LCDs used in this work, being also in agreement with the description made by Legekis and Gordon (1982).

5.4.2. Buoy time series

Figure 5.28 shows the time series of longitude, latitude and temperature measured by the buoys in the Brazil Current during the time of this study. The BC was sampled by the buoys in four time periods during 1993 and 1994. The first period represents the Austral autumn 1993, the second represents the spring 1993, the third is the summer 1993, and the last is the autumn 1994. The variations of longitude and latitude with time were similar all over the period of study, with the buoys flowing from east to west and from north to south. A visual inspection of the longitude and latitude time series shows periods of oscillation ranging between 12-20 days in the majority of the individual buoy series. Small period oscillations of about 2 days were also present in the spring 1993 series.

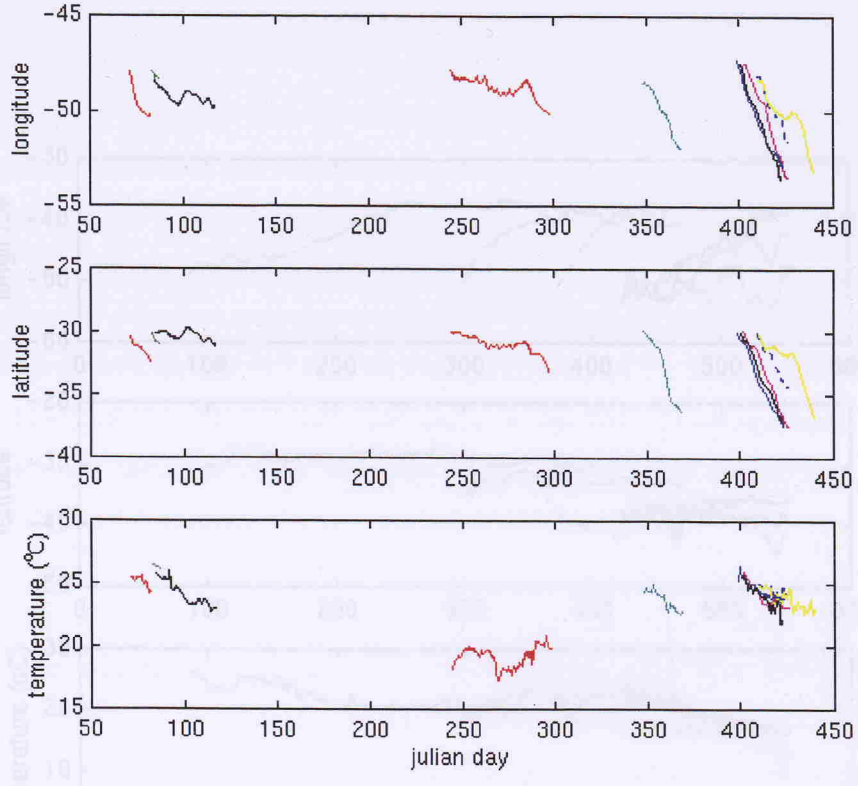

Figure 5.28. Time series of longitude, latitude and temperature for the Brazil Current (colours are in accordance with Figure 5.25).

The BC temperature time series suggests that temperatures of about 26°C occur in the vicinity of 30°S, 48°W during the autumn and summer. These temperatures dropped to about 23°C in a range of latitudes from 31°S to 37°S and longitudes from 50°W to 54°W. During the spring temperatures ranged from about 17°C to 21°C. From circa Julian day 270 to Julian day 300

the temperatures increased approximately from 17°C to 20°C at a rate of about 0.1°C/day. Since the buoy launched in the BC during the spring 1993 drifted southward to a region where cooler waters are expected to occur, the warming of BC waters to the south is likely to be happening due to the seasonal heating.

Figure 5.29 shows the time series for the South Atlantic Current. This current is seen as a zonal current, as only the longitude time series presents a considerable trend with respect to time. Regardless of the season, the latitude time series are seen oscillating parallel to the time axis, about an average position. This average however varies from one buoy to another depending on the latitude of the buoy penetration into the SAC after exiting the BC. It can also be said that regardless of the latitude of maximum penetration of the BC (which varies seasonally), the SAC flows from this point zonally in a system of currents parallel with one another.

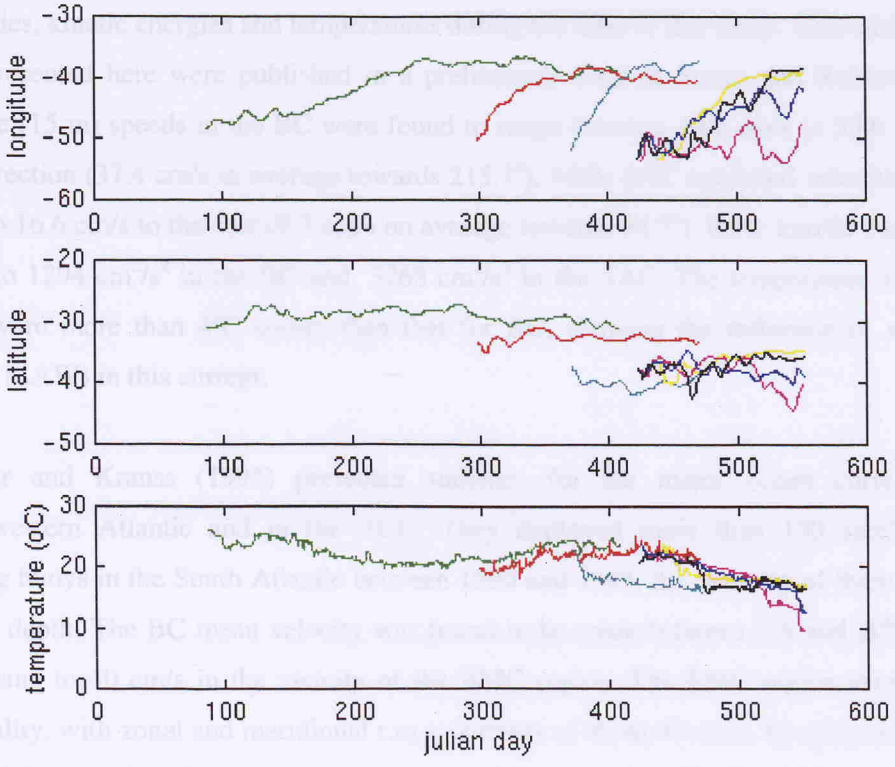

Figure 5.29. Time series of longitude, latitude and temperature for the South Atlantic Current (colours are in accordance with Figure 5.27).

Temperature measurements made by buoy 3182 in the SAC also show a seasonal oscillation. The semiannual cycle is obvious in the longer temperature time series of buoy 3182, where temperature decreases from about 25°C on Julian day 100 to 20°C on Julian day 280. This represents a rate of cooling of about 0.03°C/day from late autumn to early spring. Oscillatory peaks noticed in the longitude and latitudinal time series are related to eddy activity in the current. In general, there are no peaks or troughs in the temperature time series associated with the eddies. That is because the buoys were generally sampling the external walls of the eddies, which are formed from instabilities of the mean flow in with the buoys were previously embedded. In this case, the temperature measurements of the buoys at the wall of an eddy remained the same as the previous measurements made by the buoys along the front that generates the eddy.

5.4.3. Velocity, kinetic energy and temperature statistics

Table 5.3 shows the buoy-derived statistics obtained for BC and SAC in terms of its velocities, kinetic energies and temperatures during the time of this study. This table and other data presented here were published in a preliminary form in Souza and Robinson (1998). Surface (15 m) speeds in the BC were found to range between 12.2 cm/s to 53.6 cm/s in the SW direction (37.4 cm/s in average towards 215.7°), while SAC exhibited velocities from 4.2 cm/s to 16.6 cm/s to the east (9.7 cm/s on average towards 94.7°). Eddy kinetic energies were equal to 1294 cm^2/s^2 in the BC and 3268 cm^2/s^2 in the SAC. The temperature averages for SAC were more than 4°C cooler than that for BC, showing the influence of subantarctic waters (SAW) in this current.

Schafer and Krauss (1995) presented statistics for the major ocean currents in the Southwestern Atlantic and in the ACC. They deployed more than 130 satellite-tracked drifting buoys in the South Atlantic between 1990 and 1993, the majority of them drogued at 100 m depth. The BC mean velocity was found to be weak between 7°S and 20°S (4 cm/s), increasing to 40 cm/s in the vicinity of the BMC region. The BMC region presented large variability, with zonal and meridional r.m.s. currents of about 40 cm/s. In agreement with this work, SAC was found to be almost zonal, presenting a mean velocity of 12 cm/s. BC shows typical Eddy Kinetic Energy (EKE) varying between 200-400 cm^2/s^2. EKE values in the BMC region reach 1600 cm^2/s^2, decreasing again in the SAC further east.

Piola et al. (1987), Stevenson and Souza (1994) and Stevenson (1996) also presented EKE values for the BC derived from drifting buoy data. While Piola et al. (1987) worked with

FGGE buoys, the last authors used the COROAS drifters. As in this work, EKE dominated the BC flow in both cases, but Stevenson (1996) found these values to range between 1332 cm^2/s^2 and 4207 cm^2/s^2, while Piola et al. (1987) found 500 cm^2/s^2.

Table 5.3. BC and SAC velocity, kinetic energy and temperature statistics
(a) Brazil Current

buoy	*velocity*		*kinetic energy*				*temperature*	
	speed (cm/s)	*direction (degrees)*	*MKE (cm^2/s^2)*	*EKE (cm^2/s^2)*	*TKE (cm^2/s^2)*	*%EKE/ TKE*	*mean (°C)*	*std.dev (°C)*
3179	12.2	252.0	75	1080	1155	93.5	24.17	0.96
3181	53.6	212.1	1436	3576	5012	71.3	24.99	0.73
3182	34.0	181.7	577	371	948	39.1	26.27	0.13
3185	12.8	237.1	82	901	983	91.6	19.17	0.82
3187	47.4	214.4	1121	899	2021	44.5	23.52	0.76
3188	36.7	212.1	674	705	1379	51.1	24.52	0.43
3189	31.6	205.3	499	1009	1508	66.9	23.85	0.72
3190	49.2	212.7	1209	1530	2739	55.8	23.97	0.86
3191	46.3	214.4	1072	2132	3204	66.5	24.56	0.66
3192	50.3	215.3	1265	743	2008	37.0	24.00	0.99
mean	37.4	215.7	801	1294	2097	61.7	23.90	0.71
std.dev.	15.0	18.5	490	937	1266	20.0	1.83	0.26

(b) South Atlantic Current

buoy	*velocity*		*kinetic energy*				*temperature*	
	speed (cm/s)	*direction (degrees)*	*MKE (cm^2/s^2)*	*EKE (cm^2/s^2)*	*TKE (cm^2/s^2)*	*%EKE/ TKE*	*mean (°C)*	*std.dev. (°C)*
3182	4.2	123.0	9	1769	1778	99.5	22.56	1.61
3185	6.7	112.6	23	2509	2532	99.1	21.69	1.21
3187	16.6	74.6	138	3413	3551	96.1	17.66	1.32
3189	16.3	69.6	132	5769	5901	97.8	18.61	1.60
3190	4.2	111.2	9	2312	2321	99.6	19.08	3.19
3191	7.1	88.1	25	3876	3901	99.3	18.75	2.51
3192	12.5	83.5	78	3225	3304	97.6	18.61	2.13
mean	9.7	94.7	59	3268	3327	98.4	19.57	1.94
std.dev.	5.4	20.8	57	1315	1357	1.3	1.82	0.71

The Mean Kinetic Energy (MKE) in the BC was estimated to vary between 114-171 cm^2/s^2 by Stevenson and Souza (1994), values in good agreement with 200 cm^2/s^2 found earlier by Piola et al. (1987), but about 4 times lower than the average BC MKE presented here. Differences between BC speeds measured by all these authors led to differences in MKE estimates. The data used here represent the southernmost part of the BC flow, which is believed to have its transport increased southwards (Garfield, 1990). Following the results obtained by Schafer and Krauss (1995), BC velocity can also increase southwards, which explains why MKE values estimated here are higher than previous estimates.

5.4.4. BC and SAC energy spectra

Figures 5.30 to 5.39 present the FFT spectra of the LCDs' temperature and instantaneous (zonal and meridional) velocities time series for the BC. The FFT spectra of the LCD's time series for the SAC are seen in Figures 5.40 to 5.46. The overall peaks found in the time series of all drifters are presented, for simplicity, in Table 5.4. In the BC, peaks significant to the 95 % confidence interval were found to dominate the various spectra at 25.8 days (when the series were long enough), 12.8 days, 8.6 days, and around 6.5 days and 3.5 days. Other shorter period peaks were also found. Peaks at periods longer than 25.8 days were found in the SAC time series, as the series were longer than the BC ones. In the SAC, for instance, the time series generally presented dominant peaks of energy at 103.1 days and in the range from 22 to 30 days. Other peaks at around 41 days, 34 days, 11-13 days and shorter were abundant. Because buoy 3182 was the longest series, is was possible to find a semiannual period at 204.1 days (6.7 months), with a possible second harmonic centred at about 103 days.

The relative importance of the semiannual peak for the South Atlantic has been discussed early on in Section 5.2.2 of this thesis. According to Vivier and Provost (1999a), the domination of the MC transport estimates by a semiannual cycle is compatible to the idea of a remote forcing of this current. The finding of a semiannual peak in the SAC indicates that this current, at the BMC region, is also responding to the large scale driven mechanisms occurring elsewhere in the South Atlantic. In addition, the period found here for the semiannual peak (6.7 months) is also very similar to the one obtained before in this thesis when analysing the seasonally averaged MCSST anomalies PC3 (Table 5.1).

Garzoli and Simionato (1990) utilised the same set of inverted echo sounders as Garzoli and Garraffo (1989) in order to account for the high-frequency oscillations present at the BMC front. These echo sounders were in a group of three, being deployed at about 37.5°S, 52.5°W. Mainly due to the length of the echo sounders records, the oscillations were investigated in the periods ranging from 55 days to 2 days. The physical parameters investigated were the dynamic height, the distance of the instruments to the front and the wind stress at the surface, which was inferred from the water column ambient noise.

For a band of period centred at 37.4 days, Garzoli and Simionato (1990) found a westward propagating wave with amplitudes increasing linearly to the east (150 km to 258 km) and phase speeds of 4.6 cm/s to 8 cm/s. The wave was proved neither to be a baroclinic Rossby wave nor forced by the wind, but related to the movement of the BC/MC front. At the period

of 29.1 days, another wave similar to that previously described was also found by Garzoli and Simionato (1990). This wave had amplitudes of 250 km but propagated eastward, having the same characteristics as the topographic Rossby waves present in the Gulf Stream. The forcing mechanism driving this oscillation is supposed to be the meandering of the Brazil Current at the convergence zone.

Table 5.4. Period of the major energy peaks for the buoys' temperature and instantaneous velocity time series in the BC and SAC (dominant periods underlined)

(a) Brazil Current

buoy	*temperature (days)*	*zonal instantaneous velocity (days)*	*meridional instantaneous velocity (days)*
3179	25.8	17.1; 5.7; 2.7; 1.8	12.8; 6.5; 2.7; 2.1
3181	6.4	6.4	6.4
3182	1.6	1.6	1.6
3185	25.8	25.8; 5.7; 3.4	12.8; 3.7
3187	12.8	8.6; 3.3; 1.5	12.8
3188	12.8; 6.4; 3.2; 1.6	8.6; 1.2	12.8; 1.5
3189	12.8; 3.2; 1.4; 1.0	12.8; 4.3	12.8; 4.3
3190	12.8	12.8; 2.9	8.6
3191	12.8	6.5; 2.3; 1.2	12.8; 1.4
3192	12.8; 5.1; 2.8	8.6; 3.9; 1.4; 1.0	12.8; 2.9

(b) South Atlantic Current

Buoy	*temperature (days)*	*zonal instantaneous velocity (days)*	*meridional instantaneous velocity (days)*
3182	204.1; 41.0; 27.4; 17.1; 10.5	204.1; 41.5; 25.4; 14.3; 10.7; 6.5; 5.8; 4.5; 3.6	204.1; 71.9; 27.1; 17.4; 13.7; 7.6; 5.5; 4.5; 3.0; 2.2; 1.8
3185	103.1; 26.0; 18.9; 9.8; 7.0	103.1; 41.5; 22.4; 12.9; 10.9; 7.3; 4.0	34.2; 20.2; 9.0; 6.3; 3.5
3187	51.3; 12.8; 5.4; 3.3	51.3; 17.1; 8.6; 6.0; 3.8; 2.3; 1.7	25.4; 8.6; 6.4; 3.9; 2.6; 2.1
3189	103.1; 22.4	103.1; 24.4; 17.0; 12.6; 8.4; 6.1	29.5; 11.4; 6.8; 5.4; 4.3; 3.1; 2.7; 1.8; 1.5
3190	103.1; 22.9; 11.7	50.2; 22.9; 13.4; 7.9; 4.3	69.0; 22.9; 12.1; 4.7
3191	103.1	41.5; 26.0; 16.3; 10.9; 6.3; 3.8; 3.0; 2.1	22.9; 13.7; 9.4; 4.2; 2.9; 2.2; 1.9
3192	103.1; 18.7	34.2; 12.9; 7.6; 5.4; 3.5; 2.6; 2.0; 1.6	22.9; 10.9; 4.2; 3.1

Higher frequency peaks of 2 days to 10 days were found by Garzoli and Simionato (1990) to be not only forced by the wind stress (which gives the oscillation a seasonal variance in energy), but also by the particular characteristics of the confluence: meandering, seasonal displacement of the front, sea bottom topography (mainly the sharp slope) and changes in the front's vertical structure which lead to baroclinic instabilities.

Comparing the oscillations found by Garzoli and Simionato (1990) with the ones found in this work for the BC and SAC, it can be noticed that some of the peaks are very close in period, suggesting that the driving mechanisms proposed by Garzoli and Simionato (1990) are probably forcing some of the oscillations measured by the LCDs at 15 m depth. For instance, the peaks centred at about 22-30 days are close to the 29.1 days oscillation retrieved from the echo sounders records.

The peaks close to 41 days and 34 days found for the SAC in the LCDs' measurements are close to the 37.4 days oscillation reported by Garzoli and Simionato (1990). They can be indicating the movement of the MC/BC front. Peaks close to 70 days found for the SAC are very close to the bi-monthly incursions of the BC in the convergence suggested by Legeckis and Gordon (1982).

Some of the energy peaks of 10 days or less found in this work can also have their origins in the same forcing mechanisms described by Garzoli and Simionato (1990). Owing to the lack of other data taken *in situ* like wind data, for example, we can not link directly peaks of energy in the buoy time series to their exact forcing mechanisms.

In agreement with Garzoli and Simionato (1990), the correlation between wind data and oceanic oscillations in the Southwestern Atlantic Ocean was also reported by Stech and Lorenzzetti (1992). Working in the South Brazil Bight (SBB), a region just north of the BMC region, these authors have reported that the wind spectra has dominant peaks at 11 days and 6.5 days. Analysing sea level records at Paranaguá, Brazil (~25.8°S, 48.5°W), Stech and Lorenzzetti (1992) found a strong 7 days oscillation in the time series. With the wind data showing a similar energy peak, Stech and Lorenzzetti (1992) concluded that the passage of atmospheric systems is one of the major forcing mechanisms of the sea level in the SBB in wintertime. Considering that the variations in the currents' direction and speed caused by the passage of atmospheric fronts are more likely to be noticed at the surface layers of the sea, above the Ekman layer, these oscillations are likely to be recorded in drifting buoys tracks. Therefore, it can be assumed that the atmospheric forcing is the more likely cause of the current oscillations at periods close to a week present in the buoy time series analysed here.

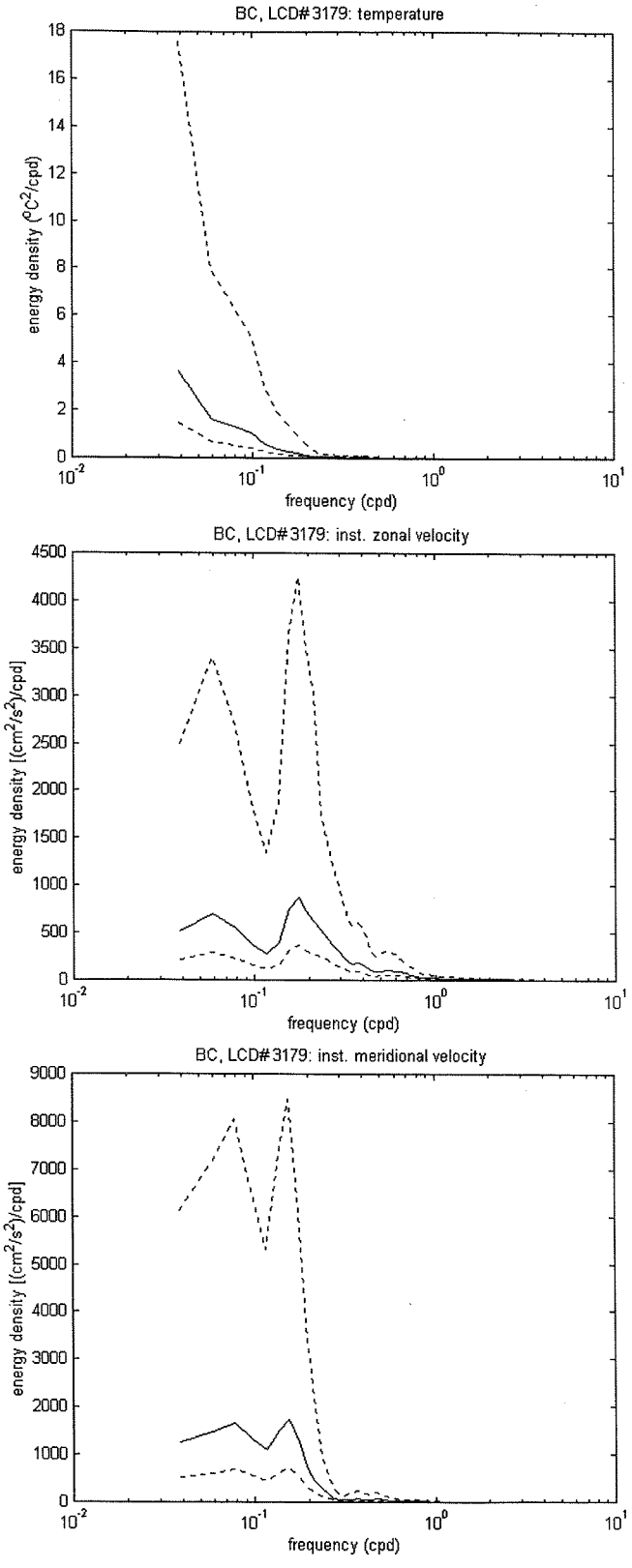

Figure 5.30. Energy preserving spectra of the LCD no. 3179's temperature (upper panel), instantaneous zonal velocity (middle panel) and instantaneous meridional velocity (lower panel) time series in the Brazil Current. The dashed lines represent the 95 % confidence interval.

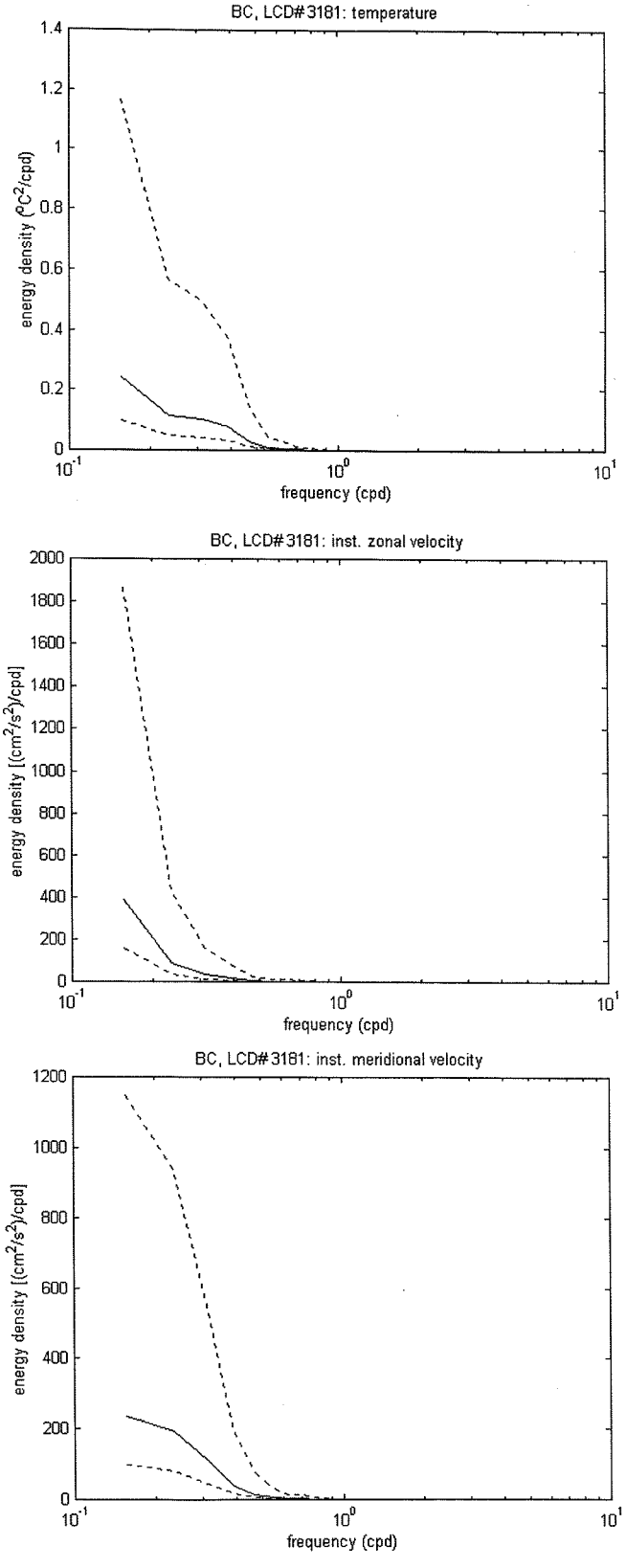

Figure 5.31. Energy preserving spectra of the LCD no. 3181's temperature (upper panel), instantaneous zonal velocity (middle panel) and instantaneous meridional velocity (lower panel) time series in the Brazil Current. The dashed lines represent the 95 % confidence interval.

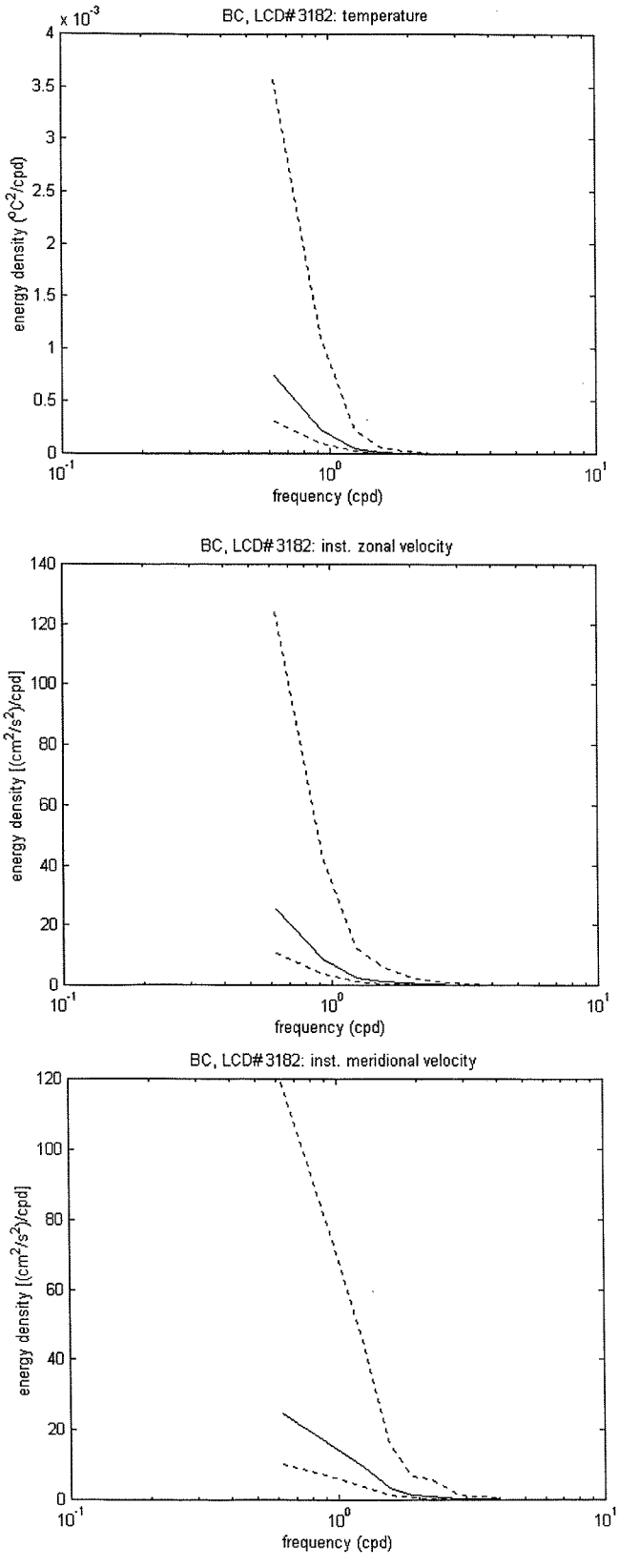

Figure 5.32. Energy preserving spectra of the LCD no. 3182's temperature (upper panel), instantaneous zonal velocity (middle panel) and instantaneous meridional velocity (lower panel) time series in the Brazil Current. The dashed lines represent the 95 % confidence interval.

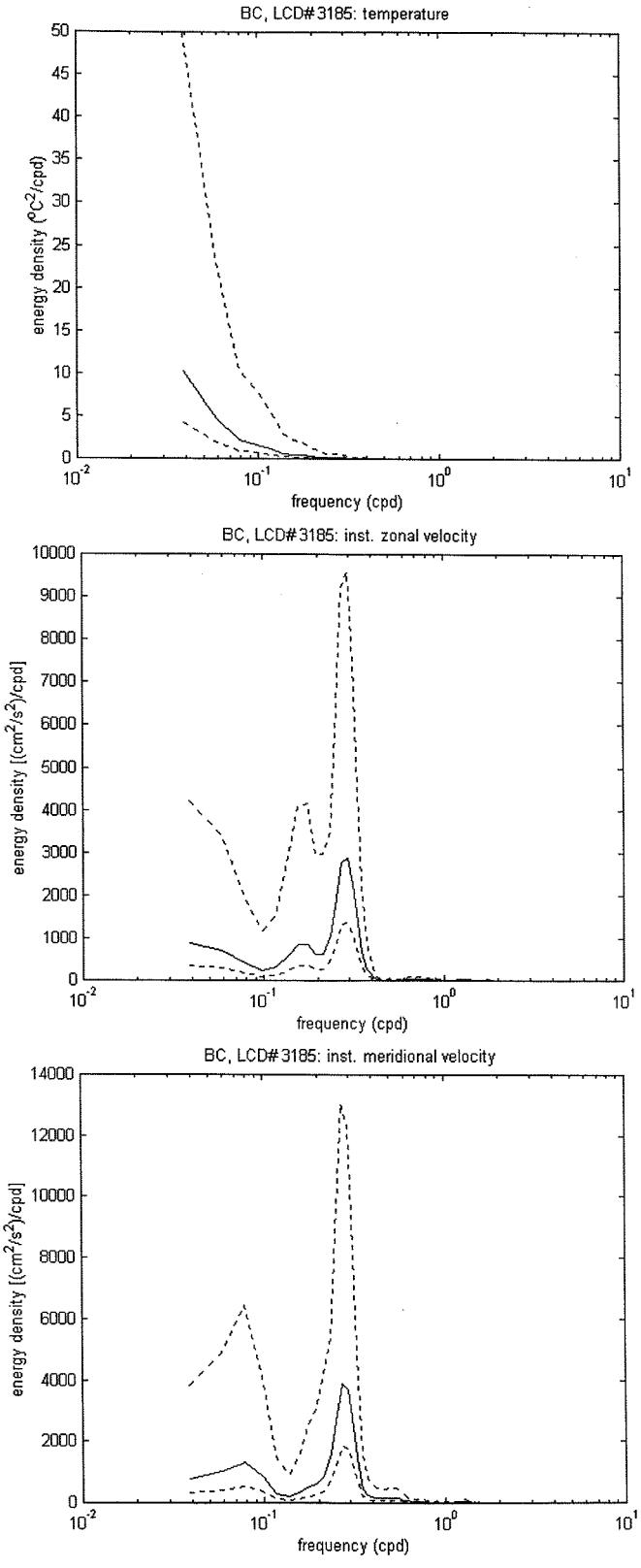

Figure 5.33. Energy preserving spectra of the LCD no. 3185's temperature (upper panel), instantaneous zonal velocity (middle panel) and instantaneous meridional velocity (lower panel) time series in the Brazil Current. The dashed lines represent the 95 % confidence interval.

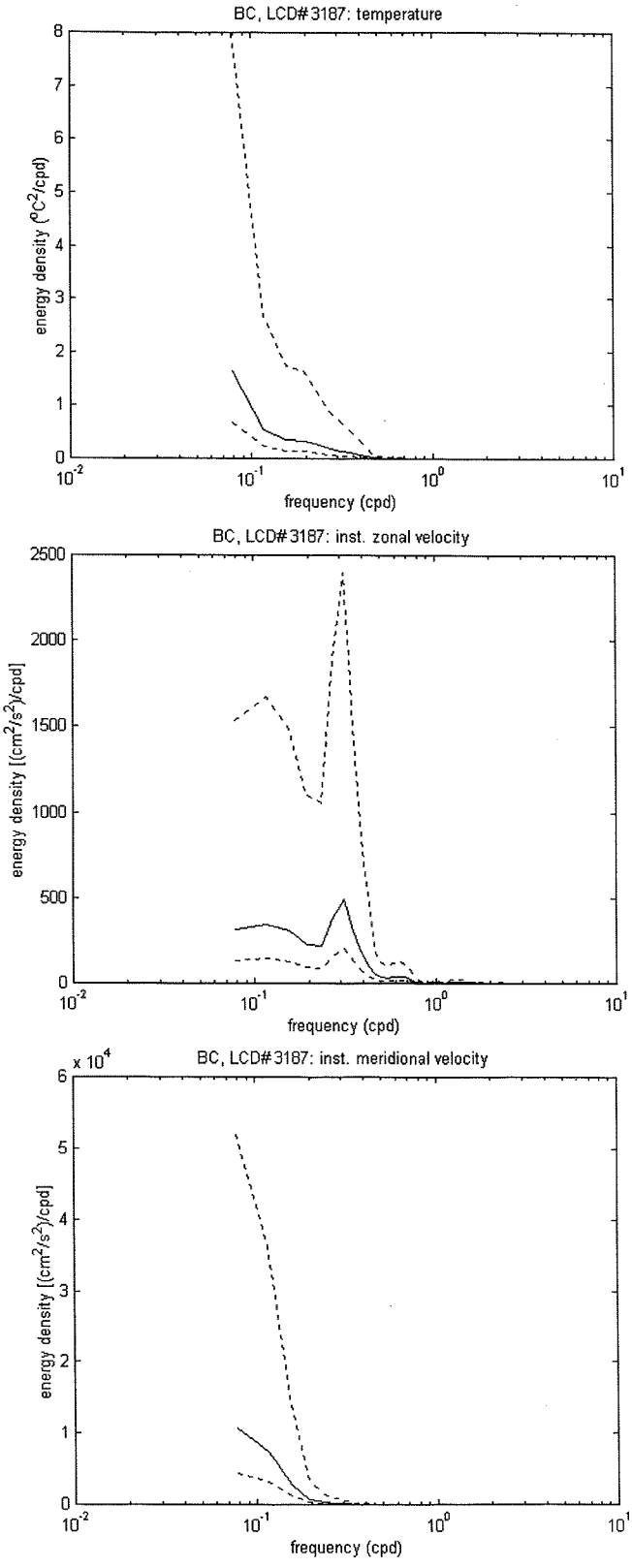

Figure 5.34. Energy preserving spectra of the LCD no. 3187's temperature (upper panel), instantaneous zonal velocity (middle panel) and instantaneous meridional velocity (lower panel) time series in the Brazil Current. The dashed lines represent the 95 % confidence interval.

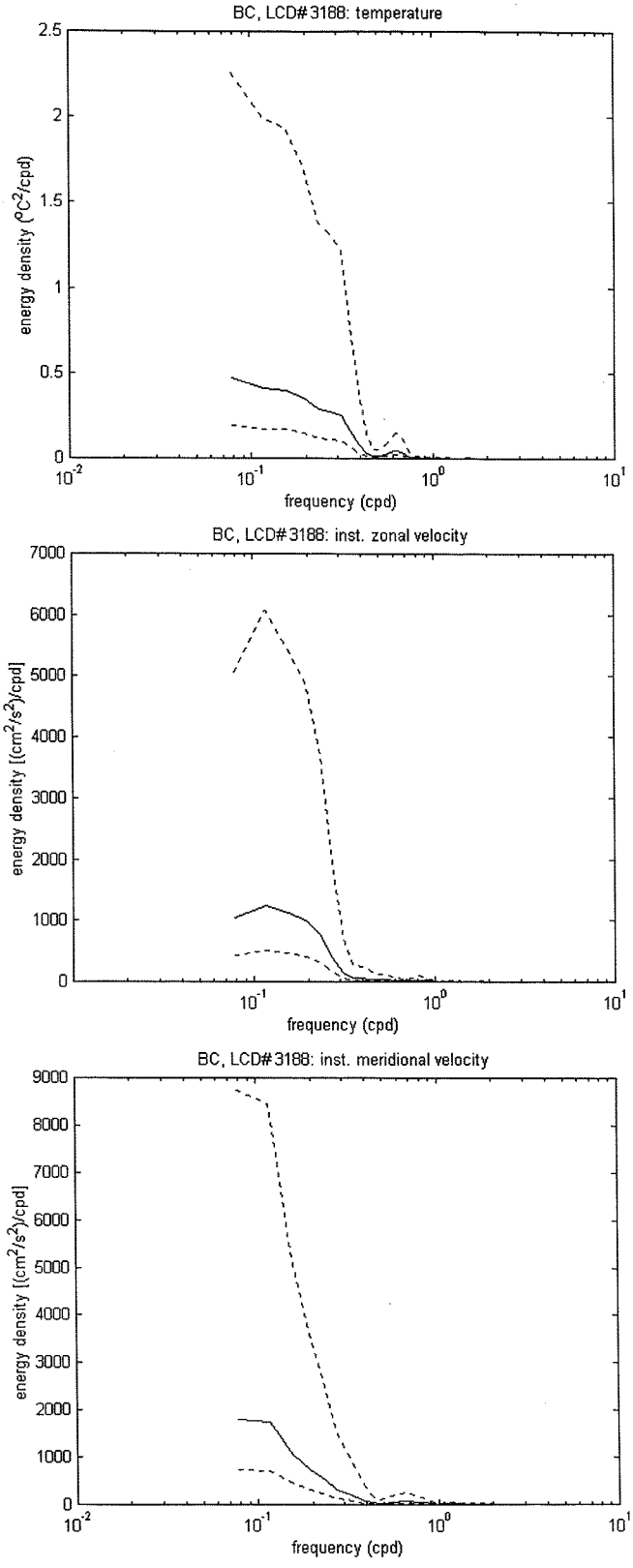

Figure 5.35. Energy preserving spectra of the LCD no. 3188's temperature (upper panel), instantaneous zonal velocity (middle panel) and instantaneous meridional velocity (lower panel) time series in the Brazil Current. The dashed lines represent the 95 % confidence interval.

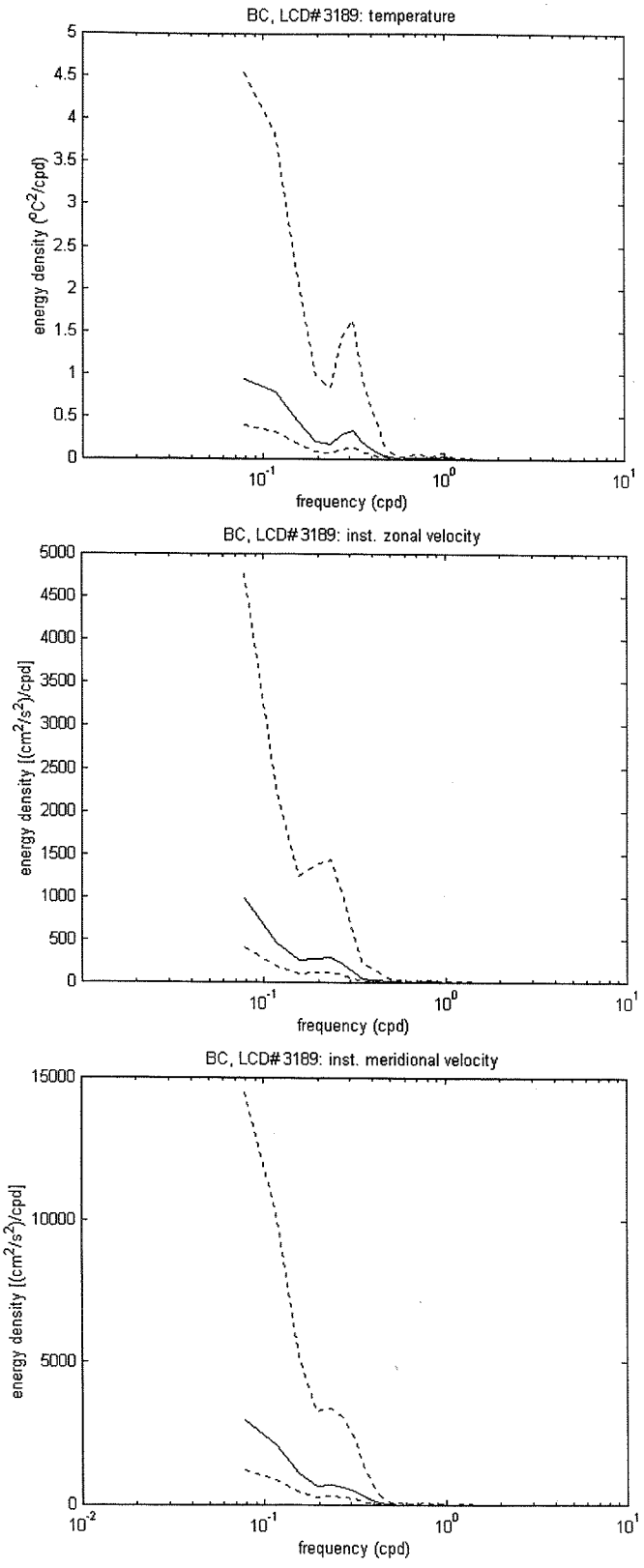

Figure 5.36. Energy preserving spectra of the LCD no. 3189's temperature (upper panel), instantaneous zonal velocity (middle panel) and instantaneous meridional velocity (lower panel) time series in the Brazil Current. The dashed lines represent the 95 % confidence interval.

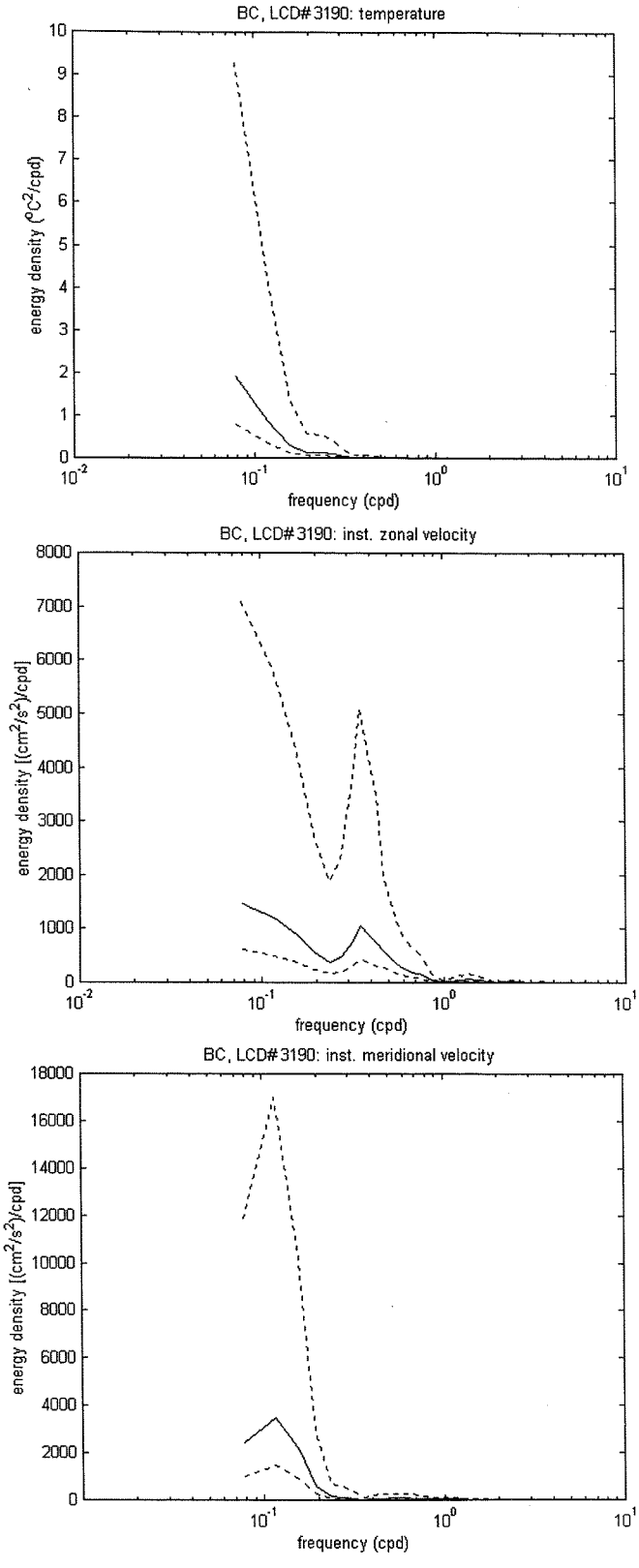

Figure 5.37. Energy preserving spectra of the LCD no. 3190's temperature (upper panel), instantaneous zonal velocity (middle panel) and instantaneous meridional velocity (lower panel) time series in the Brazil Current. The dashed lines represent the 95 % confidence interval.

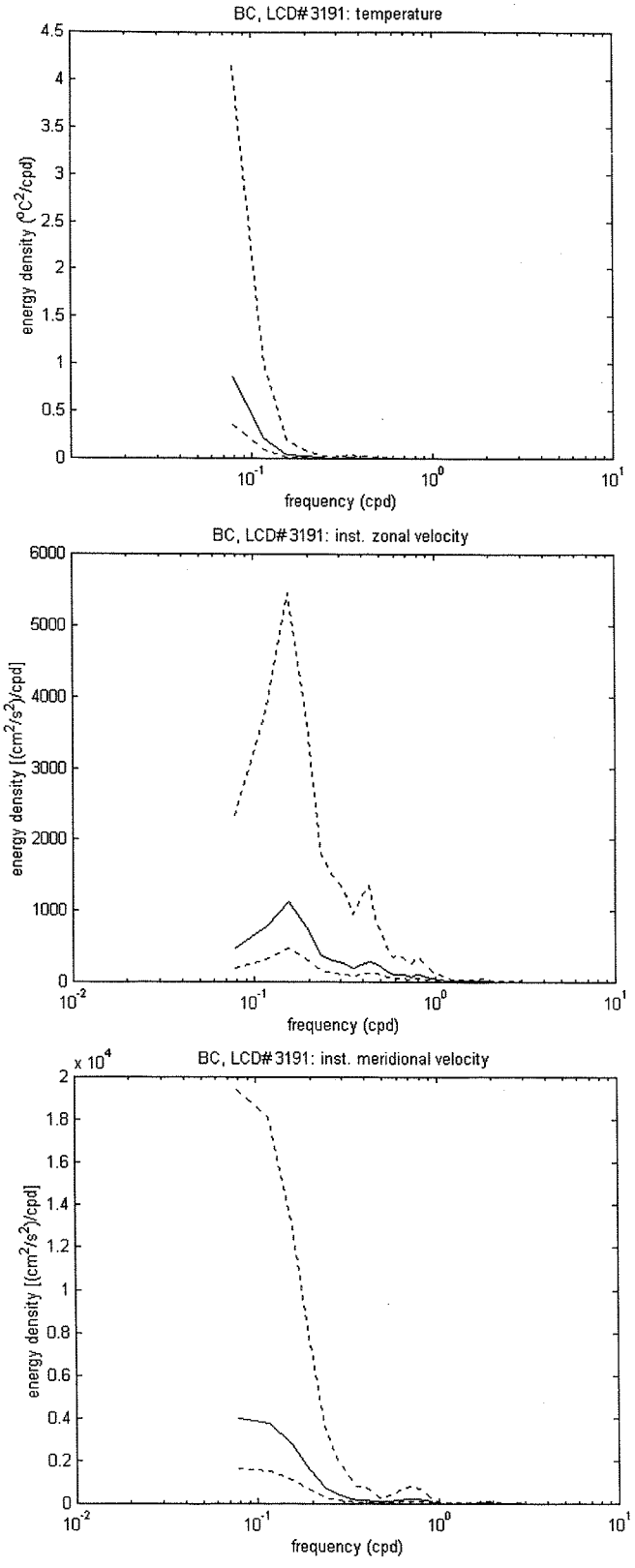

Figure 5.38. Energy preserving spectra of the LCD no. 3191's temperature (upper panel), instantaneous zonal velocity (middle panel) and instantaneous meridional velocity (lower panel) time series in the Brazil Current. The dashed lines represent the 95 % confidence interval.

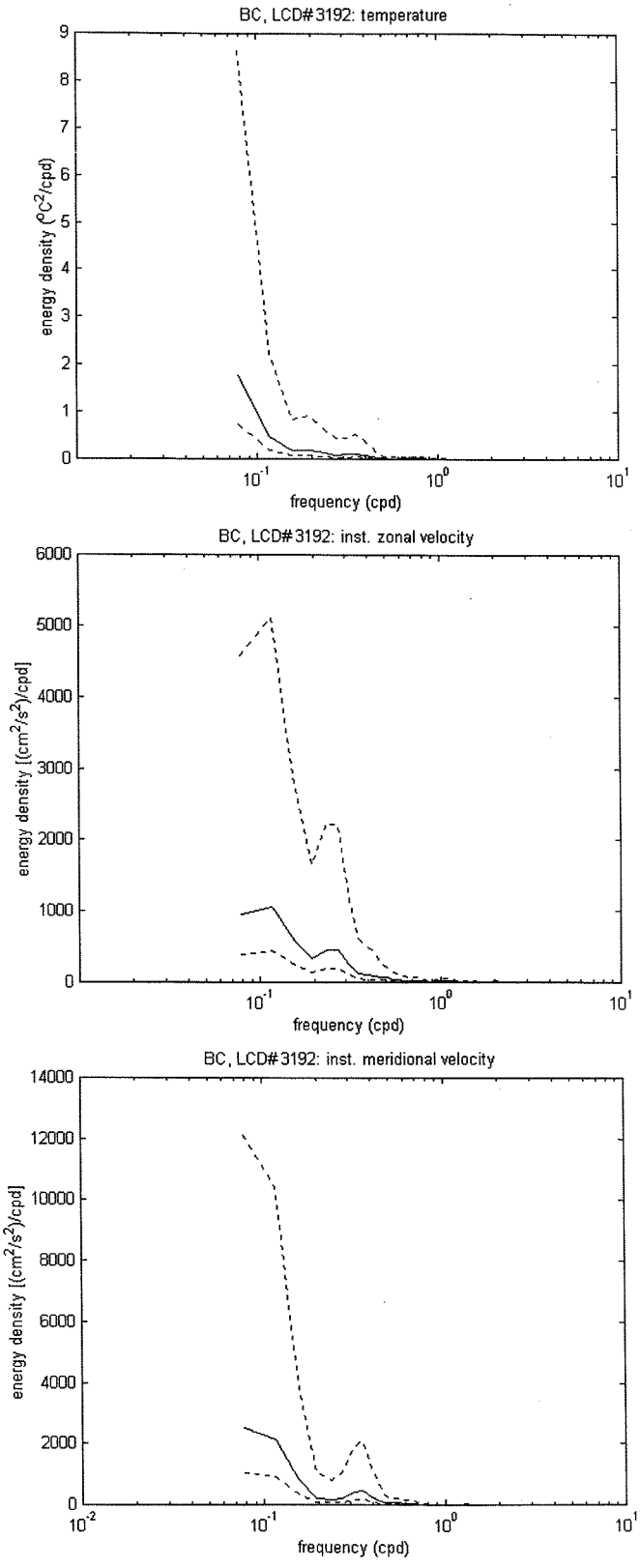

Figure 5.39. Energy preserving spectra of the LCD no. 3192's temperature (upper panel), instantaneous zonal velocity (middle panel) and instantaneous meridional velocity (lower panel) time series in the Brazil Current. The dashed lines represent the 95 % confidence interval.

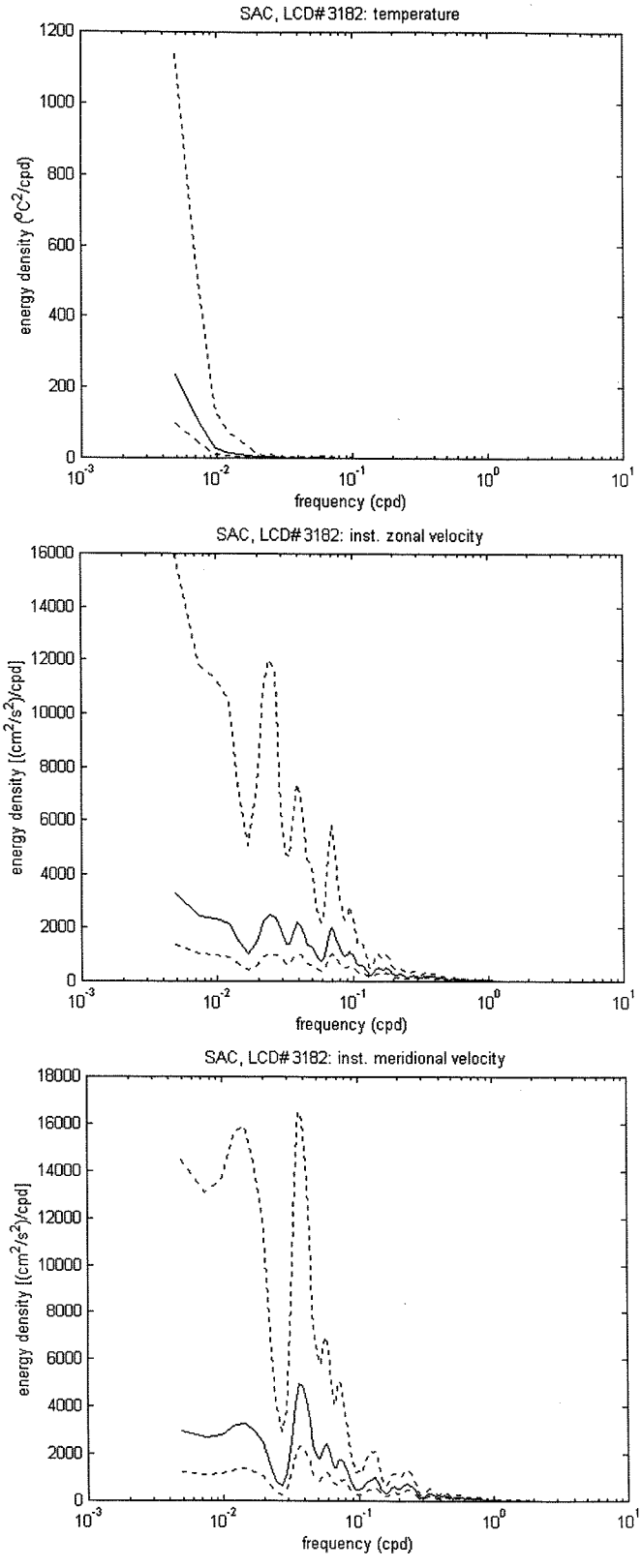

Figure 5.40. Energy preserving spectra of the LCD no. 3182's temperature (upper panel), instantaneous zonal velocity (middle panel) and instantaneous meridional velocity (lower panel) time series in the South Atlantic Current. The dashed lines represent the 95 % confidence interval.

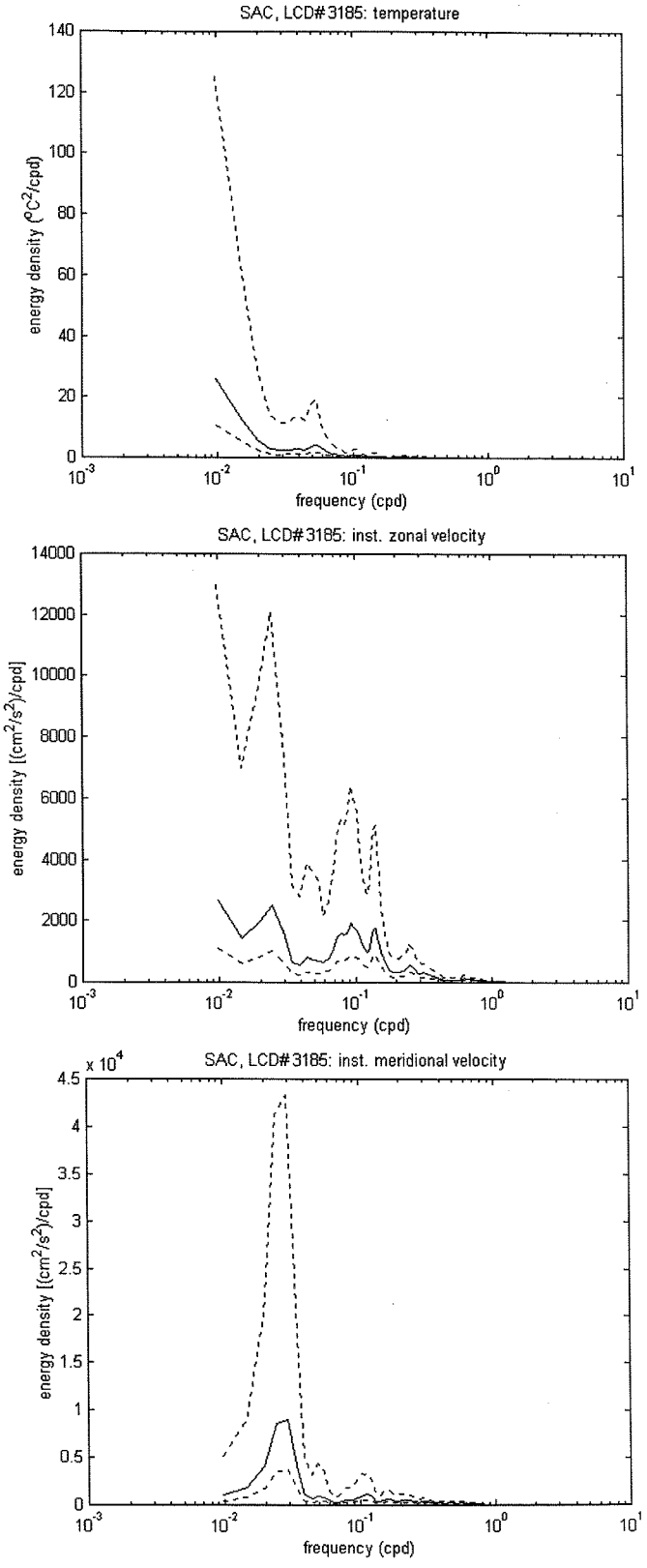

Figure 5.41. Energy preserving spectra of the LCD no. 3185's temperature (upper panel), instantaneous zonal velocity (middle panel) and instantaneous meridional velocity (lower panel) time series in the South Atlantic Current. The dashed lines represent the 95 % confidence interval.

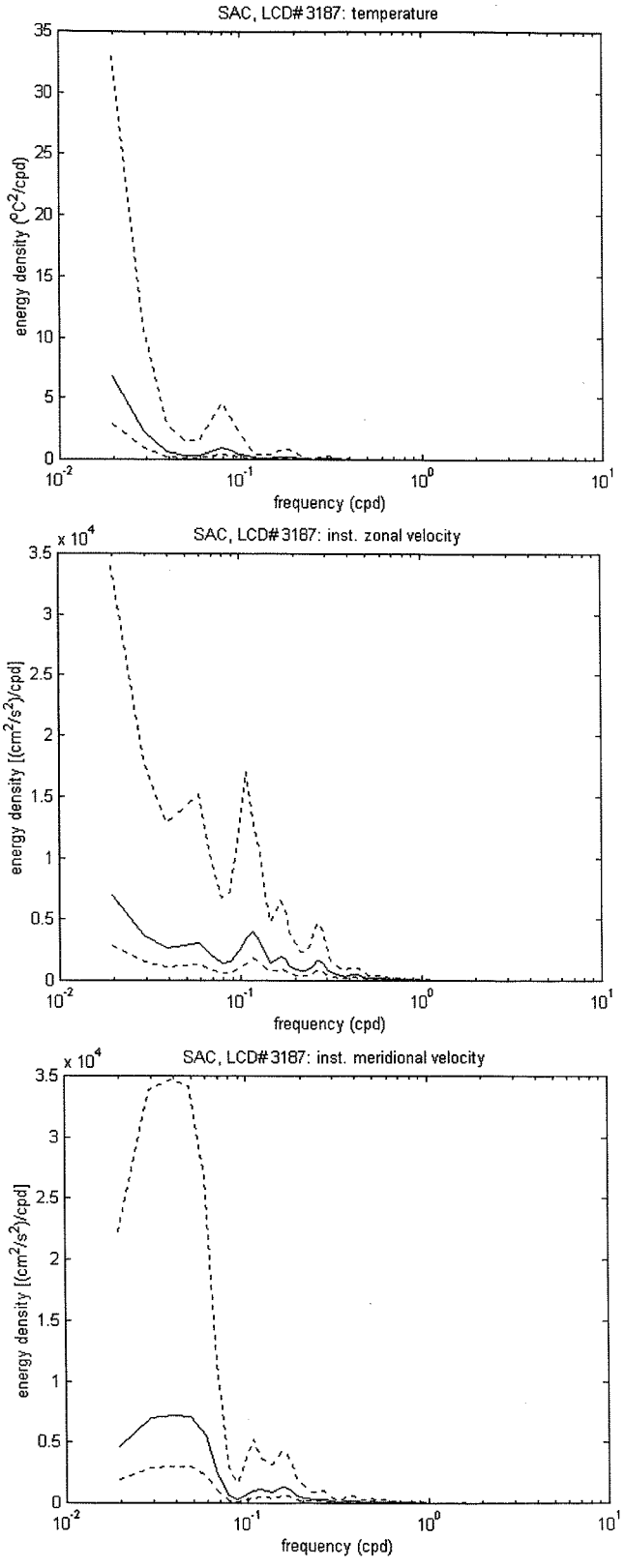

Figure 5.42. Energy preserving spectra of the LCD no. 3187's temperature (upper panel), instantaneous zonal velocity (middle panel) and instantaneous meridional velocity (lower panel) time series in the South Atlantic Current. The dashed lines represent the 95 % confidence interval.

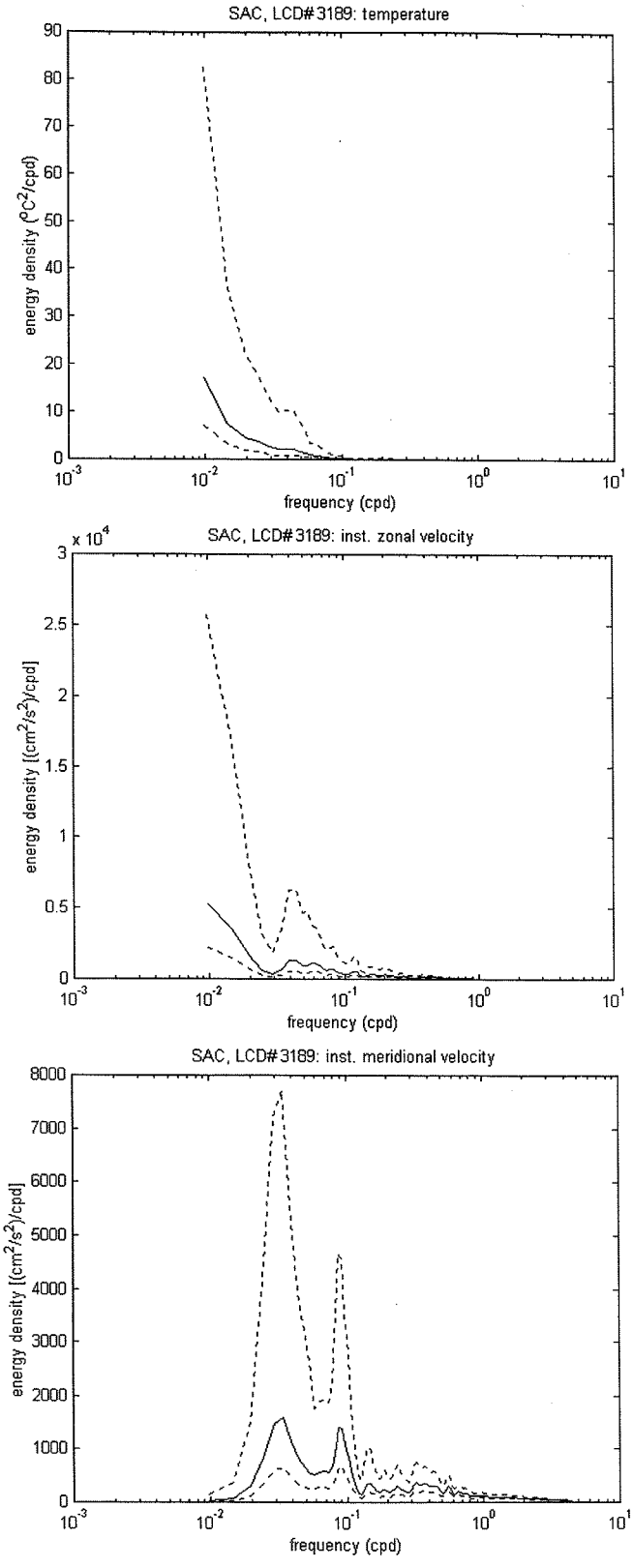

Figure 5.43. Energy preserving spectra of the LCD no. 3189's temperature (upper panel), instantaneous zonal velocity (middle panel) and instantaneous meridional velocity (lower panel) time series in the South Atlantic Current. The dashed lines represent the 95 % confidence interval.

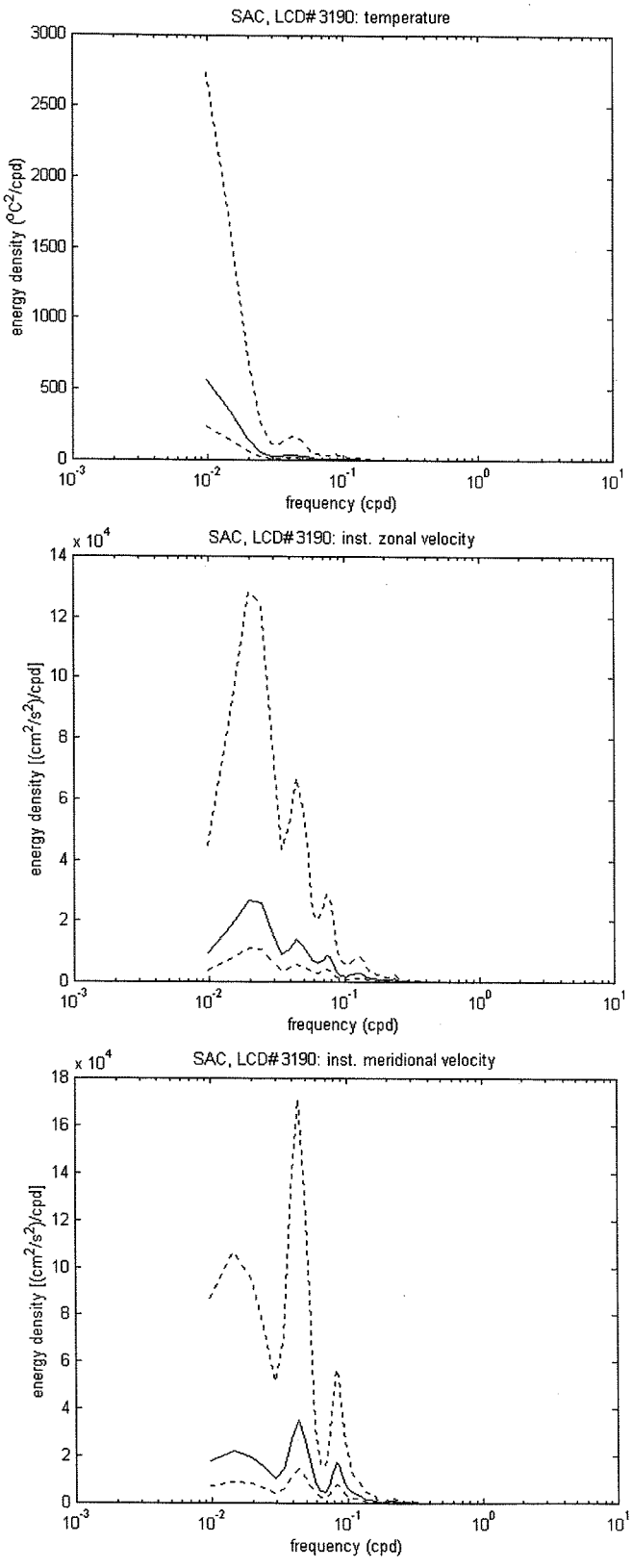

Figure 5.44. Energy preserving spectra of the LCD no. 3190's temperature (upper panel), instantaneous zonal velocity (middle panel) and instantaneous meridional velocity (lower panel) time series in the South Atlantic Current. The dashed lines represent the 95 % confidence interval.

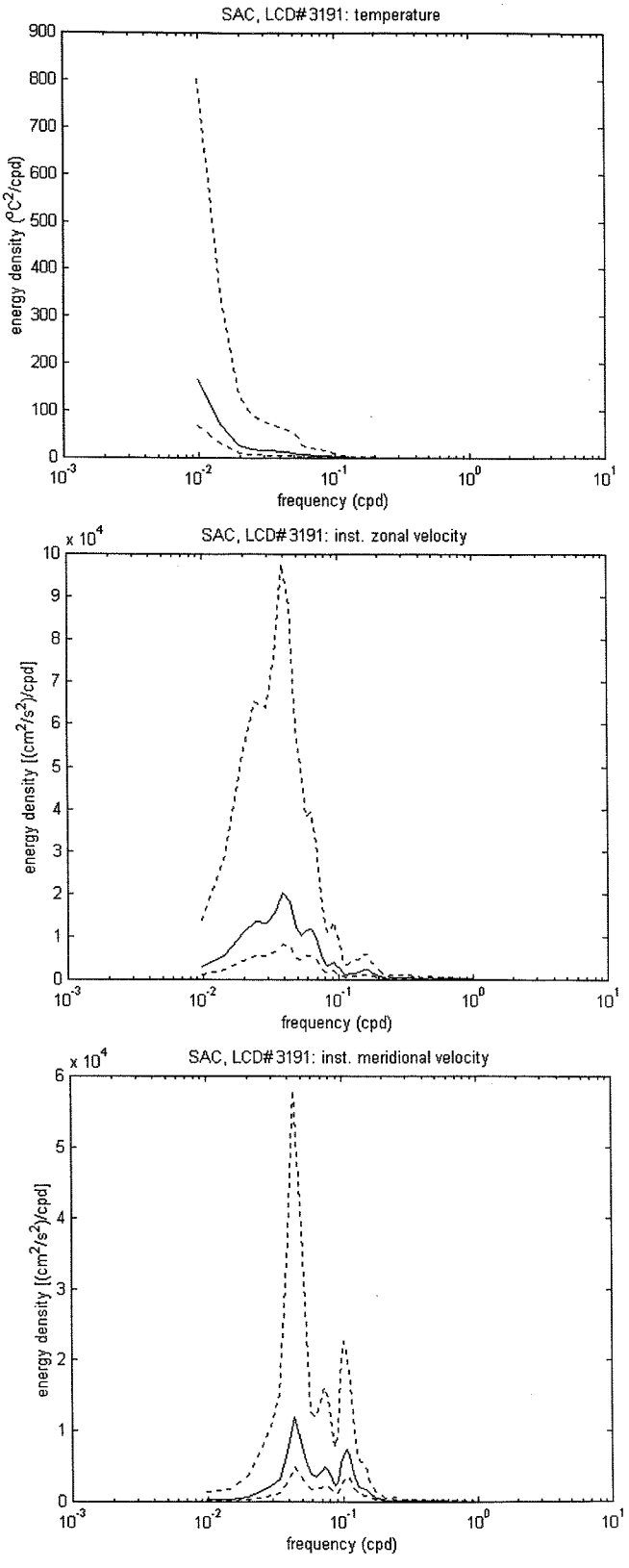

Figure 5.45. Energy preserving spectra of the LCD no. 3191's temperature (upper panel), instantaneous zonal velocity (middle panel) and instantaneous meridional velocity (lower panel) time series in the South Atlantic Current. The dashed lines represent the 95 % confidence interval.

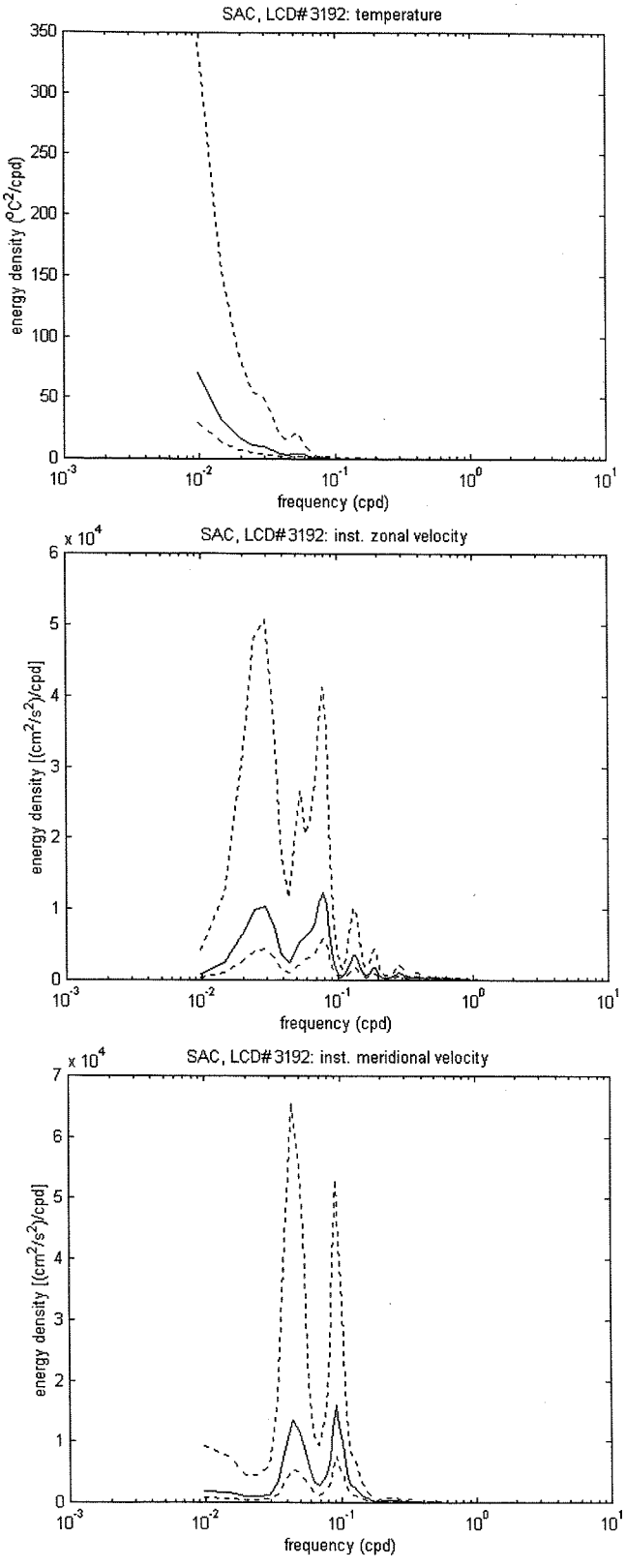

Figure 5.46. Energy preserving spectra of the LCD no. 3192's temperature (upper panel), instantaneous zonal velocity (middle panel) and instantaneous meridional velocity (lower panel) time series in the South Atlantic Current. The dashed lines represent the 95 % confidence interval.

5.5. Summary and final remarks

This chapter has studied some of the mesoscale surface processes occurring in the Brazil-Malvinas Confluence zone during the period of March 1993 to July 1994. In order to support our study, we have used a set of 168 MCSST images representing the South Atlantic as a whole. This last data set was 14 year long, each image representing a monthly average for the months from January 1982 to December 1995.

The processing of the MCSST data set provided 12 'climatological' monthly averages which were used to describe the mean behaviour of the Subtropical Front in the South Atlantic, as defined by the 20°C isotherm at the surface. Utilising the original data and the 'climatological' data, monthly anomaly SSTs were also obtained for the particular months between 1982 and 1995. They were subsequently grouped into their respective seasons. In order to account for the periodicities of present in the SST fields in the Atlantic Ocean, both 'climatological' and anomaly SST images were submitted to Principal Component (PC) analysis.

The climatological MCSST images have demonstrated that the Subtropical Front, as it was measured by the 20°C isotherm, reaches its northernmost position in September and retracts to its southernmost position in February. The shape of the 20°C isotherm in the BMC and Southern Brazilian Continental Shelf (SBCS) indicates the penetration of cold waters in the Brazilian shelf during the winter. It also shown that the meridionally orientated front between tropical and coastal/subantarctic waters that happens in winter in the Southwestern Atlantic Ocean is a continuation of the BMC or the Subtropical Front. This also supports the study reported in Chapter 6 about the characteristics of the Brazilian Coastal Current.

The PC analysis performed in the climatological MCSST images indicated that the first four components accounted for 99.92 % of the total variance of the data. The spatial amplitudes in PC1 were similar to the temporal mean of all images, while in PC2 the Subtropical gyre was isolated from the rest of the South Atlantic. In this mode the so-called Atlantic Dipole is noticed. The PC1, PC2 and PC3 eigenvectors indicate the annual cycle, which is dominant in the South Atlantic. The semiannual cycle was present in PC3.

The first four PC modes of the seasonally averaged anomaly MCSST fields accounted for 78.04 % of the total variance in the data. The dominant peak for PC1 and PC2 was centred at 5.37 years. PC3 and PC4 had their dominant periods centred at 10.7 years and 3 years,

respectively. The annual cycle was found in PC1 at 11.6 months. Intrannual oscillations were centred in peaks ranging from 6.6 months to 10 months.

Analysis of the original monthly averaged MCSST images for the period between March 1993 and July 1994 revealed that this period of time was not particularly anomalous with respect to the 'climatological' behaviour of the South Atlantic Ocean. That supports the interpretation of the SST fields obtained for this period from the high-resolution AVHRR images. The high-resolution images have demonstrated the presence of a series of mesoscale features in the study area during the study period. In agreement with the MCSST observations, the temporal sequence of high-resolution images also showed that a coastal current develops at the SBCS during the wintertime, fed by waters from the BMC region.

The frontal surface activity in the study region could also be investigated by using the high-resolution AVHRR images. Following the same procedure as for the MCSST images, the 20°C isotherm was also used in these images to indicate the position of the frontal systems in the study area. The BC/BCC front was particularly evident, lying parallel to the continental shelf above the 100-200 m isobaths off Uruguay and Brazil. Being originated in the BMC region, the front extends itself to the north of Santa Marta Cape (~28°S), a position previously thought to mark the limit in the SBCS for the penetration of waters with subantarctic influence. For the first time in the literature it is also suggested that the BMC front can extend itself to about 28°S, further north than previously described.

Thermal gradients between the BC and the core of MC in the BMC region were found to be in the order of 0.25°C/km to 0.4°C/km in horizontal scales of about 20 km to 40 km. The gradients are smaller across the South Atlantic Current, between the warm and the cold part of this current. The same is said for the gradients between eddies and their surrounding waters. Gradients in the BC/BCC front were, as expected, smaller towards the north, owing to the distance from the MC core. In a surface transect taken across the Santa Marta Cape in 3 August 1993, for example, the thermal gradient between BCC and BC was 0.07°C/km.

The description of the thermal gradients of the BMC and SBCS regions is important in many respects. Firstly, in previous literature, there were very few numeric descriptions of these gradients and of their associated fronts, although they are very typical of the Southwestern Atlantic and their strength facilitates their observation by satellite infrared sensors (Olson et al., 1988; Podestá, 1997). Secondly, the frontal systems of the BMC and southern Brazil are regions of concentration of biota, specifically fish (Castello et al., 1990, 1997). In these regions the surface fronts are also a strong indicator of the process of water mixture occurring

in the water column, as well as of the heat exchange. The monitoring of the surface waters off Brazil started with project COROAS, when consistent satellite data was obtained for a period of two years. Nevertheless, the continuous monitoring of the surface thermal fronts off Brazil is still lacking for the period after 1994. Indeed, at the present time, the utilisation of satellite images to monitor frontal systems for fisheries applications in Brazil still requires development.

Buoy trajectories and time series of position and SST measured by the drifters were used here to characterise the BC and the SAC during the period of this study. Buoy trajectories in the BC and the SAC exhibited meanders and eddies which are consistent with previous descriptions found in the literature for these two currents (e.g. Legeckis and Gordon, 1982). The SAC was found to be about four times slower and to concentrate more EKE and TKE (eddy and total kinetic energy) than the BC. In the BMC region, the BC average speed was 37.4 cm/s, while the SAC average speed was 9.7 cm/s. The BC mean temperature, as measured by the buoys, was in average about 4°C warmer than that from the SAC. BC flows in the NE-SW direction, while SAC is mainly a zonal current in the study region.

Although the mean direction and meandering characteristics of BC and SAC are known to a certain level, direct measurements of these currents are rare. Moreover, the comparisons made in this thesis about their characteristic velocities, energies and temperatures are aspects that have not been covered in known literature. In addition, the combination of satellite infrared imagery and Lagrangian data for simultaneously studying the BC and SAC has not been fully utilised until this research.

FFT spectra of the BC and SAC instantaneous velocity and temperature time series have revealed energy peaks in periods shorter than those obtained for the South Atlantic when we applied PC analysis on the MCSST data. The only time series long enough to show the semiannual oscillation revealed in the PC analysis of the MCSST images was that of buoy 3182. There, the semiannual oscillation was centred at 6.7 months but only seen in the zonal instantaneous velocity time series. The BC's most prominent peaks were centred at 25.8 days (when the series were long enough), 12.8 days, 8.6 days, and around 6.5 days and 3.5 days. In general, the SAC peaks were centred at 103.1 days, around 41 days and 34 days, 22-30 days and at 11-13 days and shorter periods.

Some of the peaks found in the buoy time series are similar to others described in the literature for the BMC region. According to Garzoli and Simionato (1990), the major forcing mechanisms that generate the oscillations in the convergence region are many: meandering of

the BC; meandering and seasonal displacement of the BMC; bottom topography; baroclinic instabilities and wind stress. Changes in the MC or in the BC transports can also lead to instabilities in the BMC. The balance between the distinct water masses including fresh water coming from the La Plata River and Patos Lagoon outflows could also play an important role in the local dynamics, but will probably affect only the western boundary currents, and not the SAC. Differences in the oscillatory peaks present in BC and SAC can be related to locally driven mechanisms acting in the BC and not in the SAC. This is an interesting subject for further investigation.

CHAPTER 6

THE BRAZILIAN COASTAL CURRENT [1]

6.1. Introduction

In this section we study the surface signature of the northeasterly coastal current which is formed in the region of the BMC and was found to spread itself over the South Brazilian Continental Shelf during the winter. High-resolution AVHRR imagery and Lagrangian data collected in 1993 and 1994 are used here to describe the temperatures, velocity, energy and oscillations present in this coastal current. These two data sets show that the current is not only fed by cold waters from the BMC region, but also receives a contribution from the Brazil Current at the surface by lateral mixing. By analysing the overall set of monthly averaged MCSST images from 1982 to 1995, this section also demonstrates that the intrusion of cold waters transported by the coastal current is a recurrent phenomenon occurring in the Brazilian shelf in latitudes up to the vicinity of 24°S during the months of June to October every year. Given its consistency, this current is named here the Brazilian Coastal Current (BCC).

In a recent review paper, Castro and Miranda (1998) presented historical evidence of the occurrence of a northeastly coastal current occurring in the region of the South Brazil Bight (SBB). Although this current has been previously reported in the lower latitudes of the SBCS, the lack of long term *in situ* data collection programmes for the SBCS region inhibited a better characterisation and monitoring of this flow. It was only recently that consistent work started being made towards a general description of this coastal current.

Satellite images have been available for Brazilian studies for many years, but it was only after the establishment of the COROAS (Oceanic Circulation in the Western Region of the South Atlantic) project in 1992 that a consistent routine for high-resolution AVHRR data collection was set up in Brazil. Among COROAS objectives, satellite images were supposed to be used

[1] This Chapter has been submitted to the Continental Shelf Research in the form of a paper entitled 'Lagrangian and satellite observations of the Brazilian Coastal Current', by Souza and Robinson.

together with simultaneous current measurements made by surface drifters for achieving a better understanding of the BC behaviour off the São Paulo State coast, at about 23°S.

Apart from the results concerning the BC, one of the new facts which came to light after the experimental phase of COROAS is that low-salinity, cold waters formed in the BMC region were found to reach latitudes of about 24°S, near Rio de Janeiro city during the winter of 1993 (Stevenson and Souza, 1994; Stevenson, 1996; Campos et al., 1996a; Campos et al., 1996b, Silva Jr. et al., 1996).

From hydrographic surveys (e.g. Ciotti et al., 1995; Castro and Miranda, 1998), the consensus in Brazilian oceanography was that cold waters coming from the south would reach maximum limits of penetration of about 28°S at Santa Marta Cape (Campos et al., 1996b) or perhaps 27°S at the Santa Catarina Island (Piccolo, 1998). Because of that and owing to the initially limited time series of satellite images collected through COROAS, the first results from this project supposed that the intrusion of waters originating in the BMC to latitudes north of 28°S was an anomalous occurrence.

In a recent paper, for instance, Stevenson et al. (1998) used COROAS and other sources of data to study the ecological aspects of the tropical Ilha Grande Bay (22°S), off Rio de Janeiro State, Brazil. These authors suggested that subantarctic organisms present there were, and are, being carried along the SBCS by the cold waters originating in the south. These waters and their associated alongshore movement were referred to by Stevenson et al. (1998) as the northward extension of the Malvinas Current.

Stevenson et al. (1998), however, still considered that the entrance of subantartic biota to Ilha Grande Bay happens in a sporadic way, leading to an interpretation that the coastal current carrying the biota could also be sporadic. Stevenson et al. (1998) cited the passage of meteorological fronts through the SBCS as an important, if not the principal, driving mechanism for carrying waters with subantarctic origin to the north.

Ciotti et al. (1995) pointed out that the southern part of the Brazilian continental shelf is the most important fishery area of the Brazilian coast. High phytoplankton biomass is related to nutrients made available from the intrusion of SAW and CW in the platform. The possibility of an extension of the most productive fishery area of the Brazilian shelf to the north of 28°S could surely have a significant economic impact in Brazil.

In this section, the behaviour of cold MC water in the BMC region and its extension in the SBCS will be studied. In particular we wish to analyse further the character of the supposed anomalous behaviour, since it could be of considerable significance for the productivity and the economic aspects of the area.

Lagrangian and high-resolution AVHRR data collected during COROAS are analysed in detail to describe the temperatures, velocities, energies and oscillations present in the BCC. Analysis of the BC/BCC thermal front, as seen in the AVHRR images, shows that surface interactions between the poleward BC and the equatorward coastal current were present in the form of small-scale (~20 km to ~50 km) shear instabilities during the 1993 and 1994 winters.

Monthly-averaged MCSST images of the South Atlantic Ocean are analysed for the period of January 1982 to December 1995 to demonstrate that the intrusion of cold waters up to latitudes near 24°S is not an anomalous phenomenon, but rather a common process occurring in the SBCS during every wintertime.

6.2. The BCC in 1993 and 1994

6.2.1. Trajectories and high-resolution imagery

The trajectories described by the LCDs in the BCC are seen in Figure 6.1. The tracks indicate the Brazilian Coastal Current flowing northeastward parallel to the Brazilian coast on the SBCS in water depths lower than 200 m. Eddy activity and meandering can also be noted along all trajectories, but major activity is seen at about 25°S, 46°W, in the region near the buoys' launching position. Although the buoys were launched together at the BC in February 1993, they entered the BCC in different positions and at different times (Table 4.2.b) after April 1993. The time delay between the entrance of each single drifter in the BCC did not result in much difference between the trajectories presented by the buoys.

Due to cloud cover, it was very difficult to match precisely the entrance times of each buoy into the BCC from the BC with high-resolution AVHRR images. An image taken on 29 April 1993 (Figure 6.2), however, shows buoy 3179 entering BCC from BC, having been captured by a small scale anticyclonic eddy, about 10 km wide, at the boundary between BC and BCC. Another (warm core) eddy of the same scale as the one described in the trajectory can also be spotted inside the core of BCC at about 31.25°S, 50.25°W in Figure 6.2.

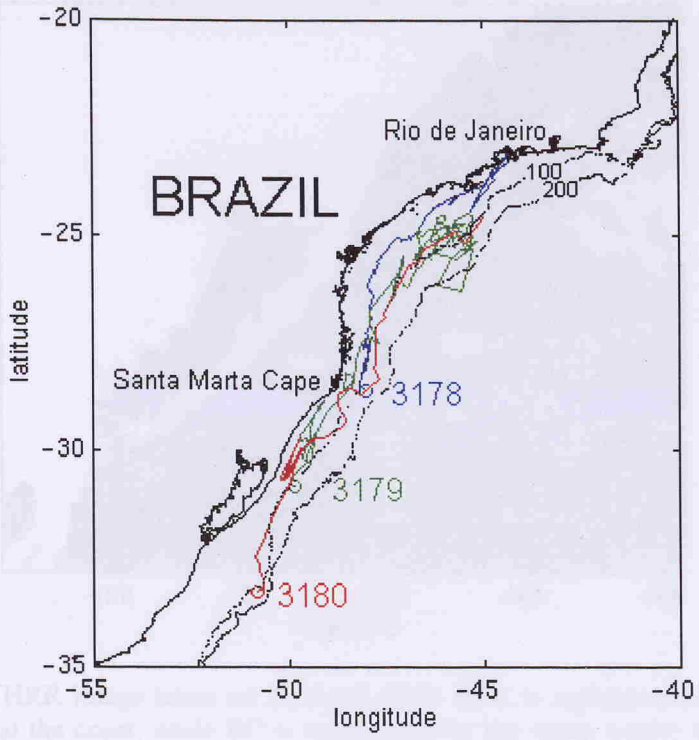

Figure 6.1. Trajectories described by the LCDs in the Brazilian Coastal Current.

The AVHRR images show that the frontal line separating BC from BCC is very distinct due to the strong thermal gradients between the waters transported by these currents. Figures 6.3 and 6.4 show examples of these images where the temperature scale was adapted to enhance the BC/BCC front. Lateral mixing is suggested by the presence of shear instabilities caused by the two currents flowing in opposite directions. As noted in Figure 6.3, these instabilities occur all along the front line between BC and BCC, and suggest that BC can feed BCC at the surface by the detachment of warm core eddies. BCC also ejects cold core rings into BC.

Figure 6.4 represents a one-day sequence illustrating the development of a mushroom-like structure in the BC in the vicinity of Santa Marta Cape at 28°S. The process of surface interleaving between BC and BCC is clear from this figure, and two warm core, cyclonic rings about 50 km wide are in the process of formation in the BC at about 27.5°S and 29°S. The eddies are apparently in the process to be expelled from the BC to the BCC. These instability features are probably not in geostrophic balance (since geostrophically balanced warm core rings have an anticyclonic gyre). Although relatively small, depending on the periodicity and number of eddies formed they could account for much of the BC exchange of heat and momentum with BCC along the front.

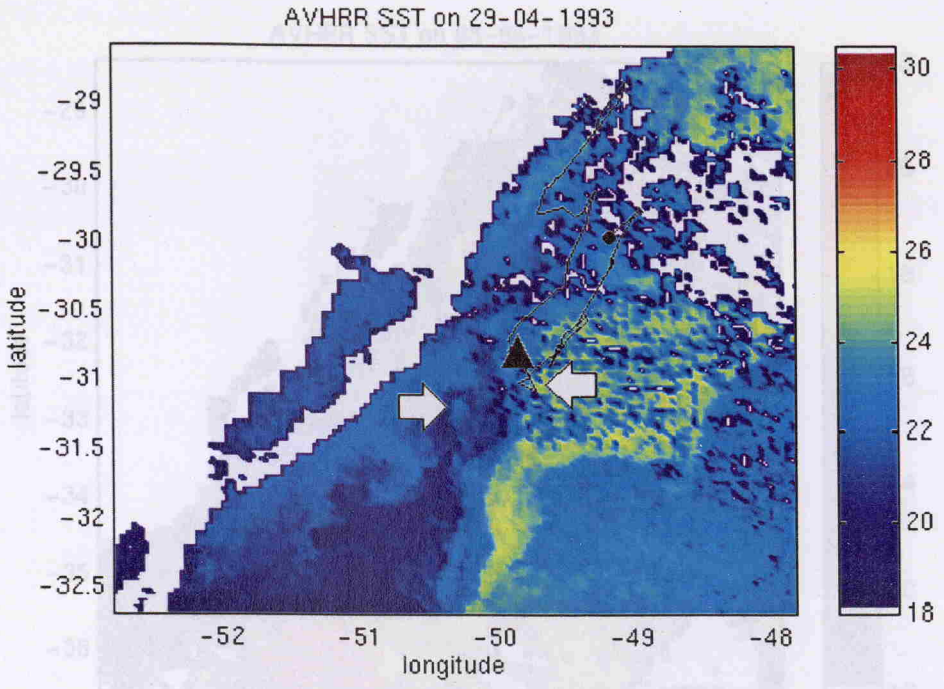

Figure 6.2. AVHRR image taken on 29 April 1993. BCC is represented by the cold waters (green to blue) at the coast, while BC is represented by the warm waters offshore (yellow to red). The image shows buoy 3179 entering BCC from BC after having been captured by a small scale warm core eddy visible in the buoy's track (indicated by the arrow pointing to the left). The possible equivalent of this eddy in the AVHRR image is indicated by the arrow pointing to the right. The circle indicates the buoy's position 20 days before the images' acquisition time, the triangle indicates the buoy position within ±12 h from the image's acquisition time. The colour bar indicates temperature in degC).

Since lateral mixing and eddy formation happens throughout the BCC, it is supposed that the position at which a particular buoy launched in the BC penetrates BCC through the front depends randomly on the location where this particular buoy is caught by a warm core eddy being formed. Both our Lagrangian and satellite observations have indicated that BC waters can enter BCC all along the front between these two currents.

The observation of interleaving or instabilities along the BCC/BC front is also reported by Lima et al. (1996). According to these authors, the entrainment of cold core eddies originating in the coastal waters at the platform to the BC is an important mechanism for providing nutrients from coastal or subantarctic origin to the oligotrophic Tropical Water (TW). Lima et al. (1996) also report that cold core eddies in the BC can induce upwelling in the shelf break and, together with the wind-driven circulation, produce a very distinct cross-shelf circulation regime from winter to summertime.

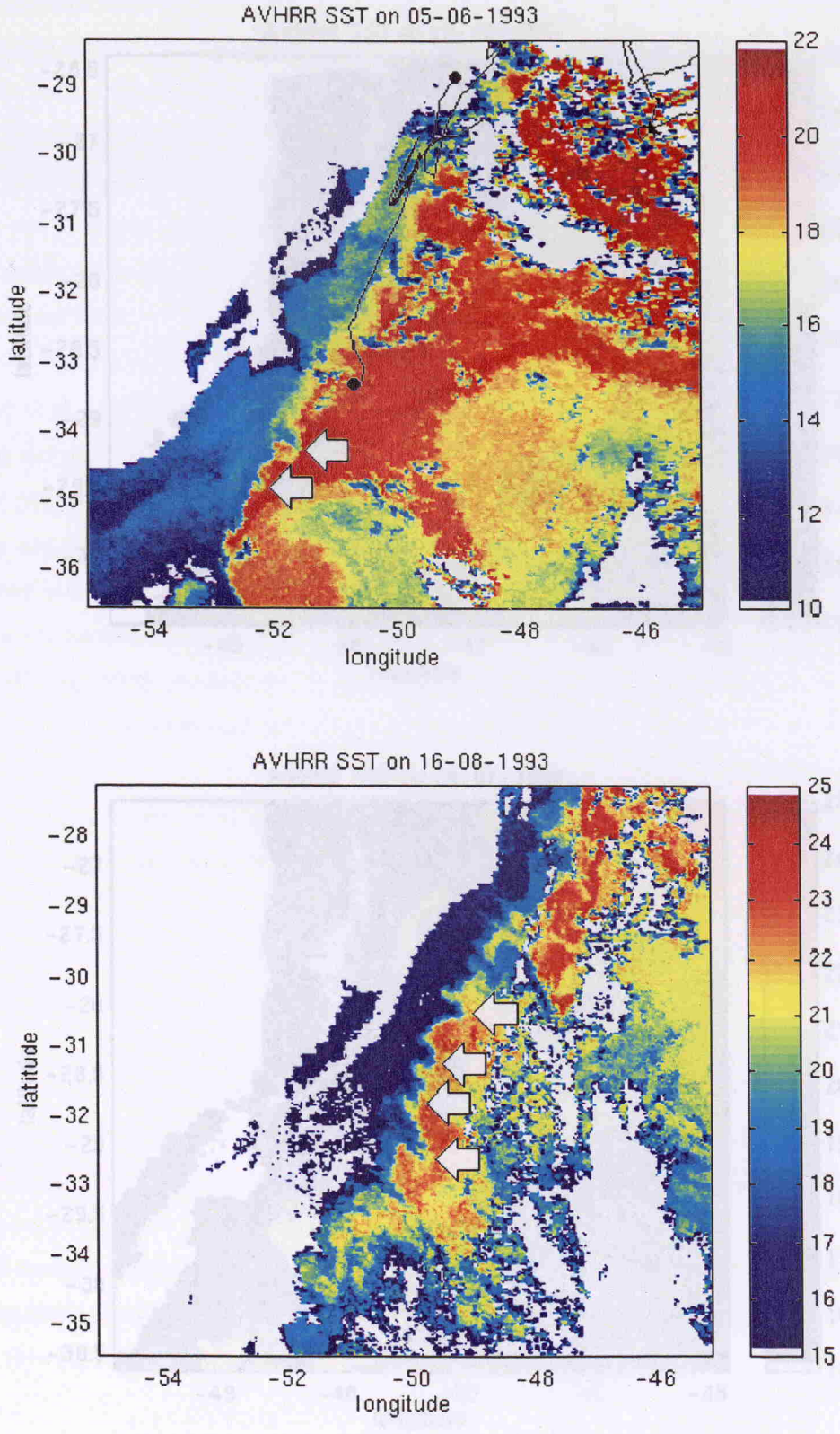

Figure 6.3. The BC/BCC front at the SBCS in 5 June 1993 (top) and 16 August 1993 (bottom). Buoys 3179 and 3180 tracks are seen in the image of 5 June 1993. Lateral mixing is suggested by the presence of shear instabilities caused by the two currents flowing in opposite directions. The arrows indicate the instability waves at the front. The circles indicate the buoys' position 20 days before the images' acquisition time. The colour bars indicate temperature in degC.

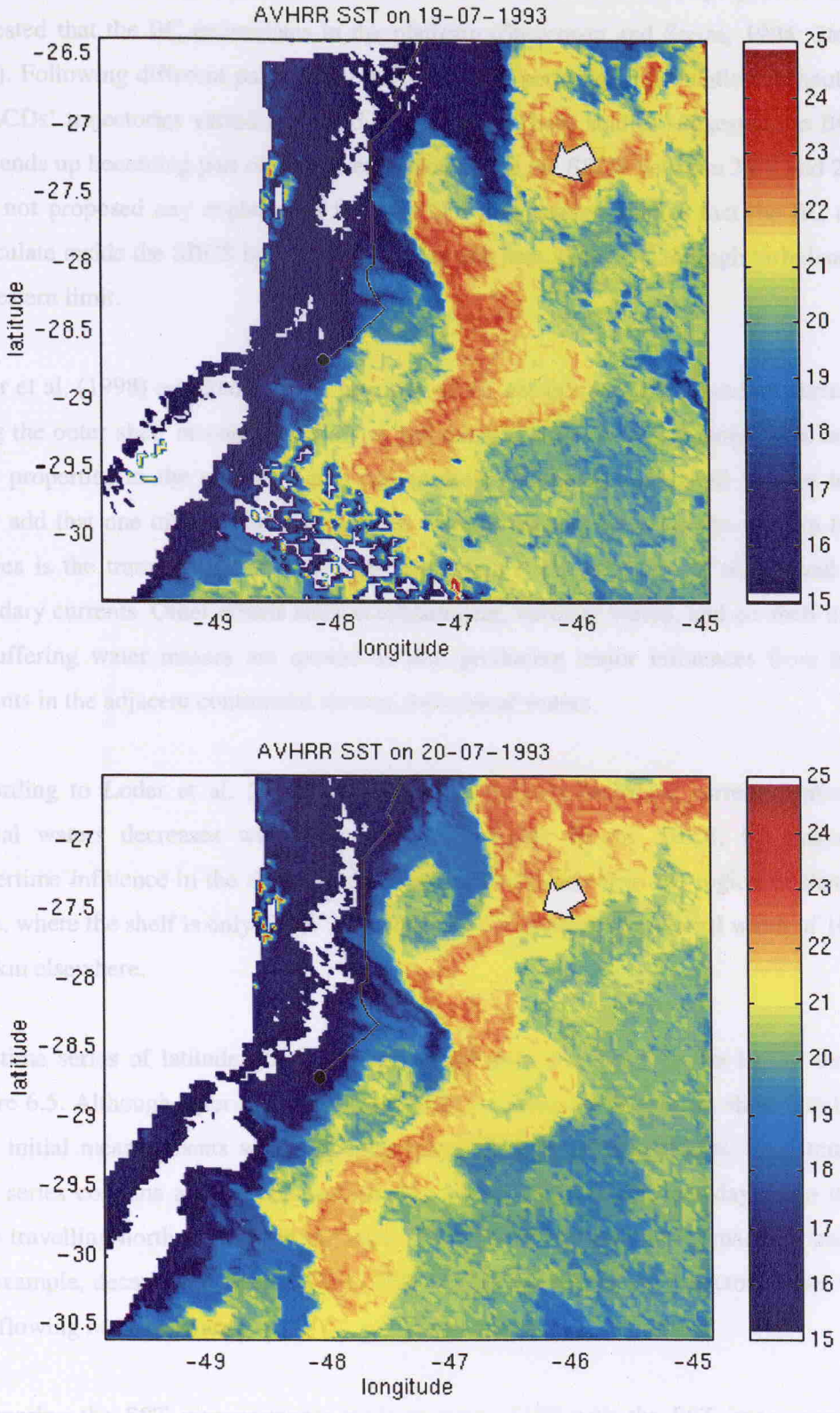

Figure 6.4. One-day sequence of AVHRR images taken in 19 July 1993 (top) and 20 July 1993 (bottom). Buoy 3180 track is seen in both images. The sequence illustrates the development of a mushroom-like structure in the BC in the vicinity of Santa Marta Cape at 28°S (indicated by the arrows). The circle indicates the buoy's position 20 days before the images' acquisition time. The colour bars indicate temperature in degC.

Early results from Lagrangian measurements made by the COROAS project in the SBCS suggested that the BC recirculates in the platform (Stevenson and Souza, 1994; Stevenson, 1996). Following different paths along the SBCS, the period of recirculation computed from the LCDs' trajectories varied from 115 to 161 days. These studies suggested the BC return flow ends up becoming part of an MC extension inside the SBCS between 33°S and 23°S, but have not proposed any explanation for that. Our data suggest that in fact the BC does not recirculate inside the SBCS but exchanges mass and heat with BCC through turbulence along its western limit.

Loder et al. (1998) reported that the majority of the ocean's western boundary currents flow along the outer shelf or continental slope, providing a large source of momentum and water mass properties to the coastal region due to their substantial associated volume transport. They add that one of the best known forms of eddy activity affecting the western boundary shelves is the transient warm core eddy generation from meanders of subtropical western boundary currents. Other effects such as entrainment, vorticity waves, and on-shelf intrusions or buffering water masses are quoted as also producing major influences from boundary currents in the adjacent continental shelves and coastal waters.

According to Loder et al. (1998), however, the western boundary currents' influence on coastal waters decreases with increasing shelf width. In the SBCS, for instance, BC wintertime influence in the shelf can be expected to be greater in the region of Santa Marta Cape, where the shelf is only about 70 km wide in comparison to a typical width of 100 km to 150 km elsewhere.

The time series of latitude, longitude and temperature measured by the LCDs are seen in Figure 6.5. Although entering the BCC on different dates, all time series show similarities in their initial measurements when the buoys were flowing northeastwards. Each temperature time series contains a quasi-constant cooling rate of about 0.12°C per day when the buoys were travelling northeastward in the BCC. Temperature measurements made by buoy 3179, for example, decay from about 22°C to 20°C during the part of the trajectory when the buoy was flowing northeastward.

Comparing the SST measurements made by buoy 3179 with the SST image presented in Figure 6.2, one can see that the warm core eddy shown there has a temperature of about 22°C and is surrounded by BCC waters at about 20°C. This leads to an interpretation that the LCDs entered the cooler BCC surrounded by warmer BC waters, probably inside small to mesoscale

eddies. Due to mixing, and consistent with the eddy dissipation, the temperatures measured in the initial part of the LCD trajectories decay with time.

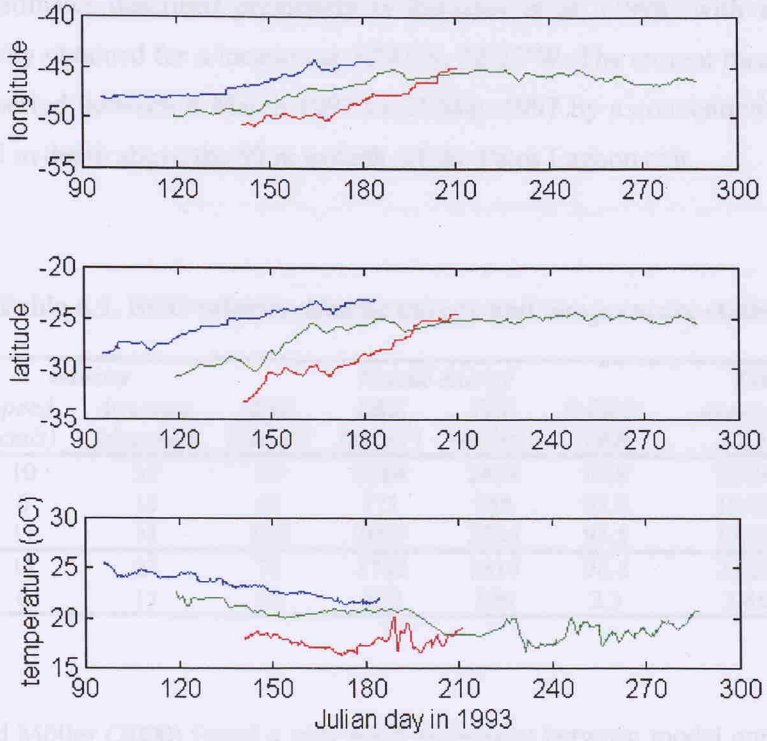

Figure 6.5. Time series of longitude, latitude and temperature for the Brazilian Coastal Current (colours are in accordance with Figure 6.1).

6.2.2. Current velocity, kinetic energies and temperatures

The mean current speed and direction, kinetic energies and basic statistics for the time series derived from the LCDs are presented in Table 6.1. Average surface (15 m depth) speed found for the BCC was 11 cm/s (std. dev. = 6 cm/s) and the mean direction was 27° (std. dev. = 11°). From the trajectories, one can see that the BCC can reach the vicinity of 23°S.

The BCC, in comparison to the BC, is relatively slow and flows in the opposite direction to the latter. The BC velocity estimates and measurements, although still sparse, are much more frequent than those of the BCC. Lagrangian estimates made using the COROAS dataset by Stevenson and Souza (1994), Stevenson (1996) and in this thesis have demonstrated that the BC speed varies from 15 cm/s to about 50 cm/s and that the current flows southwestwards.

As described before, direct measurements of the BCC are very sparse at the present. The few measurements made, some of them not even paying attention to the speeds of the current, were reported by Shaffer and Krauss (1995), Castro and Miranda (1998), Zavialov et al. (1998) and Stevenson et al. (1998). Very recently, Zavialov and Möller (2000) have compared the model estimates described previously in Zavialov et al. (1998) with a time series of current velocity obtained for a location at 32°41'S, 52°27'W. The current measurements were made for a period between 4 March 1997 to 27 May 1997 by a conventional current meter moored at 15 m depth above the 50 m isobath off the Patos Lagoon exit.

Table 6.1. BCC velocity, kinetic energy and temperature statistics

LCD	*velocity*		*kinetic energy*				*Temperature*	
	speed (cm/s)	*direction (degrees)*	*MKE (cm^2/s^2)*	*EKE (cm^2/s^2)*	*TKE (cm^2/s^2)*	*%EKE/ TKE*	*average (°C)*	*std.dev. (°C)*
3178	10	35	50	2384	2434	97.9	23.34	1.08
3179	6	15	17	771	788	97.8	19.82	1.43
3180	17	31	145	2089	2234	93.5	17.63	0.82
average	11	27	71	1748	1819	96.4	20.26	1.11
std.dev.	6	11	66	859	898	2.5	2.88	0.31

Zavialov and Möller (2000) found a very good agreement between model outputs and current meter measurements for the current flowing northeastwards off the south of the SBCS region and Uruguay. This current, named by the authors as the Rio Grande Current, was found to have a seasonal average speed of up to 50 cm/s, but instantaneous values of up to 100 cm/s were also registered in the current meter records.

Table 6.1 also indicates that the Mean Kinetic Energy (MKE) in the BCC varied from 17 cm^2/s^2 to 145 cm^2/s^2, while the Eddy Kinetic Energy (EKE) varied from 771 to 2384 cm^2/s^2. In Table 5.10 of this thesis we have presented MKE and EKE estimates for the BC and for the South Atlantic Current. The mean MKE in the Brazil Current was 801 cm^2/s^2 and the mean MKE in the South Atlantic Current was 59 $cm^2/s/^2$. Mean EKE estimates for the BC and the SAC were 1294 cm^2/s^2 and 3268 cm^2/s^2. That represents, respectively, 61.7 % and 98.4 % of the total kinetic energy present in the respective currents.

The result shown here for the BCC indicates that this current, as well as the SAC, contains more than 95 % of its energy in small scale perturbations and eddy activity rather than in the mean flow. Schaffer and Krauss (1995) have estimated that the EKE of the Malvinas Current is about 500 cm^2/s^2. A maximum of 1600 cm^2/s^2, however, was found in the BMC region,

decreasing again farther east in the SAC. This indicates that the BCC and the SAC, both extensions of the BC and the MC, respectively, seem to be less stable and more energetic than their principal originators.

The temperature statistics for the BCC are also contained in Table 6.1. The mean value of 20.26°C was found for this current. This mean is higher than that expected for the BCC as seen from the satellite images, and can only be explained by the presence of warm water from the BC being advected in the BCC, which is difficult to spot in the images. As discussed before, the buoys were probably carried by these dissipating warm core eddies inside the BCC and, therefore, the overall temperature measurements made by them probably did not represent those typical of the neighbouring BCC waters.

6.2.3. BCC energy spectra

The FFT analysis of the buoys' time series in the BCC revealed the presence of energy peaks significant at the 95 % confidence level at periods varying from 103.1 days to 1.5 days. The FFT spectra for the temperature, instantaneous zonal velocity and instantaneous meridional velocity time series obtained for the BCC are seen in Figures 6.6 to 6.8. Table 6.2 describes the more energetic peaks.

A peak at 103.1 days was found in the temperature and instantaneous meridional velocity time series of buoy 3179 (Figure 6.7). A peak at 70.4 days was present in the instantaneous meridional velocity series of buoy 3179. Both time series of temperature of buoy 3178 (Figure 6.6) and instantaneous meridional velocity of buoy 3180 (Figure 6.8) presented a peak at 51.3 days. Towards the lower periods, high energy peaks were most commonly found at about 34-35 days, 29-30 days, 20-23 days, 10-13 days and 6-7 days. Many other peaks are distributed at lower periods down to about 2 days.

The energy peaks found for the BCC are generally distinct from those found for the BC and the SAC, which were described in Section 5.5.4 in this thesis. An exception to that occurs at the periods close to 10-13 days which are mainly present in most of the BC time series but also in some of the SAC and BCC series.

According to Castro and Miranda (1998), the current variability in the middle and inner South Brazilian Bight shelf is dominated by subtidal and tidal oscillations. Large energy peaks,

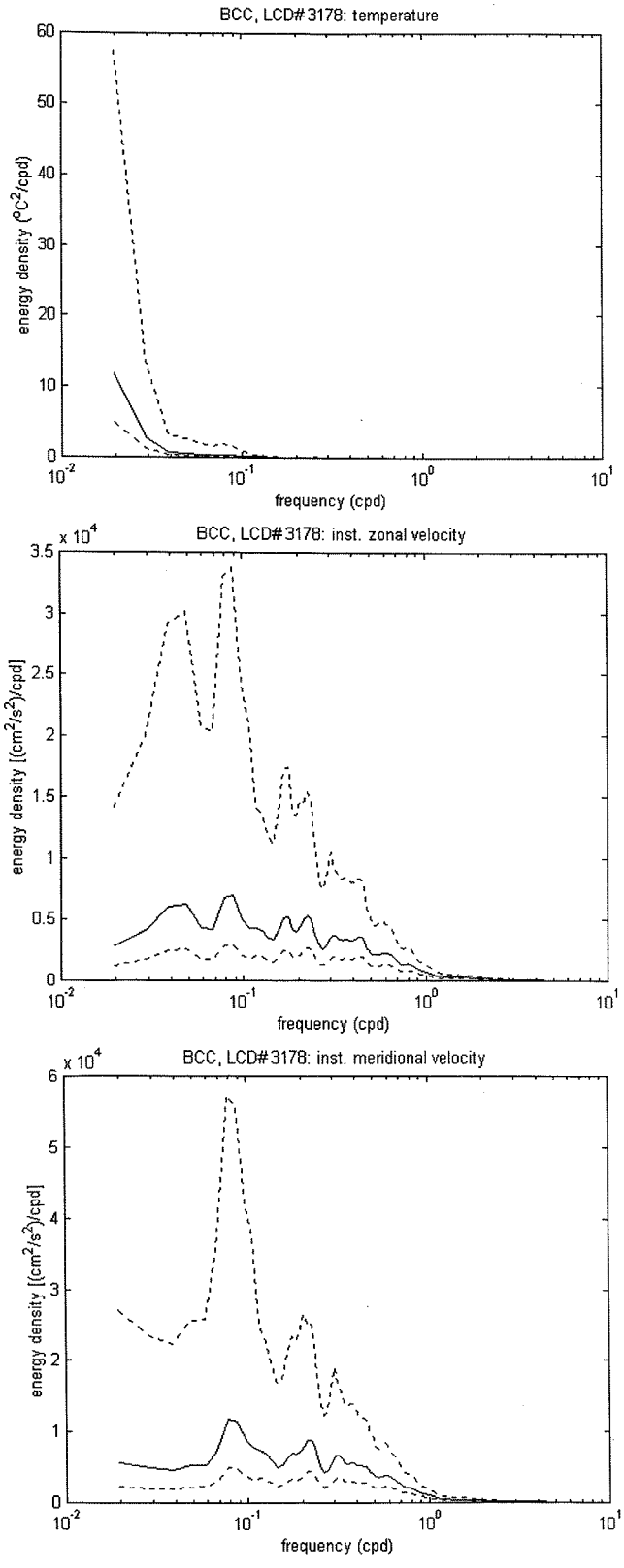

Figure 6.6. Energy preserving spectra of the LCD no. 3178's temperature (upper panel), instantaneous zonal velocity (middle panel) and instantaneous meridional velocity (lower panel) time series in the Brazilian Coastal Current. The dashed lines represent the 95 % confidence interval.

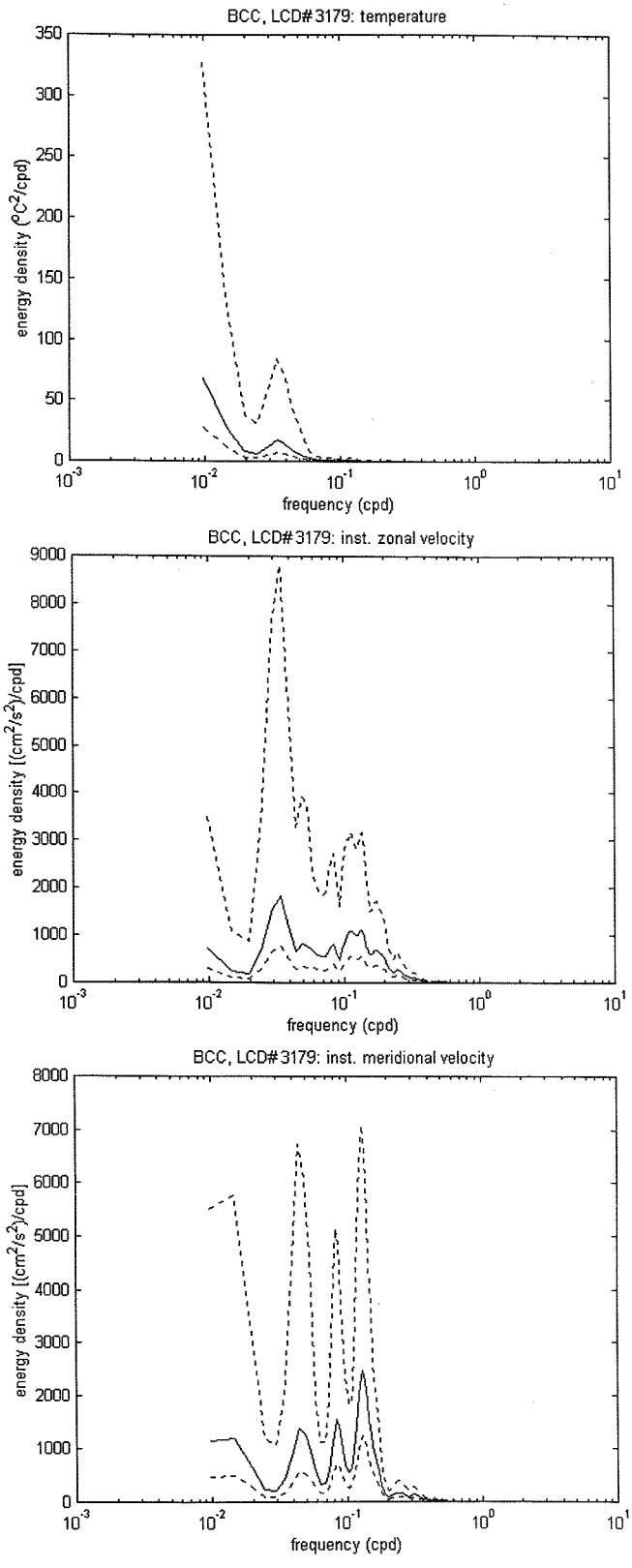

Figure 6.7. Energy preserving spectra of the LCD no. 3179's temperature (upper panel), instantaneous zonal velocity (middle panel) and instantaneous meridional velocity (lower panel) time series in the Brazilian Coastal Current. The dashed lines represent the 95 % confidence interval.

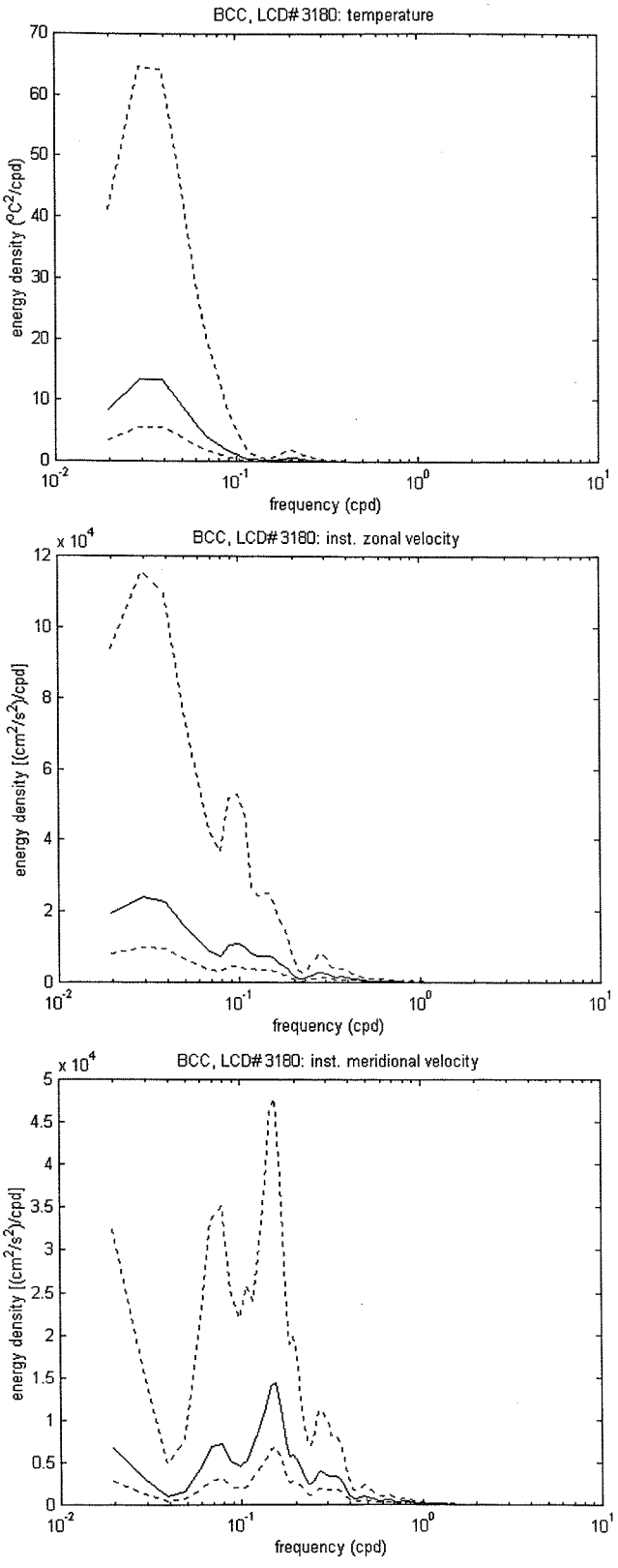

Figure 6.8. Energy preserving spectra of the LCD no. 3180's temperature (upper panel), instantaneous zonal velocity (middle panel) and instantaneous meridional velocity (lower panel) time series in the Brazilian Coastal Current. The dashed lines represent the 95 % confidence interval.

however, are concentrated in the periods of 3-7 days and at 9-15 days, the same as the wind and sea-level oscillations. These authors, for instance, report that the occurrence of the frontal systems (which are driving the winds' intensity and direction) over the Southwestern Atlantic Ocean between 20°S and 34°S has a time scale of 5-10 days between passages.

Table 6.2. Period of the major energy peaks for the buoys' temperature and instantaneous velocity time series (dominant periods underlined):

Brazilian Coastal Current

buoy	*temperature (days)*	*zonal instantaneous velocity (days)*	*meridional instantaneous velocity (days)*
3178	51.3	20.7; 11.5; 5.8; 4.5; 3.3; 2.3; 1.7	12.6; 5.7; 4.6; 3.3; 1.7
3179	103.1; 28.9	103.1; 29.5; 20.2; 12.1; 9.2; 7.4; 5.9; 4.0	70.4; 23.1; 12.1; 7.8; 4.2; 3.2
3180	34.5; 5.0	33.9; 10.4; 6.9; 3.6; 2.7	51.3; 13.0; 6.5; 3.6; 3.0; 2.1; 1.5

As reported in Chapter 5 of this thesis, peaks of 11 days and 6.5 days were found in wind data of the SBB by Stech and Lorenzzetti (1992). Analysis of sea level data in the same region demonstrated the existence of a peak centred at 7 days, which Stech and Lorenzzetti (1992) have associated with the atmospheric pressure systems crossing the SBB.

Stech and Lorenzzetti (1992) pointed out that the passage of low-pressure atmospheric systems is one of the major forcing mechanisms present in the SBB during wintertime. The cold atmospheric fronts occurring in the SBB were reported to have a displacement speed of 500 km/day in the southwest to northeast direction. This is the same direction as the BCC current. Stevenson et al. (1998), studying the intrusion of cool waters in the SBCS, also considered that the atmospheric forcing would drive the northeasterly currents in that region.

6.3. The BCC and BC extreme positions

The mean oscillation of the STF between 1982 and 1995, as seen from the MCSST monthly climatological averages, was already discussed in Section 5.2.1. As pointed out before, the western extreme of the STF indicates the BMC, and the two extreme vertices of the characteristic 'Z' shape of the 20°C isotherm in the BMC region indicate the location of the maximum penetration of both the MC (and its extension, the BCC) and the BC. In this section we analyse the overall set of 168 MCSST monthly averaged images taken from January 1982

to December 1995 to track the extreme positions reached by both the BCC and the BC during that period of time. As described in Section 4.2.3, the positions of maximum penetration for both the BC and the BCC were treated in the form of a time series of longitude and latitude per month from January 1982 to December 1995.

Because the extreme positions of MC or BCC and of BC were taken simultaneously from the same isoline in each particular MCSST image, their time series are related to each other. They will be compared here. Considering that the BCC is an extension of the MC towards the coast in the region of the SBCS, we will simply refer to the MC extreme positions as the BCC extreme positions.

Figure 6.9 shows the extreme position time series for both the BCC and the BC. Peaks in the time series are associated with the wintertime. The seasonal oscillation of the BCC and the BC extremes is clearly seen at the western extreme of the STF in Figure 5.1. Since the oscillation of the currents is parallel to the Brazilian coast, westward displacement is coupled with southward movement, and eastward movement has its northward counterpart. The time series of BC longitude extremes is noisier than the other series, and the zonal displacement of this current is wider, as expected. The BC southernmost extremes are located in the origin of the SAC, and its position is not restricted to the continental shelf.

The minimum and maximum latitudinal positions found for the BCC were 39.1°S and 23.6°S occurring in February 1984 and August 1983 (Figure 6.10), respectively. The difference between minimum and maximum latitude positions for the BCC is 15.5°, which is about 1700 km. For the BC, on the other hand, the minimum and maximum latitudinal extremes were 43.8°S and 28.3°S in February 1984 and October 1987, respectively. The latitudinal difference between the BC extremes was 15.5°, by coincidence the same as found for the BCC.

Table 6.3 and Figure 6.11 show the basic statistics (mean and standard deviation) resulting from the BCC and the BC extreme position locations for each month from January 1982 to December 1995. August was the month when in the mean both the BCC and the BC reached their northernmost limits. The mean north extreme for the BCC was 25.2°S (std.dev. = 1.6°), and for the BC 30.3°S (std.dev. = 1°). For the southernmost extremes, the BCC presented a mean latitude of 37.2°S (std.dev. = 1°), and BC of 42°S (std.dev. = 1°). Hence, the BCC was found to oscillate an average 12° in latitude, which represents 1334 km. The BC, on the other hand, was found to oscillate an average of about 11.7° in latitude or 1301 km.

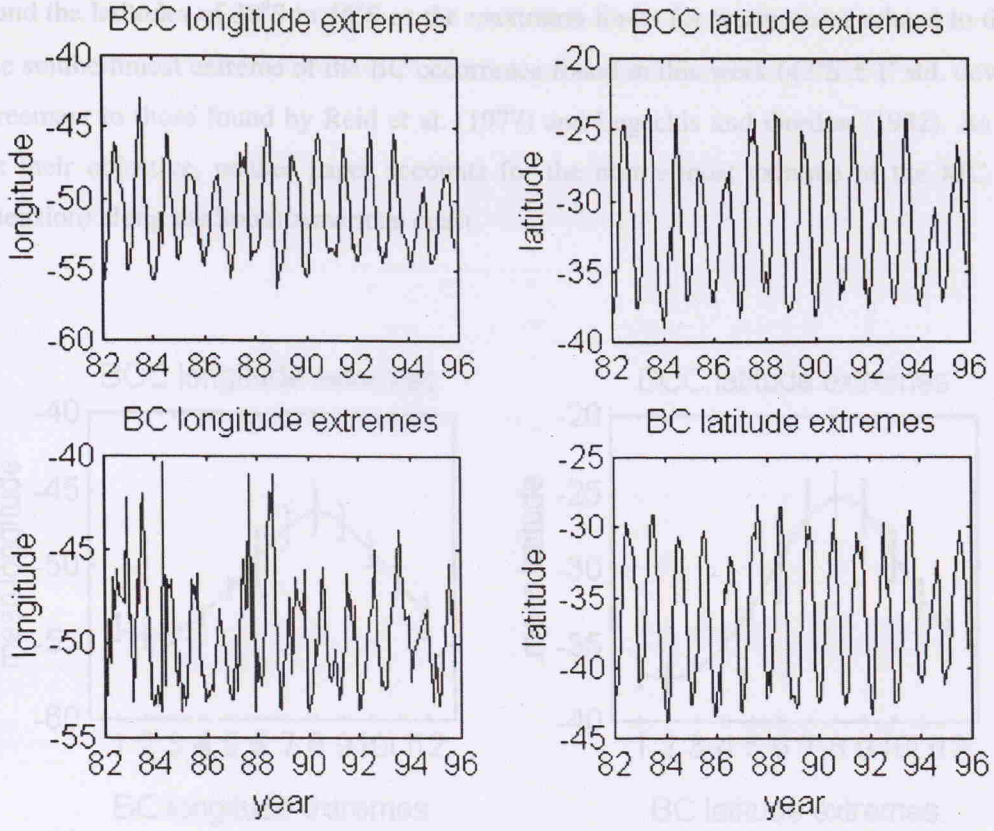

Figure 6.9. Extreme position time series for the BCC and BC.

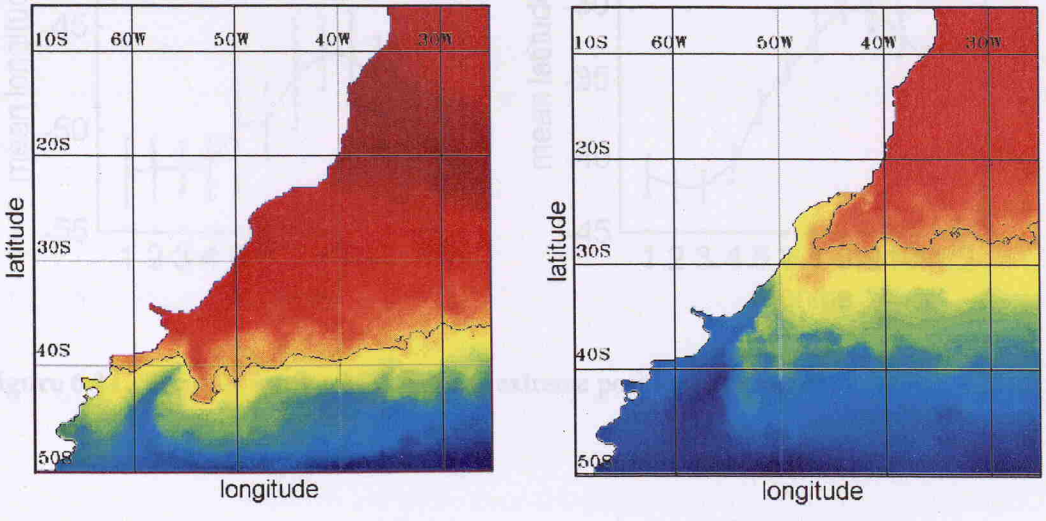

Figure 6.10. MCSST images for February 1984 and August 1983 indicating the minimum (left) and maximum (right) latitudinal position of the BCC for the period of 1984 to 1995. The black line represents the 20°C isotherm.

Reid et al. (1977) report that the position in which the BC reverses its direction (interpreted here as the BC southernmost extreme) is between 40°S and 46°S. These authors add that this position is further south than the mean BMC oscillation region. Legeckis and Gordon (1982)

found the latitudes of 38°S to 46°S as the maximum limits for warm water related to the BC. The southernmost extreme of the BC occurrence found in this work (42°S ± 1° std. dev.) is in agreement to those found by Reid et al. (1977) and Legeckis and Gordon (1982). As it was not their objective, neither paper accounts for the northermost extreme of the MC (or its extension) along the South American coast.

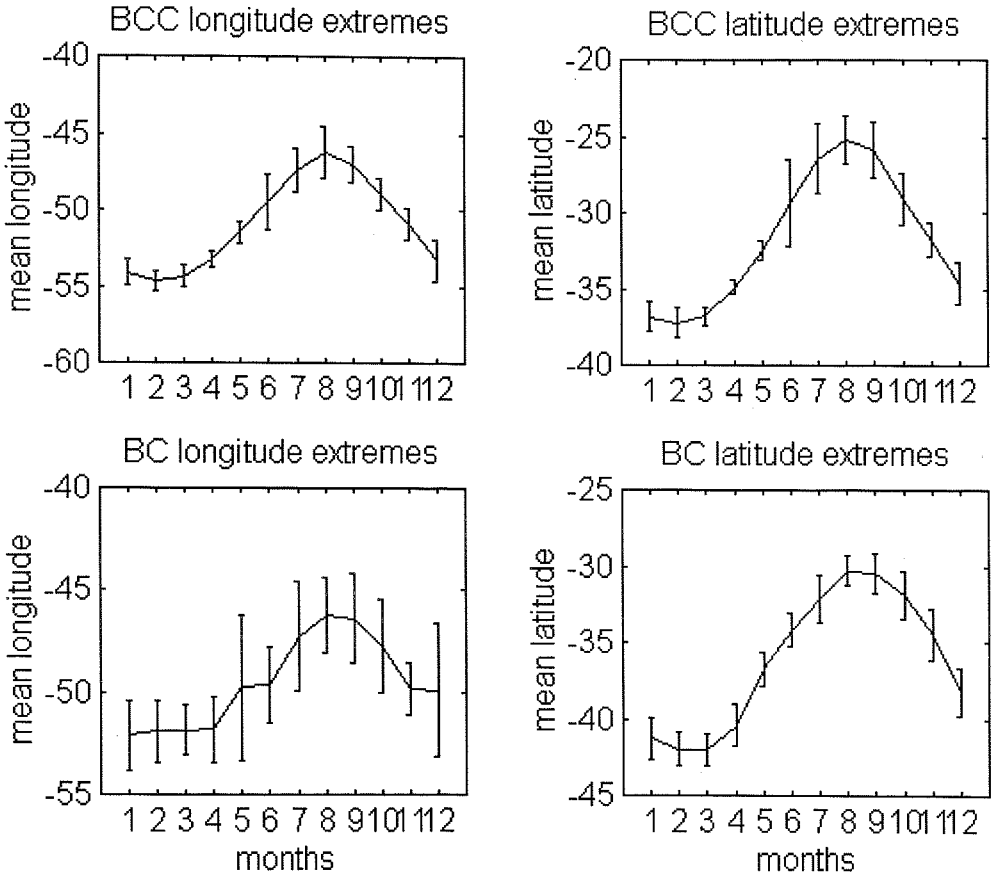

Figure 6.11. Statistics for the BCC and BC extreme positions per month.

Working with full-resolution AVHRR data collected between July 1984 to June 1987, Olson et al. (1988) established the statistical characteristics of the separation region from the continental shelf (position of crossing with the 1000 m isobath) for both the BC and the MC. Considering the BC, these authors found that this current separates from the coast at the mean latitude of 35.8°S, with a standard deviation of 1.1°. However, the total range of latitudes where the BC separates from the coast (difference between maximum and minimum values) was found to be 4.8°. This value is less than half the value of 11.7° found here for the BC

oscillation. Causes for this disagreement are possibly related to the different methodologies employed to describe the BC extremes by Olson et al. (1988) and in this thesis.

Table 6.3. Statistics for the BCC and BC extreme positions over the year

month	*lat. BCC (°S)*		*long. BCC (°W)*		*lat. BC (°S)*		*long. BC (°W)*	
	mean	*std.dev.*	*mean*	*std.dev.*	*mean*	*std.dev.*	*mean*	*std.dev.*
Jan	36.8	0.9	54.1	0.8	41.3	1.4	52.1	1.7
Feb	37.2	1.0	54.7	0.7	42.0	1.1	51.9	1.5
Mar	36.8	0.6	54.3	0.8	42.0	1.0	51.8	1.2
Apr	34.1	0.5	53.3	0.5	40.4	1.4	51.0	1.6
May	32.4	0.6	51.4	0.7	36.7	1.1	49.8	3.5
Jun	29.4	2.8	49.4	1.8	34.2	1.1	49.7	1.9
Jul	26.5	2.3	47.4	1.4	32.1	1.6	47.3	2.7
Aug	25.2	1.6	46.3	1.6	30.3	1.0	46.2	1.9
Sep	25.8	1.8	47.0	1.2	30.5	1.3	46.4	2.2
Oct	29.1	1.7	48.9	1.0	31.9	1.5	47.7	2.3
Nov	31.8	1.1	50.9	1.0	34.5	1.7	49.8	1.2
Dec	34.6	1.3	53.3	1.3	38.3	1.5	49.9	3.3

While Olson et al. (1988) described the position where the BC separated from the coast at the 1000 m isobath, in this thesis we located the position where the 20°C isoline reached its southernmost extreme in the BMC region. Besides this, the time series used in this work is far more extensive than the one used by Olson et al. (1988), which was restricted to 1984 to 1987.

As noted in Figure 6.9, the years of 1985 and 1986 (both included in Olson's paper) are also seen in the time series as years when the BCC and the BC had their wintertime northernmost limits reduced by about 3° in latitude with respect to adjacent years. This leads to an interpretation that 1985 and 1986 (as well as 1994 - note Figure 6.9) have had anomalously mild winters, which reduced the penetration of the BCC. Explanations for that cannot rely on the occurrence of El Niño, for instance, since this phenomenon did not occur either in 1985-86 or in 1994. In the winters of 1985-86, the La Plata river also did not display any anomalous outflow in relation to adjacent years (Raul Guerrero, personal communication).

In recent works, Sunyé and Servain (1998) and Sunyé (1999) investigated the effects of the climatological variability of the ocean on the sardine *Sardinella brasiliensis* fisheries in the region between Santa Marta Cape and Cabo Frio (~23°S to 28°S). Utilising historical hydrographical data, Sunyé (1999) determined the temperature fields for the South Brazil Bight and studied the penetration of waters of subantarctic origin in the study region from

1982 until 1992. The author utilised the distribution of the 20°C isotherm for the month of August to conclude that the mean latitude of maximum penetration of cold waters in the SBB is 24°S during this month. This latitude is in agreement to the one found in this work (25.2°S ± 1.6° std. dev.) and is an indication that the MCSST data set used here is reliable for use in coastal regions for climatological purposes.

Sunyé and Servain (1998) studied the landings of the sardine in three Brazilian states from the south to the north of the SBB (Santa Catarina, São Paulo and Rio de Janeiro, respectively). The principal fishing harbours at these states are, respectively: Itajaí (~27°S), Santos (~24°S) and Rio de Janeiro city (~23°S). Total catches were computed per month for the period between 1980 and 1990. The complementary percentage of the total catch of sardine per month in Santa Catarina, São Paulo and Rio de Janeiro is seen in Figure 6.12.

Following Sunyé and Servain (1998), Figure 6.12 indicates that the landings of sardine in Rio de Janeiro, in the north of the SBB, are relatively low thoughout the year. They represent 20 % of the total Brazilian catches. Each of the other two states at time, on the other hand, can alone account for up to 60 % of the total catches depending on the season of the year. In São Paulo, for instance, the landings are high in winter (maximum in August) and low in summer (minimum in February). The reverse is true in Santa Catarina state. Sunyé and Servain (1998) conclude that the sardine landings in the two Brazilian states to the south of the SBB are affected by meteorological and oceanographic parameters. The major cause of the variations in the oceanographic factors in the SBB is the penetration of the less saline (coastal or subantarctic) waters in the Brazilian shelf.

By comparing Sunyé and Servain's (1998) Figure 6.12 with Figure 6.11 it is very clear that there is a coincidence between the latitudinal extreme positions of the BCC (Figure 6.11, upper right panel) and the sardine catches in São Paulo and Santa Catarina. When BCC northern limits are to the south of SBCS during the months of summer, the sardine catches are higher in Santa Catarina. When BCC latitudinal extrema are displaced to the north in winter, the catches of sardine are higher in São Paulo. The investigation of the relationship between sardine catches and the position of the 20°C isotherm (an indication of the BCC/BC front northern extreme) measured by satellites in the SBCS can be a step forward towards the predicability of the *Sardinella braziliensis* catches in São Paulo, considering that the fisheries effort is also known.

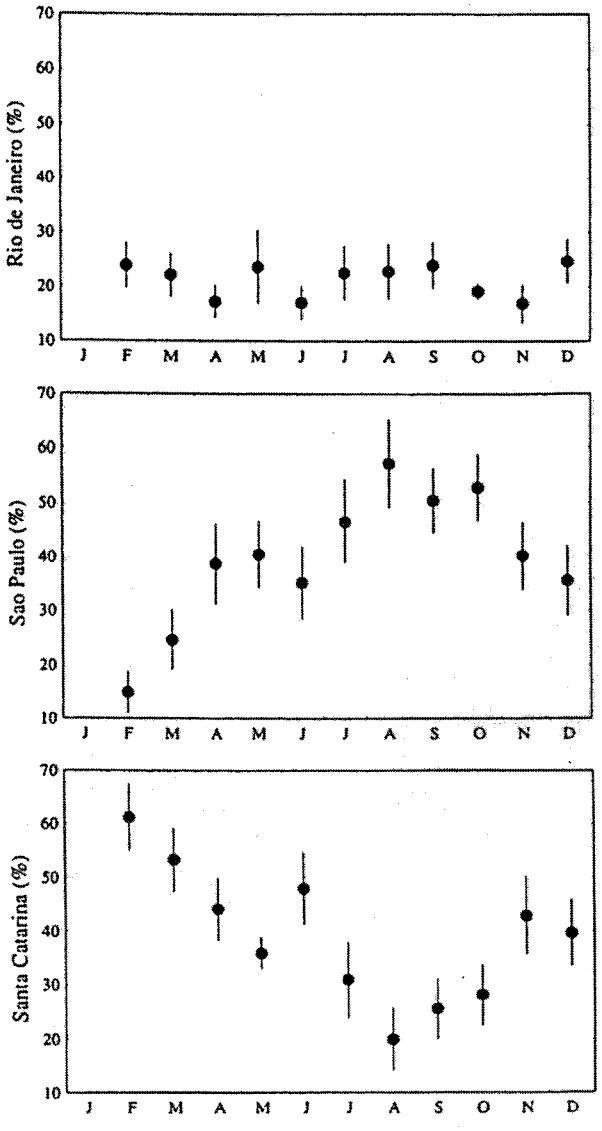

Figure 6.12. Total catch of sardine (*Sardinella brasiliensis*) in the SBB for the period between 1980 and 1990. Panels ordered from bottom to top represent complementary percentages of the total catch for three Brazilian States from south to north (Santa Catarina, São Paulo and Rio de Janeiro), respectively. Error bars represent ± 1 standard deviation. Fisheries of sardine is prohibited in January, hence there are no data available for that month. Source: Sunyé and Servain (1998).

Figure 6.13 displays the BCC and the BC extreme positions along the South American coast for the different seasons of the year (summer: December to February; autumn: March to May; winter: June to August; spring: September to November). It seems that the vicinity of 32°S marks the extremity of occurrence of the BCC during summer and autumn months. To the north of 32°S, the BCC only penetrates the SBCS during the winter or spring months. The BCC extreme position, as seen by the distribution of the crosses in Figure 6.13, is continuous along the SBCS and restricted to isobaths shallower than 200 m (not shown) in the inner shelf, consistent with the trajectories described in this current by the LCDs in 1993 (Figure

6.1). The BC distribution for all seasons, on the other hand, is broader, not shelf-constrained and resembles, as expected, the distribution of the frontal systems analysed for the study area in Chapter 5 using high-resolution AVHRR data (Figures 5.17 and 5.18).

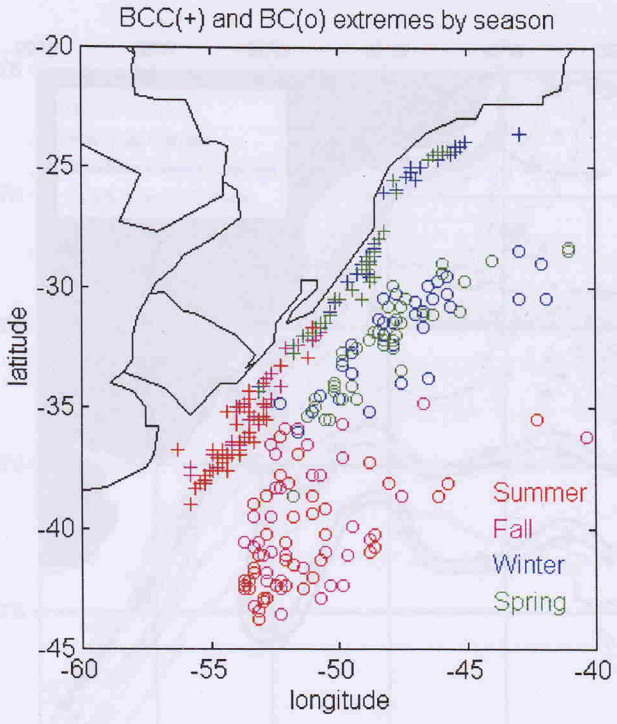

Figure 6.13. BCC and BC extreme positions per season in the SBCS.

6.4. Summary and final remarks

In this chapter, the Brazilian Coastal Current is described as a relatively slow but highly energetic coastal current, flowing in the opposite direction to the Brazil Current. The current occurs over the South Brazilian Continental Shelf during spring to wintertime, reaching its maximum extreme at about 24°S in August every (non-anomalous) year.

High-resolution satellite imagery and surface drifters have been used in conjunction to demonstrate that warm core rings expelled from the BC enter the BCC and are advected northeastward with this coastal current. MCSST data collected from 1982 to 1995 were used to track the extreme positions for the BC and the BCC, and to demonstrate that the penetration of the BCC on the SBCS to latitudes of about 24°S is not anomalous but rather the normal process occurring most years in the Brazilian continental shelf. One of the principal

mechanisms to drive the BCC penetration is believed to be related more to the large-scale oscillation of the Subtropical Front in the open South Atlantic Ocean than to the local winds at the Brazilian coast.

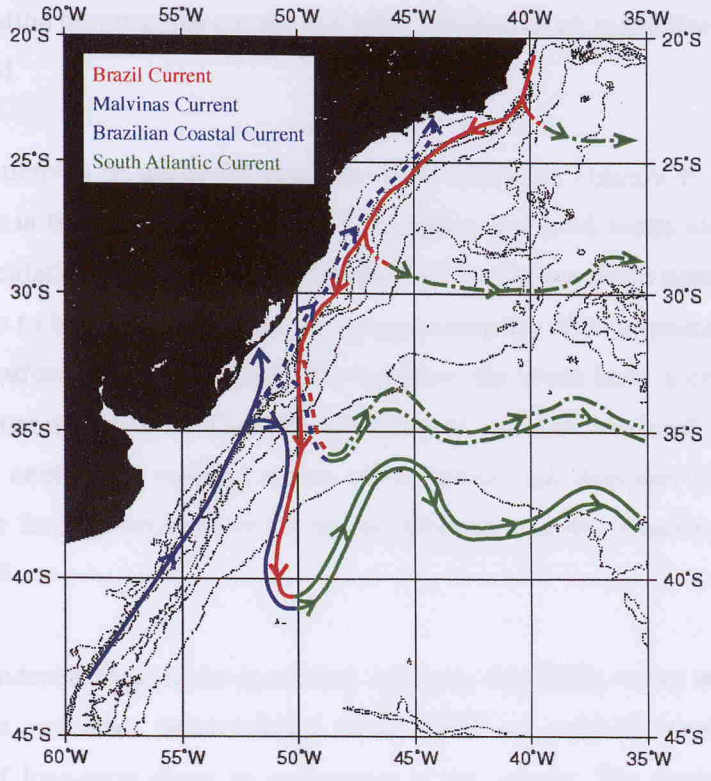

Figure 6.14. Schematic illustration of the surface currents in the SBCS and BMC regions. BCC occurs in wintertime as an extension of MC carrying coastal waters in latitudes lower than 32°S.

Using both the Lagrangian and the MCSST dataset presented here, Figure 6.14 presents a schematic interpretation of the mean BCC and BC distributions through the year at the SBCS. Although recent papers have dealt with the current distribution in the South and Southwestern Atlantic (e.g. Peterson and Stramma, 1991; Piola and Rivas, 1997; Loder et al., 1998), all of them fail to propose a satisfactory scheme for the BCC domain in the SBCS during the winter. A simple, didactic scheme like the one seen in Figure 12, was never before proposed for the Southern Brazilian continental shelf region, and can be used in future studies planned for that region.

Bearing in mind that SAW and CW transported by the BCC are much more productive than the oligotrophic TW transported by the BC (Hubold, 1980; Castello et al., 1990; Ciotti et al., 1995; Seeliger and Odebrecht, 1997; Nienchesky and Fillmann, 1997), the environmental and economic aspects of the wintertime domination of the SBCS by waters with subantarctic and coastal origin is of considerable significance and needs to be understood urgently. The relation between the BCC and the sardine fisheries in the SBCS was explored to some extent here, but the relation between this current and other fisheries stock in the Brazilian shelf ought also to be studied.

Remaining questions to be answered about the BCC behaviour concern its relation with the discharge cycles in the La Plata river and Patos Lagoon, the local winds along the Brazilian shelf and the oscillation of the STF. Although the STF oscillation in the South Atlantic Ocean is supposed here to be one of the major forces governing the BCC intrusion further north in the Brazilian platform, the local winds blowing from the south have a contribution which needs to be better understood. The Ekman transport and the sea level elevation (which depends on the continental outflow among other factors) are indicated by Zavialov et al. (1998) to be the forcing mechanisms for the northbound currents occurring at the southern part of the SBCS.

The complete understanding of the dynamical structure, variability, water mass composition, spatial signature and other characteristics of the BCC can only be assessed through the establishment of long-term direct measurements in the current. The study of the relations between the development of the BCC and the processes occurring at the BMC region, as well as connections with the large scale processes in the Atlantic or Pacific, should also be the subjects of further research.

CHAPTER 7

EDDY OBSERVATIONS AND CHARACTERISATION

7.1. Introduction

In this section we investigate the characteristics of the eddies found in the Southwestern Atlantic Ocean in 1993 and 1994 as they were measured by the combination of surface drifters and high-resolution SST images. The investigation of these eddies is made according to their characteristic sizes (perimeters or diameters), rotational periods and velocities, Rossby numbers and relation to the local internal Rossby radius of deformation.

In the Southwestern Atlantic Ocean, most of the eddy activity is related to the BMC region (e.g. Legeckis and Gordon, 1982; Olson et al., 1988). Nevertheless, the characterisation of the BMC eddies is generally restricted to their sizes and location. Given the relatively few *in situ* data, most of the works have described these structures using only remote sensing images. To our knowledge, very few references are available describing other eddy properties such as their rotational periods or tangential velocities, for instance. These are important parameters for describing the eddy field more realistically, and are studied in more detail in this thesis.

With respect to the South Brazilian Continental Shelf (SBCS), the situation is a little worse than that of the BMC region. Some previous descriptions of the eddies in the Brazil Current can be found in the works made by Garfield (1990) and Schmid et al. (1995), for example. Unfortunately, these individual efforts fail to provide a general description of the eddies across the SBCS and over long periods of time. Some eddy activity in the SBCS was also described in the first results from the COROAS project (e.g. Lorenzzetti et al., 1994; Campos et al., 1996a; Stech et al., 1996) and, very recently, in the first results of oceanographic programmes conducted by INPE (e.g. Lorenzzetti and Kampel, 1998). The initial COROAS papers, although using some of the same material as studied in this thesis, have generally dealt with specific events, neither addressing the overall COROAS experimental phase nor making any comparison to other eddies found in the Southwestern Atlantic Ocean, as will be presented in this chapter.

In our systematic study of the available data, small eddies, generally ignored when utilising remote sensing techniques because of the difficulty in spotting them, have been found to be present in both the AVHRR images and in the buoy trajectories. They were associated with the three currents studied: the BC, the BCC and the SAC. These eddies were several times smaller than the typical Rossby radius of deformation for the regions of the BMC and of the BC/BCC front, indicating extremely turbulent fluxes or wind driven circulation where inertial forces were much more important than the rotational forces.

Some of the eddies present in the BC/BCC front were similar to the shelfbreak eddies found in the Middle Atlantic Bight off the United States east coast (e.g. Garvine et al., 1988). Inshore eddies present in the BCC, however, seem to be related to current reversals probably caused by the passage of atmospheric fronts. To our knowledge, apart from references in some COROAS papers to their presence in the buoy tracks (e.g. Stevenson, 1996), neither the characteristics of the BCC eddies nor the possible driving mechanisms involved in their generation at the shelf or shelfbreak have been previously described.

Based upon the buoys' trajectories, empirical relationships were found to link the eddies' sizes to their rotational periods and tangential velocities. These relationships can be useful for monitoring the effects of the eddies in the Southwestern Atlantic Ocean by remote sensing techniques when *in situ* measurements are lacking. According to Richards and Gould (1996), the advent of remote sensing of the oceans by means of infrared sensors has strongly contributed to the study of these features and their formation mechanisms, but remote sensing on its own has some limitations like, for example, the incapacity for estimating the rotational velocities, periods of rotation or the vertical structure of the eddies.

At the present, eddy properties are being investigated for the World Ocean in order to assess the importance of such structures in the world ocean's climate and heat and mass balance. The eddies' relative importance for the ocean's circulation is being investigated through global circulation numeric models with eddy-resolving properties like the one developed by Semtner Jr. and Chervin (1988) for the World Ocean Circulation Experiment. This chapter provides several new insights on the properties of the BMC and SBCS eddies, offering new material and descriptions that are potentially useful for future work which ought to investigate the eddy field and its impact in the Southwestern Atlantic Ocean environment and physics.

7.2. The eddies in the buoy trajectories

The eddies revealed in the overall buoy tracks are seen in Figure 7.1. The figure presents the total of 126 eddies obtained from the trajectories in relation to their direction of rotation and bathymetry of the study area. As described in Section 4.1.2.4, the eddies were separated into two different classes. Class 1 accounts for about 65 % of the total number of eddies and contains the eddies with rotational periods (T_R) less than 5 days and perimeters (P) smaller than 100 km. Class 2 represents the biggest eddies where $T_R \geq 5$ days and $P \geq 100$ km.

Figure 7.1 also demonstrates that there is no obvious relation between the direction of rotation and the position of the eddy, or the particular current from which the structures have been formed (for comparison, see Figure 5.28). The eddies in the western STF are the biggest. They do not seem to be associated with the bathymetry, but rather with the troughs of the BMC meanders described in Chapter 5.

The eddies found in the final trajectories of buoys 3182 and 3185 (Figures 5.28 and 7.1), both cyclonic and anticyclonic ones, seem to be associated with the Rio Grande Rise, a topographic structure located at about 30°S, 35°W. The eddies in the BC/BCC front are smaller than the ones found in the SAC. Some of those found in the BCC, in water depths shallower than 100 m, are very elongated and reminiscent of tidal or inertial oscillations but are possibly related to current reversals caused by the passage of atmospheric frontal systems.

In fact, an animation made with the buoy trajectories showing their displacements in time intervals of 1 day (not shown here) has demonstrated that for time periods of 2-4 days in April to June 1993 (when two or three buoys were at the same time in the BCC), current reversals occurred during their advection to the north. It was a surprise to observe that, although the three buoys were being advected in the BCC in positions about 300-400 km apart one from another, they suffered the same reversals at the same time. That implies the same forcing mechanism was acting in the BCC at the SBCS over a length scale of several hundreds of kilometres. The periods and scales of these perturbations suggest the passage of cold atmospheric pressure systems over the SBCS. The signature of these reversals in the buoy trajectories are the elongated (cyclonic or anticyclonic) eddies along the Brazilian shelf seen in Figure 7.1.

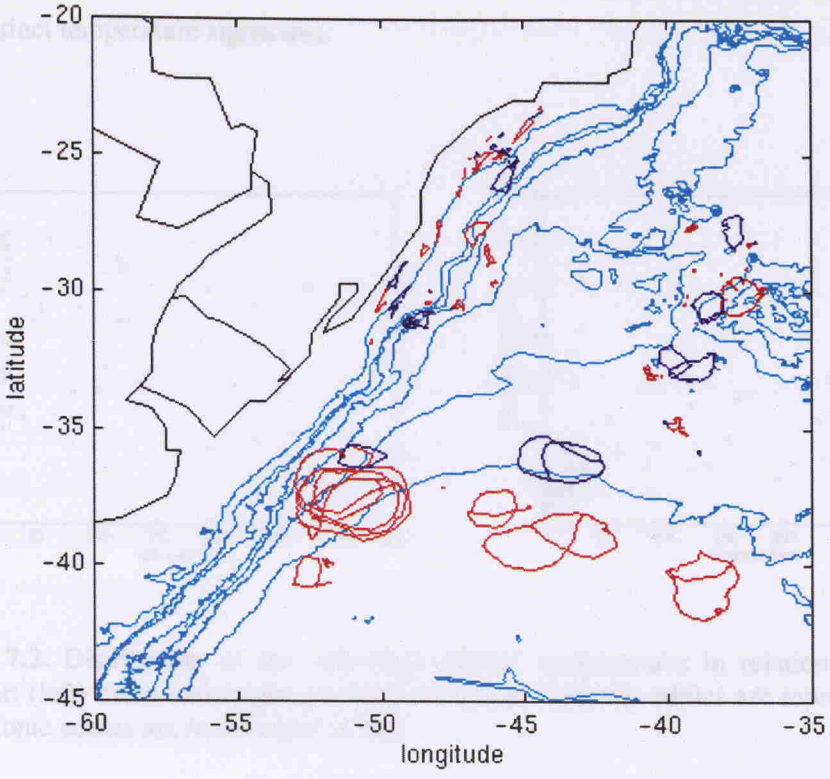

Figure 7.1. Eddies present in the overall buoy tracks. Cyclonic (clockwise rotation) eddies are represented in dark blue, anticyclonic (anticlockwise rotation) eddies are represented in red. Bathymetric contours are in accordance with Figure 1.1.

The distribution of the eddies' temperatures, as measured along the trajectories of the buoys around the eddies' perimeters, are presented in Figure 7.2. In this figure, the mean temperatures and their standard deviations are plotted against the eddies' diameters. We attempted to find some relationship between the temperature and the eddies sizes, but Figure 7.2 demonstrates that these properties are independent. Moreover, considering that the buoys which were sampling bigger eddies had more temperature retrievals then the ones sampling smaller eddies, it might be expected that the SST standard deviations would be higher for the bigger eddies. This is partially the case for the eddies in class 1, where the diameter (D) is smaller than 31.8 (100/π) km. For class 2 eddies (D $\geq$ 31.8 km), however, the scatter of the points is such that no dependency can be found between temperature and diameter.

Figure 7.2 also shows that the eddies had temperatures varying in the same range of about 17°C to 25°C independently of their sizes or direction of rotation. The temperatures around the eddies were very coherent, with standard deviations tending to be smaller than 1°C. That confirms the expected efficiency of the drifters to follow a particular water mass (represented

by a particular isotherm) and, in the case of the eddies, to delimit them from adjacent waters with distinct temperature signatures.

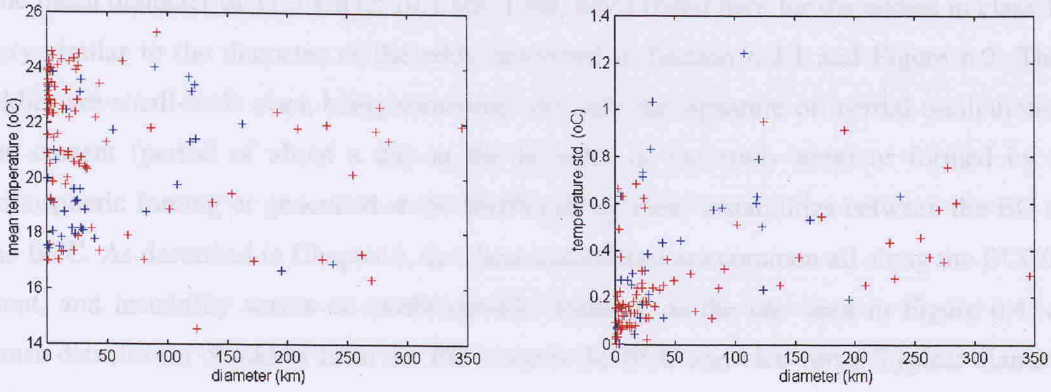

Figure 7.2. Distribution of the individual eddies' temperatures in relation to the eddies' diameter: (left) mean and (right) standard deviation. Cyclonic eddies are represented in blue, anticyclonic eddies are represented in blue.

The simple statistics obtained for the rotational period, perimeter and diameter of the eddies in class 1 and class 2 are given in Table 7.1. As described in Section 4.1.2.4, the eddies' diameters (D) were computed from the eddies' perimeters (P) supposing that the structures had a circular shape using the relation $D = P/\pi$. The diameters can be compared to measurements taken subsequently from the eddies present in the AVHRR images.

Table 7.1. Size and period statistics for the eddies found in the buoys' trajectories

	class 1 eddies				*class 2 eddies*			
	min.	***max.***	***mean***	***std.***	***min.***	***max.***	***mean***	***std.***
period (day)	0.1	4.9	2.1	1.5	5.2	42.2	16.7	9.4
perimeter (km)	1.3	99.9	36.3	31.7	103.8	1087.7	442.2	271.8
diameter (km)	0.4	31.8	11.5	10.1	33.0	346.2	140.7	86.5

The mean periods of rotation for the eddies in class 1 and 2 (2.1 days and 16.7 days, respectively) can be compared to the periods found in the FFT analysis of the buoys time series for the particular currents (Tables 5.11 and 6.2). Some of the series present energy peaks in periods very similar to the eddy rotational periods, especially if one considers the range $T_R \pm 1$ std. It is expected that some peaks of the FFT spectra of current measurements of

the mesoscale field will indicate the presence of eddy activity in the buoys' time series. To correctly correlate particular periods with the generating features, though, there is no other way than to analyse the individual eddies in an isolated way.

The mean diameter of 11.5 km (± 10.1 km, 1 std. dev.) found here for the eddies in class 1 is very similar to the diameter of the eddy described in Section 6.2.1 and Figure 6.2. These eddies are small-scale ones, being sometimes the only the signature of inertial oscillations of the current (period of about a day at the latitudes of the study area) or formed by the atmospheric forcing or generated at the shelfbreak by shear instabilities between the BC and the BCC. As described in Chapter 6, the shear instabilities are common all along the BCC/BC front, and instability waves or mushroom-like features, as the one seen in Figure 6.4, can cause detachment of eddies from the BC towards the BCC and vice-versa. Typical diameters of these eddies, as noticed in Figures 6.2, 6.3 and 6.4 are in the order of 10 to 50 km.

The mean diameter found in this thesis for the eddies in class 2 (140.7 km) is in close agreement to the diameters reported by Garzoli (1993) for the eddies in the BMC region. Working with geostrophic currents relative to 1000 m in the BMC, Garzoli (1993) indicated that both the cyclonic and anticyclonic eddies in the region have diameters ranging from 100 km to 150 km, and were either located between the southward edge of the BC and the northward edge of the MC or embedded in the main flow of one of these currents. The diameters were found to be about 2 or 3 times bigger than the typical Rossby radius of deformation for the area, computed as 57 km.

Warm core eddies from the BC were reported by Legeckis and Gordon (1982) to be elliptical with mean major and minor axis of 180 km and 120 km, respectively. An average of these axes result in a typical diameter of 150 km, a measurement very similar to the one presented by Garzoli (1993) and also very close to the mean diameter found here for the class 2 eddies.

The diameters found for the eddies in the BC, BCC and SAC, divided into classes 1 and 2, are plotted in Figure 7.3 against the typical Rossby radius of deformation (Rd) computed for the eddies' mean latitude. As described in Section 4.1.2.4, a distinct Rd was computed depending on whether the eddy was in the western STF (BMC) or in the BC/BCC front. Rd typically varied from 76 km to 48 km in the region between 28°S and 42°S, being smaller in higher latitudes and in the BC/BCC front.

The straight line in Figure 7.3 represents the line where D = Rd. Above this line, D is smaller than Rd; below this line the opposite is true. Eddies with length scales bigger than the Rossby

radius of deformation tend to be generated by detachment from meanders in the main flow, generally caused by baroclinic instabilities, and tend to be in geostrophic balance. Small-scale eddies, on the other hand, tend to follow a very unpredictable behaviour typical of turbulent flows. In the last case, D is several times smaller than Rd.

Figure 7.3 shows that class 1 eddies have diameters much smaller than Rd while the majority of class 2 eddies tend to be bigger than Rd. Although this result is expected since class 1 eddies are the smaller ones, one can also notice that in both classes the relation D/Rd is very variable. In class 1, D/Rd ranges from about 0.5 to numbers in the order of 10^{-3}. In class 2, on the other hand, D/Rd varies from 0.5 to about 4.5. This last number is in agreement with those reported by Richards and Gould (1996) to dominate typical fully developed eddy flow in the ocean.

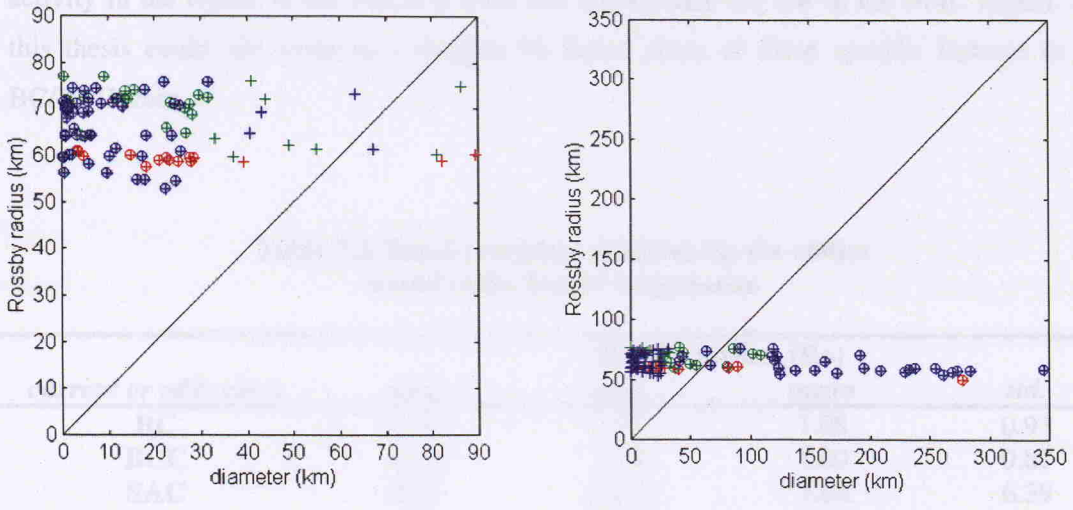

Figure 7.3. Relationship between the diameter and the internal Rossby radius of deformation for the eddies in class 1 (circles, left) and class 2 (circles, right). The particular eddies in the BC, BCC and SAC (both classes 1 and 2) are represented by crosses in red, green and blue, respectively.

Figure 7.3 also shows that not only the SAC eddies (the ones formed at the western STF) have D bigger than Rd, but also other eddies found in the BC and BCC. Analysing the circles in Figure 7.3, one can also see that both class 1 and class 2 contain eddies from all the three currents analysed here.

The Rossby number (Ro) statistics computed for the eddies found in the buoy trajectories can be seen in Table 7.2. The relationship between Ro and the eddies' diameter is presented in Figure 7.4. Apart from the mean Ro found for the eddies in class 2 (Ro = 0.24), all the other mean numbers indicate a very non-linear flow, where the acceleration forces predominate over the Coriolis force (Ro = 1 or greater). Minimum Rossby numbers for the particular currents, however, demonstrate that for some of the eddies quasi-geostrophy or geostrophy (where Ro $\approx$ 0.1 or Ro $\rightarrow$ 0, respectively) can apply. Examining both Table 7.2 and Figure 7.4 one can see that this condition is better applied for the big eddies of the SAC in class 2.

Figure 7.4 also includes the Ro/D relation found by Chassignet et al. (1990) for three eddies of the Brazil-Malvinas Confluence region. Analysing the distribution of the pair (Ro, D) of Chassignet et al.'s (1990) eddies in relation to the distribution of the eddies described in this thesis, we can conclude that they are very similar, supporting the consistency of the methods used here to describe the eddy activity in the BMC region. As mentioned before, the eddy activity in the region of the SBCS is even less known than the one at the BMC region, and this thesis could add some new insights for future study of these specific features in the BC/BCC front.

Table 7.2. Rossby number statistics for the eddies found in the buoys' trajectories

	Rossby number (Ro)			
current or eddy class	***min.***	***max.***	***mean***	***std.***
BC	0.11	2.97	1.08	0.93
BCC	0.11	3.28	1.00	0.81
SAC	0.05	26.71	3.68	6.39
class 1	0.27	26.71	3.91	6.07
class 2	0.05	1.43	0.24	0.27

As described in Section 4.1.2.4, the relationship between the eddies' rotational period (T_R), perimeter (P), diameter (D) and tangential velocity (V_T) was obtained by linear regression between these variables for classes 1 and 2 independently. The results are collated in Tables 7.3 and 7.4 and presented in Figures 7.5 to 7.8. Note that, since the eddies' P and D are directly proportional, the linear regressions between these parameters and T_R or V_T are the same, apart from a factor of π in the slope.

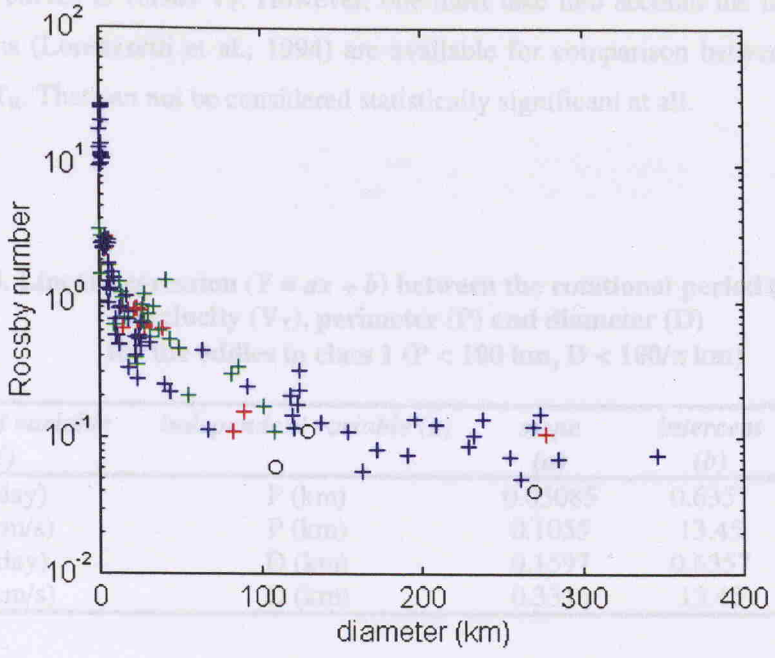

Figure 7.4. Relationship between the Rossby number and the eddies' diameters for the BC (red), the BCC (green) and the SAC (blue). Black circles indicate the same relationship for the BMC eddies investigated by Chassignet et al. (1990).

Tables 7.3 and 7.4 show that the linear regressions were better adjusted when relating P or D with T_R (r = 0.79 and r = 0.65 for classes 1 and 2, respectively) than when relating P or D with V_T. The linear regressions were applied to the overall set of eddies independently of their direction of rotation because the eddies' T_R, V_T, P and D did not present any relation with their direction of rotation. This is also illustrated in Figures 7.5 and 7.6 where distinction is made between the sense of rotation.

As quoted before, there are very few measurements of V_T or T_R for eddies in the Southwestern Atlantic Ocean. In order to 'validate' our empirical relations between P or D and V_T or T_R we compare estimations of these variables obtained from the empirical models presented in this chapter with actual measurements made by three different authors in the Southwestern Atlantic Ocean. This comparison is seen in Table 7.5.

The percentile errors between the estimated and measured V_T are in the order of 20 % to 60 %, being in average 31 %. Measurements of the eddies' rotational periods are much more sparse in the study region than those of the eddies tangential velocities. Nevertheless, the percentile errors between measured and estimated T_R are very high, of order 100 %. This was not expected, since the regression coefficient (r) for the curves D versus T_R are higher than

that of the curves D versus V_T. However, one must take into account the fact that only two observations (Lorenzzetti et al., 1994) are available for comparison between measured and estimated T_R. That can not be considered statistically significant at all.

Table 7.3. Linear regression ($Y = ax + b$) between the rotational period (T_R), tangential velocity (V_T), perimeter (P) and diameter (D) for the eddies in class 1 ($P < 100$ km, $D < 100/\pi$ km)

dependent variable (Y)	*independent variable (x)*	*slope (a)*	*intercept (b)*	N	*r*
T_R (day)	P (km)	0.05085	0.6357	86	0.79
V_T (cm/s)	P (km)	0.1055	13.45	86	0.40
T_R (day)	D (km)	0.1597	0.6357	86	0.79
V_T (cm/s)	D (km)	0.3313	13.45	86	0.40

Table 7.4. Linear regression ($Y = ax + b$) between the rotational period (T_R), tangential velocity (V_T), perimeter (P) and diameter (D) for the eddies in class 2 ($P \geq 100$ km, $D \geq 100/\pi$ km)

dependent variable (Y)	*independent variable (x)*	*slope (a)*	*intercept (b)*	N	*r*
T_R (day)	P (km)	0.02331	6.717	41	0.65
V_T (cm/s)	P (km)	0.02191	23.24	41	0.39
T_R (day)	D (km)	0.07322	6.717	41	0.65
V_T (cm/s)	D (km)	0.06883	23.24	41	0.39

Table 7.5. Comparison between measured (meas.) and estimated (est.) V_T and T_R of the surface eddies in the Southwestern Atlantic Ocean

author	*region / current*	*D (km)*	*$V_{T\,(meas.)}$ (cm/s)*	*$V_{T\,(est.)}$ (cm/s)*	*% error*	*$T_{R\,(meas.)}$ (day)*	*$T_{R\,(est.)}$ (day)*	*% error*
Chassignet et al. (1990)	BMC	270	53	42	21.1	-----	26.5	-----
Chassignet et al. (1990)	BMC	110	36	31	14.4	-----	14.8	-----
Chassignet et al. (1990)	BMC	130	77	32	58.2	-----	16.2	-----
Lorenzzetti et al. (1994)	BC	70	24	28	17.1	6	11.8	96.7
Lorenzzetti et al. (1994)	BC	275	71	42	40.6	14	26.8	91.4
Lorenzzetti and Kampel (1998)	BC	50	40	27	33.2	-----	10.3	-----

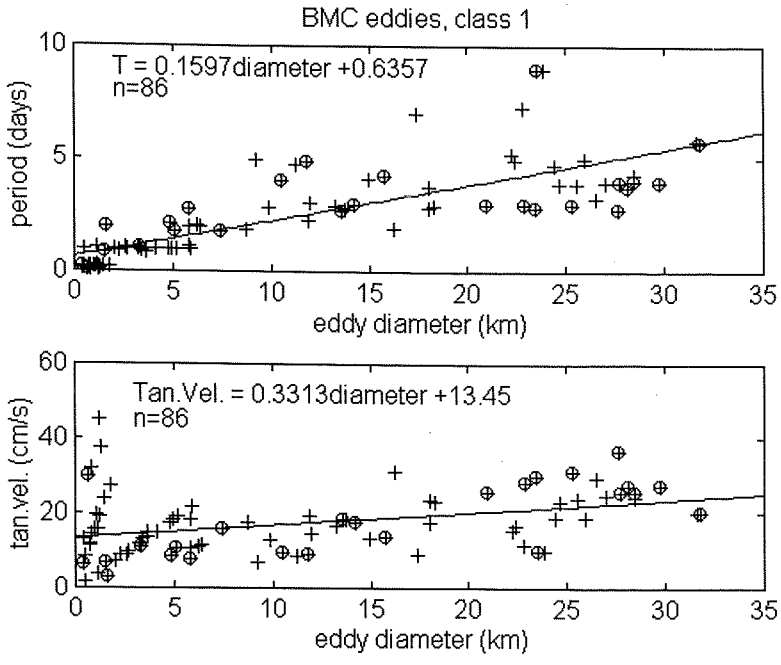

Figure 7.5. Linear regressions between the diameter, rotational period and tangential velocities for the class 1 eddies. Single crosses denote anticyclonic eddies, crosses and circles denote cyclonic ones.

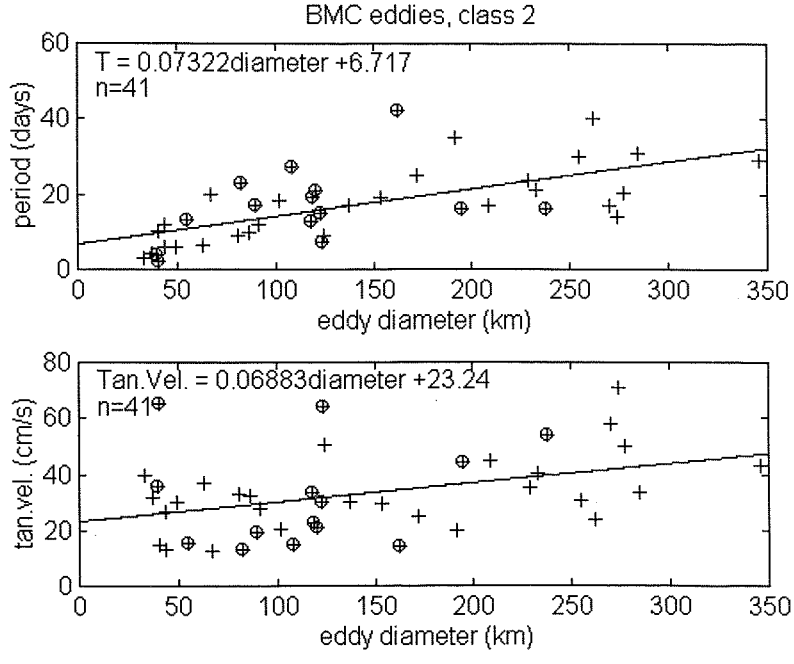

Figure 7.6. Linear regressions between the diameter, rotational period and tangential velocities for the class 2 eddies. Single crosses denote anticyclonic eddies, crosses and circles denote cyclonic ones.

7.3. The eddies in the high-resolution AVHRR images

Figure 7.7 presents the distribution of the cold core and the warm core eddies found in AVHRR images for the study area between March 1993 and July 1994. The sizes of the eddies are represented by the proportional crosses, where the eddies' major axes are represented in the meridional direction and the minor axes are represented in the zonal direction. The figure also indicates the bathymetry of the study area.

No relation was obtained between the eddies' core temperature and the position where the eddies were found. Although for the small eddies the temperature of the core does not imply a specific direction of rotation, it is generally true that the mesoscale warm core eddies are anticyclonic features, and cold core eddies are cyclonic ones. The overall positions of the eddies in Figure 7.7 agree with those observed for the eddies found in the buoys' trajectories (Figure 7.1), the smaller eddies being found in the BC/BCC front. The comparison between Figure 7.7 and 7.1 also indicates that the buoy trajectories, although not attached to the waters coming from the Malvinas Current, were good indicators of the eddy dynamics over the entire study region.

Unfortunately, it was not possible to statistically compare size measurements made in the same eddies by using buoy tracks and AVHRR images at the same time. Mainly owing to cloud coverage, very few were the images where one could superimpose buoy tracks and see fully developed eddies in both data sets. To illustrate this affirmation, one could look at the images presented in Figure 5.19. In this figure, the most prominent anticyclonic eddy noticed in the trajectories is backed-up by an AVHRR image of 11 March 1994 that shows the same structure, although with little contrast between the temperatures of the eddy and adjacent waters. In 5 May 1994, on the other hand, three eddies are seen in the trajectories but the structures seen in the AVHRR are only meanders. Having said that, one must bear in mind that most of the individual eddies described in this section were not the same as already described in the previous section. Rather, the two data sets are complementary to each other.

The distribution of the eddies' core temperatures (mean and standard deviation derived from temperature transects along the major and minor axes) is displayed in Figure 7.8 in relation to the eddy mean diameter (average between the major and minor axes). Both warm core and cold core eddies had temperatures in the same dynamical range (about 10°C to 30°C), which was a little wider than the range of temperatures found for the eddies in the buoys' trajectories (Figure 7.2). Moreover, the temperature standard deviations were also broader in the AVHRR

eddies (Figure 7.8) than in the buoys' eddies (Figure 7.2). The explanation for it is that the temperature measurements for the eddies in the buoys' trajectories were measured along their perimeters, while the measurements for the eddies in the images were from the eddies' interior, where they tend to follow a gradient from the center to the border.

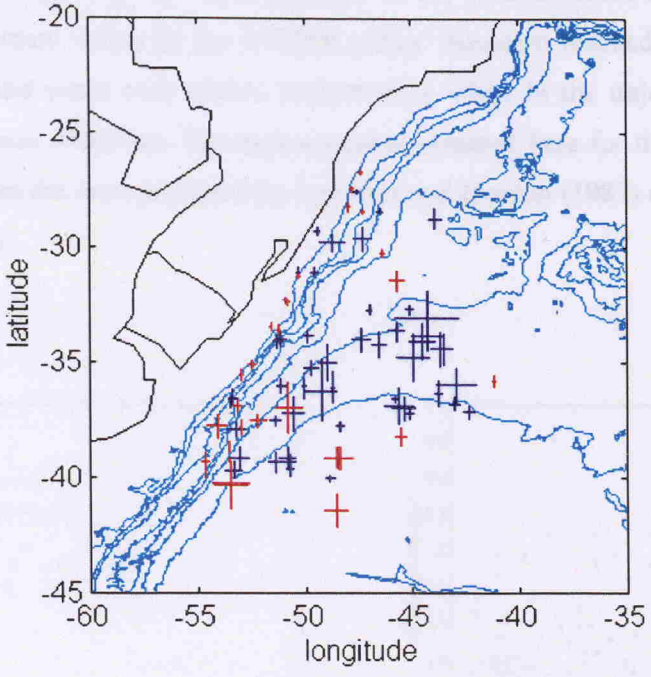

Figure 7.7. Eddies present in the high-resolution AVHRR images. Cold core eddies are represented in blue, warm core eddies are represented in red. The crosses represent the major and minor axes of the individual eddies. Bathymetric contours are in accordance to Figure 1.1.

As described in Section 4.2.4 and summarised in Figure 4.7, the distribution of the AVHRR eddies sizes (perimeter, diameter) did not follow that of the eddies found in the buoy trajectories (Figure 4.6). Instead of analysing the eddies properties in class 1 or 2, as was done with the buoy trajectories, the AVHRR eddies are described in this section in relation to their core temperatures: warm or cold. As seen in Figure 4.7 and in contradiction to what was found for the eddies in the trajectories, the majority (85 %) of the AVHRR eddies had perimeters (diameters) bigger than 100 km (31.8 km). Because of it, if any comparison is to be made between the AVHRR eddies and those revealed by the buoy trajectories, we have to consider the buoy eddies of class 2.

Following that, Table 7.6 shows the simple size statistics for the eddies found in the AVHRR images. All the parameters analysed in Table 7.6 (apart from the diameter std.) indicated that, for the area and period studied, cold core eddies were bigger than warm core ones. Moreover, the mean diameters (perimeters) found for both warm and cold core AVHRR eddies are distinct from the ones found for the class 2 (D > 31.8 km) eddies of the buoys' trajectories (Table 7.1). The mean diameters of the AVHRR cold and warm core eddies were 82 km and 65 km, respectively, while the mean diameter of the class 2 eddies in the trajectories was 140.7 km. Maximum values for the AVHRR eddies' diameters reached values of 262 km and 182 km (cold and warm core eddies, respectively), while in the trajectories the maximum eddy diameter was 346.2 km. The measurements obtained here for the AVHRR eddies are also distinct from the ones presented by Legeckis and Gordon (1982) and Garzoli (1993) for the BMC region.

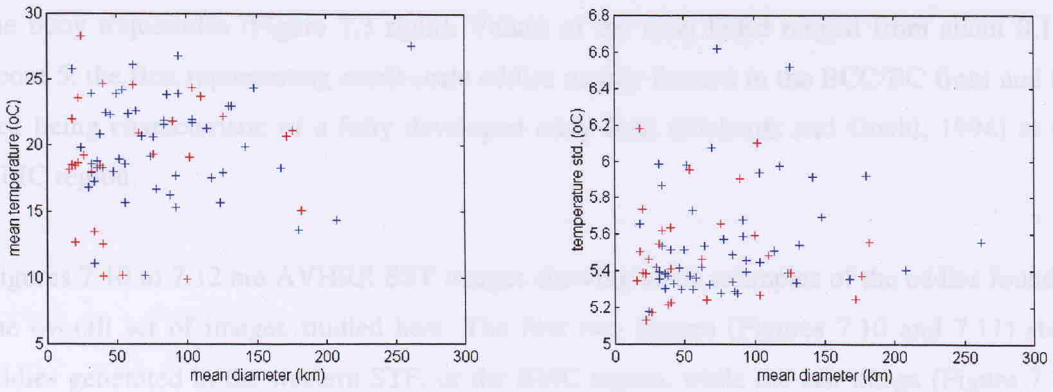

Figure 7.8. Distribution of the individual eddies' temperatures in relation to the eddies' diameter: (left) mean and (right) standard deviation. Cold core eddies are represented in blue, warm core eddies are represented in red.

When analysing Table 7.6 one must remember, however, that the observations made in this thesis for the 1993 and 1994 SST images included the anticyclonic eddy generally present at the location of the BC return flow (Figure 5.19, 11 March 1994), but missed the eddies which were possibly ejected by the BC southwards of this extreme location, since the AVHRR images used here were restricted to the latitudes lower than 42°S. Both Figure 11 in Legeckis and Gordon (1982) and Figure 1 in Olson et al. (1988) indicate the presence of anticyclonic eddies formed by detachment from the BC extremes. These eddies formed at the BC extremes generally have dimensions larger than the mean found here for the warm core eddies and have

contributed to the typical mean diameters of 100 km to 150 km described for them by Legeckis and Gordon (1982) and Garzoli (1993).

Table 7.6. Size statistics for the eddies found in the AVHRR images

	cold core eddies				*warm core eddies*			
size (km)	*min.*	*max.*	*mean*	*std.*	*min.*	*max.*	*mean*	*std.*
major axis	20	284	101	61	16	244	83	64
minor axis	12	252	63	46	8	144	48	43
diameter	18	262	82	51	16	182	65	51
perimeter	57	824	269	163	50	604	217	165

Figure 7.9 describes the relationship between the eddy diameters (D) and the typical internal Rossby radius of deformation (Rd) computed for the eddies mean latitude and origin (BMC or BC/BCC front). The relation is almost identical to the one presented for the class 2 eddies of the buoy trajectories (Figure 7.3 right). Values of the ratio D/Rd ranged from about 0.1 to about 5, the first representing small-scale eddies mainly formed in the BCC/BC front and the last being characteristic of a fully developed eddy field (Richards and Gould, 1994) at the BMC region.

Figures 7.10 to 7.12 are AVHRR SST images showing some examples of the eddies found in the overall set of images studied here. The first two images (Figures 7.10 and 7.11) show eddies generated in the western STF, or the BMC region, while the last image (Figure 7.12) presents an example of eddy formation at the BCC/BC front.

Figure 7.10 is a very good example of the cold core eddy formation in the BMC by the detachment from meanders of the South Atlantic Current. The figure shows three eddies being expelled from the main current by the breaking off from high amplitude meanders. These structures travel towards the warm part of the BMC region. They are a source of eutrophic water from subantarctic origin to the tropical domain of the BMC region, and possibly have direct association with high primary production and fish. Their fate is unknown in the BMC region, and the data set available for this work, although suggesting time scales of a month for these eddies lifetime, was unfortunately not enough to verify their complete evolution or coalescence. That limitation was mainly caused by cloud coverage.

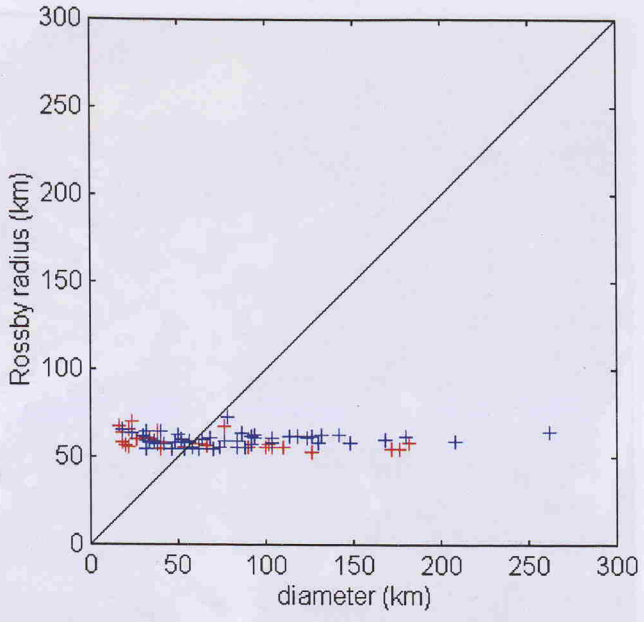

Figure 7.9. Relationship between the diameter and the internal Rossby radius of deformation for the eddies found in the AVHRR images. Cold core eddies are represented in blue, warm core eddies are represented in red.

Legeckis and Gordon (1982) have reported that the formation of cold core eddies in the BMC region is less frequent than that of the warm core eddies. The latter were reported to be formed as a detachment from the BC extremes. Garzoli and Garraffo (1989) studied 17 months worth of echo sounders records in the BMC region from November 1984 to March 1986. They have reported that during this period of time cold intrusions were present in the records with no apparent periodicity. Three of these intrusions were associated with cold core eddies which were present in the records for periods of time between 20 days and 60 days.

Garzoli and Garraffo (1989) also computed the potential energy associated with the cold core eddies (6.5×10^{15} J), adding that it is of the same order of magnitude as the Gulf Stream eddies. The AVHRR data set analysed here, although suggesting that the periods of about a month or two can reflect the time scales for the cold core eddies lifetime in the BMC region in agreement with Garzoli and Garraffo (1989), disagrees with the suggestion made by Legeckis and Gordon (1982) that the cold core eddies are less frequent than their warm counterparts in the BMC region.

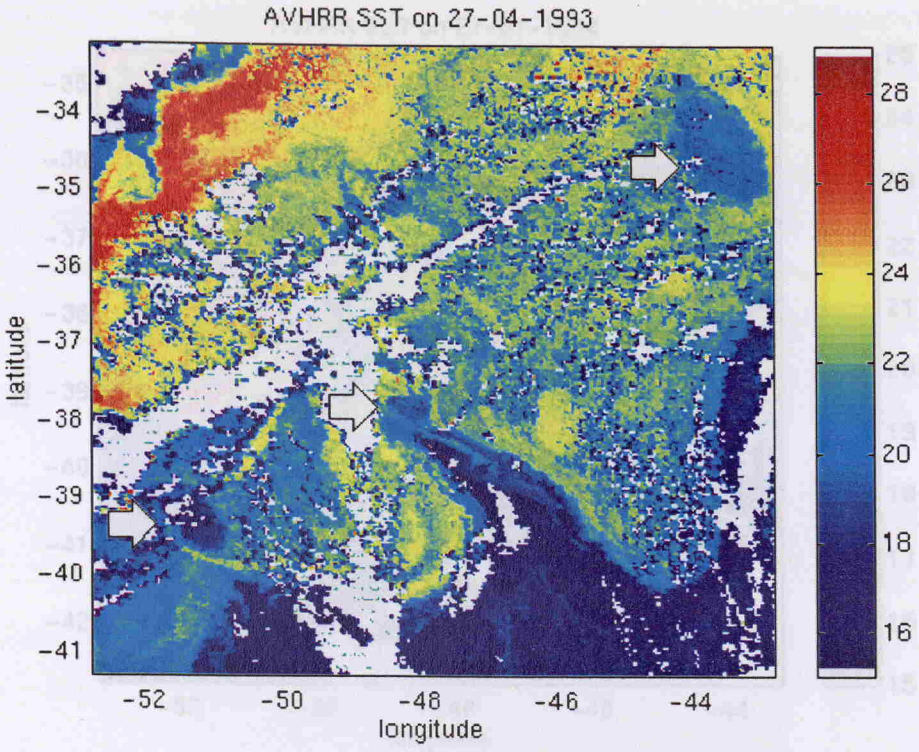

Figure 7.10. AVHRR image of 27 April 1993 showing the 'pinching off' of three cold core (cyclonic) eddies from the cold (MC) part of the western subtropical front. The eddies are indicated by the arrows. The colour bar indicates temperature in degC.

Figure 7.11 exemplifies the presence of warm core eddies which tend to be formed in the warm part of the BMC between two consecutive cold meanders in the SAC. The eddies are circular, have diameters close to 100 km, and are very typical. However, previous descriptions of the warm core eddies in the BMC generally reported the eddies formed to the west of the first SAC meander (seen in Figure 7.11 at 39°S, 52°W) or at the south of the BC extreme location, below 42°S. We have indications from the images that this sort of eddy is formed regularly at the meander's trough in the warm part of the confluence. It is unlikely that they can break through the front and travel southwards, although we did not have enough material to confirm that. If travelling towards the cold part of the front, these eddies could add a huge amount of heat, salt and momentum from the tropical to the subantarctic domain of the BMC region.

Figures 6.2, 6.4 and 7.12 are examples of eddies or frontal instabilities of the BC/BCC front. In the case of Figures 6.2 and 7.14, the features are only about 10 km in diameter, but Figure 6.4 shows that the scales can reach 50-60 km.

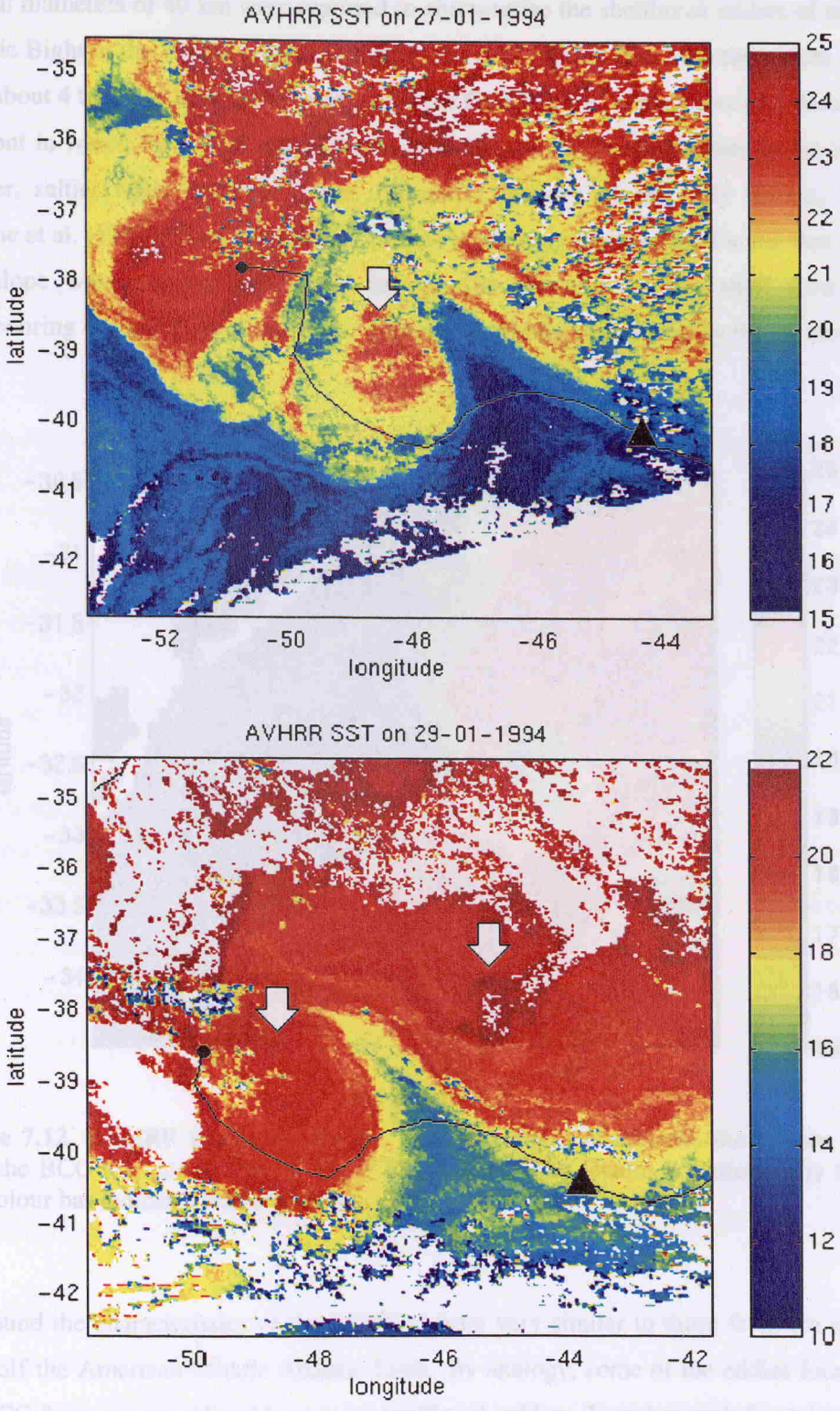

Figure 7.11. Two day sequence of AVHRR images taken in 27 January 1994 (top) and 29 January 1994 (bottom) at the western subtropical front. Buoy 3187 trajectory is seen in both images. The arrow at the top figure indicates a warm core (anticyclonic) eddy originated from the warm (BC) part of the western subtropical front. This eddy is also seen at the bottom figure. A possible second warm core eddy is present to the right of the MC meander in 29 January 1994. The circle indicates the buoy position 20 days before the image's acquisition time and the triangle indicates the buoy position within ± 12 from the image's acquisition time. The colour bar indicates temperature in degC.

Typical diameters of 40 km were reported to characterise the shelfbreak eddies of the Middle Atlantic Bight in the United States coast (Garvine et al., 1988). The structures were described to be about 4 times smaller than the eddies of the Gulf Stream. The authors also described that the front in which the eddies were formed separates cooler, fresher waters in the shelf from warmer, saltier water from the slope. Prominent features of the eddy groups, following Garvine et al. (1988), were described to be the (1) plumes of lighter shelf water that protruded into slope water curling backwards in opposite direction of the shelf flow and (2) neighbouring cyclones with slope water partially or wholly surrounded by the plumes.

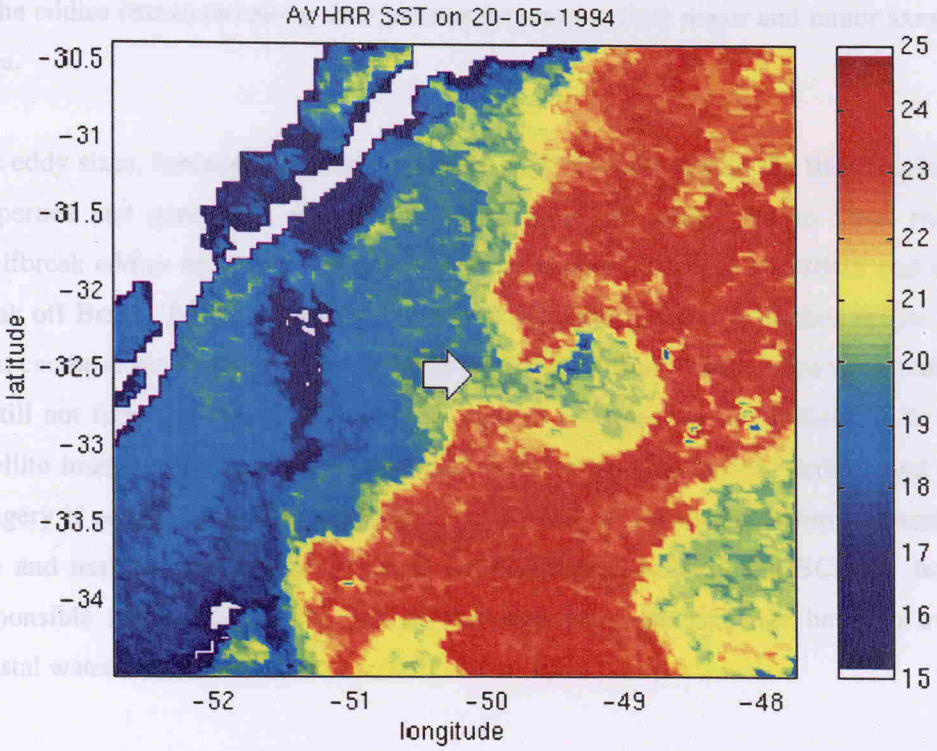

Figure 7.12. AVHRR image of 20 May 1994 showing a mushroom-like feature extending from the BCC towards the BC in the BC/BCC front. The feature is indicated by the arrow. The colour bar indicates temperature in degC.

We found the characteristics of the BC/BCC front very similar to those from the shelf/slope front off the American Middle Atlantic Bight. By analogy, some of the eddies formed in the BC/BCC front are considered here to be shelfbreak eddies. Together with frontal instabilities of the BC and BCC in the form of waves with crests protruding in direction opposite to that of the current, mushroom-like features are quite common at the BC/BCC front. These features would liberate warm core eddies from BC into BCC or cold core eddies from BCC into BC. As pointed out in Chapter 6, several structures like that are likely to be formed all along the BC/BCC front. The exchange of heat, salt and momentum between the BC and the BCC

through the detachment of small scale eddies is a process which demands further investigation.

7.4. Summary and final remarks

Buoy tracks and AVHRR images were utilised in association in this section to characterise the eddies present in the Southwestern Atlantic Ocean during the period of March 1993 to July 1994. The two data sets have indicated that there is no relationship between the temperature of the eddies (measured along their perimeter or across their major and minor axes) and their sizes.

The eddy sizes, however, were smaller in the SBCS region than in the BMC region. Distinct properties and generation mechanisms characterise the eddy field in these two regions. Shelfbreak eddies and eddies caused by current reversals occur at the SBCS and at the shelf break off Brazil. To our knowledge, they have not been previously studied before this thesis. That can be explained mainly because (1) the BC/BCC front, where some of the eddies occur, is still not fully studied or even reported and (2) because they are difficult to be spotted in satellite images. However, their presence can be revealed in surface drifters and in satellite imagery if correct enhancing techniques are applied. As mentioned before, depending on the rate and number of structures formed, the shelfbreak eddies of the BC/BCC front can be responsible for a considerable part of the mass and heat exchange between tropical and coastal waters.

In the BMC region, cold core eddies were observed to be formed by breaking off from the crests of high amplitude meanders of the South Atlantic Current. Warm core eddies were present at the BC reversal zone and in the troughs of the SAC in the confluence.

Rotational periods of the small-scale eddies were of about 2 days, while the mesoscale ones (class 2 eddies) presented a mean rotational period of about 17 days. Many of the energy peaks found in FFT analysis of the buoy positional and temperature time series match the eddies' periods of rotation.

The mean diameter for the mesoscale eddies found in the buoy trajectories is in agreement with those previously described for the BMC region (Legekis and Gordon, 1982; Garzoli, 1993), but the diameters found for the AVHRR eddies were smaller than previous

descriptions. Reasons for that can lie in the fact that the generally bigger warm core eddy formed by the detachment of the BC extreme position, to the south of 42°S, is not detected in our AVHRR images which do not cover that area.

Rossby numbers (Ro) computed for the eddies in the study area indicate very non-linear to quasi-geostrophic or geostrophic structures, these last associated to the South Atlantic Current in the BMC. The absolute values of Ro for the BMC are in agreement with those presented by Chassignet et al. (1990).

Empirical relationships were found in an attempt to relate the eddy sizes (perimeter and diameter) with the eddy rotational periods (T_R) and tangential velocities (V_T). A better linear adjustment is found between the eddy sizes and T_R (r = 0.65 to 0.79) than between the eddy sizes and V_T (r = 0.39 to 0.4). However, the validation of the models with actual measurements has demonstrated that the percentile errors are much smaller when estimating V_T than when estimating T_R. The relationships can be useful when no *in situ* data are available and satellite images are obtained in a regular basis. In this case, individual eddy sizes (diameters, perimeters) can be measured in the satellite images and their T_R or V_T inferred from the empirical relationships. The inferred variables could be used as input parameters for ocean models or useful for the Merchant navy, for example, as rotating eddies are know to slow down cruise ships and, therefore, have an economic impact for the navy.

BLANK PAGE

CHAPTER 8

THE RELATIONSHIP BETWEEN *IN SITU* AND SATELLITE SEA SURFACE TEMPERATURES

8.1. Introduction

In the previous chapters of this thesis we have dealt with the characterisation of some of the mesoscale processes occurring in the Southwestern Atlantic Ocean during 1993 and 1994. This chapter addresses the question of whether the satellite images utilised in this thesis are truly representing the sea surface temperatures (SST) of this part of the ocean, as they are commonly measured in the sea by conventional oceanographic methods.

The coefficients utilised in the multichannel and cross-product sea surface temperature algorithms (MCSST and CPSST, respectively) proposed by NOAA are obtained by regressing the satellite-measured brightness temperatures (BTs) against *in situ* SST measurements obtained by drifting or fixed buoys and ships of opportunity (McClain et al., 1985; Kidwell, 1995). With such a regression, NOAA (AVHRR) estimates are not only correcting the atmospheric attenuation of the radiation leaving the sea surface 'skin' towards the satellite, but are also losing the real temperature signal of the molecular 'skin' layer at the sea-air interface. According to Schluessel et al. (1990), this skin layer is less than a millimetre thick and generally several tenths of a degree colder than the 'bulk' temperatures measured just below the sea surface skin.

Resulting estimates of the SST obtained by the NOAA algorithms are therefore 'pseudo-bulk' temperatures which are commonly compared with conventional sub-surface SST and not with the 'skin' temperature of the sea surface. The estimates of SST obtained by the NOAA satellites are commonly used as input parameters for atmospheric models, but recently the use of the sub-surface SST has been challenged for that purpose. Donlon et al. (1999), for instance, point out that the 'skin', not the 'bulk' SST is a fundamental variable for validating coupled ocean-atmosphere models, since all the heat and gas exchange between the two environments takes place through the sea surface skin.

Differences between AVHRR estimates and *in situ* SST data can occur owing to several causes. Regional atmospheric characteristics play a role in this context, since the NOAA algorithms are global and generally do not account for regional effects of the atmosphere in the SST estimate. Strong and McClain (1984) also report that global MCSST estimates are closer to drifting buoy measurements (bias of 0.22°C, buoy warmer) than to measurements made by ships of opportunity (bias of 0.43°C, ships warmer). When comparing buoy SSTs with the SST from images presented in the previous chapters of this thesis, a question arises on how these independent variables (buoy SST representing the 'bulk' temperature of the ocean and the satellite SST representing a 'pseudo-bulk' SST) are related. This chapter addresses that question.

Furthermore, differences between the AVHRR estimates of SST obtained with the high-resolution images of the Southwestern Atlantic Ocean and SSTs measured by ships of opportunity are also investigated here. Will this other type of bulk temperature have a bigger bias in relation to AVHRR estimates for the Southwestern Atlantic than drifting buoys, as expected from the findings of Strong and McClain (1984)?

In Section 3.2.2. we reported that the ATSR SST images, in contrast to those of NOAA, represent the 'skin' SST. The availability of a set of ATSR images for the region and period of this study offered us a possibility of estimating the temperature differences (deltaT) between the AVHRR and ATSR retievals. Considering a good geolocation between ATSR and AVHRR images, the deltaTs can also be assessed in relation to their spatial variability. What will be the spatial behaviour of the deltaTs in a region of strong mesoscale variability such as the Southwestern Atlantic? What will be the importance of assessing this information? These questions are also addressed below.

8.2. Match-ups between in situ and satellite Sea Surface Temperatures

As described in Section 4.5, match-ups between *in situ* (from the drifting buoys and ships of opportunity) and satellite SSTs were performed for a maximum period of ± 3 h from the image's acquisition time. This time interval was chosen in order to avoid the effects of the diurnal warming and cooling of the upper layers of the ocean. According to Keogh et al. (1999), a time window of ± 3 h is also tight enough to prevent currents and tides from affecting the thermal structure of the sea surface in regions with weak thermal gradients.

The match-up pairs were obtained not only using the SST of a single image pixel closest in space to the equivalent *in situ* measurement, but also using an average SST representing a 5 × 5 pixels (20 km × 20 km) matrix centred at the position of the central pixel. In the first case, the temperature match-ups are referred to in this text as the 'central pixel' match-ups, whereas for the second case we use the terminology 'average pixel'. As described in Section 4.4, the measurements made by ships of opportunity in the Southwestern Atlantic were obtained from the COADS data set. They will be referred to as the COADS SSTs hereafter in this text.

Table 8.1 displays the coefficients found for the linear regressions and the deltaTs between the COADS bulk temperatures and the AVHRR BTs and SSTs. The regression coefficients were between 0.71 and 0.9, indicating a good fit for the linear model. The number of observations was N = 29 for the channel 5 and N = 32 for the other 2 channels and SST. The regression line is seen in Figure 8.1, which also indicates that both NOAA-11 and NOAA-12 algorithms seem to perform similarly in relation to the *in situ* data, for their retrievals lie closer alongside the regression curve. The match-up pairs seen in Figure 8.1 also indicate that the regression was performed over a wide range of temperature values (~5°C to ~25°C) which included very cold waters of the Malvinas Current (MC).

As expected, NOAA BTs were always smaller than the *in situ* temperatures (positive deltaTs) because they do not account for the atmospheric attenuation of the upwelling radiation towards the satellite. DeltaT between the COADS SST and the AVHRR BTs increases from channel 3 to channel 5, ranging from 1.6°C to 4.6°C in the average pixel estimates. The range of deltaT values is smaller in the central pixel estimates than in the average pixel estimates. The deltaT between the COADS SST measurements and AVHRR SST estimates was equal to -0.58°C for the central pixel and equal to -0.49°C for the average pixel. The negative deltaTs indicate that the satellite estimates are higher than the bulk temperatures. The atmospheric correction algorithms applied here (Equations 4.8 to 4.10), therefore, are overestimating the atmospheric and surface skin effects by an average of about 0.5°C.

The curve adjustments between COADS and AVHRR SSTs for average and central pixel were similar, with regression coefficients of 0.88 and 0.89, respectively (Table 8.1). The mean deltaT found for the average pixel was ~0.1°C smaller than that of the central pixel, but the standard deviation of the average pixel estimate was slightly bigger than that of the central pixel.

Table 8.1. Linear regressions between the bulk temperatures from COADS (T_{bulk}) and the AVHRR BTs and SSTs (T_{sat})

(a) central pixel

	linear regression ($T_{bulk} = a\ T_{sat} + b$)				*deltaT* = T_{bulk} - T_{sat} (°C)	
channel	*a*	*b*	N	*r*	*mean*	*std.*
3	0.817	4.292	32	0.85	1.74	3.09
4	1.038	2.429	32	0.90	2.92	2.37
5	0.7002	7.284	29	0.71	3.92	4.21
SST	0.8533	1.803	32	0.89	-0.58	2.59

(b) average pixel

	linear regression ($T_{bulk} = a\ T_{sat} + b$)				*deltaT* = T_{bulk} - T_{sat} (°C)	
channel	*a*	*b*	N	*r*	*mean*	*std.*
3	0.8373	3.89	32	0.86	1.6	2.91
4	0.9575	3.766	32	0.87	3.24	2.71
5	0.89	5.758	29	0.79	4.6	3.4
SST	0.8376	2.132	32	0.88	-0.49	2.77

Because the buoys used in this work were deployed in the Brazil Current, they did not sample the core of the cold waters originating in the MC. The dynamical range of temperature match-ups obtained with the buoys is therefore smaller than that obtained with the COADS data. For a better comparison between the linear regressions obtained between COADS measurements and satellite estimates and those obtained between buoy measurements and satellite estimates, the COADS regressions were performed again without including 6 match-up pairs sampled in the MC (see Section 4.5). The results of that are presented in Figure 8.2 and Table 8.2.

Table 8.2 also presents the deltaTs between the COADS bulk temperatures excluding MC pairs ($COADS_{lessMC}$) and the AVHRR BTs and SSTs. For both central and average pixels, the deltaTs between AVHRR BTs and $COADS_{lessMC}$ were generally bigger than those of AVHRR BTs and COADS. For the SSTs, however, the deltaTs were smaller in the $COADS_{lessMC}$ case. They were equal to -0.44°C for the central pixel and equal to -0.29°C for the average pixel. However, the scattering of deltaT points was generally bigger in the $COADS_{lessMC}$ case than in the COADS. Standard deviations for the deltaT between AVHRR SSTs and $COADS_{lessMC}$ SSTs were about 3°C.

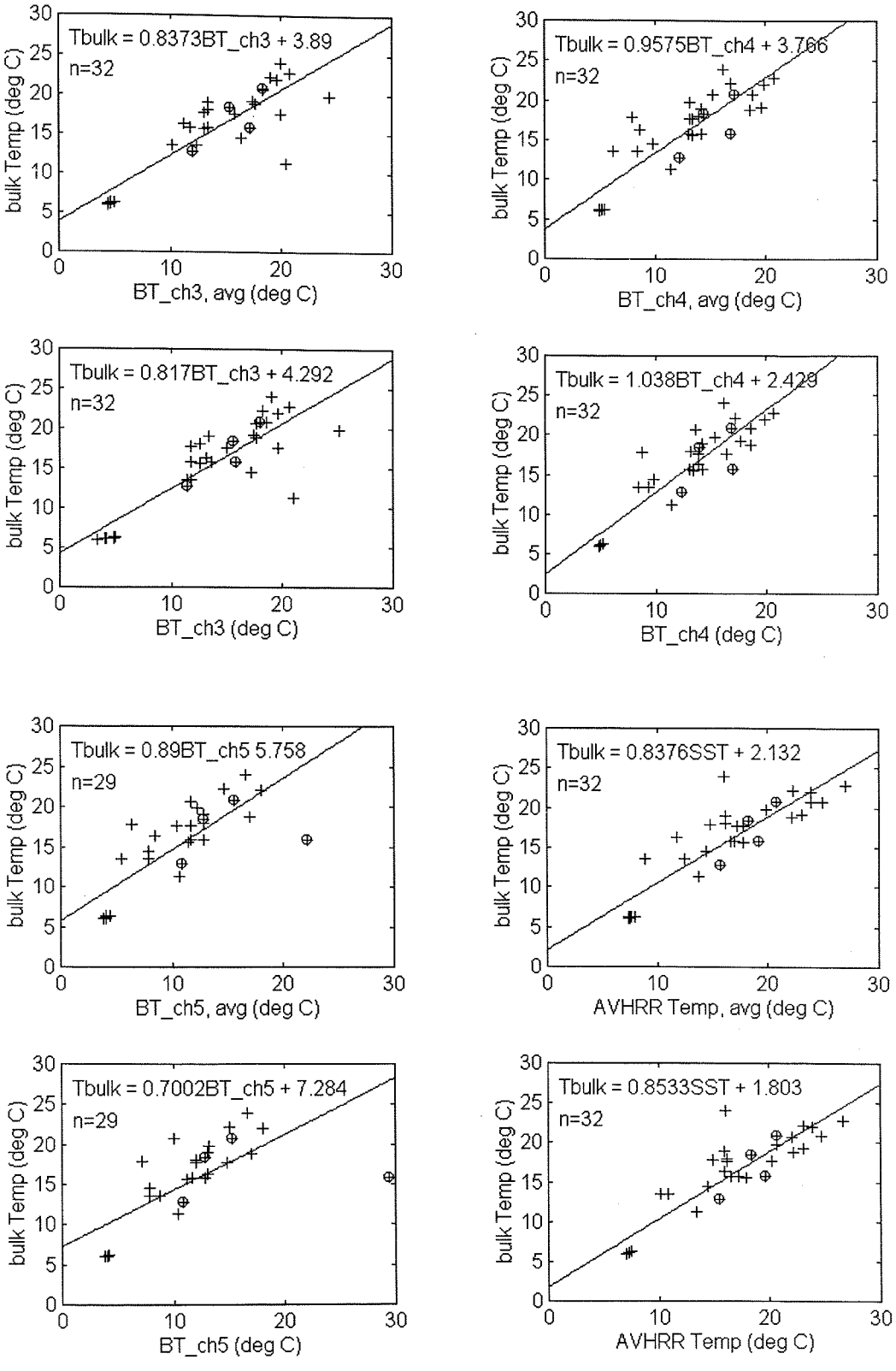

Figure 8.1. Linear regressions between AVHRR brightness temperatures and SSTs (ch_3, ch_4, ch_5 and AVHRR Temp) and bulk temperatures from COADS. Crosses indicate NOAA-11 estimates; circles and crosses indicate NOAA-12 estimates.

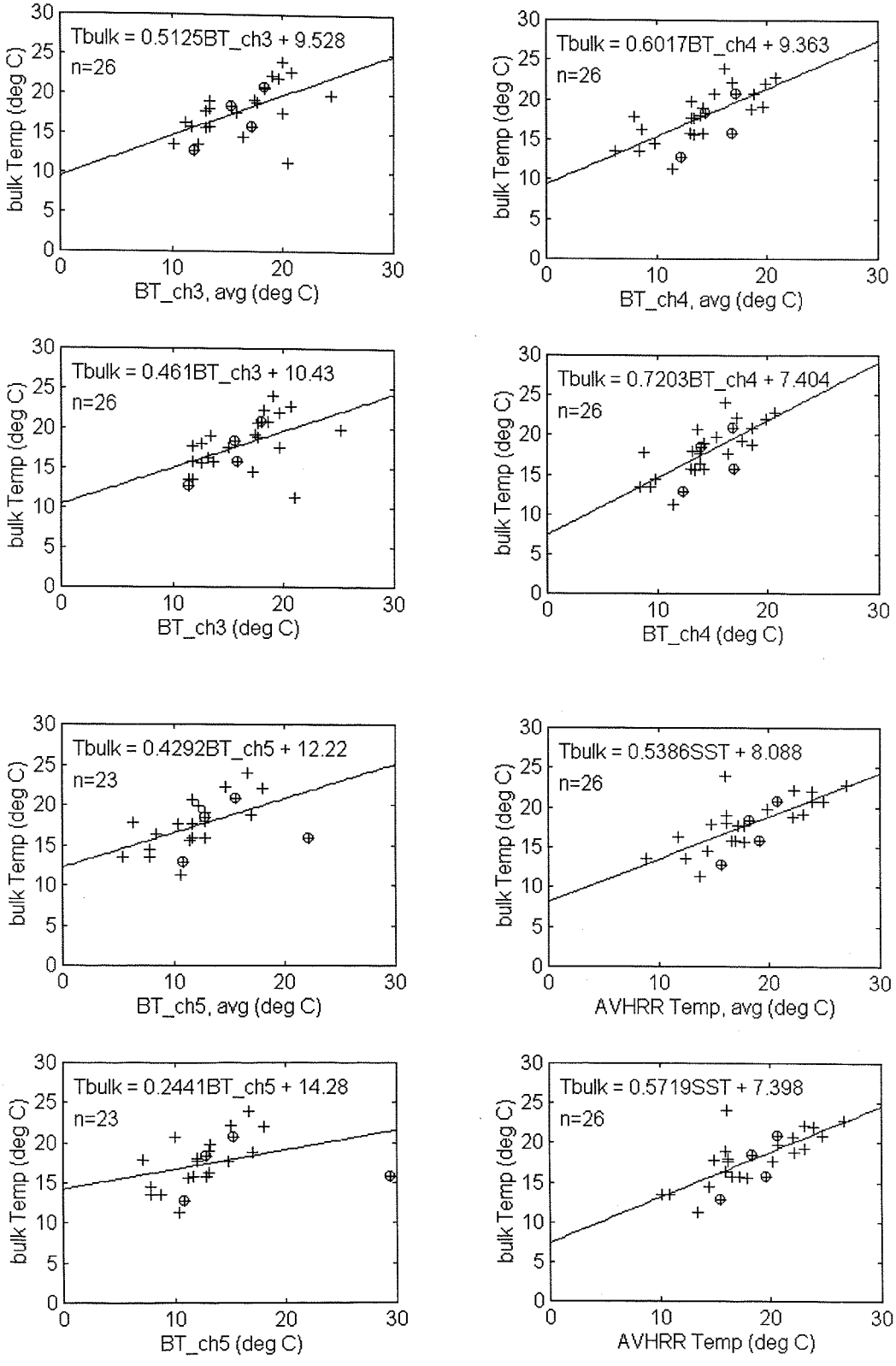

Figure 8.2. Linear regressions between AVHRR brightness temperatures and SSTs (ch_3, ch_4, ch_5 and AVHRR Temp) and bulk temperatures from COADS (discarding the bulk temperatures measured in the Malvinas Current). Crosses indicate NOAA-11 estimates; circles and crosses indicate NOAA-12 estimates.

Table 8.2. Linear regressions between the bulk temperatures from $COADS_{lessMC}$ (T_{bulk}) and the AVHRR BTs and SSTs (T_{sat})

(a) central pixel

	linear regression ($T_{bulk} = a\ T_{sat} + b$)				*deltaT* = T_{bulk} - T_{sat} (^oC)	
channel	*a*	*b*	N	*r*	*mean*	*std.*
3	0.461	10.43	26	0.51	1.73	3.44
4	0.7203	7.404	26	0.73	3.34	2.44
5	0.2441	14.28	23	0.35	4.4	4.63
SST	0.5719	7.398	26	0.74	-0.44	2.87

(b) average pixel

	linear regression ($T_{bulk} = a\ T_{sat} + b$)				*deltaT* = T_{bulk} - T_{sat} (^oC)	
channel	*a*	*b*	N	*r*	*mean*	*std.*
3	0.5125	9.528	26	0.57	1.6	3.23
4	0.6017	9.363	26	0.71	3.73	2.78
5	0.4292	12.22	23	0.52	5.24	3.56
SST	0.5386	8.088	26	0.72	-0.29	3.05

The regression coefficients between AVHRR estimates and $COADS_{lessMC}$ measurements ranged from 0.35 to 0.74. The linear regressions, therefore, were poorer in the $COADS_{lessMC}$ case than in the COADS case. That can be partially explained by the lower number of observations of the $COADS_{lessMC}$ (N = 23 to 26) regressions in relation to the COADS regressions, but can also be explained by the fact that the bigger range of temperature observations in the COADS regressions make the scattering of the warm points less crucial for the regression as a whole.

The coefficients for the linear regressions and the deltaTs between the buoy temperatures and the AVHRR BTs and SSTs are presented in Figure 8.3 and Table 8.3. The coefficients for the central pixel estimates of buoy against channels 3 to 5 BTs were very small (between 0.27 and 0.34), indicating that the linear model did not explain the relation between these variables. However, the average pixel BT estimates have presented good correlation with the buoy SSTs. The coefficients, in this case, were ranging from 0.61 to 0.73, about double the values found for the central pixel correlations. DeltaTs were also bigger for the respective BT channels in the central pixel than in the average pixel cases.

The regressions between buoy and AVHRR SSTs were good for both the central and average pixel cases (correlation coefficients of about 0.8 for both cases). DeltaT was higher in the central pixel estimate (-1.66°C, AVHRR warmer than buoy) than in the average pixel estimate (-1.44°C, AVHRR warmer than buoy). As with the findings for COADS and AVHRR SST

deltaTs, negative deltaTs indicate that the NOAA algorithms are overestimating the atmospheric attenuation occurring in the study area and period.

Table 8.3. Linear regressions between the buoy temperatures (T_{buoy}) and the AVHRR BTs and SSTs (T_{sat})

(a) central pixel

	linear regression ($T_{buoy} = a\ T_{sat} + b$)				*deltaT* = T_{buoy} - T_{sat} (°C)	
channel	*a*	*b*	N	*r*	*mean*	*std.*
3	0.1839	17.55	22	0.27	3.44	3.94
4	0.2697	16.27	22	0.34	4.16	3.38
5	0.2335	17.33	22	0.28	6.15	3.44
SST	0.65	6.177	22	0.80	-1.66	1.89

(b) average pixel

	linear regression ($T_{buoy} = a\ T_{sat} + b$)				*deltaT* = T_{buoy} - T_{sat} (°C)	
channel	*a*	*b*	N	*r*	*mean*	*std.*
3	0.6269	9.662	22	0.67	3.07	2.17
4	0.8459	6.403	22	0.73	3.79	1.79
5	0.6961	10.35	22	0.61	5.81	2.15
SST	0.6262	6.847	22	0.79	-1.44	1.99

Generally speaking, the results shown in Tables 8.1 to 8.3 indicate that the average pixel offered a better fit in the linear regressions between *in situ* and satellite retrievals than the central pixel. The deltaT estimates were also smaller in the average pixel case. For the match-ups between *in situ* and satellite SSTs, deltaTs were negative (AVHRR estimates warmer than *in situ* estimates) and several times bigger when comparing buoy and AVHRR SSTs than when comparing ships of opportunity and AVHRR SSTs. DeltaTs between COADS SST and AVHRR SST ranged from -0.29°C to -0.58°C, while deltaTs between buoy SST and AVHRR SST varied from -1.44°C to -1.66°C. This contradicts what was expected from Strong and McClain (1984). The authors found that the bias (deltaT) between ships of opportunity SSTs and global MCSST estimates was 0.43°C (ships warmer than MCSST) while the bias between drifting buoy SSTs and MCSST retrievals was 0.22°C (buoy warmer than MCSST).

Match-up points between ATSR and *in situ* SSTs proved to be very difficult to obtain. Coincidences in time (± 3 hours interval) are more unlikely between *in situ* and ATSR SSTs than between *in situ* and AVHRR. Two reasons may be suggested for that: (1) better temporal coverage of the AVHRR sensor in relation to the ATSR and (2) bigger coverage area for a

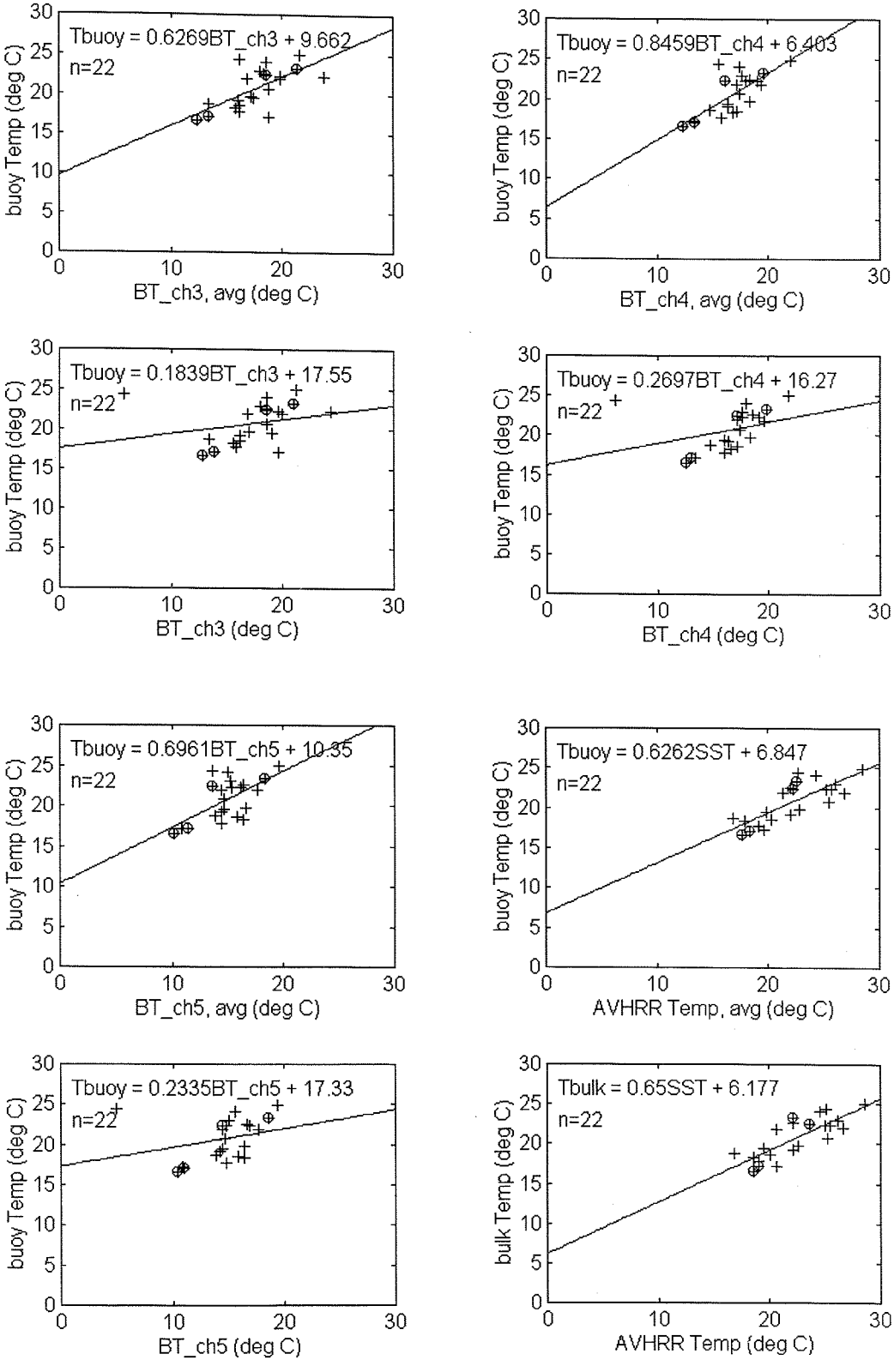

Figure 8.3. Linear regressions between AVHRR brightness temperatures and SSTs (ch_3, ch_4, ch_5 and AVHRR Temp) and buoy temperatures. Crosses indicate NOAA-11 estimates, circles and crosses indicate NOAA-12 estimates.

particular AVHRR scene in relation to a single ATSR one. With the available data set, only 2 match-ups were obtained for ATSR and COADS data, and only one for ATSR and buoy data. The deltaTs are presented in Table 8.4.

Table 8.4 indicates that the deltaTs varied from -4.36°C to 2.01°C. COADS match-ups produced the extreme deltaTs, while the buoy measurement made in 2 March 1994 was only 0.14°C colder than the ATSR 'skin' temperature. From the knowledge that the skin SST is generally colder than the bulk SST (e.g. Robinson, 1985; Schluessel et al., 1990), we would expect to have always a positive deltaT when computing bulk minus ATSR SSTs. That was the case only for the data taken in 5 May 1994. There is consistency, however, between the signal of deltaT of the central pixel and average pixels estimates, which implies that the ATSR image of 2 March 1994 can be overestimating SST.

Table 8.4. DeltaT between *in situ* temperatures ($T_{in\ situ}$) and ATSR SSTs (T_{ATSR})

image	*ATSR SST (°C)*		*in situ*	*deltaT = $T_{in\ situ}$ - T_{ATSR} (°C)*	
date	*central pixel*	*avg. pixel*	*SST (°C)*	*central pixel*	*avg. pixel*
2 Mar 94	23.68	24.01	23.54 (1)	-0.14	-0.47
2 Mar 94	27.16	23.88	22.8 (2)	-4.36	-1.08
5 May 94	7.84	8.3	9.85 (2)	2.01	1.55

Note: (1) buoy measurement; (2) COADS measurement.

Working with SST measured by a thermosalinograph onboard a research vessel off the Faeroes Islands (~ 62°N, 7°W), Forrester et al. (1992) made a preliminary validation of ATSR SSTs. The authors used a time window of ±10 h between the image and the 'bulk' SST measurement acquisition times as a compromise for obtaining a maximum number of match-up points without risking to suffer the effects of the diurnal warming and advection. The interval of ±10 h was assumed to be reasonable for use in the Faeroes area, since time intervals of 1 h to 12 h were reported to be linked to r.m.s. differences of only 0.2 degK in the sea surface temperatures of that area.

Forrester et al. (1992) found that the bias (deltaT) between bulk and ATSR (full-resolution data) SSTs was 0.25 degK (bulk temperatures warmer) with a standard deviation of 0.35 degK. The bias was assumed to be due to the skin effect and not to a bias in the ATSR estimate. The bulk-skin deltaT results of Forrester et al. (1992) are similar to those of Schluessel et al. (1990) and Donlon and Robinson (1997), for example.

The comparison of the deltaT presented by Forrester et al. (1992) with the ones presented in Table 8.4, shows that they are completely distinct. Our deltaTs are several times bigger than those currently described in the literature. That suggests another effect happening on top of a supposed low bulk-skin effect, which can either be related to a real bias in the ATSR SST algorithm or to geolocation or advection effects if the *in situ* SST data is assumed to be accurate.

The results presented in tables 8.1 to 8.4 also indicate that generally the central pixel match-ups produce bigger deltaTs than the average pixel. Supposing a good geolocation of the images (performed to a precision of a couple of kilometres or less - see sections 4.2.1 and 4.3), the bigger deltaTs found for the central pixel could have been caused by the lateral variation of the thermal field in the study area. Strong lateral gradients of temperature found in the Southwestern Atlantic Ocean could probably have caused big variation of temperature in a particular location in a period of a few hours. We have tried to eliminate this problem using a very tight temporal window of $\pm$ 3 hours for the match-ups, which apparently worked well in the research presented by Keogh et al. (1999). As discussed in the next section of this chapter, this was apparently not the case here.

Alternatively, the bigger deltaTs between *in situ* and satellite temperatures in the central pixel estimates could have been caused by mismatching of the temperature pairs in space. As seen in Chapters 5 and 6, the temperature gradients in the study area were specially high across the buoy tracks, for the buoys tended to follow the fronts. An explanation for the fact that the average pixel estimates performed better than the central pixel ones can arise from the fact that very small errors of positioning in the central pixel's position could lead the deltaT estimate to be biased towards the warm or the cold waters of the fronts. That explanation, however, does not necessarily apply to the COADS data, since the location of the SST sampling by ships of opportunity is independent of the fronts location.

8.3. ATSR and temperature difference images

As described in Section 4.6, 13 temperature difference (deltaT) images were obtained for AVHRR and ATSR images of the same dates and geolocated to the same region. Four deltaT images for ATSR daytime minus night time images were also generated.

Before considering the deltaT images, however, we will lead the discussion towards the characteristics of the ATSR images obtained for this work. They were not used in the previous chapters of the thesis mainly because they were not as numerous as the AVHRR images and also covered a much smaller area in the ground. Because of their orbit/frame characteristics and temporal resolution, it is not easy to geolocate the ATSR images to a pre-fixed area as with the AVHRR images. Moreover, the majority of the ATSR images obtained here were related to orbit/frames located at the coastal areas off southern South America. That reduced the number of pixels in the image with valid SST measurements, because the land data has to be discarded. As no quick-looks were available from ESA during the selection phase, some of the images were very clouded as well.

Nevertheless, the ATSR SST images proved to be of very good quality and able to demonstrate the meso- to small-scale structures occurring in the study area. The capability of ATSR SST images to detect fine scale thermal structures in the sea surface was first pointed out by Robinson and Donlon (1994). The authors analysed a set of ATSR images in the region of the Mediterranean Sea and in the Brazil-Malvinas convergence (BMC). In the last area, Robinson and Donlon (1994) have revealed the coherence of long filaments (down to about 2 km wide) of water entrained into eddies' periphery and in interleaving bands of cold and warm waters of the Malvinas and Brazil currents. The authors state that the complexity of detail shown by the ATSR images in the BMC region was new and not achieved before with the AVHRR images because of the poorer radiometric resolution of the latter.

The AVHRR data analysed for this thesis does not seem to corroborate Robinson and Donlon's (1994) ideas that small structures can not be detected by this sensor. However, as it was not the objective of this thesis to perform a study on the radiometric responses of the AVHRR and ATSR sensors, we leave the question open for now.

Figures 8.4, 8.5 and 8.6 are examples of ATSR image mosaics obtained for the BMC region in 8 November 1993, 9 November 1993 and 5 May 1994, respectively. The examples were chosen because they are relatively cloud-free scenes and represent some of the meso to small scale structures occurring at the sea surface in the study area. For comparison, Figure 8.4 can be checked against its AVHRR counterpart displayed in figures 5.16 (i) and 5.23. Figure 8.6 can be compared with figures 5.16 (o), 5.19 (bottom) and 5.25.

Figures 8.4 to 8.6 present thermal structures in ranges of up to 26°C. The oceanographic structures seen in these figures are typical of the BMC region. In Figure 8.4, the core of Malvinas Current (MC) is seen along the coast, located between the warmer coastal waters off

the La Plata River and the Brazil Current (BC). A jet-like, warm structure is noticed at about 38°S, 54°W. Looking to Figure 5.16 (i), this structure seems to be the cyclonic part of a mushroom-like feature of the BC extension towards the MC. In the subsequent days after 8 November 1993, the structure has possibly detached from the BC and been advected northwards alongside MC, but cloud coverage made this assumption impossible to be confirmed with the available AVHRR images.

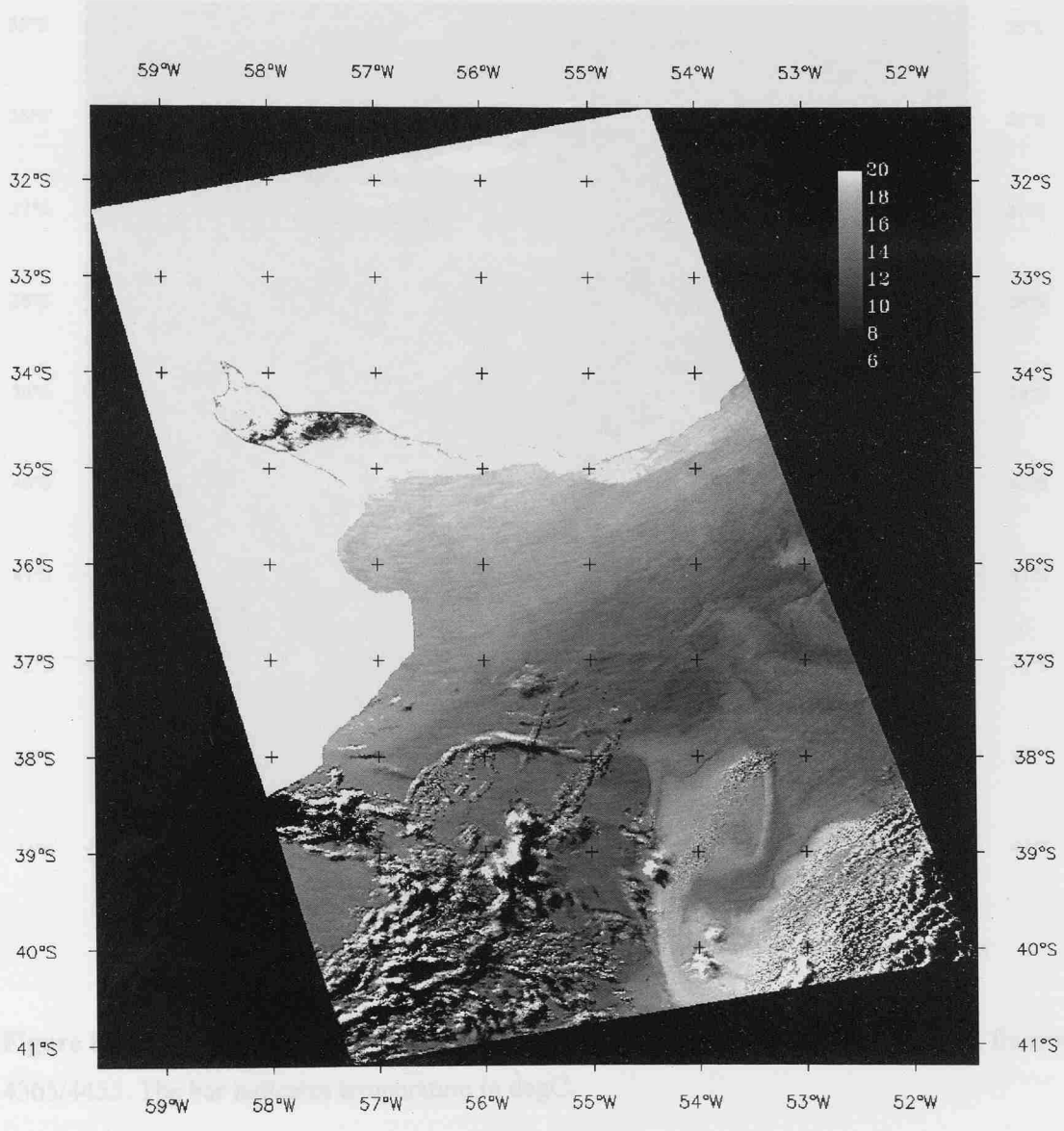

Figure 8.4. ATSR SST mosaic image of 8 November 1993, 02:37 GMT. Orbit 12100, frames 6435/6525. The bar indicates temperature in degC.

Figure 8.5 presents an open ocean scene at the interface between BC and MC. As described by Robinson and Donlon (1994) for open ocean ATSR scenes in the BMC region, several

small to mesoscale structures are present, including very long and thin filaments of water. According to Robinson and Donlon (1994), fine structures like these filaments could compromise the claim of *in situ* measurements made by buoys or ships to be representative of the real thermal state of wider areas in the BMC region.

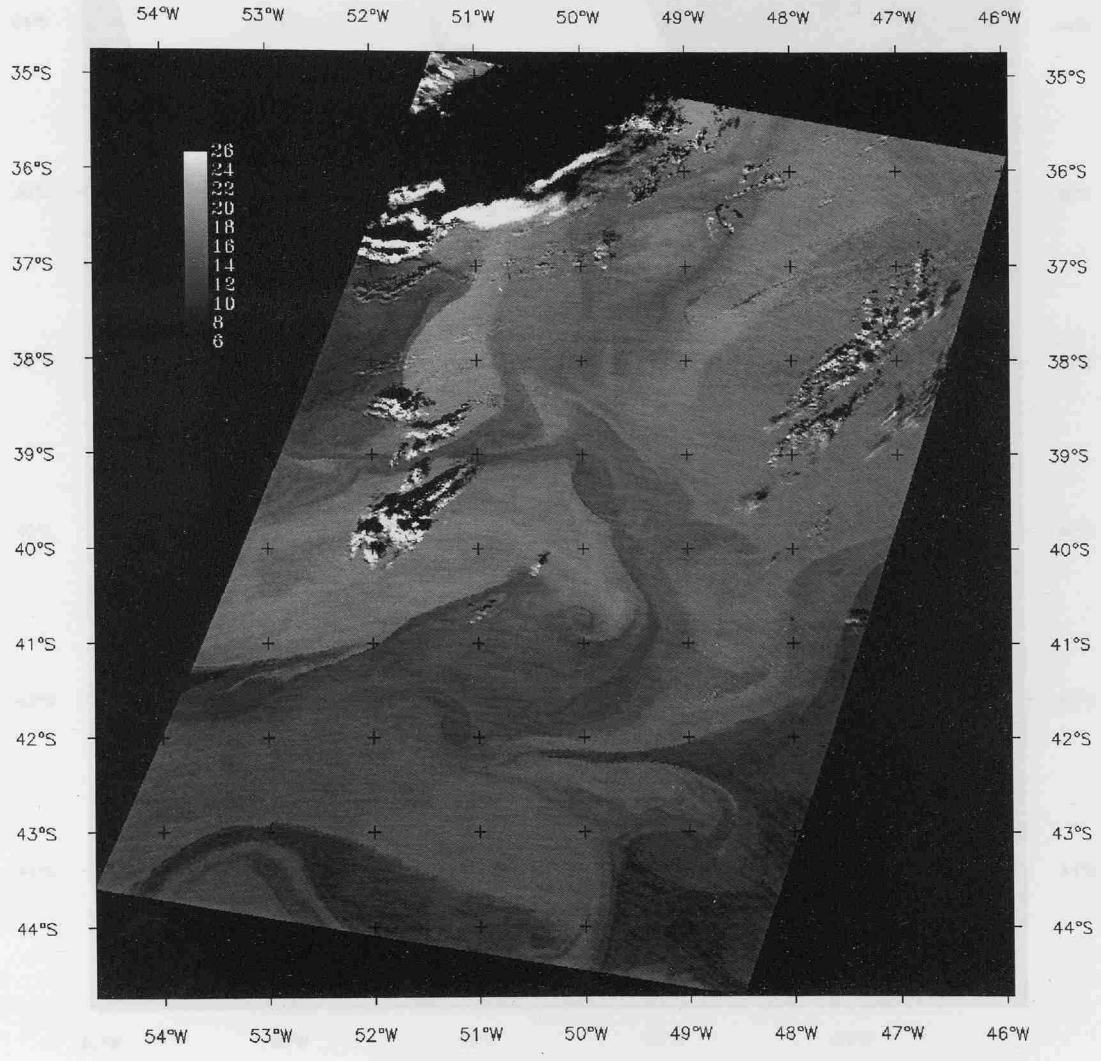

Figure 8.5. ATSR SST mosaic image of 9 November 1993, 13:21 GMT. Orbit 12121, frames 4365/4455. The bar indicates temperature in degC.

The ATSR mosaic of 5 May 1994 is presented in Figure 8.6. The figure shows the MC core alongside the coastal waters off Argentina and a small portion of BC waters at the approximate position of 38°S, 55°W.

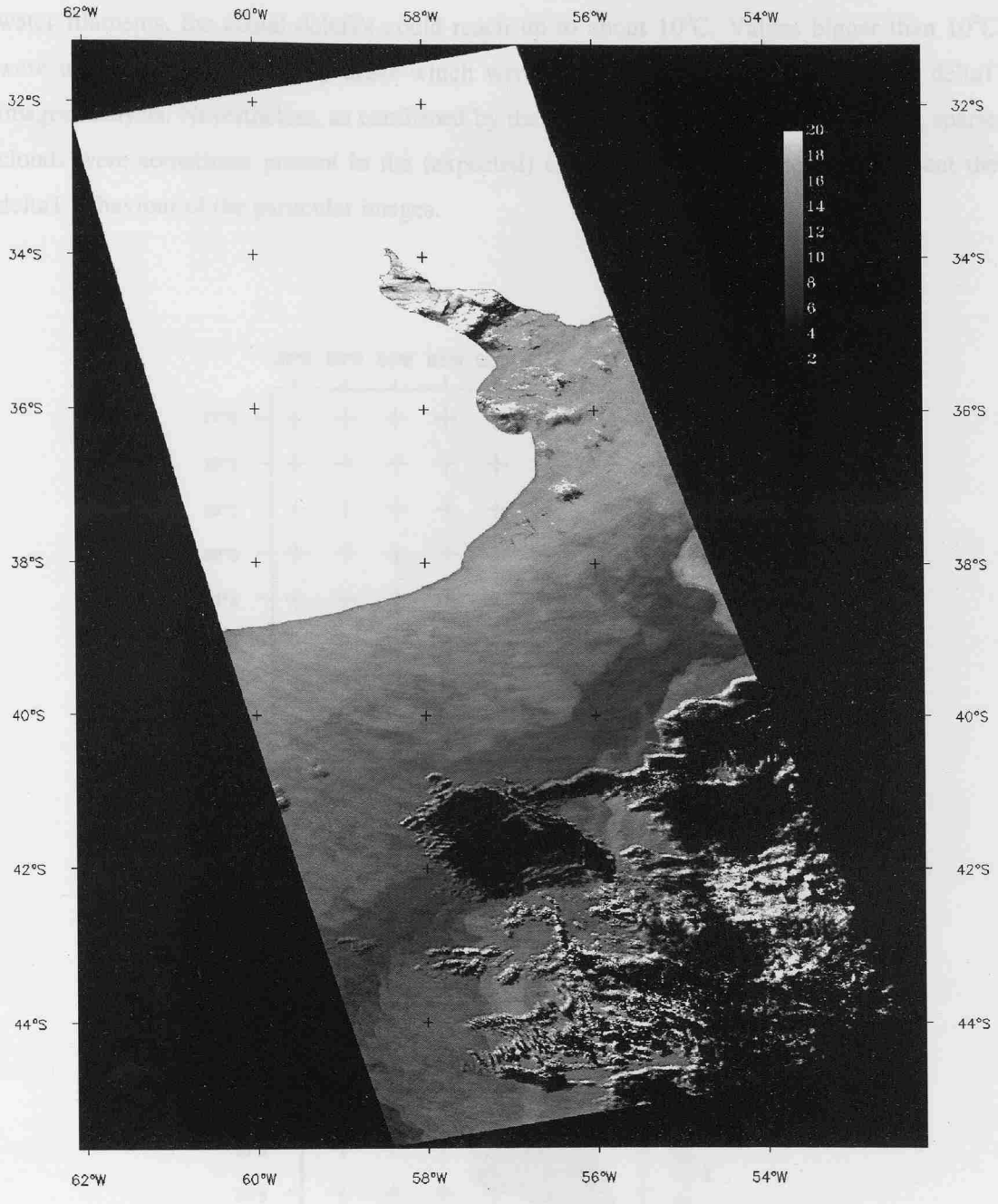

Figure 8.6. ATSR SST mosaic image of 5 May 1994, 02:46 GMT. Orbit 14651, frames 6345/6435/6525. The bar indicates temperature in degC.

The deltaT AVHRR minus ATSR images are presented in Figure 8.7. All the images were scaled to the same temperature range of -3°C to 3°C, which was about two to three times bigger than the commonly reported range of differences between 'bulk' and 'skin' sea surface temperatures. That was merely a visual scale for comparing the different deltaT images since,

in some cases of cloud free areas close to the oceanographic fronts and along small scale water filaments, the actual deltaTs could reach up to about 10°C. Values bigger than 10°C were usually related to cloudy areas which were identified and discarded from the deltaT images analysis. Nevertheless, as confirmed by the histograms presented in Figure 8.8, sparse clouds were sometimes present in the (expected) cloud free areas selected to represent the deltaT behaviour of the particular images.

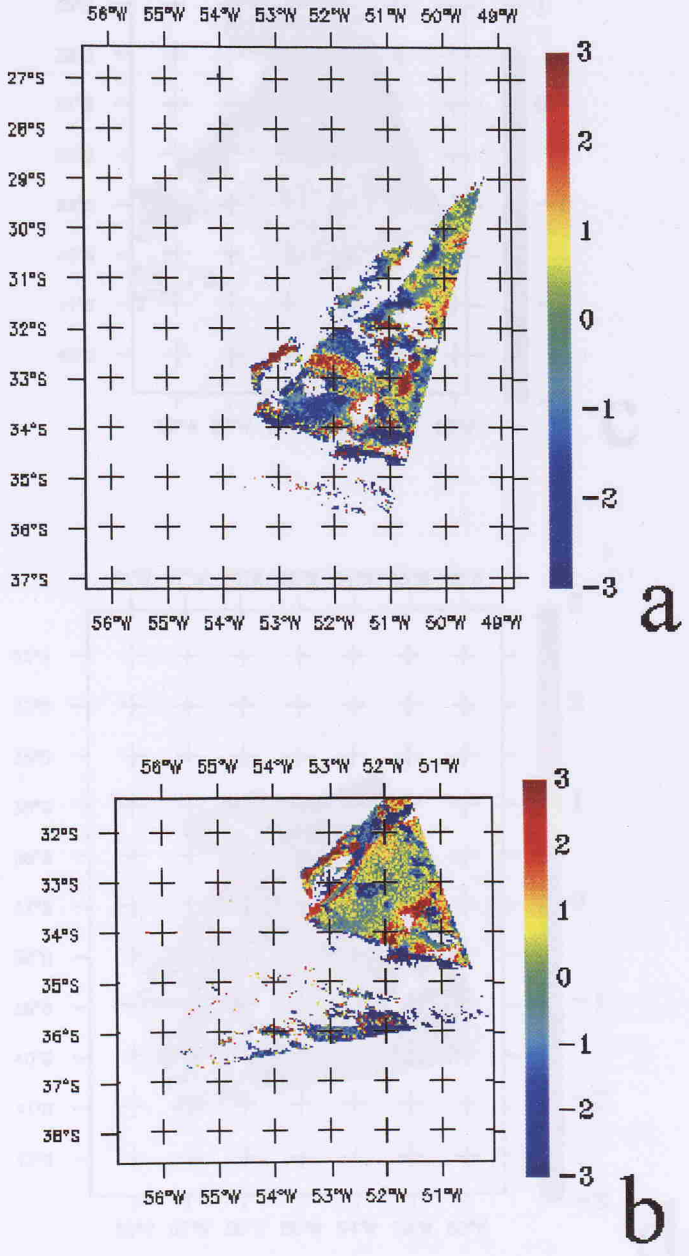

Figure 8.7. DeltaT AVHRR minus ATSR images. Labels **a** and **b** are in accordance to Table 8.5. The colour bar indicates temperature in degC.

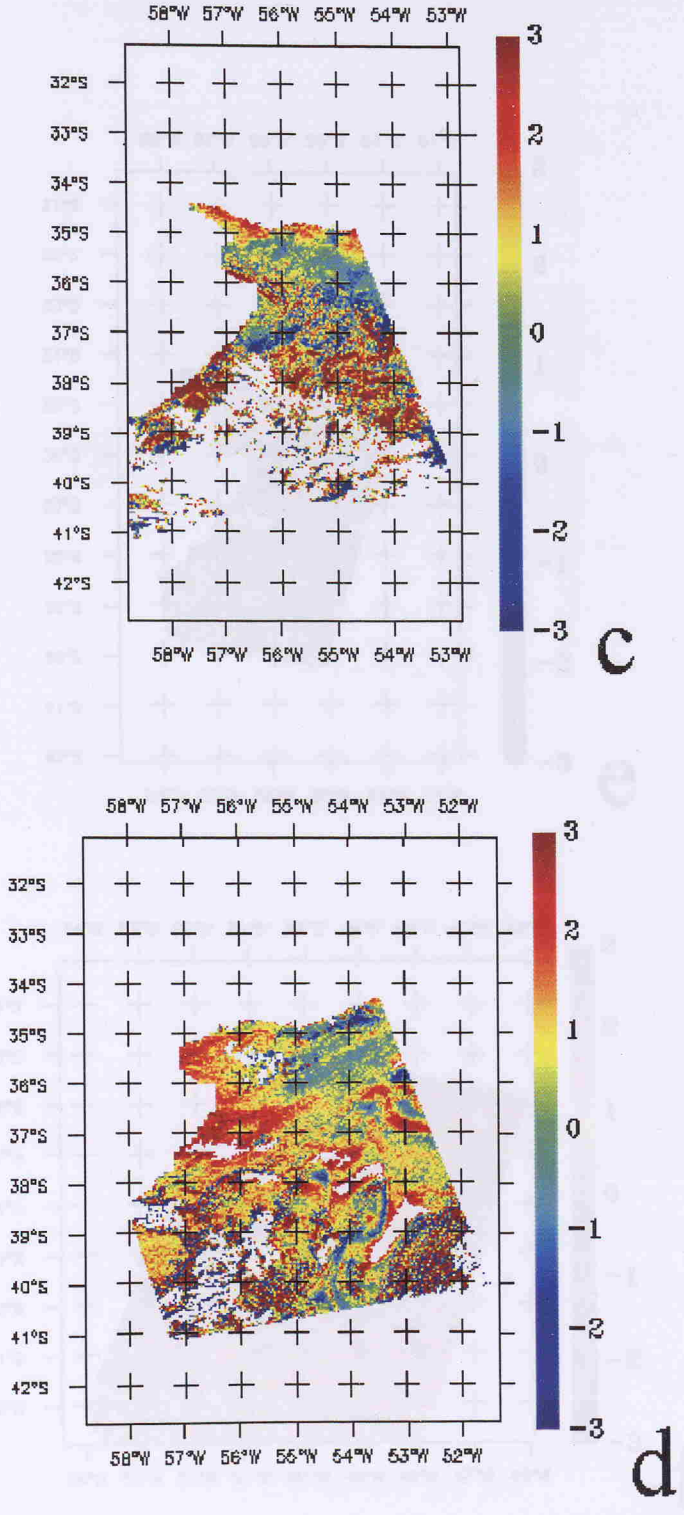

Figure 8.7 (cont.). DeltaT AVHRR minus ATSR images. Labels **c** and **d** are in accordance to Table 8.5. The colour bar indicates temperature in degC.

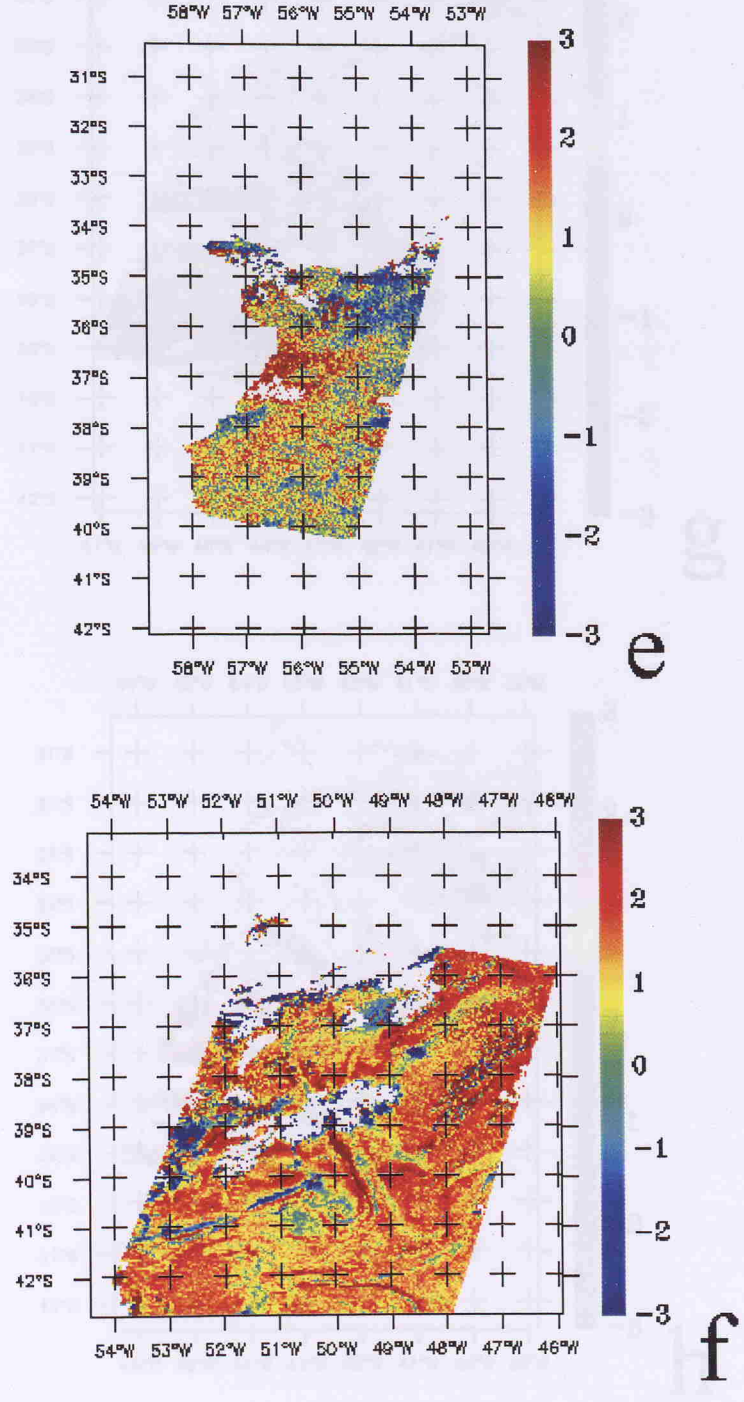

Figure 8.7 (cont.). DeltaT AVHRR minus ATSR images. Labels **e** and **f** are in accordance to Table 8.5. The colour bar indicates temperature in degC.

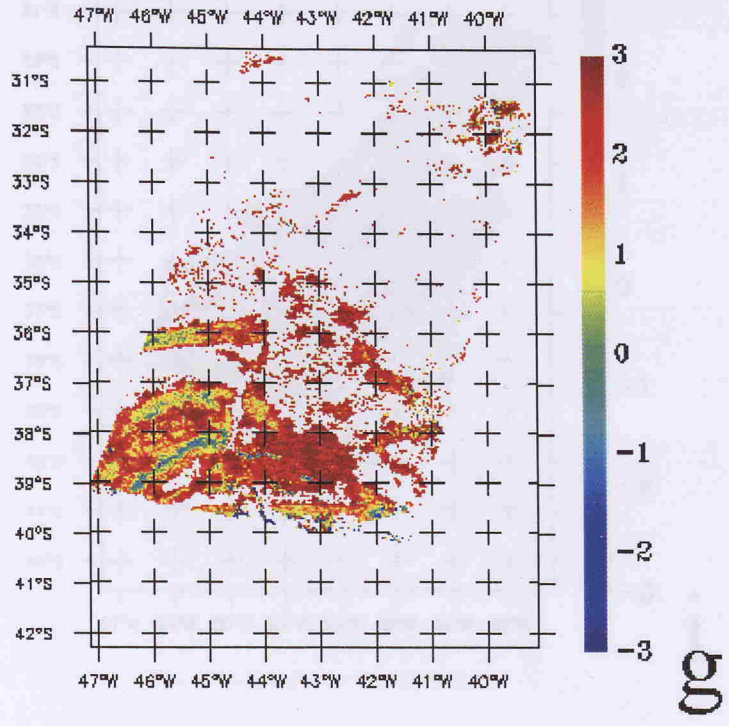

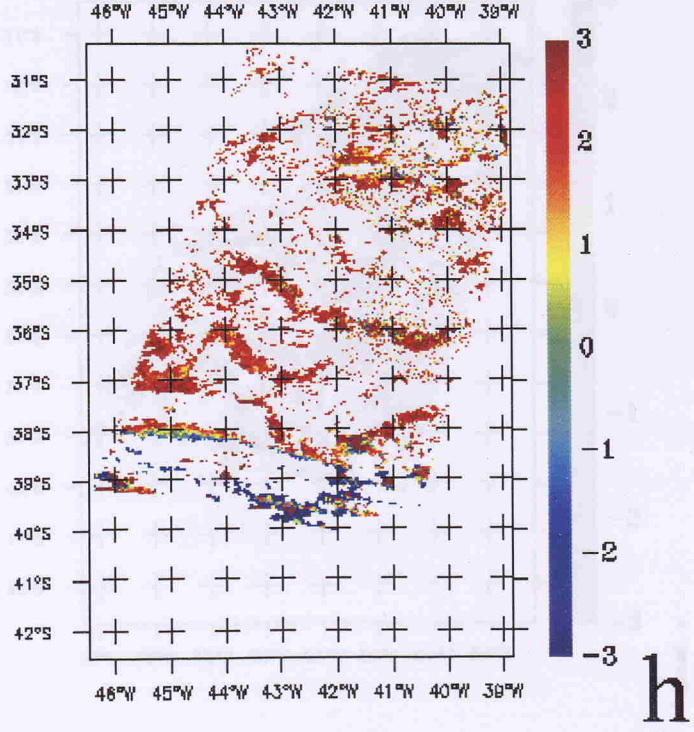

Figure 8.7 (cont.). DeltaT AVHRR minus ATSR images. Labels **g** and **h** are in accordance to Table 8.5. The colour bar indicates temperature in degC.

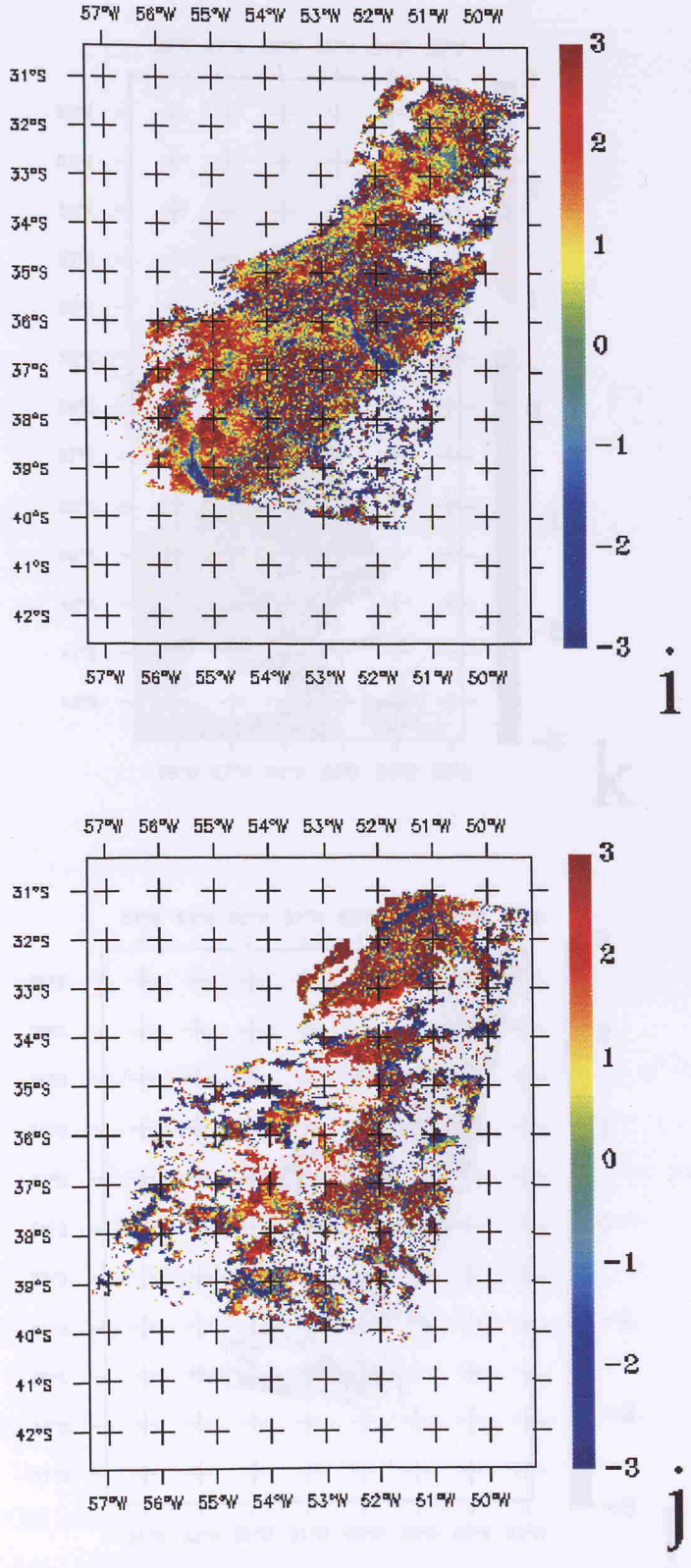

Figure 8.7 (cont.). DeltaT AVHRR minus ATSR images. Labels **i** and **j** are in accordance to Table 8.5. The colour bar indicates temperature in degC.

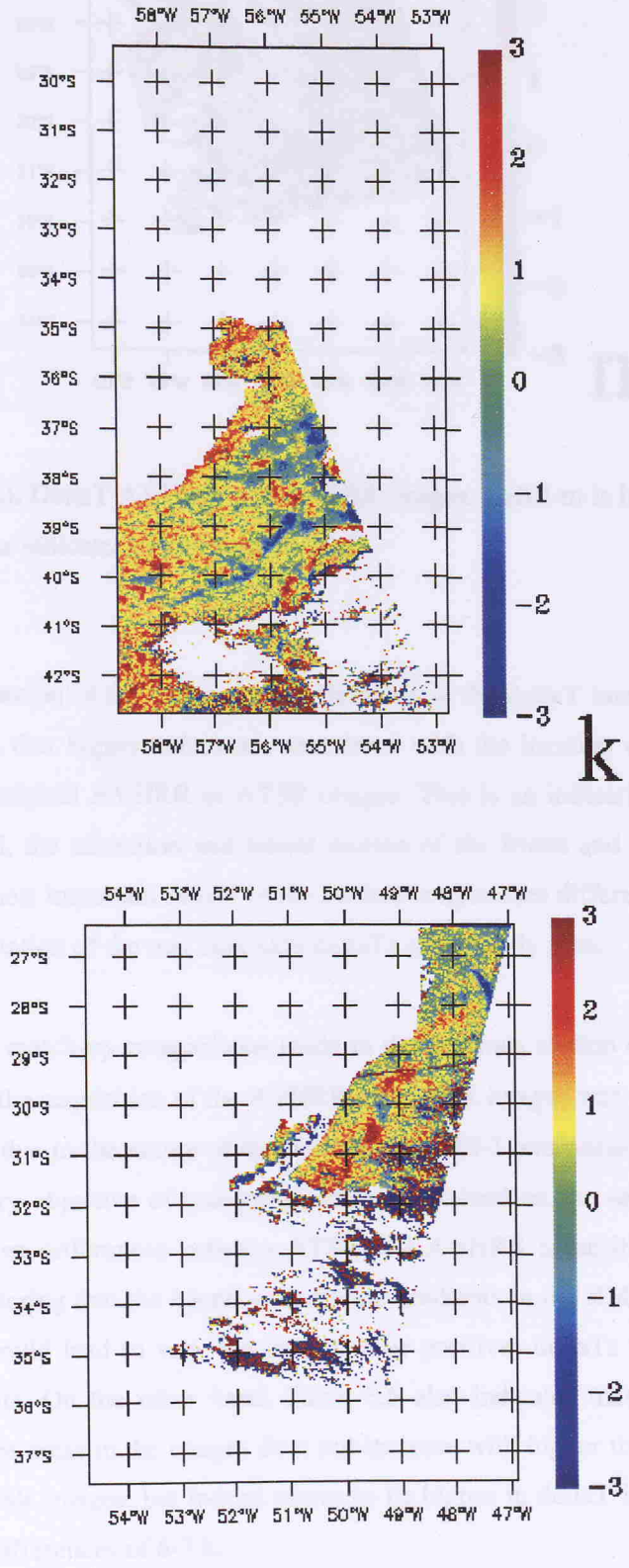

Figure 8.7 (cont.). DeltaT AVHRR minus ATSR images. Labels **k** and **l** are in accordance to Table 8.5. The colour bar indicates temperature in degC.

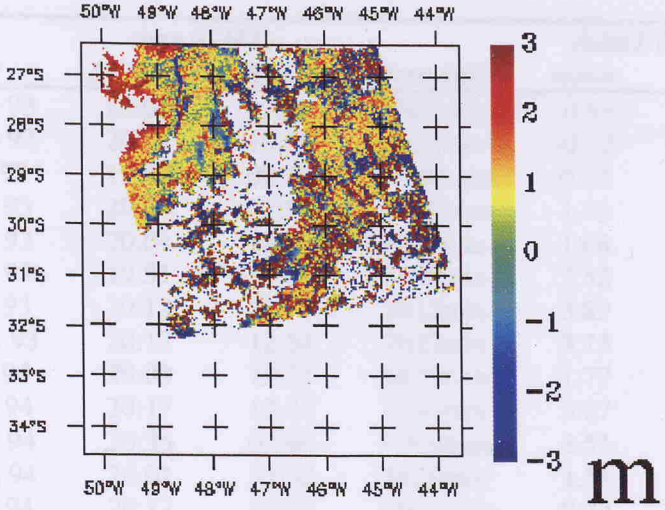

Figure 8.7 (cont.). DeltaT AVHRR minus ATSR images. Label **m** is in accordance to Table 8.5. The colour bar indicates temperature in degC.

The spatial distribution of the temperature differences in the deltaT images, as seen in Figure 8.7, demonstrates that bigger values are associated with the location of the fronts or water filaments in the original AVHRR or ATSR images. This is an indication that, for the study region and period, the advection and lateral motion of the fronts and small scale structures were one of the most important causes of the surface temperature differences. These processes mask our interpretation of the real bulk-skin deltaTs in the study area.

In contrast to the match-up comparisons made in the previous section of this thesis, the time interval between the acquisition of the AVHRR and ATSR images was not restricted to ± 3 h. That was mainly due to the nature of the NOAA and ERS-1 overpasses above the study area and to the primary objective of comparing images obtained on the same days. As noted in Table 8.5, the time differences between ATSR and AVHRR acquisitions were up to more than 18 h. Considering that the lateral temperature gradients in the BMC region are very big, lateral motions could lead to very big (negative or positive) deltaTs in particular locations close to the fronts. On the other hand, Table 8.5 also indicates that the mean deltaTs of selected cloud free areas in the images does not increase with higher time difference between AVHRR and ATSR images, but indeed seems to be higher in deltaT images associated with the shorter time differences of 6-7 h.

Table 8.5. Statistics for the deltaT AVHRR minus ATSR images

deltaT		*time (GMT)*			*deltaT (°C)*		
image	*date*	*AVHRR*	*ATSR*	*time diff.*	*mean*	*std.*	N
a	28 Sep 93	20:01	02:26	17h35min	-0.89	1.72	1393
b	28 Sep 93	20:01	13:39	6h22min	-0.12	1.22	884
c	7 Oct 93	19:52	02:43	17h09min	0.12	1.02	1221
d	8 Nov 93	20:04	02:37	17h27min	1.46	1.01	2028
e	8 Nov 93	20:04	13:51	6h13min	1.68	1.09	6955
f	9 Nov 93	19:51	13:21	6h30min	2.52	1.17	10891
g	2 Dec 93	20:12	12:57	7h15min	3.89	1.32	11710
h	18 Dec 93	20:17	12:54	7h23min	3.73	1.04	10341
i	6 Feb 94	20:09	13:37	6h32min	1.77	1.43	1409
j	2 Mar 94	20:17	13:37	6h40min	3.87	1.30	1038
k	5 May 94	20:36	02:46	17h50min	1.51	1.27	9045
l	26 Jun 94	20:01	13:32	6h29min	1.34	1.06	3373
m	11 Jul 94	20:17	01:57	18h29min	0.37	0.86	1051
mean	-----	-----	-----	----	1.63	1.19	-----

Table 8.5 indicates that the mean deltaT for the 13 images seen in Figure 8.7 have ranged from -0.89°C to 3.89°C. The overall mean value for deltaT computed from all images is 1.63°C. The standard deviations of deltaT ranged from 0.86°C to 1.72°C, being equal to 1.19°C in average. The mean and standard deviations presented in Table 8.5 were computed from sub-scenes of each particular image free of clouds and land. The number of pixels in these sub-scenes is denoted as 'N' (number of observations) in Table 8.5. The sub-scenes were defined to be as big and representative of the cloud free deltaT fields as possible. The histograms obtained from the deltaT images' sub-scenes are seen in Figure 8.8. Generally, all the histograms have a Gaussian form with generally a positive mean. Extreme deltaT values can be contaminated by sparse clouds difficult to be detected in the original images.

As pointed out in Section 4.6, there is a difficulty in assessing the spatial patterns of deltaT between AVHRR and ATSR images owing to the fact that geolocation of the images obtained from the different sensors is not easy to perform. It is also difficult to obtain a series of simultaneous cloud free scenes from the two sensors over the same area and time. In fact, deltaT AVHRR minus ATSR images have not been previously published to our knowledge.

From all the references utilised in this thesis, only Kizu and Sakaida (1996) have provided maps of deltaT which resemble the ones presented here. Kizu and Sakaida (1996), however, have mapped the deltaTs between daytime and night time MCSST images. They worked in the area around Japan, but have demonstrated that a negative diurnal SST cycle (night time

SSTs higher than day time ones) are possible to be found, which adds even more problems to the attempt of understanding the spatial behaviour of the deltaTs.

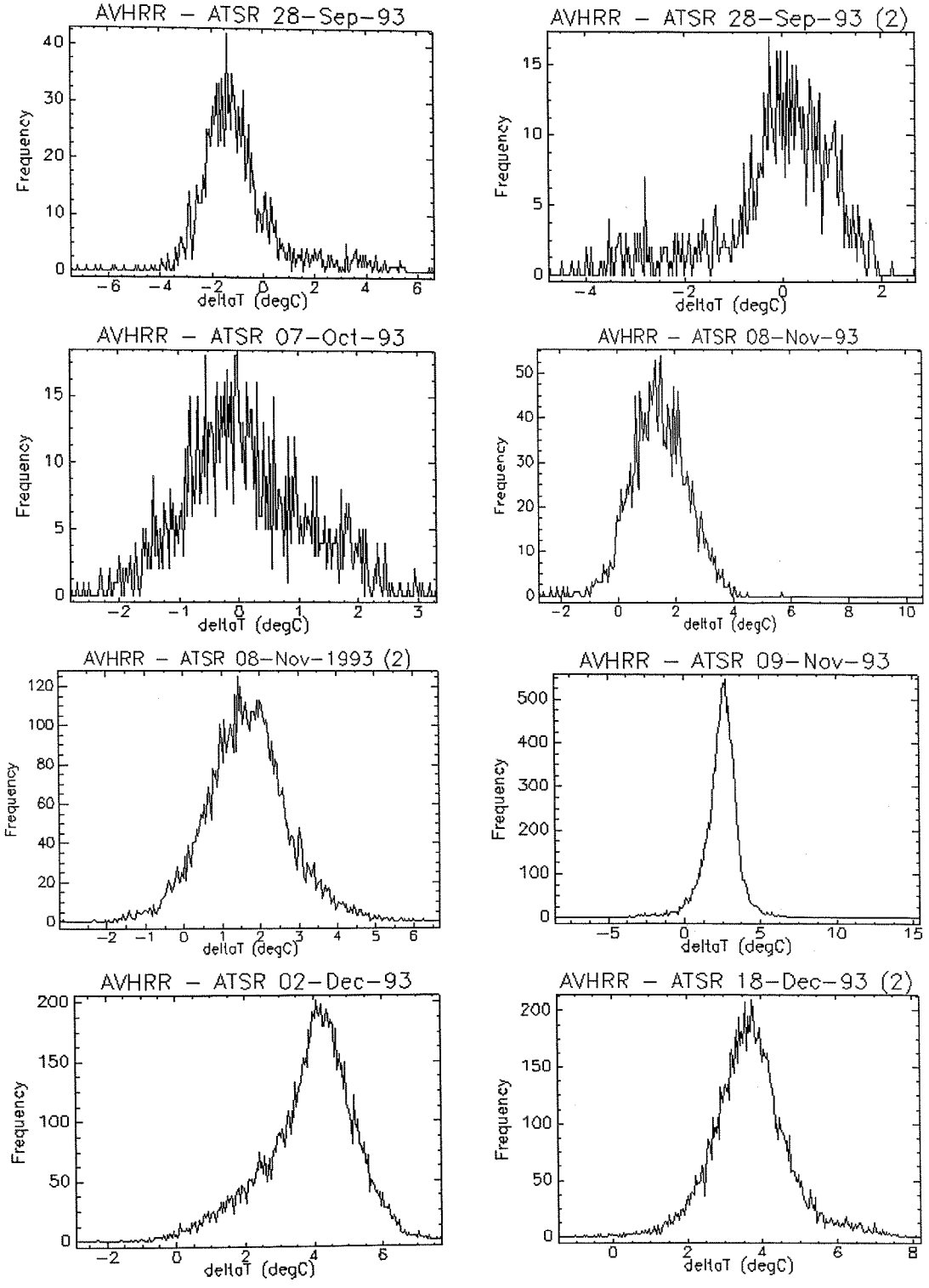

Figure 8.8. Frequency histograms of representative cloud free sub-scenes of the deltaT AVHRR minus ATSR images. Panels from top left to bottom right represent Table 8.5 images **a** to **h**, respectively.

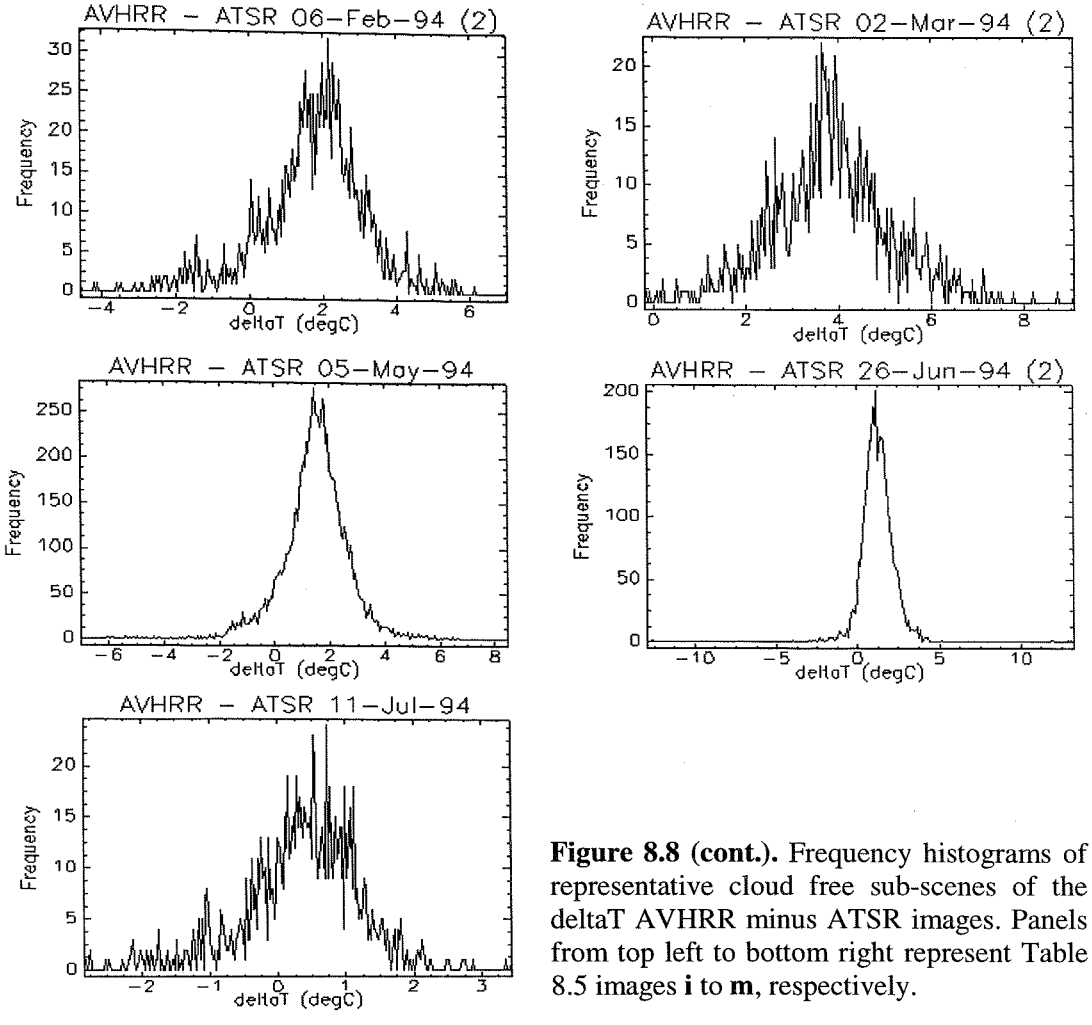

Figure 8.8 (cont.). Frequency histograms of representative cloud free sub-scenes of the deltaT AVHRR minus ATSR images. Panels from top left to bottom right represent Table 8.5 images **i** to **m**, respectively.

Barton et al. (1994) have specifically worked with the intercomparison of AVHRR and ATSR products. Those authors, however, have performed a preliminary study utilising only one image of each sensor for an arbitrary transect off the northeast coast of Australia. The images were obtained within 4 h in relation to each other during the night time in 13 September 1991. Comparing the AVHRR and ATSR temperatures, Barton et al. (1994) reported a 'good agreement' between the variables and suggested that the deltaTs are about 2°C, AVHRR temperatures warmer than ATSR ones. Although no straight-forward comparison can be made between Barton's et al. (1994) results and the ones displayed here, the numbers provided by these authors is very similar to the overall mean deltaT value of 1.63°C indicated in Table 8.5 for the BMC region.

The deltaT ATSR day time minus ATSR nightime images are shown in Figure 8.9. The deltaT spatial distribution in these images seem to be more uniform than those of the AVHRR minus ATSR images, although here we have less images and also the cloud free sub-scenes

are smaller than the other deltaT images seen in Figure 8.7. Table 8.6, indicates that the overall mean deltaT for daytime minus night time ATSR images was 0.16°C. The standard deviations, however, are several times bigger than the mean deltaTs. The time interval between the daytime and night time overpasses of the ERS-1 satellite over coincident areas was about 11 h 15 min. The superimposition of the ascending and descending frames of the ATSR images is also clear in Figure 8.9.

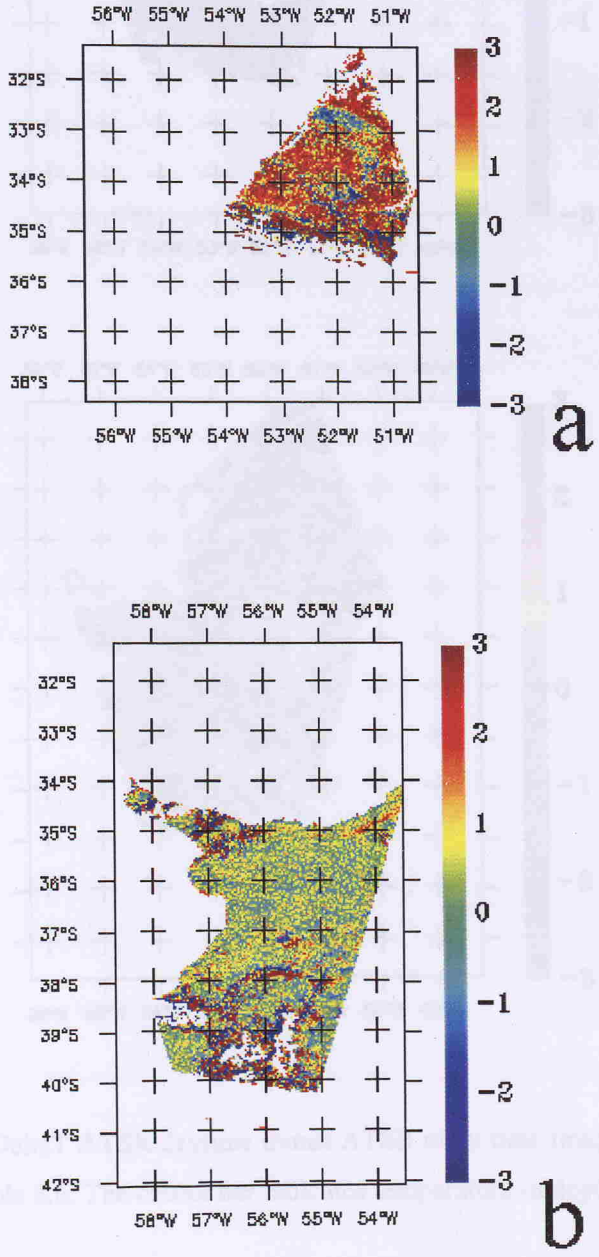

Figure 8.9. DeltaT ATSR daytime minus ATSR night time images. Labels **a** and **b** are in accordance to Table 8.6. The colour bar indicates temperature in degC.

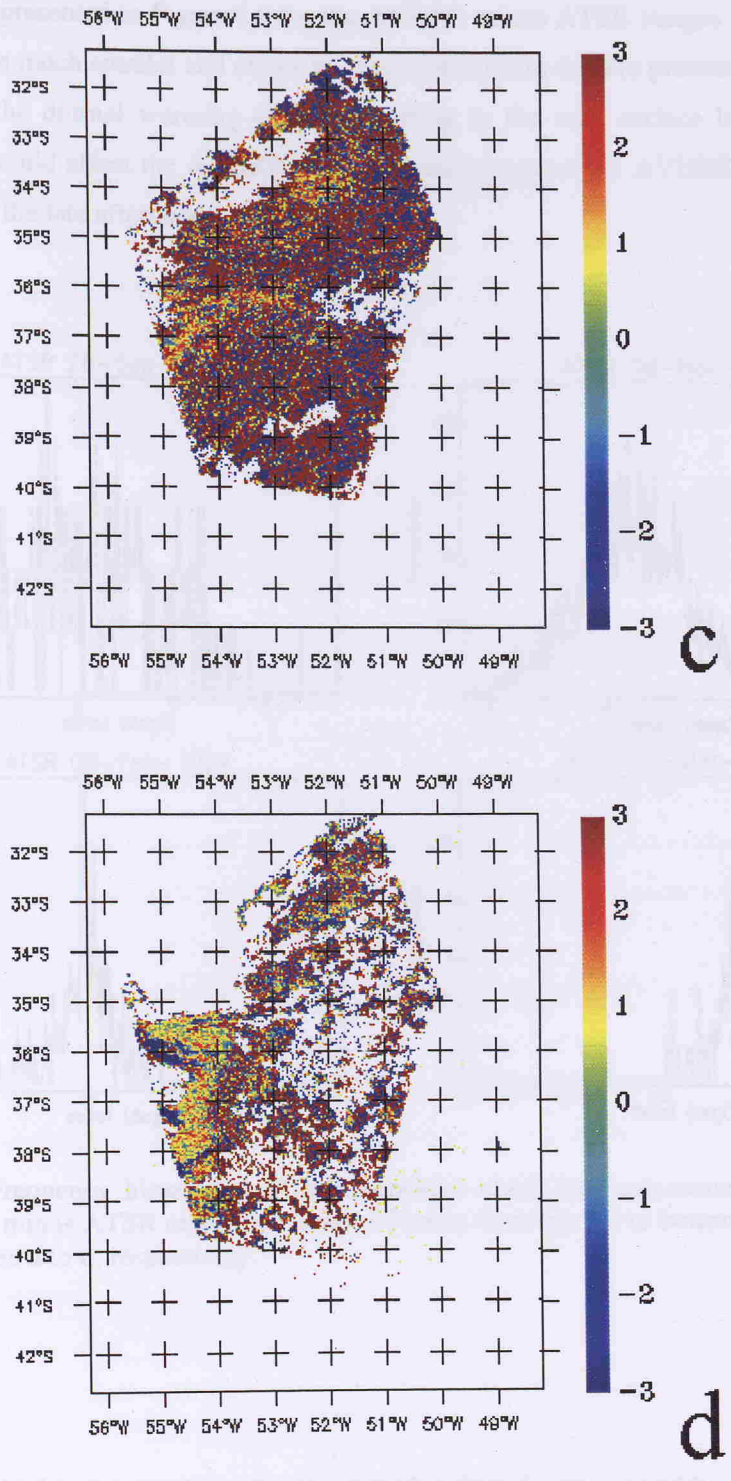

Figure 8.9 (cont.). DeltaT ATSR daytime minus ATSR night time images. Labels **c** and **d** are in accordance to Table 8.6. The colour bar indicates temperature in degC.

Figure 8.10 shows the frequency histograms of the cloud free sub-scenes taken as representative of the particular ATSR daytime minus night time deltaT images. They are

similar to those presented in Figure 8.8 for the AVHRR minus ATSR images, except that the mean deltaTs are much smaller and closer to zero. These mean deltaTs presented in Table 8.6 could indicate the diurnal warming effects occurring in the near surface layer of the sea surface which would affect the AVHRR data even more because the AVHRR data is mainly obtained during the late afternoon (see Table 8.5).

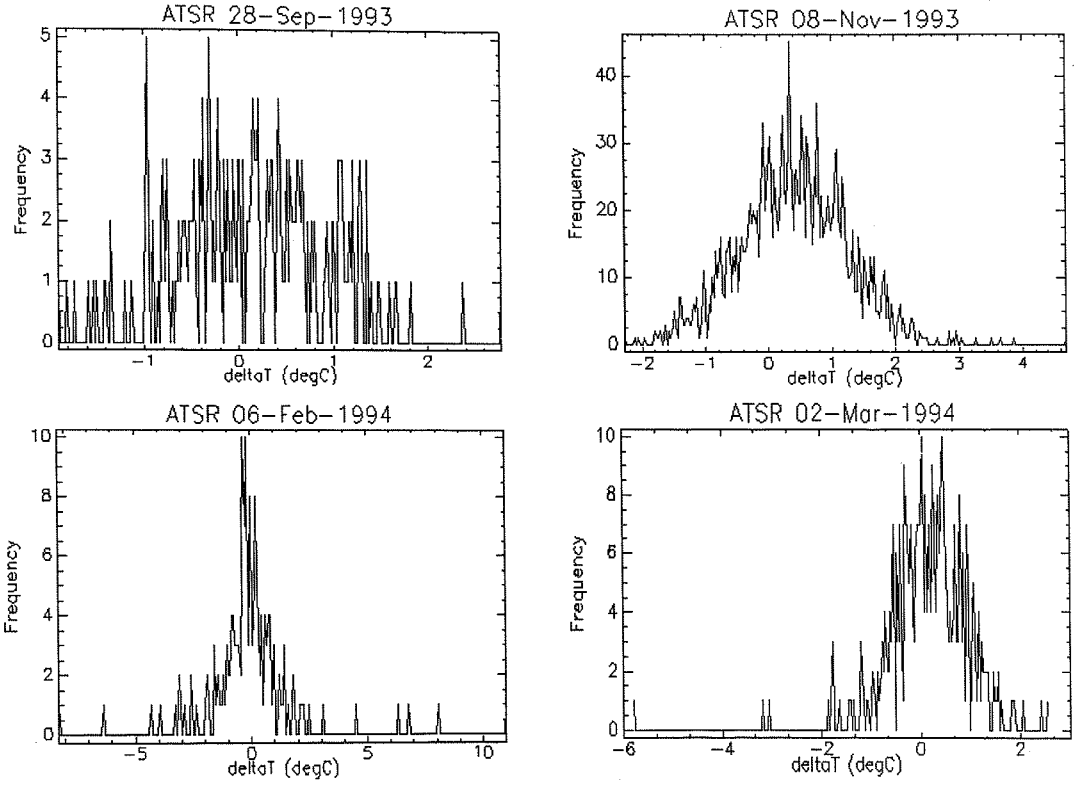

Figure 8.10. Frequency histograms of representative cloud free sub-scenes of the deltaT ATSR daytime minus ATSR night time images. Panels from top left to bottom right represent Table 8.6 images **a** to **d**, respectively.

Table 8.6. Statistics for the deltaT ATSR daytime ($ATSR_{day}$) minus ATSR night time ($ATSR_{night}$) images

deltaT		*time (GMT)*			*deltaT (°C)*		
image	*date*	$ATSR_{day}$	$ATSR_{night}$	*time diff.*	*mean*	*std.*	N
a	28 Sep 93	13:39	02:26	11h13min	0.14	0.78	242
b	8 Nov 93	13:51	02:37	11h14min	0.40	0.85	1968
c	6 Feb 94	13:37	02:24	11h13min	-0.05	1.95	165
d	2 Mar 94	13:37	02:24	11h13min	0.17	0.82	350
mean	-----	-----	-----	-----	0.16	1.08	-----

8.4. Summary and final remarks

The combined utilisation of satellite and *in situ* SST data was able to demonstrate the discrepancies in the measurements or estimations of SST obtained by these two sources of data in the BMC region. Moreover, it was also indicated that very big variations in deltaT can occur at the location of the surface fronts and other strong thermal structures present in the study region. The very active nature of the advection processes occurring in very small periods of time are pointed out as the possible causes for the higher deltaT values being particularly distributed in the frontal regions.

As the drifting buoys used in the majority of the validation programmes (especially the NOAA ones) can present the predictable tendency of concentrating in regions of strong thermal gradients at the sea surface, their temperature measurements would inevitably be subject to mismatching with satellite data because of the lateral motions of the fronts. This effect is definitely stronger in the western boundary currents and in regions of convergence, e.g. Brazil Current and Gulf Stream, where shear effect is present between currents transporting waters of very distinct thermal characteristics. The nature of the deltaTs is also associated with the time interval between the *in situ* and satellite SST retrievals.

The results presented in this chapter indicated that the deltaTs obtained from match-ups between buoy and AVHRR were higher than those obtained between ships of opportunity and AVHRR. This was not expected, since the SST measurements produced by oceanographic buoys have better accuracy than those produced by ships of opportunity. On the other hand, ship routes are not dependent on the distribution of the thermal fronts in the ocean and, in regions where those fronts are common, ships can offer a reliable way of sampling SST in different water masses.

The regressions between *in situ* and satellite SST have also demonstrated that a linear fit can be applicable to correct the satellite (NOAA) retrievals in respect to the temperatures measured by buoy or ships of opportunity. That can be useful in future applications of satellite data where exact temperatures are requested rather than only temperature gradients. This

could be the case when studying regions away from the BMC region in the core of the currents or in ecological studies where exact temperatures are linked to limits of occurrence of certain species of biota, such as, for example, the tuna (*Thunnus sp.*)

Although there is a bias between *in situ* and satellite estimated SSTs, the spatial analysis of the water masses and currents presented in chapters 5 and 6 of this thesis is still valid. The particular location of a specific isotherm, like the 20°C isotherm for example, could have been previously misplaced but, as proved before, this specific isotherm is found exactly on the BMC or BC/BCC frontal systems. In this case, due to the strength of the surface thermal gradients, several isotherms are constrained to a space of a few kilometres, and the error produced by tracking a 'biased' 20°C isoline would be at worse restricted to that few kilometres. However, when comparing specific values of temperature measured by buoys with specific pixels in the images, the application of the linear fit adjusting one variable in respect to the other is highly recommended.

CHAPTER 9

CONCLUSIONS AND FUTURE WORK

The research described in this thesis arose from an opportunity of studying the mesoscale surface processes of the Southwestern Atlantic Ocean by means of a combination of high-resolution satellite and Lagrangian data in the period of March 1993 to July 1994. To obtain an overview of the processes related to the large scale climatology of the sea surface temperature fields of the South Atlantic, an auxiliary data set composed of monthly averaged, low resolution multichannel sea surface temperatures (SST) was also analysed for the period between January 1982 and December 1995.

Both low and high resolution satellite data were used to describe the SST fields of the South Atlantic, the Brazil-Malvinas (Falkland) Convergence zone (BMC) and the South Brazilian Continental Shelf (SBCS) region. The variability of the SST fields and of the surface currents in those regions also were assessed for the period of this study. Oscillations with periods ranging from 6 months to interannual were found for the South Atlantic Ocean by applying Principal Component analysis to climatological averages and to anomaly SST fields of the South Atlantic.

Buoy time series have also been used to assess the major energy peaks of the spectra of the Brazil, Brazilian Coastal and South Atlantic currents. The peaks revealed oscillations ranging from a couple of days (atmospheric driven) to the semiannual period. Velocity measurements and kinetic energy estimates have indicated that the extension currents, such as the South Atlantic Current and the Brazilian Coastal Current (BCC) are slower and have higher kinetic energy than their originators, e.g. the Brazil Current (BC) and the Malvinas (Falkland) Current (MC), respectively.

The behaviour of the BCC was studied and its northward penetration along the SBCS proved to be seasonal. The mean latitude of the BCC penetration in August, the winter peak, was found to be 25.2°S ± 1.6 °, well to the north of the conventional understanding which limited the current to the maximum latitude of 28°S. This was identified utilising the 20°C isotherm

as an indicator of the BCC advection supported by direct measurements performed in this current by 3 low cost drifters which trajectories followed the isobaths and thermal fields of the SBCS region during 1993 to 1994. The oscillation of the BCC northern position, as described in this thesis, has direct relation with historical hydrographic data sets presented by other authors. Moreover, sardine (*Sardinella brasiliensis*) catch statistics presented by Sunyé and Servain (1998) are fully consistent with the results presented here for the BCC oscillation.

Eddies present in the Southwestern Atlantic have generally distinct formation mechanisms in the BMC and in the SBCS regions. In the former region, the classical description for geostrophically balanced eddies applies. In the SBCS region, on the other hand, eddies formed by current reversals or shelf break activity occur. Their sizes can be about a tenth of those of the classical BMC eddies found in this thesis and in previous work (e.g. Legeckis and Gordon, 1982; Olson et al., 1988). Empirical relationships were found between the eddies' sizes (diameters and perimeters) and their tangential velocities (V_T) or rotational periods (T_R). In the absence of direct measurements at the sea, measurements of eddies sizes in satellite images can feed these models to empirically predict their V_T or T_R. Such an approach can be useful for the fisheries fleet, for the merchant navy and perhaps for dynamical studies in the region.

The investigation of the temperature differences between *in situ* measurements and satellite estimates have demonstrated that, in contrast to what was expected, the higher values of deltaT were found for match-ups between buoys and AVHRR SSTs than for match-ups between ships of opportunity and AVHRR SSTs. Analysis of the deltaT spatial distributions (AVHRR minus ATSR, regarded in principle as the 'bulk' minus 'skin' temperature) have demonstrated that buoy measurements can produce biased match-ups with satellite SST estimates because the buoys tend to concentrate in regions of thermal gradients. Advection of these gradients could lead to both negative or positive deltaTs. However, the temporal variations of deltaT are still unknown for regions of high variability such as the BMC region. The wind effect on the deltaT behaviour is also unknown for the study region.

Although this thesis has provided some new insights into the mesoscale variability of the surface processes in the Southwestern Atlantic Ocean, the work is far from complete. Many questions still need to be answered, both in respect to the ocenoagraphic and to the remote sensing issues.

Questions linked to the oceanography of the study area remain on the real nature of the BCC, for example, since at the present we only have reports of a few sparse direct measurements made in this current. The seasonal behaviour, vertical structure and penetration limits of the BCC need urgently to be assessed, for not only economical aspects are involved in the process (fisheries), but because the present delimitation of biogeographical regions (Boltovskoy et al., 1999) is apparently dependent on the extension and behaviour of this current.

The biological productivity associated with eddies in both the BMC region and in the BC/BCC front is equally important to be investigated. At the same time we ought to know more about the vertical structure of these eddies and their mechanisms of formation and dissipation. During the dissipation phase, we need to investigate the mechanisms of heat and salt exchange between the eddies and the surrounding waters, because the assimilation of eddies in global models could indicate the importance of such structures in the global climate and weather, for example.

The relationship between sea surface heights (SSH) obtained from radar altimeters such as the TOPEX/Poseidon (T/P) and sea surface temperature is reported to be very strong, specially in the BMC region (Jones, 1997). T/P has tracks across the South American coast, which can be very useful for assessing full-resolution (along-track SSH measurements are about 6 km apart from each other) SSH anomalies of the ocean in transects across the BMC region. As both the BC and the MC are currents flowing along the coast of the South American continent before meeting, across-shelf transects of SSH seem to be ideal for studing the temporal variability and lateral surface signature of these currents. If a correlation is found to be strong between SSH and SST, the former can be used to monitor the currents in cloudy conditions which are very commom in the BMC area.

Finally, the study of the deltaTs in the Southwestern Atlantic have raised a series of interesting questions such as the behaviour of the deltaTs in the frontal zones and the role of the advection on biasing the deltaT estimate. *In situ* surveys measuring the skin and bulk temperatures have been performed along meridional transects in the South Atlantic (e.g. Donlon and Robinson, 1997), but perhaps a more localised cruise is worth being planned for the BMC region. The deployment of an instrumented buoy equipped with an infrared radiometer and a thermistor chain to obtain time series of deltaT between bulk and skin temperatures in a fixed position is still a goal whose fulfilment depends on long term planning, money and technology.

The research presented in this thesis has demonstrated that the combination of Lagrangian (buoy) and satellite data for studying the mesoscale processes of the Southwestern Atlantic Ocean offers many advantages not available when these two sources of data are used independently. For instance, the Lagrangian data in the Brazilian Coastal Current corroborated the findings of a northward movement of cold waters that was noticed in the satellite images, adding direct measurements of velocity and kinetic energy that satellites can not provide.

The synergism between buoy and satellite data was also important to demonstrate the eddy activity and thermal fronts of the BMC and SBCS regions. The resulting empirical relationships between eddy sizes and tangential velocities or rotational periods can be the base for a monitoring system that uses only satellite data and provides kinematic properties of the eddy field.

Combining buoy and satellite data also promoted an opportunity of noticing that the buoys used in this work, like many in the western boundary currents of the world ocean, tend to concentrate in the frontal regions of these currents even before arriving at the convergence zones. With the satellite data, it was shown that a particular pixel location in the frontal areas can present considerable temperature fluctuations in time scales of hours. Present-day validation algorithms for atmospheric correction of AVHRR data (e.g. McClain et al., 1985) consider buoy data to be of better quality than ships of opportunity data. Having analysed buoy, ships of opportunity and satellite data together in this thesis, we conclude that this may not be the case. Based on the work of this thesis it is recommended that studies of other oceanic regions would benefit from a similar combination of buoy and satellite data.

REFERENCES

ARGOS (1988) *ARGOS User's Manual.* CLS ARGOS, Toulouse, France.

Barton, I.J.; Mutlow, C.T.; Zavody, A.M.; Llewellyn-Jones, D.T. (1994) *Intercomparison of AVHRR and ATSR data products.* In: Proceedings. Second ERS-1 Symposium - Space at the Service of our Environment. Hamburg, Germany, 11-14 October 1994, p. 1099-1102.

Bianchi, A.A.; Giulivi, C.F.; Piola, A.R. (1993) *Mixing in the Brazil-Malvinas Confluence.* Deep-Sea Research, 40(7):1345-1358.

Boltovskoy, D.; Gibbons, M.J.; Hutchings, L. Binet, D. (1999) *General biological features of the South Atlantic.* In: Boltovskoy, D. (Ed.) South Atlantic Zooplankton, Vol. 1. Backhuys Publishers, Leiden. 868pp.

Campos, E.J.D.; Ikeda, Y.; Castro, B.M.; Gaeta, S.A.; Lorenzzetti, J.A.; Stevenson, M. R. (1996a) *Experiment studies circulation in the Western South Atlantic.* EOS Transactions Am. Geophys. Union, 77(27):253,259.

Campos, E.J.D., Lorenzzetti, J.A., Stevenson, M.R., Stech, J.L., Souza, R.B. (1996b). *Penetration of waters from the Brazil-Malvinas Confluence region along the South Amaerican Continental Shelf up to 23°S.* Anais da Academia Brasileira de Ciências, 68(Supl. 1): 49-58.

Campos, E.J.D., Lentini, C.D.; Miller, J.L.; Piola, A.R. (1999) *Interannual variability of the sea surface temperature in the South Brazil Bight.* Geophysical Research Letters, 26(14): 2061-2064.

Castello, J.P.; Haimovici, M.; Odebrecht, C.O.; Vooren, C.M. (1997) *The continental shelf and slope.* In: Chapter 6.7, Seeliger, U.; Odebrecht, C.; Castello, J.P. (Eds.) Subtropical Convergence Environments: The coast and sea in the Southwestern Atlantic. Springer-Verlag, Berlin Heidelberg. 308pp.

Castello, J.P.; Duarte, A.; Moller Jr., O.O.; Nienchesky, L.F.; Odebrecht, C.; Weiss, G.; Habiaga, R.P.; Belloto, V.R.; Kitzmann, D.; Souto, C.; Souza, R.B.; Ciotti, A.M.; Fillmann, G.; Schwingel, P.R.; Bersano, J.C.; Cirano, M.; Freire, K.; Lima Jr., I.; Mello, R.; Monteiro, A.; Resgalla Jr., C.; Soares, I.D.; Suzuky, M. (1990) *On the importance of coastal and subantarctic waters for the shelf ecosystem off Rio Grande do Sul.* Proceedings. 2nd. Symposium on Structure, Function and Management of Ecosystems of the South and Southeast Coast. Vol. 1, p.112-129, Águas de Lindóia, S.Paulo, Brazil.

Castro, B.M., Miranda, L.B. (1998) *Physical oceanography of the Western Atlantic continental shelf located between 4°N and 34°S, coastal segment (4,W).* In: Robinson, A.R., Brink, K.H. (Eds.), The Sea, vol. 11. John Wiley and Sons.

Ciotti, A.M.; Odebrecht, C.; Fillmann, G.; Moller Jr., O.O (1995) *Freshwater outflow and Subtropical Convergence influence on phytoplankton biomass on the southern Brazilian continental shelf.* Continental Shelf Research, 15(14):1737-1756.

Clowes, A.J. (1933) *Influence of the Pacific on the circulation in the South-West Atlantic Ocean.* Nature, 131:189-191.

Daniault, N. and Menard, Y. (1985) *Eddy kinetic energy distribution in the Southern Ocean from altimetry and FGGE drifiting buoys.* Journal of Geophysical Research, 90(11):11877-11889.

Deacon, G.E.R. (1933) *A general account of the hydrology of the South Atlantic Ocean.* Discovery Reports, 7:171-238.

Deacon, G.E.R. (1937) *The hydrology of the Southern Ocean.* Discovery Reports, 15:3-122.

Deacon, G.E.R. (1977) *The Antarctic Ocean.* Interdisciplinary Science Reviews, 2(2):109-123.

Defant, A. (1936) *Die troposphäre. Deutsche Atlantische Expedition "Meteor" 1925-1927.* Wiss. rg., Bd. VI, Teil I, 3. Lief., 289-411.

Diaz, A.F.; Studzinski, C.D.; Mechoso, C.R. (1998) *Relationships between precipitation anomalies in Uruguay and Southern Brazil and sea surface temperature in the Pacific and Atlantic Oceans.* Journal of Climate, 11: 251-271.

Donlon, C.J.; Castro, S.L.; Kaye, A. (1999) *Aircraft validation of ERS-1 ATSR and NOAA-14 AVHRR sea surface temperature measurements*. International Journal of Remote Sensing, 20(18): 3503-3513.

Emilsson, I. (1961) *The shelf and coastal waters off Southern Brazil*. Boletim do Instituto Oceanográfico da Universidade de São Paulo, 11:101-112.

Evans, D.L. and Signorini, S.S. (1985) *Vertical structure of the Brazil Current*. Nature, 315:48-50.

Figueroa, H.A. and Olson, D.B. (1989) *Lagrangian statistics in the South Atlantic as derived from SOS and FGGE drifters*. Journal of Marine Research, 47:525-546.

Fiúza, A.F.G. (1992) *The measurement of sea surface temperature from satellites. In: Space Oceanography*. Cracknell, A.P. (ed.). World Scientific Publishing Co. Pte. Ltd. 1992, 388pp.

Forrester, T.N.; Guymer, T.H.; Challenor, P.G. (1992) *Preliminary validation of ATSR sea surface temperatures near the Faeroes*. In: Proceedings. First ERS-1 Symposium - Space at the Service of our Environment. Cannes, France, 4-6 November 1992, p. 807-811.

Fu, L. (1981) *The general circulation and meridional heat transport of the subtropical South Atlantic determined by inverse methods*. Journal of Physical Oceanography, 11:1171-1193.

Garcia, C.A.E. (1997) *Physical Oceanography*. In: Chapter 6.2, Seeliger, U.; Odebrecht, C.; Castello, J.P. (Eds.) Subtropical Convergence Environments: The coast and sea in the Southwestern Atlantic. Springer-Verlag, Berlin Heidelberg. 308pp.

Garfield, N. III. (1990) *The Brazil Current at subtropical latitudes*. Ph.D. Thesis, University of Rhode Island, USA, 122pp.

Garvine, R.W.; Wong, K-C.; Gawarkiewicz, G.G.; McCarthy, R.K.; Houghton, R.W.; Aikman III, F. (1988) *The morphology of shelf break eddies*. Journal of Geophysical Research, 93(C12): 15593-15607.

Garzoli, S. (1993) *Geostrophic velocity and transport variability in the Brazil-Malvinas Confluence*. Deep-Sea Research, 40(7):1379-1403.

Garzoli, S. and Garraffo, Z. (1989) *Transports, frontal motions and eddies at the Brazil-Malvinas Currents Confluence*. Deep-Sea Research, 36(5):681-703.

Garzoli, S. and Simionato, C. (1990) *Baroclinic instabilities and forced oscillations in the Brazil/Malvinas confluence front*. Deep-Sea Research, 37(6):1053-1074.

Goni, G.; Kamholz, S.; Garzoli, S.; Olson, D. (1996) *Dynamics of the Brazil-Malvinas Confluence based on inverted echo sounders and altimetry*. Journal of Geophysical Research, 101(C7):16273-16289.

Gordon, A.L. (1989) *Brazil-Malvinas Confluence - 1984*. Deep-Sea Research, 36:359-384.

Gordon, A.L. and Greengrove, C.L. (1986) *Geostrophic circulation of the Brazil-Falkland confluence*. Deep-Sea Research, 33(5):573-585.

Grimm, A.M.; Ferraz, S.E.T.; Gomes, J. (1998) *Precipitation anomalies in Southern Brazil associated with El Niño and La Niña events*. Journal of Climate, 11: 2863-2880.

Guerrero, R.A., Acha, E.M., Framiñan, M.B., Lasta, C.A. (1997) *Physical oceanography of the Rio de la Plata Estuary, Argentina*. Continental Shelf Research, 17(7):727-742.

Guerrero, R.A., Piola, A.R. (1997) *Masas de agua en la plataforma continental*. In: Boschi, E.E. (Ed.), El mar argentino y sus recursos pesqueros, Tomo 1, Antecendentes históricos de las exploraciones en el mar y las características ambientales. INIDEP, Secretaría de Agricultura, Ganadería, Pesca y Alimentación, Mar del Plata, Argentina. (in Spanish)

Hoffmann, J.A.J.; Núñez, M.N.; Piccolo, M.C. (1997) *Características climáticas del Océano Atlántico Sudoccidental*. In: Boschi, E.E. (Ed.), El mar argentino y sus recursos pesqueros, Tomo 1, Antecendentes históricos de las exploraciones en el mar y las características ambientales. INIDEP, Secretaría de Agricultura, Ganadería, Pesca y Alimentación, Mar del Plata, Argentina.

Hofmann, E.E. (1985) *The large-scale horizontal structure of the Antarctic Circumpolar Current from FGGE drifters*. Journal of Geophysical Research, 90(C4):7087-7097.

Holyer, R.J. and Peckinpaugh, S.H. (1989) *Edge detection applied to satellite imagery of the oceans*. IEEE Transactions on Geoscience and Remote Sensing, 27(1):46-56.

Hooker, S.B. and Brown, J.W. (1996) *Dipole rings and vortex interactions of the Brazil Current*. IEEE Transactions on Geoscience and Remote Sensing, 34(6):1323-1330.

Hubold, G. (1980) *Hydrography and plankton off Southern Brazil and Rio de La Plata, August-November 1977*. Atlântica, 4:1-22.

Jenkins, G.M. and Watts, D.G. (1968) *Spectral analysis and its applications*. Holden-Day, san Francisco, 525pp.

Jensen, J.R. (1986) *Introductory digital image processing: a remote sensing perspective*. Prentice-Hall, Englewood Cliffs, New Jersey, 379pp.

Jones, M.S. (1997) *Satellite techniques for studing ocean circulation*. Ph.D. Thesis. Mullard Space Science Laboratory, University College London, Dorking, UK. 195pp.

Josey, S. A.; Kent, E. C.; Taylor, P. K. (1998) *The Southampton Oceanography Centre (SOC) Ocean - Atmosphere Heat, Momentum and Freshwater Flux Atlas*. Southampton Oceanography Centre Report No. 6, 30 pp. plus figures.

Kalnay, E.; Kanamitsu,M.; Kilster, R.; Collins, W.; Deaven, D.; Gandin, L.; Iredell, M.; Saha, S.; White, G.; Woollen, J.; Zhu, Y.; Chelliah, M.; Ebisuzaki, W.; Higgins, W.; Janowiak, J.; Mo, K. C.; Ropelewski, C.; Wang, J.; Leetmaa, A.; Reynolds, R.; Jenne, R.; Joseph, D. (1996). *The NCEP/NCAR 40-Year Reanalysis Project*. Bulletin of the American Meteorological Society, 77:437-471.

Kampel, M. and Silva Jr., C.L. (1996) Análise EOF da Confluência Brasil-Malvinas a partir de imagens AVHRR. In: Proceedings. VIII Simpósio Brasileiro de Sensoriamento Remoto. Salvador, Brazil, 14-19 April 1996. INPE, Selper. CD-ROM. (in Portuguese)

Keogh, S.J.; Robinson, I.S.; Donlon, C.J.; Nightingale, T.J. (1999) *The accuracy of AVHRR SST determined using shipborne radiometers*. International Journal of Remote Sensing, 20(14): 2871-2876.

Kidwell, K.B. (1995) *NOAA Polar Orbiter Data users guide (TIROS-N, NOAA-6, NOAA-7, NOAA-8, NOAA-9, NOAA-10, NOAA-11, NOAA-12, NOAA-13 and NOAA-14.* NOAA/NESDIS National Climatic Data Center, Satellite Data Services Division, Washington, D.C.

Kizu, S. and Sakaida, F. (1996) *A new set of MCSST equations for NOAA-9/AVHRR.* Journal of Oceanography, 52:235-249.

Knauss, J.A. (1997) *Introduction to physical oceanography.* 2nd. Ed. Prentice-Hall, London, 309pp.

Lagerloef, G.S.E. and Berstein, R.L. (1988) *Empirical Orthogonal Function analysis of Advanced Very High Resolution Radiometer temperature patterns in Santa Barbara Channel.* Journal of Geophysical Research, 93(C6):6863-6873.

Legeckis, R. (1978) *A survey of worldwide sea surfece temperature fronts detected by environmental satellites.* Journal of Geophysical Research, 83(C9):4501-4522.

Legeckis, R. and Gordon, A.L. (1982) *Satellite observations of the Brazil and Falkland Currents - 1975 to 1976 and 1978.* Deep-Sea Research, 29:375-401.

Llewellyn-Jones, D.T.; Minnett, P.J.; Saunders, R.W.; Zavody, A M. (1984) *Satellite multichannel infrared measurements of sea surface temperature of the N.E. Atlantic Ocean using AVHRR/2.* Quarterly Journal of the Royal Meteorological Society, 110:613-631.

Lima, I.D., Garcia, C.A.E., Möller Jr., O.O. (1996) *Ocean surface processes on the southern Brazilian shelf: characterization and seasonal variability.* Continental Shelf Research, 16(10): 1307-1317.

Little, J.N. and Shure, L. (not dated) *Signal processing toolbox for use with Matlab.* The MathWorks, Inc. np.

Loder, J.W., Boicourt, W.C., Simpson, J.H. (1998) *Western ocean boundary shelves coastal segment (W).* In: Robinson, A.R., Brink, K.H. (Eds.), The Sea, vol. 11. John Wiley and Sons.

Longhurst, A. (1998) *Ecological geography of the sea*. Academic Press, San Diego. 398pp.

Lorenzzetti, J.A. and Gaeta, S.A. (1996) *The Cape Frio Upwelling effect over the South Brazil Bight northern sector shelf waters: a study using AVHRR images*. In: Proceeding of the International Archives of Photogrammetry and Remote Sensing, Vol. XXXI, Part B7, Vienna, Austria. p. 448-453.

Lorenzzetti, J.A.; Stevenson, M.R.; Silva Jr., C.L.; Souza, R.B. (1994) *Behaviour of a semi-permanent Eddy as observed from AVHRR images and WOCE drifters*. In: Abstracts from the Symposium: The South Atlantic - present and past circulation. Bremen, Germany, 15-19 August 1994. Berichte, Fachbereich Geowissenschaften, Universitat Bremen, No. 52, p. 83-84.

Lorenzzetti, J.A. and Kampel, M. (1998) *Remote sensing of the SW South Atlantic using satellite tracked drifters and AVHRR images*. In: Proceedings. IX Simpósio Brasileiro de Sensoriamento Remoto. Santos, Brazil, 11-18 September 1998. INPE, Selper. CD-ROM paper No. 92.

Matano, R.P. (1993) *On the separation of the Brazil Current from the coast*. Journal of Physical Oceanography, 23:79-90.

Matano, R.P.; Schlax, M.G.; Chelton, D.B. (1993) *Seasonal variability in the Southwestern Atlantic*. Journal of Geophysical Research, 98(C10):18027-18035.

Maul, G.A. (1985) *Introduction to satellite oceanography*. Martinus Nijhoff Publishers, Dordrecht, 606pp.

McClain, E.P.; Pichel, W.G.; Walton, C.C. (1985) *Comparative performance of AVHRR-based multi-channel sea surface temperatures*. Journal of Geophysical Research, 90:11587-11601.

McClain, E.P.; Fu, G.; Darzi, M.; Firestone, J.K. (1992) *PC-Seapak User's Guide, Version 4.0*. NASA, Goddard Space Flight Center, Greenbelt, MD, USA, 332pp. (NASA Technical Memorandum 104557).

McDonagh, E.L. and Heywood, K.J. (1999) *The origin of an anomalous ring in the Southeast Atlantic*. Journal of Physical Oceanography, 29:2025-2064.

Müller, T.J.; Ikeda, Y.; Zangenberg, N.; Nonato, L.V. (1998) *Direct measurements of western boundary currents off Brazil between 20°S and 28°S*. Journal of Geophysical Research, 103(C3):5429-5437.

Mutlow, C.T.; Závody, A.M.; Barton, I.J.; Llewellyn-Jones, D.T. (1994) *Sea surface temperature measurements by the along-track scanning radiometer on the ERS 1 satellite: Early results*. Journal of Geophysical Research, 99(C11):22575-22588.

Nienchesky, L.F. and Fillmann, G. (1997) *Chemical characteristics*. In: Chapter 6.3, Seeliger, U.; Odebrecht, C.; Castello, J.P. (Eds.) Subtropical Convergence Environments: The coast and sea in the Southwestern Atlantic. Springer-Verlag, Berlin Heidelberg. 308pp.

Niiler, P.P.; Paduan, J.D.; Sybrandy, A.L.; Sombardier, L. (1991) *The WOCE/TOGA Lagrangian surface drifter*. In: Proceedings of the 1991 IEEE Oceans (Oceans 91). October 1-3, 1991. Honolulu, Hawaii, USA. Vol. 2, p.839-843.

Niiler, P.P.; Sybrandy, A.S.; Paulan, P.M.; Bitterman, D. (1995) *Measurements of the water-following capability of holey-sock and TRISTAR drifters*. Deep-Sea Research, 42 (11/12):1951-1964.

Nobre, P. and Shukla, J. (1996) *Variations of sea surface temperature, wind stress, and rainfall over the Tropical Atlantic and South America*. Journal of Climate, 9:2464-2479.

National Remote Sensing Centre Limited (NRSCL) (1995) ERS-1 Along Track Scanning Radiometer Products User Guide, Issue 1.0. NRSCL, UK. (PF-UG-NRL-OP-0002).

Odebrecht, C. and Garcia, V.M.T. (1997) *Phytoplankton*. In: Chapter 6.7, Seeliger, U.; Odebrecht, C.; Castello, J.P. (Eds.) Subtropical Convergence Environments: The coast and sea in the Southwestern Atlantic. Springer-Verlag, Berlin Heidelberg. 308pp.

Olson, D.B., Podestá, G.P., Evans, R.H., Brown, O . B. (1988) *Temporal variations in the separation of Brazil and Malvinas currents*. Deep-Sea Research, 35(12):19711-1990.

Parada, M. and Cantón, M. (1998) *Sea surface temperature variability in Alborán sea from satellite data*. International Journal of Remote Sensing, 19(13): 2439-2450.

Patterson, S.L. (1985) *Surface circulation and kinetic energy distributions in the Southern hemisphere oceans from FGGE drifting buoys*. Journal of Physical Oceanography, 15:865-884.

Peterson, R.G. (1992) *The boundary currents in the western Argentine Basin*. Deep-Sea Research, 39:623-644.

Peterson, R.G. and Stramma, L. (1991) *Upper-level circulation in the South Atlantic Ocean*. Progress in Oceanography, 26:1-73.

Peterson, R.G.; Johnson, C.S.; Krauss, W.; Davis, R.E. (1996) *Lagrangian measurements in the Malvinas Current*. In: Wefer, G.; Berger, W.H.; Siedler, G.; Webb, D.J. (Eds.). The South Atlantic: Present and past circulation. Springer-Verlag, Berlin, 1996. 644 pp.

Piccolo, M.C. (1998) *Oceanography of the Western South Atlantic continental shelf from 33 to 55 °S*. In: Robinson, A.R., Brink, K.H. (Eds.), The Sea, vol. 11. John Wiley and Sons.

Piola, A.R.; Figueroa, H.A.; Bianchi, A.A. (1987) *Some aspects of the surface circulation south of 20°S revealed by first GARP Global Experiment drifters*. Journal of Geophysical Research, 92(C5):5101-5114.

Piola, A.R. and Rivas, A.L. (1997) *Corrientes en la plataforma continental*. In: Boschi, E.E. (Ed.), El mar argentino y sus recursos pesqueros, Tomo 1, Antecendentes históricos de las exploraciones en el mar y las características ambientales. INIDEP, Secretaría de Agricultura, Ganadería, Pesca y Alimentación, Mar del Plata, Argentina. (in Spanish)

Podestá, G. (1997) *Utilización de datos satelitarios en investigaciones oceanográficas y pesqueras en el Océano Atlántico Sudoccidental*. In: Boschi, E.E. (Ed.), El mar argentino y sus recursos pesqueros, Tomo 1, Antecendentes históricos de las exploraciones en el mar y las características ambientales. INIDEP, Secretaría de Agricultura, Ganadería, Pesca y Alimentación, Mar del Plata, Argentina. (in Spanish)

Pond, S. and Pickard, G.L. (1983) *Introductory dynamical oceanography*. 2nd. Ed. Butterworth-Heinemann Ltd., Oxford, 329pp.

Preisendorfer, R.W. (1988) *Principal component analysis in meteorology and oceanography*. Elsevier, Amsterdam, 425 pp.

Press, W.H.; Teukolsky, S.A.; Vetterling, W.T.; Flannery, B.P. (1992) *Numerical recipes in fortran 77: the art of scientific computing*. Vol. 1 of Fortran numerical recipes. Cambridge University Press, UK. 933pp.

Provost, C.; Garcia, O.; Garçon, V. (1992) *Analysis of satellite sea surface temperature time series in the Brazil-Malvinas Current Confluence region: Dominance of the annual and semiannual periods*. Journal of Geophysical Research, 97(C11):17841-17858.

Provost, C. and Le Traon, P-Y. (1993) *Spatial and temporal scales in altimetric variability in the Brazil-Malvinas Current Confluence region: Dominance of the semiannual period and large spatial scales*. Journal of Geophysical Research, 98(C10):18037-18051.

Reid, J.L. (1989) *On the total geostrophic circulation of the South Atlantic Ocean: Flow patterns, tracers and transports*. Progress in Oceanography, 23:149-244.

Reid, J.L.; Nowlin Jr., W.D.; Patzerd, W.C. (1977) *On the characteristics and circulation of the Southwestern Atlantic Ocean*. Journal of Physical Oceanography, 7:62-91.

Richards, K.J. and Gould, W.J. (1996) *Ocean weather - eddies in the sea*. In: Chapter 4, Summerhayes, C.P. and Thorpe, S.A. (Eds.) Oceanography: an illustrated guide. Manson Publishing Ltd., London, 352pp.

Robinson, I.S. (1985) *Satellite Oceanography - an introduction for oceanographers and remote-sensing scientists*. Ellis Horwood Ltd., Chichester, U.K., 455pp.

Robinson, I.S. and Donlon, C. (1994) *Filaments and fine structure of sea surface temperatures in ATSR image data*. In: Proceedings. Second ERS-1 Symposium - Space at the Service of our Environment. Hamburg, Germany, 11-14 October 1994, p. 1087-1092.

Sarukhanyan, E'.I. (1987) *Structure and variability of the Antarctic Circumpolar Current*. New Delhi, India, A.A. Balkema/Rotterdam. 108pp. (Russian Translation Series, 44).

Saunders, R.W.; Smith, A.H.; Harrison, D.L. (1993) *Sea-surface temperature measurements by the ATSR*. The Meteorological Magazine, 122(1450):105-113.

Schäer, H. and Krauss, W. (1995) *Eddy statistics in the South Atlantic as derived from drifters drogued at 100 m*. Journal of Marine Research, 53:403-431.

Schmid, C.; Schafer, H.; Podestá, G.; Zenk, W. (1995) The Vitória eddy and its relation to the Brazil Current. Journal of Physical Oceanography, 25(11): 2532-2546.

Schluessel, P.; Emery, W.J.; Grassi, H.; Mammen, T. (1990) *On the bulk-skin temperature difference and its impact on satellite remote sensing of sea surface temperature.* Journal of Geophysical Research, 95(C8): 13341-13356.

Schowengerdt, R.A. (1997) *Remote Sensing: models and methods for image processing.* Academic Press, San Diego, CA, 522 pp.

Seeliger, U. and Odebrecht, C. (1997) *Introduction and overview.* In: Chapter 1, Seeliger, U.; Odebrecht, C.; Castello, J.P. (Eds.) Subtropical Convergence Environments: The coast and sea in the Southwestern Atlantic. Springer-Verlag, Berlin Heidelberg. 308pp.

Seeliger, U.; Odebrecht, C.; Castello, J.P. (Eds.) (1997) *Subtropical Convergence Environments: The coast and sea in the Southwestern Atlantic.* Springer-Verlag, Berlin Heidelberg. 308pp.

Semtner Jr., A.J. and Chervin, R.M. (1988) *A simulation of the global ocean circulation with resolved eddies.* Journal of Geophysical Research, 93(C12): 15502-15522.

Servain, J. (1991) *Simple climatic indices for the Tropical Atlantic Ocean and some applications.* Journal of Geophysical Research, 96(C8): 15137-15146.

Servain, J.; Busalacchi, A.J.; McPhaden, M.J.; Moura, A.D.; Reverdin, G.; Vianna, M.; Zebiak, S.E. (1998) *A Pilot Research moored Array in the Tropical Atlantic (PIRATA).* Bulletin of the American Meteorological Society, 79(10): 2019-2031.

Silva Jr., C.L.; Kampel, M.; Araujo, C.E.S.; Stech, J.L. (1996) *Observação da penetração do ramo costeiro da Corrente das Malvinas na costa sul-sudeste do Brasil a partir de imagens AVHRR.* In: Proceeding of the 8th Brazilian Symposium on Remote Sensing. Salvador, Brazil, 14-19 April 1996. (in Portuguese)

Smith, E. (1992) *A user's guide to the NOAA Advanced Very High Resolution Radiometer Multichannel Sea Surface Temperature data set.* Rosenstiel School of Marine and Atmospheric Science, University of Miami, PO-DAAC, JPL.

Smythe-Wright, D.; Gordon, A.L.; Chapman, P.; Jones, M.S. (1996) *CFC-113 shows Brazil Eddy crossing the South Atlantic to the Agulhas Retroflexion region.* Journal of Geophysical Research, 101(C1):885-895.

Souza, R.B. and Cabral, A.P. (1996) *Effects of topography on the Brazil Current at 31°S.* Symposium on Oceanography, 3. IOUSP, São Paulo, Brazil, December 02-06, 1996. Abstracts.

Souza, R.B. and Robinson, I.S. (1998) *Lagrangian and infrared observations of surface currents in the Brazil-Malvinas Confluence Zone, 1993-1994.* International WOCE Newsletter 31:32-35.

Stech, J.L.; Lorenzzetti, J.A.; de Souza, J.M.C.; Araujo, C.E.S. (1996) *A mesoscale Brazil Current frontal eddy observed through AVHRR images and current meter moorings.* In: Proceedings from the International Archives of Photogrammetry and Remore Sensing. Vienna, Austria, 1996, Vol. 31, Part B7, p. 650-653.

Stevenson, M.R. (1996) *Recirculation of the Brazil Current South of 23°S.* International WOCE Newsletter 22: 30-32.

Stevenson, M.R. and Souza, R.B. (1994) *Recirculation of the Brazil Current South of 20°S.* In: Abstracts from the Symposium: The South Atlantic - present and past circulation. Bremen, Germany, 15-19 August 1994. Berichte, Fachbereich Geowissenschaften, Universitat Bremen, No. 52, p. 149.

Stevenson, M.R., Castro Filho, B.M. (1996) *Comparison of surface layer currents determined by satellite tracked drifters and in situ anchored current meters off Southeast Brazil.* In: Proceedings of the International Archives of Photogrammetry and Remote Sensing, Vienna, Austria, Vol. 31, Part B7, p. 654-659.

Stevenson, M.R., Dias-Brito, D., Stech, J.L., Kampel, M. (1998) *How do cold water biota arrive in a tropical bay near Rio de Janeiro, Brazil?* Continental Shelf Research, 18:1595-1612.

Stramma, L.; Ikeda, Y.; Peterson, R.G. (1990) *Geostrophic transport in the Brazil Current region north of 20°S.* Deep-Sea Research, 37:1875-1886.

Strong, A.E. and McClain, E.P. (1984) *Improved ocean surface temperatures from space - comparisons with drifting buoys*. Bulletin American Meteorological Society, 65(2): 138-142.

Stech, J.L., Lorenzzetti, J.A . (1992) *The response of the South Brazil Bight to the passage of wintertime cold fronts*. Journal of Geophysical Research, 97(C6):9507-9520.

Sunyé, P.S. (1999) *Effet de la variabilité climatique régionale sur la pêche de la sardinelle le long de la côte sud-est du Brésil (1964-1993)*. PhD thesis. Institut Universitaire Européen de la Mer, Université de Bretagne Occidentale, 130 pp. (in French)

Sunyé, P.S. and Servain, J. (1998) *Effects of seasonal variations in meteorology and oceanography on the Brazilian sardine fishery*. Fisheries Oceanography, 7(2): 89-100.

Sverdrup, H.U.; Johnson, M.W.; Fleming, R.H. (1942) *The Oceans: Their Physics, Chemistry and General Biology*. Prentice-Hall, Englewood Cliffs, N.J. 1060pp.

Sybrandy, A.L. and Niiler, P.P. (1991) *The WOCE/TOGA Lagrangian drifter construction manual*. SOI Report 91/6, WOCE Report 63. 58pp.

Sybrandy, A.L.; Martin, C.; Niiler, P.P.; Charpentier, E.; Meldrum, D.T. (1995) *WOCE Surface Velocity Programme barometer drifter construction manual*. SOI Report 95/27, WOCE Report 134/95. Version 1.0. 63pp.

Thomsen, H. (1962) *Masas de agua caracteristicas del Oceano Atlantico parte Sudoeste*. Publication H632, Secretaria de Marina, Servicio de Hidrografia Naval, Buenos Aires, 22pp. (in Spanish)

Tomczac, M. and Godfrey, J.S. (1994) *Regional oceanography: an introduction*. Pergamon, Elsevier Science Ltd., England, 422pp.

Tseng, Y.C. (1974) *Study of the surface boundary of the Brazil and Falkland currents*. In: Proceedings. Seminar on Space Applications of Direct Interest to Developing Countries. Instituto Nacional de Pesquisas Espaciais, São José dos Campos, Brazil, Vol. 2.

Tseng, Y.C.; Inostroza, H.M.; Kumar, R. (1977) Study of the Brazil and Falkland currents using THIR images of Nimbus V and oceanographic data in 1972 to 1973. In: Proceedings. International Symposium on Remote Sensing of the Environment, 11. ERIM, Michigan, p. 859-871.

Vivier, F. and Provost, C. (1999a) *Volume transport of the Malvinas Current. Can the flow be monitored by TOPEX/POSEIDON?* Journal of Geophysical Research, 104(C9): 21105-21122.

Vivier, F. and Provost, C. (1999b) *Direct measurements in the Malvinas Current.* Journal of Geophysical Research, 104(C9): 21083-21103.

Vazquez, J.; Perry, K.; Kilpatrick, K. (1998) *NOAA/NASA AVHRR Oceans Pathfinder, Sea Surface Temperature Data Set, User's Reference Manual, Version 4.0.* (JPL Publication D-14070).

Woodruff, S.D.; Lubker, K.W.; Worley, S.J.; Elms, J.D. (1993) *Comprehensive Ocean-Atmosphere Data Set (COADS) release 1a: 1980-92.* Earth System Monitor, 4(1):4-8.

Zambianchi, E. and Griffa, A. (1994) *Applicability of a stochastic model for particle motion to drifter data in the Brazil/Malvinas extension.* Annali della Facolta' di Scienze Nutiche, Instituto Universitario Navali, Naples, Italy, Vol. LXI, p. 75-90.

Zavialov, P.O.; Ghisolfi, R.D.; Garcia, C.A.E. (1998) *An inverse model for seasonal circulation over the Southern Brazilian Shelf: near-surface velocity from the heat budget.* Journal of Physical Oceanography, 28:545-562.

Zavialov, P.O. and Möller, O.O. (2000) Modeling and observations of currents off Southern Brazil and Uruguay: the Rio Grande Current. In: Zatsepin, A.G. (Ed.) Oceanic fronts and related phenomena. UNESCO Workshop Report series (in press).

Závody, A.M.; Gorman, M.R.; Lee, D.J.; Eccles, D.; Mutlow, C.T.; Llewellyn-Jones, D.T. (1994) *The ATSR data processing scheme developed for the EODC.* International Journal of Remote Sensing, 15(4):827-843

Závody, A.M; Mutlow, C.T.; Llewellyn-Jones, D.T. (1995) *A radiative transfer model for sea surface temperature retrieval for the along-track scanning radiometer.* Journal of Geophysical Research, 100(C1):937-952

SOUTHAMPTON UNIVERSITY LIBRARY

USER'S DECLARATION

AUTHOR: SOUZA, RONALD BUSS DE TITLE: SATELLITE AND LAGRANGIAN OBSERVATIONS OF MESOSCALE SURFACE PROCESSES IN THE SOUTHWESTERN ATLANTIC OCEAN

DATE: 2000

I undertake not to reproduce this thesis, or any substantial portion of it, or to quote extensively from it without first obtaining the permission, in writing, of the Librarian of the University of Southampton.

To be signed by each user of this thesis

DATE	SIGNATURE	ADDRESS